Ludwig-Maximilians-Universität
Department of Earth and Environmental Sciences

Seismic Wave Simulation
for Complex Rheologies on
Unstructured Meshes

Josep de la Puente

Acknowledgments

I would like to express my gratitude to all those who have made this thesis possible. First of all to my supervisor Heiner Igel, for his enthusiasm, inspiration and encouragment as well as sound advice. Without his trust on me this thesis would have never been possible.

I am strongly indebted to my co-supervisor Martin Käser, who has worked with me shoulder to shoulder through these three years and has always been there to help and put me on the right track. If the product of my research is any good is, to a large extent, thanks to him. Many thanks also to Michael Dumbser, for his brilliant ideas and always positive thinking. Also for allowing me to use and modify the *SeisSol* code.

Thanks a lot to Peter Moczo for inspiration and for accepting to revise and evaluate this thesis. Also to Jean-Paul Ampuero, José María Carcione, Dimitri Komatitsch and Fabian Krzikalla for providing reference solutions. The whole Bratislava crew is also acknowledged for their great work setting up their excellent online validation tool.

A huge thanks to the SPICE project and to all people who have made it possible and produced something way bigger than the sum of its parts. It has provided to students like me the best education in numerical seismology one could ever wish. Also to my colleagues at the Department, especially to my office mates Marco Stupazzini, Nguyen Pham Dihn and Verena Hermann for sharing lots of good and bad moments and helping me in many ways.

The Munich supercomputing center LRZ, as well as the Stuttgart HLRS, are acknowledged for making available their computing facilities. Also the excellent IT resources and support at Geophysics in Munich.

Very especially to Agnieszka, for constant support and sheer love and for being my true and only driving force. To all the wonderful people that I have been lucky to meet in Munich. A mi familia y colegas, que siempre están y siempre han estado, va por vosotros.

München, September 2007
Josep de la Puente

Zusammenfassung

In vorliegender Arbeit wird die Anwendung numerischer Methoden hoher Approximationsordung zur Simulation seismischer Wellen in komplexen Medien mithilfe unstrukturierter Gitter untersucht. Speziell die neuartige Diskontinuierliche Galerkin (DG) Finite-Elemente-Methode wird dazu auf verschiedene rheologische Modelle erweitert, die viskoelastische, anisotrope und poroelastische Medien beschreiben. Zunächst wird jedoch die DG-Methode für den rein elastischen, isotropen Fall auf unstrukturiertenn Tetraedergittern behandelt. Danach wird die Methodik auf die viskoelastische Wellenausbreitung erweitert, die auf der Formulierung durch generalisierte Maxwell-Körper basiert. Dies erlaubt die Beschreibung eines quasi-konstanten Dämpfungsverhaltens über das gesamte betrachtete Frequenzband. Anschlieend werden anisotrope Materialeigenschaften im allgemeinsten Fall der triklinen Symetrieklasse in das numerische Verfahren mit einbezogen und mit den Effekten der Viskoelastizität verbunden. Abschlieend werden auch poroelastische Medien für Wellen im hochfrequenten und niederfrequenten, diffusiven Bereich berücksichtigt. Für alle rheologischen Modelle werden Konvergenzraten hoher Ordnung sowohl im Raum als auch in der Zeit für dreidimensionale Testprobleme erzielt. Die Konvergenzanalysen und weitere Anwendungsbeispiele bestätigen die Genauigkeit dieses neuen Ansatzes. Durch den lokalen Charakter der DG-Methode und der Verwendung von Tetraedergittern kann das vorgestellte Verfahren auf realistische, groskalige Wellenausbreitungsprobleme in der Vorwärtsmodellierung seismischer Wellen in geometrisch und physikalisch komplexen Medien angewandt werden.

Abstract

The possibility of using accurate numerical methods to simulate seismic wavefields on unstructured meshes for complex rheologies is explored. In particular, the Discontinuous Galerkin (DG) finite element method for seismic wave propagation is extended to the rheological types of viscoelasticity, anisotropy and poroelasticity. First is presented the DG method for the elastic isotropic case on tetrahedral unstructured meshes. Then an extension to viscoelastic wave propagation based upon a Generalized Maxwell Body formulation is introduced which allows for quasi-constant attenuation through the whole frequency range. In the following anisotropy is incorporated in the scheme for the most general triclinic case, including an approach to couple its effects with those of viscoelasticity. Finally, poroelasticity is incorporated for both the propagatory high-frequency range and for the diffusive low-frequency range.

For all rheology types, high-order convergence is achieved simultaneously in space and time for three-dimensional setups. Applications and convergence tests verify the proper accuracy of the approach. Due to the local character of the DG method and the use of tetrahedral meshes, the presented schemes are ready to be applied for large scale problems of forward wave propagation modeling of seismic waves in setups highly complex both geometrically and physically.

Contents

Introduction

The Earth's interior real image is nowadays largely unknown. Direct observation and active imaging cannot reach the deep structure of our planet so that we are forced to use other indirect information to infer our planet's inner structure. The most successful observable used to that purpose is still the signal of the ground motion caused by earthquakes, whose seismic waves travel across our planet's interior. The recorded seismograms contain information on each and every material the wave has traveled through.

The physics governing mechanical wave propagation are well known since the XVIII century. The fundamental laws of linear elastic mechanics predict that solid bodies react to excitation by propagating energy in the form of elastic waves. The velocity at which the waves propagate is solely dependent on the material properties of the media, thus imposing a deterministic link between the travel time of the wave from source to receiver and the mechanical properties of the material crossed by its ray path.

Using such simple model to describe the Earth, as is assuming that it is an elastic isotropic and perfectly spherical body, we have retrieved most of the information on our planet's structure we possess nowadays. The discovery of the Mohorovicić discontinuity in the early XX century and the existence of the Gutenberg discontinuity or of a liquid inner core in the 1930s are some remarkable examples. This classical mechanical model explains such phenomena as the existence of a variety of surface and body waves and their particular properties, the amount of energy transmitted and reflected at a material's interface, the angle of reflection and refraction of such waves generated at an interface or how do their amplitudes decrease with increasing distance from the source. A spherically layered Earth model with different elastic properties can describe to a very good extent the general traits of the observed seismograms. However, when looked at them in detail, a large amount of observed features in those seismograms cannot be fitted by such oversimplified mechanics and geometry. It has become clear in the last decades that a richer description of our planet is needed.

Present models of the Earth [6, 69, 103, 116] show that its mechanical behavior is closer to that of a viscoelastic ellipsoid which shows anisotropic properties in many regions. The discontinuities' depths vary from one point of the planet's surface to the other. Also some parts of it behave as a liquid in the timescales of up to hours, which are relevant in seismology.

The validation of the various proposed models of Earth is performed by solving the forward problem in which the source and material model are assumed to be known and one just wants to obtain a synthetic output. Many different mathematical approaches can be used to that goal. One could wish to exactly solve the equations describing the physics involved in the process of wave propagation, but analytical or quasi-analytical solutions have been found only for very simple geometries, often requiring strong symmetries. Unfortunately the Earth models at hand are not so simple and the results obtained by these methodologies, although formally exact, are of minor practical utility. A different approach, known as discrete or mesh methods, is based on the discretization of the space and time dimensions thus solving the governing equations locally. A big advantage is that heterogeneities and other geometrical complexities can be included much more easily, but the accuracy is decreased as a drawback.

By far, the most popular methods for solving seismic wave propagation problems are finite differences (FD) [93, 102] and finite elements (FE) [142]. The FD method is a grid-point method, meaning that the unknowns are only described at a collection of nodes and no assumptions are made on their values elsewhere. This method can be simple to implement in some cases and its local nature makes it easy to parallelize. Additionally, most numerical methods in seismology rely on FD approaches for the time integration. This method, in its basic form, has the drawback of being less adaptable to complex geometrical models, as the grids are usually chosen to be of a cartesian nature. The FE method is based upon a variational formulation of the equations and is much more flexible geometrically due to the usage of deformed computational cells. Additionally, boundary conditions are handled more easily with FE because it uses the so-called weak form of the equation system. However, FE computations can become very expensive, specially when involving high-degree polynomials. Other popular methods like the pseudo-spectral (PS) [34, 129] and spectral-element (SE) [85, 114, 123] have increased a lot the accuracy with which the wavefields can be solved and to some extent can handle complex geometries by using deformed quadrilateral or hexahedral elements in the space discretization. At present time, the SE method is the only method to be applied for fully 3D simulations of the whole planet Earth. However, when it comes to really strong topographies and heterogeneity distribution, these element types often fail to $mesh$ our desired model properly. Standard finite volumes (FV) [51], as well as FE, can get around this problem by using triangular or tetrahedral meshes but their accuracy is limited (commonly first- or second-order schemes).

The aim of this thesis is to provide solutions for the forward model which can be used on completely unstructured (triangular or tetrahedral) meshes with $high-order$ accuracy and beyond purely elastic and isotropic models. One method will be explored in detail: the Discontinuous Galerkin (DG) method [40, 115]. The DG method has been extremely successful in the Computational Fluid Dynamics

(CFD) community as it is able to solve fluid-flow problems with very accurate results in cases where unstructured meshing is convenient. This method can be understood as a spectral version of the classic FV, meaning that fewer elements are required to obtain the same accuracy as a polynomial representation of the unknowns is used inside each computational cell. Although classically coupled with Runge-Kutta type time discretization schemes, a much more efficient and arbitrary high-order time integration based upon ADER (Arbitrary high-order DERivatives) concepts [131] has been recently developed and successfully applied to the DG framework [52]. The resulting scheme, called ADER-DG, automatically has the same accuracy order in space and time without requiring storage of sub steps of information between one time step and the next. Consequently, the scheme has global high-order convergence properties, an unprecedented property in mesh-based seismic wave propagation solvers.

The application of this method to seismology problems is very recent [55, 75] and has shown to be able to handle most important boundary conditions (free surface, absorbing boundaries), source types (point sources, extense kinematic rupture models) and intercell heterogeneity. In order to apply this method to practical problems, complex rheologies have been accurately treated in the present work so that the convergence properties of the method are conserved for all cases. Three major linear non-standard rheology types are explored: viscoelastic, anisotropic and poroelastic. The results show that the method described here can solve simple problems with comparable or better accuracy than other common methods, with the advantage of being potentially able to handle geometrical complexity which is beyond reach for regular-grid based methods.

In order to cope with the size of contemporary seismology problems, the method has been parallelized and installed in a variety of computational facilities, from middle-size clusters to high-performance computers. All together the result of this work is a method which is not only very accurate but also very flexible in terms of the complexity of the models that can be solved and the physics that can be reproduced.

This thesis is subdivided into four major parts, arranged as follows:

In **Chapter 1** the ADER-DG scheme is introduced. Some basic concepts on numerical fluxes and hyperbolic equation systems are described and upon them the ADER-DG method's algorithm is outlined. Special detail is given to the basis functions used and how to improve the method's efficiency through quadrature-free integration and reference element mapping. The Cauchy-Kovalewski procedure [131], which allows for high-order ADER time integration, is fully described as well. Finally further details on computational aspects are given and the method's performance in a large-scale test is shown to validate both the mathematical approach and its implementation.

In **Chapter 2** the application of the ADER-DG method to viscoelastic rheologies

is discussed. The soil is known to act as a lossy medium at all scales [1]. Energy is dissipated as the rock shows properties slightly deviating from the elastic regime, in a way which can be ideally described by a combination of mechanical springs and dashpots which mimics a viscoelastic behavior. In a viscoelastic material one expects waves to be both damped and dispersive due to energy losses [92]. Here we show how to incorporate realistic viscoelastic behavior in the time-domain with quasi-constant Q values by using the Generalized Maxwell Body rheology type [63]. Additional variables (anelastic functions) are used to overcome the apparition of convolutional products. A study on the accuracy, as well as the impact in computational costs of the viscoelastic rheology is further shown.

In **Chapter 3** the field of elastic anisotropy and its implementation with the ADER-DG method is explored. Rocks show often intrinsic anisotropy due to the crystalline distribution of its components [22]. As a result the properties of them are not the same in different directions. Also macroscopically one can observe anisotropy due to the stacking of intermixed fine layers of different materials which are individually isotropic. When a seismic wave travels through such a medium, in general, the particle motion induced becomes a mixed state of pressure and shear motion, called *quasi*-waves. As a consequence, not only the travel times vary with the direction of propagation of the wave but also its polarization state [27]. In the Earth, anisotropy is present in many areas as a minor but not-negligible effect, and as such it is in this Chapter implemented for the most general triclinic case. In the case of a method based upon unstructured meshes this is a further challenging effort as the computational elements are not aligned with the symmetry axes of the modeled anisotropic materials. The scheme is shown to remain high-order by convergence tests and its accuracy is verified by comparing its results with some other methods and available analytical solutions.

In **Chapter 4** the ADER-DG schemes are applied to the poroelastic case. This rheology type is not observed at seismological timescales for the globe, but can be very important at smaller scales. Poroelasticity describes the properties of a porous solid material filled completely with some fluid. The motion of the solid and fluid particles is then coupled and they can be treated macroscopically as a whole single entity. Biot's theory [12, 13] describes such behavior, which is introduced here for the ADER-DG scheme. A new wave type (the *slow P*-wave) appears in this case which is successfully reproduced in shown simulations. A fundamental problem appears when reaching low-frequencies in Biot's theory, which is the conversion of the slow wave into a diffusive mode [12]. For time-domain explicit solvers this ends up in instability problems [24]. A space-time discontinuous method (ADER-DG(ST)) is introduced [54], which is a locally implicit method. This ADER-DG variant is able to avoid such instabilities by keeping the convergence properties of standard ADER-DG schemes, having little additional cost in computation terms. The ADER-DG(ST) results are compared with those obtained

applying a fraction-step method to separate the non-diffusive hyperbolic equation system from the diffusive one. It is shown with examples that the ADER-DG(ST) method successfully captures both the propagatory and the diffusive effects much more accurately than classical splitting techniques.

Chapters 2 to 4 are fairly independent, and thus conclusions for them are written at the end of each respective Chapter. A final **Outlook** will summarize the conclusions of this thesis as well as considerations concerning open problems and ideas for future research.

Additionally **Appendix A** and **B** provide additional information on the basis functions used and their coordinate rotation.

The results shown in this thesis have been computed making use of the *SeisSol* software. *SeisSol* is a strongly modified version of the original *HydSol* code developed at the IAG Stuttgart and adapted by M. Dumbser and M. Käser to the seismic wave propagation problem. In order to compute the results shown in the present work, further modifications by the author have expanded the functionality of the code to the viscoelastic, anisotropic and poroelastic problems. *SeisSol* is programmed in Fortran90 and uses MPI libraries for parallel computation.
A variety of computing facilities have been used to perform the simulations shown in the present work. A local cluster *Tethys* at Geophysics Munich has helped developing and testing the implementations while the super computing facilities at the HLRS Stuttgart and LRZ Munich have been widely used to produce most final results. Special attention deserves the new HLRB2 SGI shared memory system, whose outstanding performance has made possible to run some of the most computationally demanding applications.

The practical totality of the reference solutions used to validate the results of this thesis is available at the SPICE Software Library (www.spice-rtn.org/library). Further, the SPICE Code Validation (see www.nuquake.eu/SPICECVal) webpage displays the results of SeisSol for the elastic and viscoelastic application examples, which can be thoroughly compared online to other existing solutions for the same problems.

Chapter 1

The ADER-DG Method for Seismic Wave Propagation

In this Chapter the ADER-DG method for solving the elastic wave equations in three-dimensional media is introduced. First, an overview on numerical methods applied to seismology is presented. Later on a discussion on the elastic isotropic wave equations, on hyperbolic partial differential equation systems and their properties and on the concept of numerical fluxes provides the required background for understanding the ADER-DG method. The method itself, as well as the time marching scheme, are fully developed and described in the following Section. The most common boundary conditions are treated in a Section of their own, followed by some computational aspects relevant to the method's implementation. Finally a large scale application is shown to verify the accuracy of the scheme and we give a brief description of some characteristics of the other methods for seismic wave propagation on unstructured meshes which can be an alternative to the ADER-DG method. This Chapter and the whole thesis will follow [55, 75], and try to keep as close as possible to the notation used by the authors for practical purposes.

1.1   General Overview

Contemporary seismology relies heavily on numerical computations to understand phenomena observed in nature. For example, the conditions of pressure and temperature associated with the seismogenic fault zones are unreachable in laboratories. Such limitations are also present in other geophysical processes thus making of computers an alternative tool to validate assumptions in geosciences. In seismic wave propagation the state has been reached in which the physics governing the phenomena are fully understood, thus leaving discrepancies between observational and computed data solely a function of two major factors: wrong model assumptions or inaccurate mathematical solutions.
Despite the formal accuracy of exact solutions derived analytically, the higher

flexibility in the model's parametrization that offer mesh-based methods is preferred for practical studies. A variety of numerical algorithms to solve the elastic wave equations using mesh methods have been developed within the last decades. First approaches were constrained by the limited computational power available at the time to simplified 1D and 2D cases, whereas in the last decade the application of fully 3D schemes has grown popular. Early attempts used the Finite Differences (FD) principles because of its easy implementation and robust properties. Various formulations and specific algorithms have been developed, e.g. [89, 93, 102, 136, 137], improving both accuracy and efficiency. A summary of recent developments in FD is given in [100]. Similarly Pseudo-Spectral (PS) methods [34, 72, 129] opt for using collocation points associated to known analytical functions for achieving more precise results in the solution of the integro-differential equations. These two methods have the drawback of being badly suited to obtain solutions for non-Cartesian geometries. On the other hand, Finite-Element (FE) techniques show a very good flexibility as they can be applied to many cell types other than cubes [142]. This is extremely useful for meshing complicated geometries, thus making FE a tool of choice for engineers during the last decades. Unfortunately, their accuracy is limited and a large amount of elements are required in order to successfully capture wave phenomena in real applications. In addition to these methods, the Spectral Element Method (SEM) [85, 114, 123] deserves special attention. This method, essentially a high-order FE method using PS-like spatial integration, has proved to be extremely accurate and efficient in solving wave propagation problems. It is based upon hexahedral meshes, where the use of Gauss-Lobatto-Legendre integration points and Legendre polynomials as basis functions helps building up a method which, in addition, is well suited for parallelization and thus applicable to solve very large scale problems. The hexahedra forming the SEM mesh can be deformed and unstructured as FE cells do. However, when it comes to very complex geometries, the hexahedral meshing approaches (known as paving and sweeping) are not optimal, especially when compared to tetrahedra or Voronoi cell types.

The Discontinuous Galerkin (DG) method (see [39] for a review), on the other hand, has been widely used for electromagnetic and fluid flow problems. A DG method can be understood as an FE method combined with numerical fluxes, which are essential to the FV method framework. When using a DG method, each element contains a local discretization of the solution, for which a set of basis functions are used. The number of basis functions and particular expressions can be many as long as they behave as good interpolants. In the present case, the Dubiner basis is used as it is orthogonal and complete to interpolate polynomials of a desired degree. The values of the variables at the intercell boundaries are not required to be continuous. A proper solution to the intercell discontinuity is obtained by using numerical fluxes to handle the surface integrals.

The DG method has recently been extended to the seismic wave propagation problem [55, 75] in combination with the Arbitrary high-order DERivatives (ADER)

concepts introduced by Dumbser and Munz in [52, 61, 60] for linear hyperbolic systems with constant coefficients or for linear systems with variable coefficients in conservative form. The ADER approach, originally introduced by Toro *et al.* [134] and further developed in [131, 121, 122] in the FV framework and the Discontinuous Galerkin finite element method, offers the unprecedented possibility of obtaining high-order explicit solutions without requiring the storage of intermediate time stages of e.g. Runge-Kutta schemes. Additionally, the meshing process is strongly simplified by the use of tetrahedra with no effect on the scheme's accuracy.

1.2   Elastic Wave Equations

The theory governing the propagation of elastic waves is that of linear elasticity [1, 7]. Although many formulations of the problem are available, here we have chosen a first-order equation system, well suited to introduce the concepts of numerical fluxes and the Cauchy-Kowalevski procedure, as will be seen in the following Sections. The explicit expression of the first-order elastic wave equations, essentially a combination of isotropic Hooke's law and Newton's laws of motion, can be written in velocity-stress formulation as (see [90])

$$
\begin{aligned}
\frac{\partial}{\partial t}\sigma_{xx} - (\lambda + 2\mu)\frac{\partial}{\partial x}u - \lambda\frac{\partial}{\partial y}v - \lambda\frac{\partial}{\partial z}w &= 0\,, \\
\frac{\partial}{\partial t}\sigma_{yy} - \lambda\frac{\partial}{\partial x}u - (\lambda + 2\mu)\frac{\partial}{\partial y}v - \lambda\frac{\partial}{\partial z}w &= 0\,, \\
\frac{\partial}{\partial t}\sigma_{zz} - \lambda\frac{\partial}{\partial x}u - \lambda\frac{\partial}{\partial y}v - (\lambda + 2\mu)\frac{\partial}{\partial z}w &= 0\,, \\
\frac{\partial}{\partial t}\sigma_{xy} - \mu(\frac{\partial}{\partial x}v + \frac{\partial}{\partial y}u) &= 0\,, \\
\frac{\partial}{\partial t}\sigma_{yz} - \mu(\frac{\partial}{\partial z}v + \frac{\partial}{\partial y}w) &= 0\,, \\
\frac{\partial}{\partial t}\sigma_{xz} - \mu(\frac{\partial}{\partial z}u + \frac{\partial}{\partial x}w) &= 0\,, \\
\rho\frac{\partial}{\partial t}u - \frac{\partial}{\partial x}\sigma_{xx} - \frac{\partial}{\partial y}\sigma_{xy} - \frac{\partial}{\partial z}\sigma_{xz} &= 0\,, \\
\rho\frac{\partial}{\partial t}v - \frac{\partial}{\partial x}\sigma_{xy} - \frac{\partial}{\partial y}\sigma_{yy} - \frac{\partial}{\partial z}\sigma_{yz} &= 0\,, \\
\rho\frac{\partial}{\partial t}w - \frac{\partial}{\partial x}\sigma_{xz} - \frac{\partial}{\partial y}\sigma_{yz} - \frac{\partial}{\partial z}\sigma_{zz} &= 0\,,
\end{aligned}
\tag{1.1}
$$

where λ and μ are the *Lamé constants* and ρ is the mass density of the material. The normal stress components are given by σ_{xx}, σ_{yy}, and σ_{zz}, and the shear stresses are σ_{xy}, σ_{yz}, and σ_{xz}. The components of the particle velocities in x-, y-, and z-direction are denoted by u, v and w, respectively.

In the following the physical properties of the material are assumed to be functions of space but constant in time, i.e. $\lambda = \lambda(\vec{x})$, $\mu = \mu(\vec{x})$, and $\rho = \rho(\vec{x})$, in order to describe heterogeneous material.

The system (1.1) can be now rewritten as

$$\frac{\partial Q_p}{\partial t} + \vec{\nabla} \cdot \left(A_{pq}\hat{i} + B_{pq}\hat{j} + C_{pq}\hat{k} \right) Q_q = 0, \qquad (1.2)$$

where $\hat{i}$, $\hat{j}$ and $\hat{k}$ are the unit vectors in the three Cartesian directions x, y, and z respectively. The expression (1.2) can be further re-arranged in the more compact form

$$\frac{\partial Q_p}{\partial t} + A_{pq}\frac{\partial Q_q}{\partial x} + B_{pq}\frac{\partial Q_q}{\partial y} + C_{pq}\frac{\partial Q_q}{\partial z} = 0, \qquad (1.3)$$

where Q is the vector of the p unknown variables, i.e.

$$Q = (\sigma_{xx}, \sigma_{yy}, \sigma_{zz}, \sigma_{xy}, \sigma_{yz}, \sigma_{xz}, u, v, w)^T. \qquad (1.4)$$

Notice, that the homogeneous expression (1.3) could have source terms in the right-hand side for each variable p of arbitrary shape in space and time. The source term will be skipped in the following as it does not affect the discussion. A full description on how to incorporate source terms in the ADER-DG framework can be found in [55, 75, 77]. Note, that classical tensor notation is used, which implies summation over each index that appears twice. The matrices $A_{pq} = A_{pq}(\vec{x})$, $B_{pq} = B_{pq}(\vec{x})$, and $C_{pq} = C_{pq}(\vec{x})$ are space dependent matrices of size $p \times q$, with $p, q = 1, ..., 9$, and are given through

$$A_{pq} = \begin{pmatrix} 0 & 0 & 0 & 0 & 0 & 0 & -(\lambda + 2\mu) & 0 & 0 \\ 0 & 0 & 0 & 0 & 0 & 0 & -\lambda & 0 & 0 \\ 0 & 0 & 0 & 0 & 0 & 0 & -\lambda & 0 & 0 \\ 0 & 0 & 0 & 0 & 0 & 0 & 0 & -\mu & 0 \\ 0 & 0 & 0 & 0 & 0 & 0 & 0 & 0 & 0 \\ 0 & 0 & 0 & 0 & 0 & 0 & 0 & 0 & -\mu \\ -\frac{1}{\rho} & 0 & 0 & 0 & 0 & 0 & 0 & 0 & 0 \\ 0 & 0 & 0 & -\frac{1}{\rho} & 0 & 0 & 0 & 0 & 0 \\ 0 & 0 & 0 & 0 & 0 & -\frac{1}{\rho} & 0 & 0 & 0 \end{pmatrix}, \qquad (1.5)$$

$$B_{pq} = \begin{pmatrix} 0 & 0 & 0 & 0 & 0 & 0 & 0 & -\lambda & 0 \\ 0 & 0 & 0 & 0 & 0 & 0 & 0 & -(\lambda + 2\mu) & 0 \\ 0 & 0 & 0 & 0 & 0 & 0 & 0 & -\lambda & 0 \\ 0 & 0 & 0 & 0 & 0 & 0 & -\mu & 0 & 0 \\ 0 & 0 & 0 & 0 & 0 & 0 & 0 & 0 & -\mu \\ 0 & 0 & 0 & 0 & 0 & 0 & 0 & 0 & 0 \\ 0 & 0 & 0 & -\frac{1}{\rho} & 0 & 0 & 0 & 0 & 0 \\ 0 & -\frac{1}{\rho} & 0 & 0 & 0 & 0 & 0 & 0 & 0 \\ 0 & 0 & 0 & 0 & -\frac{1}{\rho} & 0 & 0 & 0 & 0 \end{pmatrix}, \qquad (1.6)$$

$$C_{pq} = \begin{pmatrix} 0 & 0 & 0 & 0 & 0 & 0 & 0 & 0 & -\lambda \\ 0 & 0 & 0 & 0 & 0 & 0 & 0 & 0 & -\lambda \\ 0 & 0 & 0 & 0 & 0 & 0 & 0 & 0 & -(\lambda + 2\mu) \\ 0 & 0 & 0 & 0 & 0 & 0 & 0 & 0 & 0 \\ 0 & 0 & 0 & 0 & 0 & 0 & 0 & -\mu & 0 \\ 0 & 0 & 0 & 0 & 0 & 0 & -\mu & 0 & 0 \\ 0 & 0 & 0 & 0 & 0 & -\frac{1}{\rho} & 0 & 0 & 0 \\ 0 & 0 & 0 & 0 & -\frac{1}{\rho} & 0 & 0 & 0 & 0 \\ 0 & 0 & -\frac{1}{\rho} & 0 & 0 & 0 & 0 & 0 & 0 \end{pmatrix}. \tag{1.7}$$

As the equation system (1.1) can be written in the form (1.3), and the matrices A_{pq}, B_{pq}, and C_{pq} (known as *Jacobian* matrices) are all diagonalizable with real eigenvalues, the system (1.1) is called a *hyperbolic* system (see [90]), and its properties will be studied in the following Section.

1.3   Hyperbolic Equation Systems

The theory of hyperbolic equation systems tells us that most of the information on the propagating waves allowed by a system written as (1.3) can be obtained by simple eigendecomposition of the Jacobians A_{pq}, B_{pq}, and C_{pq}. In particular, the possible plane-waves and their propagation velocities are, for the x-direction, the result of solving the system

$$A\vec{R}_i = \alpha_i \vec{R}_i \tag{1.8}$$

so that the α_i are the Jacobian's *eigenvalues* and $\vec{R}_i$ its corresponding *eigenvectors*. The physical meaning of the eigenvectors is the allowed modes of propagation (plane waves) in the chosen propagation direction. The corresponding eigenvalues are the wave propagation velocities of each of those allowed modes. By imposing an increasing ordering of the eigenvalues one obtains, for the case of (1.3), the following eigenvalues

$$\begin{aligned} \alpha_1 &= -c_p, & \alpha_2 &= -c_s, & \alpha_3 &= -c_s, \\ \alpha_4 &= 0, & \alpha_5 &= 0, & \alpha_6 &= 0, \\ \alpha_7 &= c_s, & \alpha_8 &= c_s, & \alpha_9 &= c_p, \end{aligned} \tag{1.9}$$

the values of which can be expressed using the Lamé parameters as

$$c_p = \sqrt{\frac{\lambda + 2\mu}{\rho}}, \quad \text{and} \quad c_s = \sqrt{\frac{\mu}{\rho}}, \tag{1.10}$$

which are the P-wave and S-wave velocities respectively. Furthermore, for the isotropic case, the wave speeds in (1.9) and (1.10) do not depend on the propagation direction. The eigenvalues show, that the two P-waves propagate with

speeds α_1 and α_9 and the four S-waves propagate with speeds α_2, α_3 and α_7, α_8, although with different polarizations. The three remaining are *static* modes and therefore will not be further discussed. The eigenvectors of (1.5), $R_1, ..., R_9$, can be expressed in matrix notation as $R^A = \left[\vec{R}_1, \vec{R}_2, \ldots, \vec{R}_9 \right]$, which is explicitly

$$R^A_{pq} = \begin{pmatrix} \lambda + 2\mu & 0 & 0 & 0 & 0 & 0 & 0 & 0 & \lambda + 2\mu \\ \lambda & 0 & 0 & 0 & 1 & 0 & 0 & 0 & \lambda \\ \lambda & 0 & 0 & 0 & 0 & 1 & 0 & 0 & \lambda \\ 0 & \mu & 0 & 0 & 0 & 0 & 0 & \mu & 0 \\ 0 & 0 & 0 & 1 & 0 & 0 & 0 & 0 & 0 \\ 0 & 0 & \mu & 0 & 0 & 0 & \mu & 0 & 0 \\ c_p & 0 & 0 & 0 & 0 & 0 & 0 & 0 & -c_p \\ 0 & c_s & 0 & 0 & 0 & 0 & 0 & -c_s & 0 \\ 0 & 0 & c_s & 0 & 0 & 0 & -c_s & 0 & 0 \end{pmatrix} . \tag{1.11}$$

The expressions (1.9) and (1.11) will be extensively used in the derivation of the ADER-DG scheme in Section 1.5.

1.4   Fluxes

The concept of numerical fluxes is a milestone of the DG schemes and as such deserves special attention before further developing the scheme itself. Fluxes are, first and foremost, an extension of Gauss' theorem

$$\int_V \left(\vec{\nabla} \cdot \vec{Z}(\vec{x}) \right) dV = \int_{\partial V} \vec{Z}(\vec{x}) d\vec{S}. \tag{1.12}$$

This theorem, also known as divergence theorem, states that integrals of the divergence of a field $\vec{Z}(\vec{x})$ on a given volume V can be substituted by surface integrals of $\vec{Z}(\vec{x})$ as long as the integration surface ∂V is the one that closes and defines volume V.

This purely mathematical result has clear physical relevance if one, for example, takes a look at the advection equation. This equation describes the motion of some *tracer* in a fluid moving at constant and homogeneous velocity $\vec{c}$. By a tracer we mean a substance present in very small amount in a fluid, such that its concentration does not affect the motion of the fluid itself. The equation describing the motion of this tracer can be written as (see [90])

$$\frac{\partial}{\partial t} \rho(\vec{x}) = - \vec{\nabla} \cdot [\vec{c}\, \rho(\vec{x})] , \tag{1.13}$$

where $\rho(\vec{x})$ is the density of tracer and $\vec{c}$ the vector of velocity of the fluid. If the equation is integrated over an imaginary closed volume V, we obtain

$$\int_V \frac{\partial}{\partial t} \rho(\vec{x}) dV = - \int_V \vec{\nabla} \cdot [\vec{c} \, \rho(\vec{x})] \, dV. \tag{1.14}$$

Applying (1.12) to this last result and taking out of the integral sign the derivatives which don't depend on dV results in

$$\frac{\partial}{\partial t} \int_V \rho(\vec{x}) dV = -\vec{c} \int_{\partial V} \rho(\vec{x}) d\vec{S}. \tag{1.15}$$

Now the left-hand term can be identified as the temporal variation of the mass of tracer existing in V. Then, conceptually, it can be understood that any change in that mass inside V *has to be produced* by flow or flux of tracer trough the boundaries of V, that have been here called ∂V. For the advection equation, this physical flux of a tracer through ∂V can be directly identified with the right-hand side of (1.15). However, the result (1.15), can be extended to any hyperbolic system as is (1.1). The meaning of the flux in these other physical problems, however, can not be identified with the intuitive concept of *flux of a tracer* anymore.

The general theory of fluxes for hyperbolic systems has been developed mainly for Finite Volume methods [133]. The most general first-order hyperbolic system can be expressed as

$$\frac{\partial}{\partial t} Q(\vec{x}, t) + \vec{\nabla} \cdot \vec{f}(Q(\vec{x}, t)) = 0, \tag{1.16}$$

of which (1.2) is just a particular case. By applying a simple procedure as that shown in (1.13-1.15) the following form can be derived

$$\frac{\partial}{\partial t} \int_V Q(\vec{x}, t) \, dV = - \int_{\partial V} \vec{n} \cdot \vec{f}(Q(\vec{x}, t)) \, dS \equiv -\mathbb{F}, \tag{1.17}$$

where it has been explicitly separated $d\vec{S} = dS \cdot \vec{n}$. After time-integrating the system from t to $t + \Delta t$ it follows

$$\int_V Q(\vec{x}, t + \Delta t) \, dV - \int_V Q(\vec{x}, t) \, dV = -\Delta t \int_t^{t+\Delta t} \mathbb{F} dt. \tag{1.18}$$

A classical FV scheme would conclude that the change in the value of Q inside a given volume V in a time increment Δt is only due to the time-integrated flux $\Delta t \int \mathbb{F} dt$ across its boundary ∂V. In actual FV schemes both sides of (1.18) are divided by V, so that instead of the integral value of Q in V one is interested in the *average* value of Q, but this does not affect the discussion here. Note also that the flux formulation does not impose any conditions on the shape of computational cell. Therefore flux-based schemes, as are FV and DG methods, are more flexible in the choice of such computational cells than other methodologies.

As a final remark it should be made clear that in order to compute $\mathbb{F}$ it is not required to have continuous values of Q at both sides of ∂V. For some given initial conditions at both sides and hyperbolic system, solving the value of $\mathbb{F}$ is called solving the *Riemann Problem*, and many exact and approximated ways to solve it exist in the literature (see e.g. [90, 133]). In general, the solution of a Riemann Problem depends both on the variables' state and the governing hyperbolic equation.

1.4.1   Godunov-type Fluxes

A popular flux type for hyperbolic systems is the upwinding exact Riemann solver known as Roe or Godunov flux, as given in [133]. By upwinding we mean that the eigendecomposition of the system is used to solve the fluxes. Let's remember that the values of Q at both sides of the surface ∂V are not required to be continuous. The states at both sides of ∂V will be then called Q^- and Q^+, using the convention that $\vec{n}$ points from Q^- towards Q^+. It is assumed in the following that fluxes are computed for the '-' side of ∂V, so that fluxes from Q^- to Q^+ will be *outgoing* fluxes or fluxes traveling outwards, while fluxes from Q^+ to Q^- will be *incoming* fluxes or fluxes traveling inwards. It will also be assumed that $\vec{n}$ points in the positive x-direction for simplicity. In the following, A^+ is irrelevant, and it will therefore be used $A = A^-$.

From the theory on numerical fluxes [90] is known that if *any* discontinuity exists at a given surface, it will then generate a number of waves given by the amount of eigenvectors and eigenvalues associated with the Jacobian matrix A, which have been found in Section 1.3. In the present case this means that three (a P- and two S-) waves will propagate towards positive normal direction to the surface and other 3 will do so in the negative direction, corresponding to the 6 non-zero eigenvalues of A obtained in (1.9). It will prove useful now to define the $|A|$ matrix as the absolute value of the Jacobian matrix A, which has the meaning of applying the absolute value operator to the eigenvalues given in (1.9), i.e.

$$|A_{qr}| = R^A_{qp} |\Lambda_{ps}| \left(R^A_{sr} \right)^{-1}, \quad \text{with} \quad |\Lambda_{ps}| = \text{diag}\left(|\alpha_1|, |\alpha_2|, ... \right). \qquad (1.19)$$

This new Jacobian $|A|$ has the same physical properties than A but it only allows for waves to propagate in the positive direction.

If the values at the outer side, Q^+, are let to be zero then the flux will be proportional to $A_{pq}Q^-_q$, meaning propagation of the 6 waves naturally generated by the variables' jump just created, towards both the positive and negative directions. On the other hand, $|A_{pq}| Q^-_q$ would give exactly the same waves propagating outwards but the remaining three would be shifted as to also propagate outwards instead of inwards. By averaging both processes we obtain $1/2 \left(A_{pq} + |A_{pq}| \right) Q^-_q$, thus giving us the actual *outgoing* flux through the ∂V interface *only* for the case in which

is assumed that the outer values Q^+ are zero. Let's invert the assumption by making now the inner variable values Q^- zero instead of the outer ones. The process can be repeated by now using $-|A_{pq}|Q_q^+$, which produces waves solely traveling inwards. Then, the average value $1/2\left(A_{pq} - |A_{pq}|\right)Q_q^+$ will only leave us with the actual *incoming* flux through the ∂V interface *only* for the case in which it is assumed that the outer values Q^+ are zero. The case one wishes to solve, though, is the total case in which both Q^- and Q^+ have non-zero values. Then, the additive properties of the fluxes can be used to produce a total flux integrand which reads

$$f_p = \frac{1}{2}\left(A_{pq} + \Theta_{pq}\right)Q_q^- + \frac{1}{2}\left(A_{pq} - \Theta_{pq}\right)Q_q^+, \tag{1.20}$$

where the numerical viscosity matrix Θ_{pq}, for the Godunov case, has the value

$$\Theta_{pq}^{\text{Godunov}} = |A_{pq}|. \tag{1.21}$$

This integrand has now to be inserted in (1.17), and integrated over the surface ∂V to obtain the total flux $\mathbb{F}$. It is noteworthy that, to compute the flux from the '-' side, no information on the material parameters from the '+' side is used, as the A matrix's values used in (1.19), (1.20) and (1.21) are only those of the '-' side. Further, note that the clear separation between inflow and outflow makes it remarkably easy to implement special boundary conditions as will be further seen in Section 1.6.

1.4.2 Rusanov-type Fluxes

As has just been seen, the use of Godunov fluxes requires knowledge of the eigenvectors R^A of the hyperbolic system, and this is not always an easy task. A much simpler approach is that of the local Lax-Friedrichs or Rusanov fluxes. One way of looking at this flux type is trying to ask oneself the question of whether it would make a change to use $|A| = 0$ so that (1.20) is just an average flux of both sides of the investigated surface. By doing so the method becomes unstable, unless one adds some other numerical viscosity to cancel out the spurious oscillations produced. It has been shown [90] that this numerical viscosity can be, in the Rusanov case, the simple expression

$$\Theta_{pq}^{\text{Rusanov}} = \max_i(\alpha_i) \cdot I_{pq}, \tag{1.22}$$

being I_{pq} the identity matrix. By substituting the term in (1.22) into the expression (1.20) one obtains the full Rusanov-type flux. For the case of the isotropic elastic wave equations (1.5) it holds that $\max_i(\alpha_i) = c_p$ as the largest eigenvalue always coincides with the P-wave propagation velocity (see (1.9)). It should be clear from (1.20), (1.21) and (1.22) that the flux type can be specified just by setting the value of the numerical viscosity Θ_{pq}. Rusanov-based schemes are more

dissipative than Godunov-based ones, but are as robust and therefore an alternative when finding the correct $|A|$ values is difficult. For high-order DG schemes, the choice of flux often does not pose a big difference as the accuracy is driven by the amount of inner degrees of freedom inside every cell.

1.5   The Numerical Scheme

For the construction of the numerical scheme, let's consider the general linear hyperbolic system of equations with variable coefficients given in (1.3). The computational domain $\Omega \in \mathbb{R}^3$ is divided into conforming tetrahedral elements $\mathcal{T}^{(m)}$ being addressed by a unique index (m) which in general are connected to other four tetrahedra $\mathcal{T}^{(m_j)}$ with $j = 1, \cdots, 4$ in a conforming way. Those tetrahedra are supposed to have completely flat sides, in the following. This will mean that a single vector defines the surface's normal for each of the sides of the tetrahedra. Furthermore, let's suppose the matrices A_{pq}, B_{pq}, and C_{pq} to be piecewise constant inside an element $\mathcal{T}^{(m)}$. It should be noted that these last two assumptions are not an intrinsic limitation of this method, which has already been extended to cases with varying physical parameters inside the elements and curved-sided tetrahedral faces (see e.g. [59]).

1.5.1   Orthogonal Basis Functions

As a standard procedure for high-order Finite Element computations, it is required to have a basis of functions that supports the solutions inside each element. In the following we choose to use tetrahedra as computational elements. Each tetrahedron can be defined by 4 vertices $\vec{x}_1, \cdots, \vec{x}_4$ with $\vec{x}_i = (x_i, y_i, z_i)$ and $i = 1, \cdots, 4$ (see Figure 1.1). A particular tetrahedron is the rectangular tetrahedron defined by the 4 points $\vec{x}_1 = (0, 0, 0)$, $\vec{x}_2 = (1, 0, 0)$, $\vec{x}_3 = (0, 1, 0)$ and $\vec{x}_4 = (0, 0, 1)$. The rectangular or reference tetrahedron, referred to as $\mathcal{T}_E$ in the following, will be used as support for the basis functions. Any point inside any tetrahedron can be mapped in the local coordinate system of the reference tetrahedron, denoted by the three Cartesian coordinates ξ, η and ζ, by making use of equations (B.1) in Appendix B. Note that $0 \leq \xi + \eta + \zeta \leq 1$ inside the tetrahedron. Then the aim is to obtain a variable vector Q_h which is a numerical solution to the equation (1.3) inside the tetrahedron $\mathcal{T}^{(m)}$, so that $Q_h \approx Q$ being Q defined in (1.4). In order to build up Q_h we use a linear combination of space-dependent but time-independent polynomial basis functions $\Phi_l(\xi, \eta, \zeta)$ of degree N with support $\mathcal{T}_E$ and with only time-dependent degrees of freedom $\hat{Q}_{pl}^{(m)}(t)$:

$$\left(Q_h^{(m)} \right)_p (\xi, \eta, \zeta, t) = \hat{Q}_{pl}^{(m)}(t) \Phi_l(\xi, \eta, \zeta) , \qquad (1.23)$$

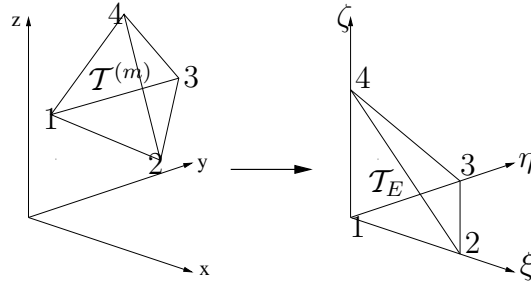Figure 1.1: Transformation from the physical tetrahedron $\mathcal{T}^{(m)}$ to the canonical reference tetrahedron $\mathcal{T}_E$ with nodes $(0, 0, 0)$, $(1, 0, 0)$, $(0, 1, 0)$, and $(0, 0, 1)$.
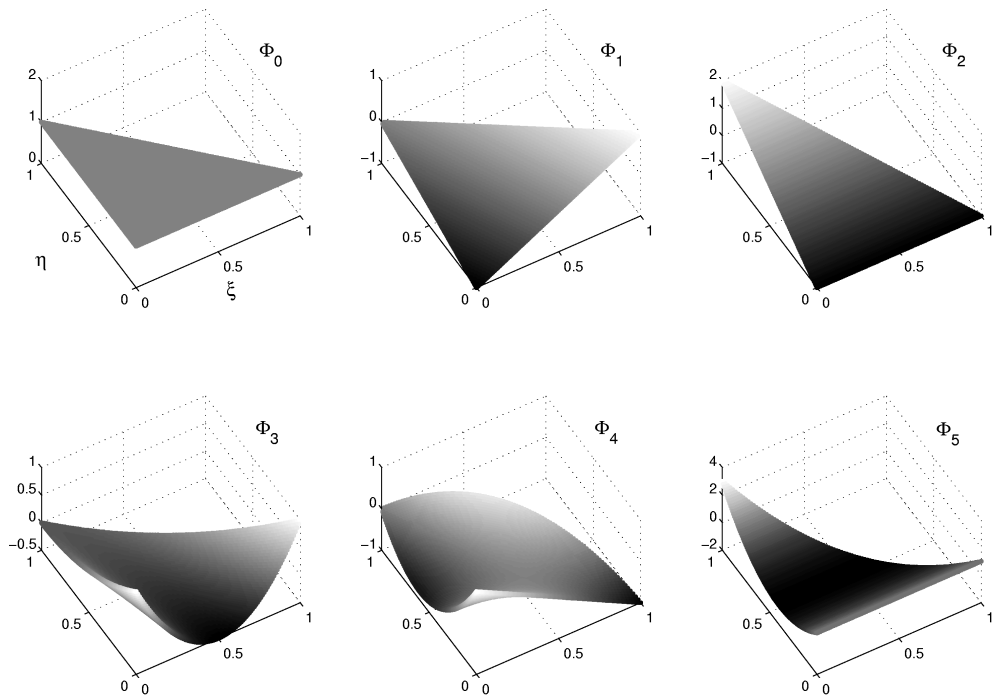
Figure 1.2: The Dubiner's basis functions for the $N = 2$ case in two-dimensions. The total number of basis functions for this case is six. This basis can be used for DG schemes of up to order 3.

The index p stands for the $p-$th unknown in the vector Q and l indicates the l-th basis function. The orthogonal basis functions Φ_k used for the DG scheme presented here are those given in [39]. The basis is complete for a given polynomial degree N by using a total of $L = (N+1)(N+2)(N+3)/6$ basis functions. It is also a hierarchical basis in the sense that the basis functions for a given degree N always include the basis functions for a lesser degree $N-1$ as a subset. An example of the shape of these functions is shown in Figure 1.2, in the two-dimensional case for clarity. Notice that in two-dimensions the required number of basis functions becomes $L = (N+1)(N+2)/2$. The approximated interpolation g^h of an exact function g can be performed with the linear combination

$$g^h = \hat{g}_i \Phi_i \,, \tag{1.24}$$

with the $\hat{g}_i$ coefficients obtained from the projection

$$\hat{g}_i = \frac{\int\limits_{\mathcal{T}_E} g \Phi_j dV}{\int\limits_{\mathcal{T}_E} \Phi_j \Phi_i dV} \,, \tag{1.25}$$

where the integrals are performed by Gaussian integration of sufficient accuracy. An example of the interpolant capabilities of the basis in 2D can be seen in Figure 1.3, where the exact function is $g(x,y) = sin\left(2\pi(x-0.5)/W\right) + cos\left(2\pi(x-0.5)/W\right) + 2$ with $W = 2r/3$ and being r the inradius of the triangular element. In this case $N = 3$ has been chosen so that 10 basis functions are used to describe g^h. The integrations have been performed with a total of 13 gaussian integration points.

It should be remarked that, although the basis is defined in the reference tetrahedron $\mathcal{T}_E$, a conventional linear coordinate transformation can express the Φ_k in other Cartesian systems, as will further be seen in Section 1.5.3.

1.5.2   Discontinuous Galerkin Method

The DG method is first and foremost a Galerkin method, so that the first step in solving (1.2) is to multiply it by a test function Φ_k, which is one of the basis functions, and integrating over a tetrahedral element $\mathcal{T}^{(m)}$ thus giving

$$\int\limits_{\mathcal{T}^{(m)}} \Phi_k \frac{\partial Q_p}{\partial t} dV + \int\limits_{\mathcal{T}^{(m)}} \Phi_k \left[\vec{\nabla} \cdot \left(A_{pq}\hat{i} + B_{pq}\hat{j} + C_{pq}\hat{k} \right) Q_q \right] dV = 0. \tag{1.26}$$

Integration of equation (1.26) by parts [142] then yields

$$\int\limits_{\mathcal{T}^{(m)}} \Phi_k \frac{\partial Q_p}{\partial t} dV + \int\limits_{\mathcal{T}^{(m)}} \vec{\nabla} \cdot \left[\Phi_k \left(A_{pq}\hat{i} + B_{pq}\hat{j} + C_{pq}\hat{k} \right) Q_q \right] dV -$$
$$- \int\limits_{\mathcal{T}^{(m)}} (\nabla \Phi_k) \cdot \left[\left(A_{pq}\hat{i} + B_{pq}\hat{j} + C_{pq}\hat{k} \right) Q_q \right] dV = 0. \tag{1.27}$$
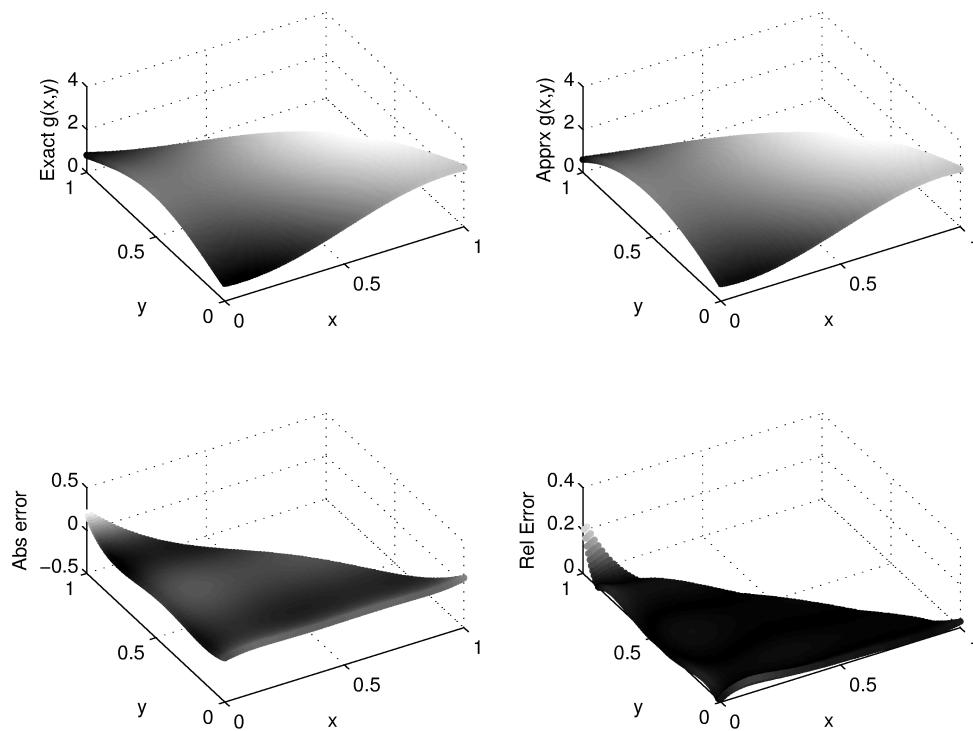
Figure 1.3: Example of interpolation for $N = 3$ case in two-dimensions.The exact (top left) and interpolated (top right) functions can be seen, together with the absolute error (bottom left) and relative error (bottom right) committed by the interpolation.

Now it can be seen that the second term can be transformed with Gauss' theorem (1.12) into a surface integral such as

$$
\int_{\mathcal{T}^{(m)}} \Phi_k \frac{\partial Q_p}{\partial t} dV + \int_{\partial \mathcal{T}^{(m)}} \Phi_k \left[\left(A_{pq}\hat{i} + B_{pq}\hat{j} + C_{pq}\hat{k} \right) Q_q \right] \cdot \vec{n} \, dS
$$
$$
- \int_{\mathcal{T}^{(m)}} (\nabla \Phi_k) \cdot \left[\left(A_{pq}\hat{i} + B_{pq}\hat{j} + C_{pq}\hat{k} \right) Q_q \right] dV = 0.
\tag{1.28}
$$

At this point one can identify the second term with the flux as it is defined in (1.17). For further clarity now the scalar products can be solved to obtain the expression

$$
\int_{\mathcal{T}^{(m)}} \Phi_k \frac{\partial Q_p}{\partial t} dV + \int_{\partial \mathcal{T}^{(m)}} \Phi_k f_p^h dS -
$$
$$
- \int_{\mathcal{T}^{(m)}} \left(\frac{\partial \Phi_k}{\partial x} A_{pq} Q_q + \frac{\partial \Phi_k}{\partial y} B_{pq} Q_q + \frac{\partial \Phi_k}{\partial z} C_{pq} Q_q \right) dV = 0 ,
\tag{1.29}
$$

where a numerical flux *integrand* f_p^h has been introduced in the surface integral since Q_h may be discontinuous at an element boundary. Notice that the fluxes in this case are not the only contribution to the change in Q_h values, as in (1.17) and in any FV scheme. In equation (1.29) there is also a *stiffness* term, common to spectral methods. In the particular case in which one uses $N = 0$, so that only one basis function exists of constant value, the stiffness term disappears and a first-order FV scheme is recovered.

As rotational invariance of the system in (1.3) is supposed for the isotropic case, the flux can be derived for a coordinate system, which is aligned with the outward pointing unit normal vector $\vec{n}$ of an element boundary, i.e. a triangular face of a tetrahedron. The anisotropic case will be explored in Chapter 3. The coordinate change to the $\vec{n}$-aligned system requires the transformation (rotation) of the unknowns in vector Q_p from the global Cartesian system to the vector Q_q^n in a local normal, i.e. *face-aligned*, coordinate system is given by

$$
Q_p = T_{pq} Q_q^n .
\tag{1.30}
$$

The rotation matrix used to express the variable vector Q_p in a different coordinate Cartesian system is just a combination of the rotation matrices for tensors (stress) and vectors (particle velocity). For the particular case presented here T_{pq} in (1.30) reads as

$$
T = \begin{bmatrix} T^t & 0 \\ 0 & T^v \end{bmatrix} \in \mathbb{R}^{9 \times 9},
\tag{1.31}
$$

where $T^t \in \mathbb{R}^{6 \times 6}$ is the rotation matrix responsible for the stress tensor rotation

as in the purely elastic part and is given as

$$T^t = \begin{pmatrix} n_x^2 & s_x^2 & t_x^2 & 2n_x s_x & 2s_x t_x & 2n_x t_x \\ n_y^2 & s_y^2 & t_y^2 & 2n_y s_y & 2s_y t_y & 2n_y t_y \\ n_z^2 & s_z^2 & t_z^2 & 2n_z s_z & 2s_z t_z & 2n_z t_z \\ n_y n_x & s_y s_x & t_y t_x & n_y s_x + n_x s_y & s_y t_x + s_x t_y & n_y t_x + n_x t_y \\ n_z n_y & s_z s_y & t_z t_y & n_z s_y + n_y s_z & s_z t_y + s_y t_z & n_z t_y + n_y t_z \\ n_z n_x & s_z s_x & t_z t_x & n_z s_x + n_x s_z & s_z t_x + s_x t_z & n_z t_x + n_x t_z \end{pmatrix} . \quad (1.32)$$

The matrix $T^v \in \mathbb{R}^{3 \times 3}$ is the rotation matrix responsible for the velocity vector rotation as in the purely elastic part and is given as

$$T^v = \begin{pmatrix} n_x & s_x & t_x \\ n_y & s_y & t_y \\ n_z & s_z & t_z \end{pmatrix} . \quad (1.33)$$

Matrices (1.32)-(1.33) have as entries the components of the normal vector $\vec{n} = (n_x, n_y, n_z)^T$ and the two tangential vectors $\vec{s} = (s_x, s_y, s_z)^T$ and $\vec{t} = (t_x, t_y, t_z)^T$, which lie in the plane determined by the boundary face of the tetrahedron and are orthogonal to each other and the normal vector $\vec{n}$. Usually the vector $\vec{s}$ is defined so that it points from the local face node 1 to the local face node 2, see Table 1.1. As the tetrahedra's boundaries are flat, only one $\vec{n}$ exists per tetrahedron's face. The total surface integral over $\partial \mathcal{T}^{(m)}$ will then be the sum of the integrals over the four triangular faces.

The flux term in (1.29) can be solved with Godunov's or Rusanov's fluxes, as described in detail in Sections 1.4.1 and 1.4.2. In this case the two sides of the flux in (1.20) correspond to elements $\mathcal{T}^{(m)}$ and the neighbor $\mathcal{T}^{(m_j)}$, $j = 1, 2, 3, 4$. As the vector defining the interface $\vec{n}$ has an arbitrary orientation, the transformation (1.31) and its inverse are used to align the problem to the side's normal. Then the numerical flux integrand becomes

$$\begin{aligned} f_p^h &= \tfrac{1}{2} T_{pq} \left(A_{qr}^{(m)} + \Theta_{qr}^{(m)} \right) (T_{rs})^{-1} \hat{Q}_{sl}^{(m)} \Phi_l^{(m)} \\ &+ \tfrac{1}{2} T_{pq} \left(A_{qr}^{(m)} - \Theta_{qr}^{(m)} \right) (T_{rs})^{-1} \hat{Q}_{sl}^{(m_j)} \Phi_l^{(m_j)}, \end{aligned} \quad (1.34)$$

where $\hat{Q}_{sl}^{(m)} \Phi_l^{(m)}$ and $\hat{Q}_{sl}^{(m_j)} \Phi_l^{(m_j)}$ are the boundary extrapolated values of the numerical solution from element $\mathcal{T}^{(m)}$ and the j-th side neighbor $\mathcal{T}^{(m_j)}$, respectively. The matrix $(T_{rs})^{-1}$ represents the back-transformation into the global xyz-system. Now, after integrating f_p^h over the surface dS, the flux through a given side of the element has been computed.

Inserting (1.23) and (1.34) into (1.29) and splitting the boundary integral into the

contributions of each face j of the tetrahedron $\mathcal{T}^{(m)}$, we obtain

$$
\frac{\partial}{\partial t}\hat{Q}_{pl}^{(m)} \int\limits_{\mathcal{T}^{(m)}} \Phi_k \Phi_l dV \quad +
$$

$$
+ \quad \sum_{j=1}^{4} \tfrac{1}{2} T_{pq}^{j} \left(A_{qr}^{(m)} + \Theta_{qr}^{(m)} \right) (T_{rs}^{j})^{-1} \hat{Q}_{sl}^{(m)} \int\limits_{\left(\partial \mathcal{T}^{(m)} \right)_j} \Phi_k^{(m)} \Phi_l^{(m)} dS +
$$

$$
+ \quad \sum_{j=1}^{4} \tfrac{1}{2} T_{pq}^{j} \left(A_{qr}^{(m)} - \Theta_{qr}^{(m)} \right) (T_{rs}^{j})^{-1} \hat{Q}_{sl}^{(m_j)} \int\limits_{\left(\partial \mathcal{T}^{(m)} \right)_j} \Phi_k^{(m)} \Phi_l^{(m_j)} dS -
$$

$$
\tag{1.35}
$$

$$
- \quad A_{pq} \hat{Q}_{ql}^{(m)} \int\limits_{\mathcal{T}^{(m)}} \frac{\partial \Phi_k}{\partial x} \Phi_l dV -
$$

$$
- \quad B_{pq} \hat{Q}_{ql}^{(m)} \int\limits_{\mathcal{T}^{(m)}} \frac{\partial \Phi_k}{\partial y} \Phi_l dV -
$$

$$
- \quad C_{pq} \hat{Q}_{ql}^{(m)} \int\limits_{\mathcal{T}^{(m)}} \frac{\partial \Phi_k}{\partial z} \Phi_l dV \quad = \quad 0 \,.
$$

This is the so-called semi-discrete local Discontinuous Galerkin for tetrahedra, in the particular case of using upwinding Godunov fluxes. To obtain a fully discrete solution one has still to time integrate the equation (1.35). Before this, however, some ways of reducing computational effort by using mapping transformations from general tetrahedra to a reference element will be explored in the following Section.

1.5.3   Transformation into Reference Element

Equation (1.35) is written in the global xyz-system. If each physical tetrahedron $\mathcal{T}^{(m)}$ is transformed to a canonical reference tetrahedron $\mathcal{T}_E$ in a $\xi\eta\zeta$-reference system as shown in Figure 1.1, the method can be implemented much more efficiently, since many integrals can be pre-computed beforehand in this reference system.

With respect to the coordinate transformation into the $\xi\eta\zeta$-reference system it holds furthermore

$$
dx\,dy\,dz = |J|\,d\xi\,d\eta\,d\zeta, \tag{1.36}
$$

and the transformed gradients are given by

$$
\begin{pmatrix} \frac{\partial}{\partial x} \\ \frac{\partial}{\partial y} \\ \frac{\partial}{\partial z} \end{pmatrix} = \begin{pmatrix} \frac{\partial \xi}{\partial x} & \frac{\partial \eta}{\partial x} & \frac{\partial \zeta}{\partial x} \\ \frac{\partial \xi}{\partial y} & \frac{\partial \eta}{\partial y} & \frac{\partial \zeta}{\partial y} \\ \frac{\partial \xi}{\partial z} & \frac{\partial \eta}{\partial z} & \frac{\partial \zeta}{\partial z} \end{pmatrix} \begin{pmatrix} \frac{\partial}{\partial \xi} \\ \frac{\partial}{\partial \eta} \\ \frac{\partial}{\partial \zeta} \end{pmatrix}. \tag{1.37}
$$

Integrating in the reference system using (1.36) and (1.37), the semi-discrete DG formulation of (1.35) in the reference element $\mathcal{T}_E$ reads as

$$
\begin{aligned}
&\frac{\partial}{\partial t}\hat{Q}_{pl}^{(m)}\,|J|\int\limits_{\mathcal{T}_E}\Phi_k\Phi_l d\xi d\eta d\zeta \quad + \\
&+\sum_{j=1}^{4}T_{pq}^{j}\tfrac{1}{2}\left(A_{qr}^{(m)}+\Theta_{qr}^{(m)}\right)(T_{rs}^{j})^{-1}\hat{Q}_{sl}^{(m)}\,|S_j|\,F_{kl}^{-,j} \quad + \\
&+\sum_{j=1}^{4}T_{pq}^{j}\tfrac{1}{2}\left(A_{qr}^{(m)}-\Theta_{qr}^{(m)}\right)(T_{rs}^{j})^{-1}\hat{Q}_{sl}^{(m_j)}\,|S_j|\,F_{kl}^{+,j,i,h} \quad - \\
&-A_{pq}^{*}\hat{Q}_{ql}^{(m)}\,|J|\int\limits_{\mathcal{T}_E}\frac{\partial\Phi_k}{\partial\xi}\Phi_l d\xi d\eta d\zeta - \\
&-B_{pq}^{*}\hat{Q}_{ql}^{(m)}\,|J|\int\limits_{\mathcal{T}_E}\frac{\partial\Phi_k}{\partial\eta}\Phi_l d\xi d\eta d\zeta - \\
&-C_{pq}^{*}\hat{Q}_{ql}^{(m)}\,|J|\int\limits_{\mathcal{T}_E}\frac{\partial\Phi_k}{\partial\zeta}\Phi_l d\xi d\eta d\zeta \quad = \quad 0 \quad ,
\end{aligned}
\tag{1.38}
$$

where $|S_j|$ denotes the area of face j and the special linear combination of the Jacobians

$$
A_{pq}^{*}=A_{pq}\frac{\partial\xi}{\partial x}+B_{pq}\frac{\partial\xi}{\partial y}+C_{pq}\frac{\partial\xi}{\partial z},
\tag{1.39}
$$

$$
B_{pq}^{*}=A_{pq}\frac{\partial\eta}{\partial x}+B_{pq}\frac{\partial\eta}{\partial y}+C_{pq}\frac{\partial\eta}{\partial z},
\tag{1.40}
$$

$$
C_{pq}^{*}=A_{pq}\frac{\partial\zeta}{\partial x}+B_{pq}\frac{\partial\zeta}{\partial y}+C_{pq}\frac{\partial\zeta}{\partial z}.
\tag{1.41}
$$

The integrals

$$
M_{kl}=\int\limits_{\mathcal{T}_E}\Phi_k\Phi_l d\xi d\eta d\zeta,
\tag{1.42}
$$

$$
K_{kl}^{\xi}=\int\limits_{\mathcal{T}_E}\frac{\partial\Phi_k}{\partial\xi}\Phi_l d\xi d\eta d\zeta,
\tag{1.43}
$$

$$
K_{kl}^{\eta}=\int\limits_{\mathcal{T}_E}\frac{\partial\Phi_k}{\partial\eta}\Phi_l d\xi d\eta d\zeta,
\tag{1.44}
$$

$$
K_{kl}^{\zeta}=\int\limits_{\mathcal{T}_E}\frac{\partial\Phi_k}{\partial\zeta}\Phi_l d\xi d\eta d\zeta.
\tag{1.45}
$$

over the reference element $\mathcal{T}_E$ can be easily calculated beforehand by a computer algebra system. Furthermore, the flux matrices $F_{kl}^{-,j}$ and $F_{kl}^{+,j,i,h}$ in (1.38) can be calculated analytically once on the reference element as will be seen in the

Table 1.1: Face definition on tetrahedrons

Face	Points		
1	1	3	2
2	1	2	4
3	1	4	3
4	2	3	4

Table 1.2: (a) 3-D volume coordinates $\vec{\xi}^{(j)}$ as function of the face parameters χ and τ. (b) Transformation of the face parameters χ and τ of the tetrahedron's face to the face parameters $\tilde{\chi}$ and $\tilde{\tau}$ in the neighbor tetrahedron according to the three possible orientations h of the neighbour face.

j	1	2	3	4
$\xi^{(j)}(\chi,\tau)$	τ	χ	0	$1-\chi-\tau$
$\eta^{(j)}(\chi,\tau)$	χ	0	τ	χ
$\zeta^{(j)}(\chi,\tau)$	0	τ	χ	τ

(a)

h	1	2	3
$\tilde{\chi}^{(h)}(\chi,\tau)$	τ	$1-\chi-\tau$	χ
$\tilde{\tau}^{(h)}(\chi,\tau)$	χ	τ	$1-\chi-\tau$

(b)

following.

First, one must define the local faces with their local vertex ordering according to Table 1.1, where the vertex numbering is strictly counter-clockwise in 2D as well as in 3D (see Figure 1.1). Then, the vector of volume coordinates $\vec{\xi}$ is given on the faces via mapping functions from the face parameters χ and τ, as shown in Table 1.2(a). Last but not least, for flux computation over the face, one has to integrate along the face inside the element as well as in the neighbor. This is done consistently by the transformation from the face parameters χ and τ inside the element to the corresponding face parameters $\tilde{\chi}$ and $\tilde{\tau}$ in the neighbour face. Whereas in 2D this transformation is always $\tilde{\chi} = 1 - \chi$, in 3D the transformation depends on the orientation of the neighbor's face with respect to the local face of the considered element $\mathcal{T}^{(m)}$, since via rotation of the triangular faces there may be three possible orientations. The corresponding mappings are given in Table 1.2(b).

In three dimensions, all possible flux matrices are given by

$$F_{kl}^{-,j} = \int_{\partial(T_E)_j} \Phi_k\left(\vec{\xi}^{(j)}\right) \ \Phi_l\left(\vec{\xi}^{(j)}\right) d\chi d\tau, \tag{1.46}$$

where $1 \leq j \leq 4$, and

$$F_{kl}^{+,j,i,h} = \int_{\partial(T_E)_j} \Phi_k\left(\vec{\xi}^{(j)}\right) \Phi_l\left(\vec{\xi}^{(i)}\left(\tilde{\chi}^{(h)}, \tilde{\tau}^{(h)}\right)\right) d\chi d\tau, \tag{1.47}$$

where $1 \leq i \leq 4$ and $1 \leq h \leq 3$. The left state flux matrix (superscript '-') $F_{kl}^{-,j}$ accounts for the contribution of the element (m) itself to the fluxes over face j and the right state flux matrix (superscript '+') $F_{kl}^{+,j,i,h}$ accounts for the contribution of the element's direct side neighbor (k_j) to the fluxes over the face j. Index $1 \leq i \leq N_E$ indicates the local number of the common face as it is seen from neighbor (k_j) and depends on the mesh generator. Index $1 \leq h \leq 3$ denotes the number of the local node in the neighbor's face which lies on the local vertex 1 of face j in tetrahedron number (m). Index h also depends on the mesh generator. On a given tetrahedral mesh, where indices i and h are known, only four of the 48 possible matrices $F_{kl}^{+,j,i,h}$ are used per element.

The whole process of mapping to the reference elements and performing the integrations there makes us pre-compute and store a series of numbers depending on the number of degrees of freedom per element L with $L = (N + 1)(N + 2)(N + 3)/6$. This amount of values to be precomputed is

$$\begin{aligned} n\left(F^+\right) &= 4 \cdot L^2 \\ n\left(F^-\right) &= 12 \cdot L^2 \\ n\left(K^\xi + K^\eta + K^\zeta\right) &= 3 \cdot L^2 \\ n\left(M\right) &= L \end{aligned} \tag{1.48}$$

of which the K and F are sparse matrices, thus involving fewer operations per cycle to be performed. If the semi-discrete equation (1.38) is integrated in time, a quadrature-free DG scheme is obtained (see [3]). Different time-integration schemes can be implemented for such equations but in order to keep a globally high-order scheme one must use a high-order time integration. In the following we present the ADER time integration technique, making extensive use of the governing equation (1.3).

1.5.4   The ADER Time Discretization

The problem of time integrating an equation system such as (1.3) for a time step Δt, assuming that origin time is $t = 0$, can be performed in many ways. Formally, we have

$$\int_0^{\Delta t} \frac{\partial Q_p}{\partial t} dt = - \int_0^{\Delta t} \left[A_{pq} \frac{\partial Q_q}{\partial x} + B_{pq} \frac{\partial Q_q}{\partial y} + C_{pq} \frac{\partial Q_q}{\partial z} \right] dt, \qquad (1.49)$$

so that the left-hand side has the trivial solution

$$\int_0^{\Delta t} \frac{\partial Q_p}{\partial t} dt = Q_p \left(\Delta t \right) - Q_p \left(0 \right). \qquad (1.50)$$

The integral of the right-hand side of (1.49), however, is not straightforward and many techniques and assumptions can be applied to solve it. The most obvious assumption is to impose the integrand in the right-hand side of (1.49) to be constant in time for the interval $t = [0, \Delta t]$. Then the integral can be solved trivially and (1.49) has the form

$$Q_p \left(\Delta t \right) = Q_p \left(0 \right) - \Delta t \left[A_{pq} \frac{\partial Q_q}{\partial x} + B_{pq} \frac{\partial Q_q}{\partial y} + C_{pq} \frac{\partial Q_q}{\partial z} \right], \qquad (1.51)$$

which is known as Euler integration. Unfortunately, it is only first-order accurate. Other advanced time integration schemes exist which make weaker assumptions and allow for higher-order time integration, as Runge-Kutta or Leap-Frog schemes, but they usually require the solution and storage of intermediate steps. Furthermore their efficiency decreases drastically when trying to reach very high orders of accuracy.

The ADER approach will be applied to the semi-discrete form of the DG scheme (1.38) in order to achieve the same accuracy of the time discretization as for the space discretization. Its formulation is described in the following.

The main ingredients of the ADER approach are a Taylor expansion in time, the solution of Derivative Riemann Problems (DRP) [132] to approximate the space derivatives at the interface and the Cauchy-Kovalewski procedure for replacing the time derivatives in the Taylor series by space derivatives. As an example

one might want to see what happens if Q_p is expanded in a Taylor series around $t = \Delta t$. The expansion then takes the shape

$$Q_p(\Delta t) = Q_p(0) + \frac{\partial}{\partial t} Q_p(0)\,\Delta t + \frac{1}{2}\frac{\partial^2}{\partial t^2}Q_p(0)\,\Delta t^2 + \cdots \tag{1.52}$$

In principle the values of the time derivative of $Q_p(t)$ are unknown but one could invert the governing equation (1.3) such that we obtain

$$\frac{\partial Q_p}{\partial t} = -\left(A_{pq}\frac{\partial}{\partial x} + B_{pq}\frac{\partial}{\partial y} + C_{pq}\frac{\partial}{\partial z} \right) Q_q, \tag{1.53}$$

meaning that the time-derivatives can be expressed as a function of space-derivatives. In principle the space derivatives of the solution at a given time can be known, so that by substituting (1.53) into (1.52) is obtained

$$Q_p(\Delta t) = Q_p(0) - \Delta t \left[A_{pq}\frac{\partial Q_q(0)}{\partial x} + B_{pq}\frac{\partial Q_q(0)}{\partial y} + C_{pq}\frac{\partial Q_q(0)}{\partial z} \right], \tag{1.54}$$

which is the Euler time integration again. The important issue is that this procedure can be expanded as more terms of the Taylor series (1.52) can be used. This way we successively obtain time-derivatives of Q_p as a function of the space derivatives. In short, the general process for a polynomial of degree N requires the Taylor expansion

$$Q_p(x,y,z,t) = \sum_{k=0}^{N} \frac{t^k}{k!}\frac{\partial^k}{\partial t^k}Q_p(x,y,z,0), \tag{1.55}$$

together with the generalised expression of (1.53), which reads

$$\frac{\partial^k Q_p(x,y,z,t)}{\partial t^k} =$$
$$= (-1)^k \left(A_{pq}\frac{\partial}{\partial x} + B_{pq}\frac{\partial}{\partial y} + C_{pq}\frac{\partial}{\partial z} \right)^k Q_q(x,y,z,t). \tag{1.56}$$

Now, by recursively substituting the time derivatives of (1.55) into (1.56), what is known as the *Cauchy-Kovalewski* procedure, we finally obtain the high-order expression of the time-expansion of the variables Q_p

$$Q_p(x,y,z,t) =$$
$$= \sum_{k=0}^{N} \frac{t^k}{k!}(-1)^k \left(A_{pq}\frac{\partial}{\partial x} + B_{pq}\frac{\partial}{\partial y} + C_{pq}\frac{\partial}{\partial z} \right)^k Q_q(x,y,z,0). \tag{1.57}$$

This last expression can be time integrated as t appears only as monomials. The expression (1.57) is the center piece of the ADER high-order time integration process.

In the following this process will be applied to the particular DG scheme presented here. Since the basis functions Φ_l in (1.23) are given in the $\xi\eta\zeta$-system, we need a Cauchy-Kovalewski procedure which makes use of the spatial derivatives with respect to ξ, η, and ζ. Therefore, the original PDE (1.3) can be rewritten with the use of (1.37) as

$$
\begin{aligned}
\frac{\partial Q_p}{\partial t} \ &+ \ A_{pq}\left(\frac{\partial \xi}{\partial x}\frac{\partial Q_q}{\partial \xi} + \frac{\partial \eta}{\partial x}\frac{\partial Q_q}{\partial \eta} + \frac{\partial \zeta}{\partial x}\frac{\partial Q_q}{\partial \zeta}\right) + \\
&+ \ B_{pq}\left(\frac{\partial \xi}{\partial y}\frac{\partial Q_q}{\partial \xi} + \frac{\partial \eta}{\partial y}\frac{\partial Q_q}{\partial \eta} + \frac{\partial \zeta}{\partial y}\frac{\partial Q_q}{\partial \zeta}\right) + \\
&+ \ C_{pq}\left(\frac{\partial \xi}{\partial z}\frac{\partial Q_q}{\partial \xi} + \frac{\partial \eta}{\partial z}\frac{\partial Q_q}{\partial \eta} + \frac{\partial \zeta}{\partial z}\frac{\partial Q_q}{\partial \zeta}\right) = 0.
\end{aligned}
$$

Rearranging this equation leads to

$$
\begin{aligned}
\frac{\partial Q_p}{\partial t} \ &+ \ \frac{\partial Q_p}{\partial t}\left(A_{pq}\frac{\partial \xi}{\partial x} + B_{pq}\frac{\partial \xi}{\partial y} + C_{pq}\frac{\partial \xi}{\partial z}\right)\frac{\partial Q_q}{\partial \xi} + \\
&+ \ \frac{\partial Q_p}{\partial t}\left(A_{pq}\frac{\partial \eta}{\partial x} + B_{pq}\frac{\partial \eta}{\partial y} + C_{pq}\frac{\partial \eta}{\partial z}\right)\frac{\partial Q_q}{\partial \eta} + \\
&+ \ \frac{\partial Q_p}{\partial t}\left(A_{pq}\frac{\partial \zeta}{\partial x} + B_{pq}\frac{\partial \zeta}{\partial y} + C_{pq}\frac{\partial \zeta}{\partial z}\right)\frac{\partial Q_q}{\partial \zeta} = 0,
\end{aligned}
$$

and finally, by using the definitions in (1.39), (1.40), and (1.41), one obtains

$$
\frac{\partial Q_p}{\partial t} + A_{pq}^*\frac{\partial Q_q}{\partial \xi} + B_{pq}^*\frac{\partial Q_q}{\partial \eta} + C_{pq}^*\frac{\partial Q_q}{\partial \zeta} = 0 \,. \tag{1.58}
$$

The k-th time derivative as a function of pure space derivatives in the $\xi\eta\zeta$-reference system is the result of the Cauchy-Kovalewski procedure (1.56) applied to (1.58) and is given by

$$
\begin{aligned}
\frac{\partial^k Q_p(\xi,\eta,\zeta,t)}{\partial t^k} &= \\
&= \ (-1)^k \left(A_{pq}^*\tfrac{\partial}{\partial \xi} + B_{pq}^*\tfrac{\partial}{\partial \eta} + C_{pq}^*\tfrac{\partial}{\partial \zeta}\right)^k Q_q(\xi,\eta,\zeta,t).
\end{aligned} \tag{1.59}
$$

Now, it just remains to replace the time derivatives in the Taylor expansion (1.55), using (1.59):

$$
\begin{aligned}
Q_p(\xi,\eta,\zeta,t) &= \\
&= \ \sum_{k=0}^{N}\frac{t^k}{k!}(-1)^k\left(A_{pq}^*\tfrac{\partial}{\partial \xi} + B_{pq}^*\tfrac{\partial}{\partial \eta} + C_{pq}^*\tfrac{\partial}{\partial \zeta}\right)^k Q_q(\xi,\eta,\zeta,0).
\end{aligned} \tag{1.60}
$$

The Discontinuous Galerkin approximation (1.23) is then introduced to obtain

$$
\begin{aligned}
Q_p(\xi, \eta, \zeta, t) &= \\
&= \sum_{k=0}^{N} \frac{t^k}{k!} (-1)^k \left(A_{pq}^* \frac{\partial}{\partial \xi} + B_{pq}^* \frac{\partial}{\partial \eta} + C_{pq}^* \frac{\partial}{\partial \zeta} \right)^k \Phi_l(\xi, \eta, \zeta) \hat{Q}_{ql}(0).
\end{aligned}
\tag{1.61}
$$

This approximation can now be projected onto each basis function in order to get an approximation of the evolution of the degrees of freedom during one time step from time level n to time level $n+1$. As a result it is obtained

$$
\begin{aligned}
\hat{Q}_{pl}(t) &= \\
&= \frac{\left\langle \Phi_n, \sum_{k=0}^{N} \frac{t^k}{k!} (-1)^k \left(A_{pq}^* \frac{\partial}{\partial \xi} + B_{pq}^* \frac{\partial}{\partial \eta} + C_{pq}^* \frac{\partial}{\partial \zeta} \right)^k \Phi_m(\xi,\eta,\zeta) \right\rangle}{\langle \Phi_n, \Phi_l \rangle} \hat{Q}_{qm}(0)
\end{aligned}
\tag{1.62}
$$

where $\langle a, b \rangle = \int_{\mathcal{T}_E} a \cdot b \, dV$ denotes the inner product over the reference tetrahedron $\mathcal{T}_E$ and the division by $\langle \Phi_n, \Phi_l \rangle$ denotes the multiplication with the inverse of the mass matrix. This reduces indeed to division by its diagonal entries since the mass matrix is diagonal due to the orthogonality of the basis functions Φ_l. Equation (1.62) can be integrated analytically in time, thus obtaining

$$
\begin{aligned}
\int_0^{\Delta t} \hat{Q}_{pl}(t) dt &= \\
&= \frac{\left\langle \Phi_n, \sum_{k=0}^{N} \frac{\Delta t^{(k+1)}}{(k+1)!} (-1)^k \left(A_{pq}^* \frac{\partial}{\partial \xi} + B_{pq}^* \frac{\partial}{\partial \eta} + C_{pq}^* \frac{\partial}{\partial \zeta} \right)^k \Phi_m(\xi,\eta,\zeta) \right\rangle}{\langle \Phi_n, \Phi_l \rangle} \hat{Q}_{qm}(0).
\end{aligned}
\tag{1.63}
$$

Introducing the definition

$$
\begin{aligned}
I_{plqm}(\Delta t) &= \\
&= \frac{\left\langle \Phi_n, \sum_{k=0}^{N} \frac{\Delta t^{(k+1)}}{(k+1)!} (-1)^k \left(A_{pq}^* \frac{\partial}{\partial \xi} + B_{pq}^* \frac{\partial}{\partial \eta} + C_{pq}^* \frac{\partial}{\partial \zeta} \right)^k \Phi_m(\xi,\eta,\zeta) \right\rangle}{\langle \Phi_n, \Phi_l \rangle}
\end{aligned}
\tag{1.64}
$$

the time-integrated degrees of freedom in equation (1.63) can be expressed as

$$
\int_0^{\Delta t} \hat{Q}_{pl}(t) dt = I_{plqm}(\Delta t) \hat{Q}_{qm}(0),
\tag{1.65}
$$

where $I_{plqm}(\Delta t)$ is a four-dimensional tensor including the Cauchy-Kovalewski procedure and $\hat{Q}_{qm}(0)$ denotes the $q \times m$-matrix of the degrees of freedom at time level n. Finally, the fully discrete ADER-DG scheme by integration of (1.38) in

time is given by:

$$
\left[\left(\hat{Q}_{pl}^{(m)}\right)^{n+1} - \left(\hat{Q}_{pl}^{(m)}\right)^{n}\right] |J| \, M_{kl} \quad +
$$

$$
+ \quad \tfrac{1}{2} \sum_{j=1}^{4} T_{pq}^{j} \left(A_{qr}^{(m)} + \Theta_{qr}^{(m)}\right) (T_{rs}^{j})^{-1} |S_j| \, F_{kl}^{-,j} \cdot I_{slmn}(\Delta t) \left(\hat{Q}_{mn}^{(m)}\right)^{n} +
$$

$$
+ \quad \tfrac{1}{2} \sum_{j=1}^{4} T_{pq}^{j} \left(A_{qr}^{(m)} - \Theta_{qr}^{(m)}\right) (T_{rs}^{j})^{-1} |S_j| \, F_{kl}^{+,j,i,h} \cdot I_{slmn}(\Delta t) \left(\hat{Q}_{mn}^{(m_j)}\right)^{n} -
$$

$$
- \quad A_{pq}^{*} |J| \, K_{kl}^{\xi} \cdot I_{qlmn}(\Delta t) \left(\hat{Q}_{mn}^{(m)}\right)^{n} -
$$

$$
- \quad B_{pq}^{*} |J| \, K_{kl}^{\eta} \cdot I_{qlmn}(\Delta t) \left(\hat{Q}_{mn}^{(m)}\right)^{n} -
$$

$$
- \quad C_{pq}^{*} |J| \, K_{kl}^{\zeta} \cdot I_{qlmn}(\Delta t) \left(\hat{Q}_{mn}^{(m)}\right)^{n} = 0 \, .
$$

$$(1.66)$$

The scheme is quadrature-free and performs high-order time-integration from time level t^n to t^{n+1} in one single step. It thus needs the same memory as a first-order explicit Euler time stepping scheme (1.51). It should be stressed out that the above mentioned scheme is globally high-order and as a consequence possesses superior convergence properties with respect to most common available solvers. For a numerical verification of the convergence properties of the scheme and comparison to other schemes, the reader is addressed to check the convergence tests in [55, 75]

The stability of the explicit ADER time stepping scheme is controlled by the CFL number, introduced by Courant, Friedrichs and Lewy in [42]. For the particular case of the scheme shown here, this means that for element (m)

$$
\Delta t^{(m)} \leq C \frac{1}{2N+1} \frac{l^{(m)}}{c_{max}^{(m)}}
$$

$$(1.67)$$

where l is the element size, for tetrahedra the diameter of the inscribed sphere, and c_{max} the maximum wave speed supported by the element's material properties. The coefficient C has been shown [53] to have a maximum value of 0.7, being often 0.5 a recommendable value. For the scheme to be stable no element must violate (1.67). Therefore, the Δt used in the scheme presented here has to be the minimum of the local $\Delta t^{(m)}$, values present in the computational mesh. For a thorough investigation of the linear stability properties of the ADER-DG schemes via a von Neumann analysis see [53].

A major breakthrough in the ADER-DG framework is the possibility of making use of a *local time stepping* scheme as has been shown in [58]. This scheme type is designed to optimize the constraints induced by Courant's stability criterion. Basically, each of the cells in the computational domain is assigned a local

time step value which is the maximum allowed for stability reasons as computed with (1.67). They also possess a local time value, mainly their own $\Delta t^{(m)}$ value times the number of times they have been updated, i.e the number of their local iterations. Then, as time marches in the scheme, an element m updates its variables if and only if after a (local) time step it would have a smaller local time than if any of the four direct neighbors k_j with $j = 1, \cdots, 4$ would add a time step to their local time. Explicitly,

$$t^{(m)} + \Delta t^{(m)} \leq \min\left(t^{(k_j)} + \Delta t^{(k_j)}\right) \qquad \forall\, k_j. \tag{1.68}$$

Additionally and in order to synchronize the cell's updating, when an element is updated fulfilling (1.68), the numerical fluxes between two elements $T^{(m)}$ and $T^{(k_j)}$ have to be computed in the time interval

$$[t_1; t_2] = \left[\max\left(t^{(m)}, t^{(k_j)}\right); \min\left(t^{(m)} + \Delta t^{(m)}, t^{(k_j)} + \Delta t^{(k_j)}\right)\right]. \tag{1.69}$$

The use of local time stepping instead of a global time stepping (LTS and GTS from now on) does not change the fundamental properties of the ADER-DG method nor its accuracy as is described in more detail in [58]. It only produces an, often remarkable, reduction in the computational time required when element sizes are very different. LTS has been implemented for all the rheology types covered in the present study and used whenever it was advantageous in terms of efficiency.

1.6 Boundary Conditions

As has been previously remarked in Section 1.4.1, the usage of fluxes simplifies the implementation of many boundary types, as fluxes determine all the communication between neighboring cells. Therefore, any effect coming from the sides of a cell not directly connected to any other can be solved by assigning proper values to a *ghost* element which would theoretically connect to a boundary element. The ghost element does not explicitly appear in the computation as only its variable's values at the boundary are necessary to properly implement the desired boundary conditions.

1.6.1 Absorbing Boundaries

At absorbing boundaries, no waves are supposed to enter the computational domain and the waves traveling outward should pass the boundary without reflections. As has been shown in (1.20), the flux can be separated in an incoming and an outgoing part, as a consequence of using an upwinding method. A rough approach to get absorbing boundaries can be obtained by solving an inverse Riemann problem. This means that the aim is to obtain the state of variables at both

sides of the interface such that the flux produces some required variables' values at the interface. For the absorbing boundary case one sets the incoming flux values to zero, so that waves are only allowed to flow out of the computational domain. This is formally equivalent to assuming that a ghost element has value of zero for all variables at the boundary. This translates into having the following value for the flux in (1.66) at all those tetrahedral faces that coincide with an absorbing boundary:

$$f_p^{\text{AbsorbBC}} = \frac{1}{2} T_{pq} \left(A_{qr}^{(m)} + \Theta_{qr}^{(m)} \right) (T_{rs})^{-1} \hat{Q}_{sl}^{(m)} \Phi_l^{(m)}, \tag{1.70}$$

which is the absorbing boundary condition we apply. This approach still produces reflections of non-negligible amplitudes and thus often is more practical to just enlarge the computational domain with very coarse elements in order to delay the interference of these waves with the actual signal one wants to model. Although a totally non-reflecting boundary for wave propagation problems does not exist, some approaches can get much better results. Perfectly Matched Layers (PML) [8] are applied in [41, 84] and are very effective but are not formally boundary conditions, in the sense that they are not exclusively applied to the boundary of the domain. They are applied on a buffer layer of elements, where some physical properties are imposed, which strongly damp waves traveling through it. In practice, for time-domain computations the computational cost is increased due to the additional elements incorporated to the model and the increased complexity of the wave equations to solved in this buffer layer.

1.6.2   Free Surface Boundaries

The free-boundary condition aims at representing the contact of an elastic material with air or void. In finite-element based computations the condition is satisfied very naturally by imposing the value of the bulk stress and shear stresses associated to the direction normal to the free surface to be zero at the boundary. When using numerical fluxes, the concept of inverse Riemann problem discussed in last Section is recalled. The free boundary condition can be reached by assigning to the ghost element values for these components that mirror the above mentioned stresses. As a consequence the flux will assign a zero value for those variables at the boundary. The rest of the variables should be the same as in the inner element, so that the fluxes don't change its boundary extrapolated values. If the inner element's variable state is Q_p, then the free-surface condition's flux function in (1.66) can be formulated as follows,

$$\begin{aligned} f_p^{\text{FreeBC}} = \quad & \tfrac{1}{2} T_{pq} \left(A_{qr}^{(m)} + \Theta_{qr}^{(m)} \right) (T_{rs})^{-1} \hat{Q}_{sl}^{(m)} \Phi_l^{(m)} \quad + \\ & + \ \tfrac{1}{2} T_{pq} \left(A_{qr}^{(m)} - \Theta_{qr}^{(m)} \right) \Gamma_{rs} (T_{st})^{-1} \hat{Q}_{tl}^{(m)} \Phi_l^{(m)}, \end{aligned} \tag{1.71}$$

where the matrix $\Gamma_{rs} = \text{diag}\,(-1, 1, 1, -1, 1, -1, 1, 1, 1)$ accounts for the mirroring of normal and shear stresses with respect to the face-normal direction. It should be clear from (1.71) that no values are stored or computed for the ghost element, but rather the condition is directly applied to the Q_p state vector of the inner cell. The calculation (1.71) is only happening at the boundary surface and not beyond it.

1.6.3 Inflow Boundaries

The effects of a wave entering the computational domain from outside of its spatial extent can be also successfully handled by using the so-called inflow boundary type. Let's suppose an arbitrary function $u_s(x, y, z, t)$ that describes the desired inflow wave value of each variable component s. Such function can be integrated in space at an element's triangular inflowing boundary using Gaussian integration, thus obtaining $U_s^{\text{Inflow}} = \sum\limits_{i=1}^{nGP} \omega_i u_s(\xi_i, \eta_i, \zeta_i, t)$, where nGP is the number of gaussian integration points required to exactly integrate functions up to the accuracy order of the scheme and w_i are the corresponding integration weights. The general shape of the inflow flux will then be

$$
\begin{aligned}
f_p^{\text{InflowBC}} = \quad & \tfrac{1}{2} T_{pq} \left(A_{qr}^{(m)} + \Theta_{qr}^{(m)} \right) (T_{rs})^{-1} Q_s^{(m)} + \\
+ \quad & \tfrac{1}{2} T_{pq} \left(A_{qr}^{(m)} - \Theta_{qr}^{(m)} \right) (T_{rs})^{-1} U_s^{\text{Inflow}},
\end{aligned}
\tag{1.72}
$$

where it should be noticed that the outflow part of the flux, essentially the first term of (1.34), remains the same while the second term is now imposed depending on the desired inflow wave. In the present study the interest will be further reduced to pure plane waves. The eigenstructure analysis of the Jacobian matrices allows us to find the eigenvectors R_j^A related to each plane wave type. Therefore to reproduce a P-wave traveling in the z direction it has to be chosen the 9th eigenvector, associated to the eigenvalue $+\alpha_9 = c_p$ (see (1.9)), thus obtaining $u_s(\xi_i, \eta_i, \zeta_i, t) = R_9^A S(t)$, being $S(t)$ the time shape function of the plane wave. If the boundary is perpendicular to the plane wave propagation direction, all spatial dependence of u_s vanishes.

In order to include this new flux into the scheme one has to further obtain the projection of U_s^{Inflow} into the DG basis as $U_s^{\text{Inflow}} = \hat{U}_{sl}^{\text{Inflow}} \phi_l$, thus obtaining

$$
\begin{aligned}
f_p^{\text{InflowBC}} = \quad & \tfrac{1}{2} T_{pq} \left(A_{qr}^{(m)} + \Theta_{qr}^{(m)} \right) (T_{rs})^{-1} \hat{Q}_{sl}^{(m)} \phi_l + \\
+ \quad & \tfrac{1}{2} T_{pq} \left(A_{qr}^{(m)} - \Theta_{qr}^{(m)} \right) (T_{rs})^{-1} \hat{U}_{sl}^{\text{Inflow}} \phi_l,
\end{aligned}
\tag{1.73}
$$

A final remark is that the ADER procedure cannot be applied to the inflow part of this flux. Instead, we perform a high-order gaussian time-integration of $S(t)$,

which should be exact for a sufficiently sampled $S(t)$ function. Notice that this boundary type automatically works as an open boundary for outflowing waves (compare to (1.70)). The analysis can be expanded to the general case of waves with an arbitrary incidence angle, thus requiring a rotation of the eigenvectors R^A associated to the wave and a time synchronization of $u_s(x, y, z, t)$ to account for the fact that now not everywhere in the boundary holds the same state of u_s.

1.7 Computational Aspects

Besides its mathematical formulation and accuracy properties, a series of aspects of the ADER-DG method are related to practical issues regarding computational science. In the following Chapter we will discuss some of these aspects which are relevant to the common use of the method as well as its potential for being applied for large scale problems.

1.7.1 Efficiency

The usefulness of a numerical solver depends on the computational effort it requires in addition to its accuracy. In this Section we show a rough calculation of the amount of operations per element to be performed by a scheme such as (1.38). One should recall that the number of degrees of freedom per element and variable involved in the computation is $L = (N + 1)(N + 2)(N + 3)/6$. The number $\mathcal{O}$ of operations per element and variable to be performed can be counted, by taking into account only terms proportional to L^p with $p \geq 1$ and by separating the computation into flux, stiffness and mass contributions. This leads to

$$\mathcal{O}_{\text{total}} = 4 \cdot \mathcal{O}_{\text{flux}} + 3 \cdot \mathcal{O}_{\text{stiff}} + \mathcal{O}_{\text{mass}} \tag{1.74}$$

as the flux is computed for 4 sides of the tetrahedron and the stiffness for each reference element component ξ, η and ζ. One can now take a closer look at all the $\mathcal{O}$ values in (1.74). The fluxes, for instance, involve a rotation of the variables as in (1.30) (a 9x9 matrix-vector product per each degree of freedom) and the integration of the degrees of freedom as shown in (1.46-1.47) (a sparse LxL matrix-vector product per each variable). As required by the flux expression (1.34), this operations will be performed once per the inflowing and once for the outflowing fluxes of each element's side. The stiffness operations involve the product of the star jacobians (1.39-1.41) by the vector of unknowns (a 9x9 matrix-vector product per each degree of freedom, where a maximum of 27 entries of the star matrices are non-zero) and the integration of the derivatives of the degrees of freedom as shown in (1.43-1.45) (a sparse LxL matrix-vector product per each variable). Finally, the mass matrix is diagonal so the product of the degrees of freedom by its inverse is a simple L-size vector-vector product per each variable. Individually, each of these parts has to perform a total of operations equal to

$$\begin{aligned}
\mathcal{O}_{\text{flux}} &= 2\left(9Z^{\text{flux}}L^2 + 81L\right) \\
\mathcal{O}_{\text{stiff}} &= 9Z^{\text{stiff}}L^2 + 27L \\
\mathcal{O}_{\text{mass}} &= 9L,
\end{aligned} \tag{1.75}$$

where Z^{flux} and Z^{stiff} reflect the sparsity of some of the involved matrix operations, being the ratio between non-zero entries and total entries of the F and K matrices respectively. In total, the number of operations will be

$$\mathcal{O}_{\text{total}} = 27Z^{\text{flux}}L^2 + 72Z^{\text{stiff}}L^2 + 738L \tag{1.76}$$

For example, in the order 4 case ($L = 20$) holds $Z^{\text{stiff}} = 0.17$ and $Z^{\text{flux}} = 0.51$. Then the cost would be

$$\mathcal{O}_{\text{total}} = 40.6L^2 + 738L. \tag{1.77}$$

Additionally, we can observe that for the case of order 4 the fluxes perform approximately an 87% of the workload. Although this calculation doesn't take into account the costs of the time-integration chosen, the timestep allowed or the total number of elements required to solve a particular problem, it should give an idea on the cost of execution of the scheme. In comparison, an SEM code with a structure as SPECFEM3D [83] would require $\mathcal{O}_{\text{SEM}} = 18L^{4/3} + 99L$ which is clearly inferior. Taking into account that SEM works on a basis with $L = (p+1)^3$, this leads to a factor of 2.81 less operations per variable and element in favor of SEM for the case of polynomial basis of degree 3. It should also be pointed out that this is a theoretical calculation and that actual efficiency is strongly dependant on how is the scheme specifically programmed. Additionally, a number of other factors should be taken into account for a full efficiency comparison as is the size of the timestep allowed, the number of elements required to fill a certain volume, the number of variables used in the scheme or the cost of the time integration scheme used. Some numerical results concerning these two methods for a simple setup will be seen in Chapter 3.

1.7.2 Meshing

The ADER-DG scheme works on tetrahedral meshes, which is an advantage when trying to discretize very complex geometrical objects. Basically a given geometrical model is first discretized in volumes and surfaces describing the geological and topographical features relevant for the simulation. This can be done externally using Computer Aided Design (CAD) tools. Once the geometry is well defined, meshing software can perform the discretization of the volumes in conforming tetrahedra. This process is fully automated and the user is often allowed to control a few meshing parameters as are the average element size, crucial for the balance between resolution and stability in wave propagation problems. The created mesh can be then exported as a file containing all relevant information about the elements, including its indexing, connectivity of the mesh and specific boundary

conditions. A number of different mesh generators can be used. The running algorithm then just needs to read the mesh generator's output file, whose format depends of the generator used, to apply that mesh information for the simulation process.

The use of tetrahedral elements with plane element interfaces, as in the ADER-DG algorithm, is not an intrinsic limitation of the ADER-DG method and super-parametric elements can be used, where the element faces are also represented by higher-order polynomial surfaces [59]. Of course, the geometrical precision can be enhanced when aligning such meshes with curved material interfaces, especially when the analytical shape of the curvature is known or a very fine grid describing it is available. However in the present thesis the superparametric case is not discussed.

For most of the test cases computed up to now for validation purposes of the ADER-DG method, the geometry is quite simple and the use of tetrahedral meshes does not provide any particular advantage with respect to the more popular regular or structured hexahedral meshes. However, for complicated geometries, the duration of the model setup and mesh generation using tetrahedral instead of hexahedral elements can be reduced by more than one magnitude [58].

1.7.3   Parallelization

The parallelization of the proposed algorithm for large scale applications is a further key issue. The partitioning of the tetrahedral mesh into a number of sub domains is performed by the free METIS software [74]. It automatically performs partitioning of meshes with several millions of elements within seconds while minimizing the surface to volume ratio of the resulting sub domains. Roughly, the volume of a given partition can be associated with processor load whereas the surface of a partition is associated to communication between processors. As communication is orders of magnitude slower than the computational load, the better the volume/surface ratio for all partitions, the more efficiently the parallel algorithm can work. In the present implementation of the method each partition is handled by one processor or core. As shown in Section 1.5, the ADER-DG method has a very local character as the update of the variables in one element depends only on the element itself and its four direct neighbors. Additionally, the amount of data communication between processors is small as only variables of the elements exactly at an interface between two sub domains have to be passed between processors. Recall, that the size of these interfaces is exactly the parameter minimized by METIS. Furthermore, this information has to be passed only once every time step as the ADER-DG scheme is a one-step scheme without intermediate stages. MPI (Message Passing Interface) libraries are used to perform the communication between processors.
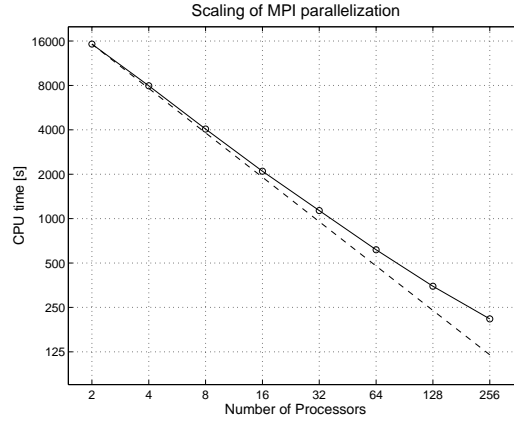
Figure 1.4: Graph of the scaling properties of the MPI parallelization for an ADER-DG $\mathcal{O}5$ scheme. The problem is computed on a cube discretized by 69120 regular tetrahedral elements as used also for the convergence test in [55]. The computations are carried out on the HLRB2 supercomputer of the Leibniz Rechenzentrum in München on $2, 4, 8, 16, 32, 128$ and 256 CPUs. The dashed line shows the theoretical optimum for comparison assuming 100% MPI efficiency.

How the ADER-DG scheme scales with increasing number of processors is displayed in Fig. 1.4. For this scaling analysis we use an ADER-DG $\mathcal{O}5$ scheme. The computational domain is discretized by a mesh of 69120 tetrahedral elements. As a reference we also plot the line of the theoretical optimum supposing 100% MPI efficiency, meaning that the CPU time would exactly reduce by a factor of F if the number of processors is increased by the same factor F.

1.8 Application Example

To verify the performance of the ADER-DG method we will use the setup proposed in the SPICE Code Validation (www.nuquake.eu/SPICECVal) and developed by Peter Moczo, Jean Paul Ampuero, Jozef Kristek, Steven M. Day, Miriam Kristekova, Peter Pazak, Heiner Igel, Renata Tothova, and Martin Galis. The problem itself, named WP1-HSP1a (Wave Propagation, Homogeneous Space) aims at assessing dispersion errors and local errors at different distances and propagation directions. The medium is described in Table 1.3. The seismic source is a point dislocation, represented by a double couple source, where the only non-zero entries of the seismic moment tensor are $M_{xy} = M_{yx} = M_0 = 10^{18} Nm$. The location of the point source is the coordinate origin $(x_s, y_s, z_s)=(0m, 0m, 0m)$. The moment-rate time history is given through the source time function

$$S^T(t) = \frac{t}{T^2} \exp(-\frac{t}{T}), \qquad (1.78)$$
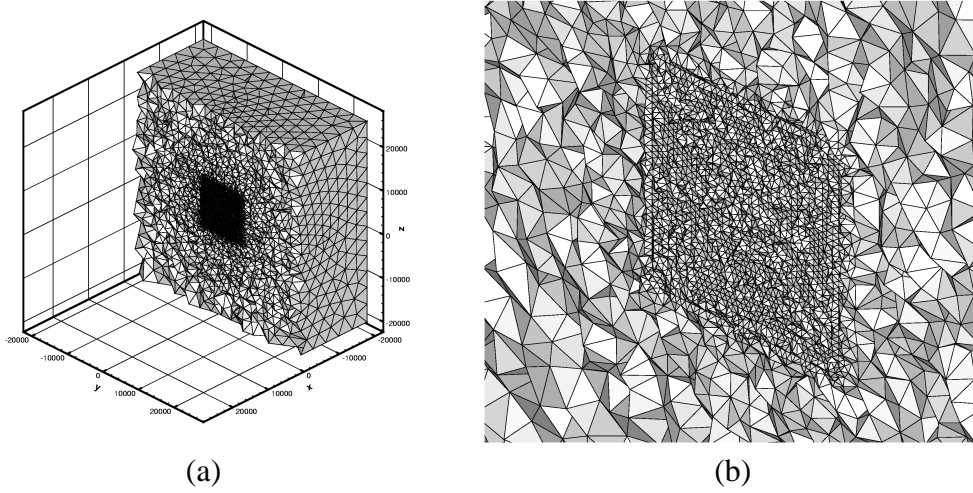
Figure 1.5: (a) Mesh used for the application example. (b) Zoom of the region of interest, where a strong refinement has been applied.

where the smoothness parameter T, controlling the frequency content and amplitude of the source time function, is set to $T = 0.1$s. The frequency window expected is from 0.13Hz to 5Hz and the receivers are at a maximum distance of $10,000$m from the source. In order to avoid boundary effects, the domain is selected large enough so that no reflections can reach the receivers. This domain is a cube defined by points $(-20000m, -20000m, -20000m)$, $(-20000m, -20000m, 26000m)$, $(-20000m, 26000m, -20000m)$ and $(26000m, -20000m, -20000m)$. The receiver list is shown in Table 1.4. The domain was discretized by a tetrahedral mesh refined to have elements of $300m$ edge size in the area between source and receivers and further coarsened in the rest of the domain, where accurate results are no longer needed (see Fig. 1.5). An ADER-DG $\mathcal{O}6$ scheme was used, meaning that polynomials of degree 5 were used to describe the unknown functions. A total of $623,920$ elements was used. The simulation lasted for less than 23 hours in 128 Intel Itanium2 1.6GHz processors. A local time stepping algorithm is used to save computational time, as is briefly outlined in Section 1.5.4, thus concentrating the computational load in the small tetrahedra of the area of interest. The numerical results are compared to those obtained with an analytical solution as outlined in [1]. The resulting seismograms are shown in Figures 1.6, 1.7 and 1.8 together with the root mean square error (r.m.s) of the numerical solution. This r.m.s. misfit is computed through

$$E = \sum_{j=1}^{n_t}(s_j - s_j^a)^2 / \sum_{j=1}^{n_t}(s_j^a)^2, \qquad (1.79)$$

where n_t is the number of time samples of the seismogram, s_j is the numerical value of the particular seismogram at sample j and s_j^a is the corresponding ana-

Table 1.3: Material parameters for the WP1-HSP1 test case.

$c_p[m/s]$	$c_s[m/s]$	$\rho[kg/m^3]$
6000	3464	2700

Table 1.4: Location of the receivers for the WP1-HSP1 test case.

Receiver	$x[m]$	$y[m]$	$z[m]$
1	0	693	0
2	0	5543	0
3	0	10392	0
4	490	490	0
5	3919	3919	0
6	7348	7348	0
7	400	400	400
8	3200	3200	3200
9	6000	6000	6000
10	555	370	185
11	4443	2962	1481
12	8331	5554	2777

lytical value. Notice that the numerical results are totally *unfiltered* and *unscaled*. The accuracy is further assessed using the concepts of phase misfit and envelope misfit described in [87]. These misfits are then compared to those of a Discrete Wavenumber (DWN) solution, often considered a quasi-analytical solution and shown in Table 1.5. The ADER-DG method performs very well as can be seen in Table 1.5, specially for phase misfits, at some receivers even surpassing DWN's accuracy. The computational costs are, however, very expensive and clearly inappropriate for such a geometrically simple setup as is the one covered in this example. However it should be remarked that the purpose of this application in only to assess numerical accuracy.

1.9 Other Methods for the Simplex

In the following the other methods developed for wave propagation in the simplex (triangles and tetrahedra in 2D and 3D) will be briefly outlined and put in
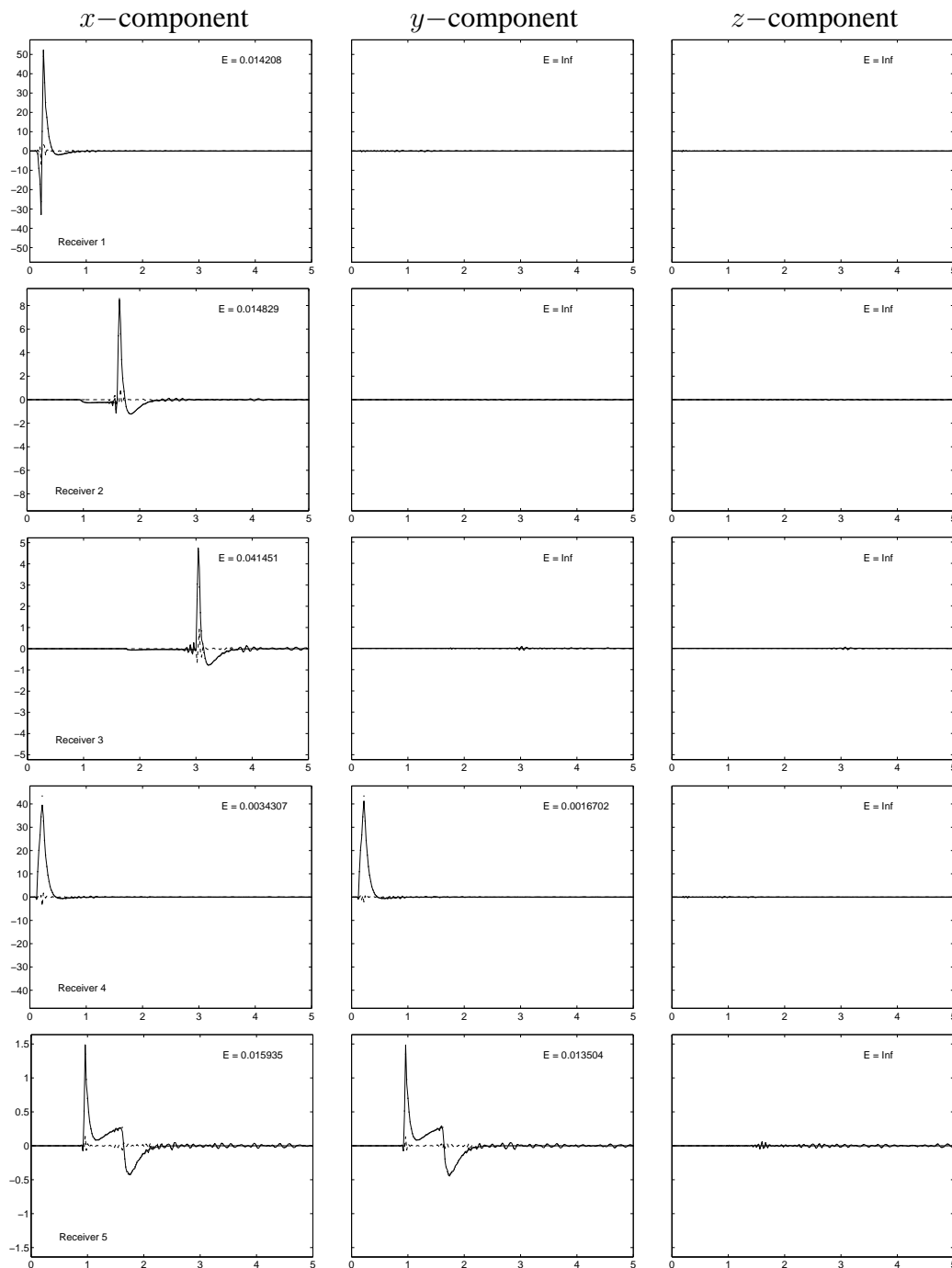
Figure 1.6: Seismograms showing particle velocities for the ADER-DG (solid) and analytical solution (dotted) for receivers 1 to 5. The three columns correspond to the $x-$, $y-$ and $z-$ components. The residuals (dashed) and the r.m.s errors E are shown.

Figure 1.7: Seismograms showing particle velocities for the ADER-DG (solid) and analytical solution (dotted) for receivers 6 to 10. The three columns correspond to the $x-$, $y-$ and $z-$ components. The residuals (dashed) and the r.m.s errors E are shown.

Table 1.5: Envelope and phase misfits in % for WP-HSP1a against a reference solution. DWN results are included for comparison.

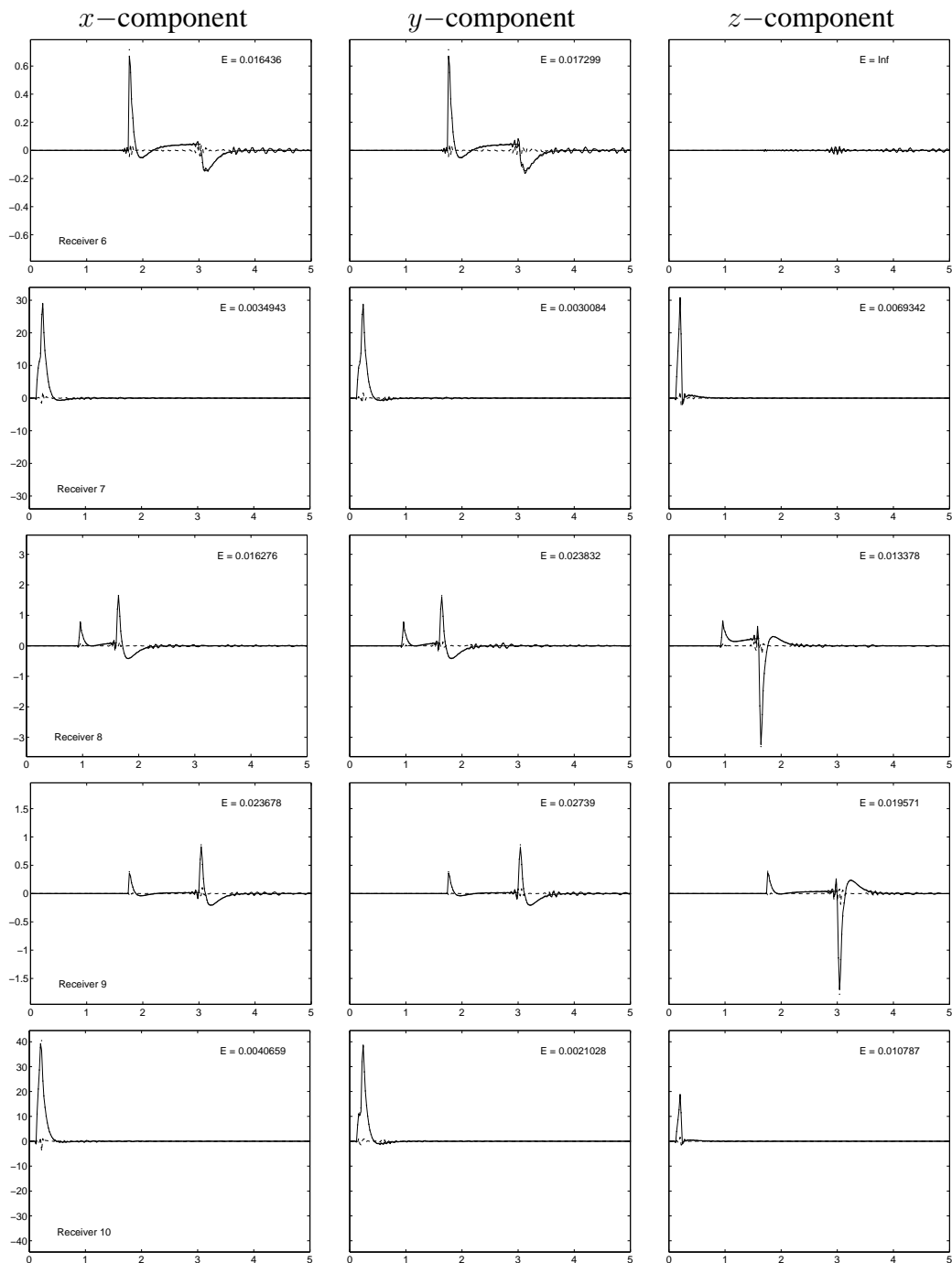|	x		y		z		$\text{Max}_{(\text{DG})}$		$\text{Max}_{(\text{DWN})}$	
Rec.	EM	PM	EM	PM	EM	PM	EM	PM	EM	PM
1	2.7	0.2	0.5	0.0	0.3	0.0	2.7	0.2	3.0	0.5
2	1.7	0.5	0.6	0.0	0.3	0.0	1.7	0.5	1.5	0.3
3	2.2	0.5	0.5	0.0	0.3	0.0	2.2	0.5	1.2	0.3
4	1.1	0.3	1.1	0.3	0.3	0.0	1.1	0.3	1.2	0.3
5	3.4	0.3	3.1	0.3	2.7	0.0	3.4	0.3	1.3	0.2
6	2.2	0.3	2.5	0.3	2.1	0.0	2.5	0.3	0.8	0.1
7	0.7	0.4	1.0	0.3	1.3	0.3	1.3	0.4	1.0	0.5
8	1.6	0.4	2.0	0.2	2.1	0.4	2.1	0.4	1.6	0.2
9	1.7	0.4	1.3	0.2	1.9	0.5	1.9	0.5	1.2	0.3
10	1.4	0.3	0.7	0.3	0.6	0.1	1.4	0.3	1.1	0.3
11	1.5	0.2	2.1	0.4	2.0	0.3	2.1	0.4	1.2	0.3
12	1.0	0.1	2.1	0.4	1.1	0.3	2.1	0.4	0.9	0.3
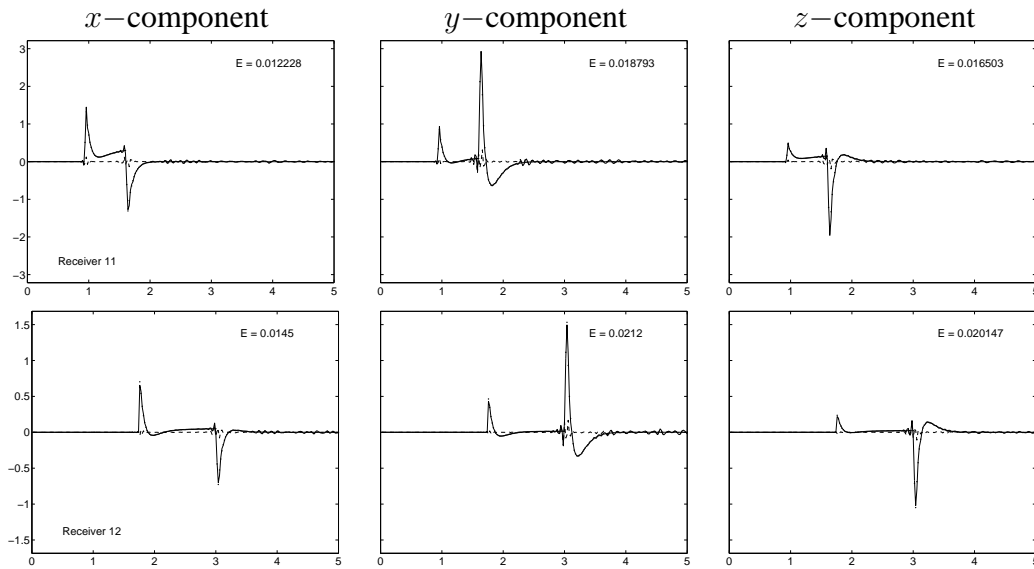
Figure 1.8: Seismograms showing particle velocities for the ADER-DG (solid) and analytical solution (dotted) for receivers 11 to 12. The three columns correspond to the $x-$, $y-$ and $z-$ components. The residuals (dashed) and the r.m.s errors E are shown.

perspective to the ADER-DG method. This is not an extensive study but rather aims at pointing out the main virtues and drawbacks of these methodologies with particular stress on how they compare to the ADER-DG method described in this thesis.

1.9.1 Finite Elements

The FE method is a favorite for mechanical studies among the engineering community. As a Galerkin method, it shares many principles with the DG methods. The elements support some polynomials which act as a basis upon which derivatives are computed, usually point-wise. Continuity conditions are imposed between elements and the resulting schemes are commonly quite simple and computationally inexpensive. Furthermore, free boundary conditions are natural for this method. Most successful implementations of the FE method are typically first- or second-order accurate in space and thus show strong dispersive properties. This makes them sufficiently accurate for static problems but not enough accurate for simulating waves requiring propagation of many wavelengths. Higher-order implementations exist to avoid such problems but they incur in the construction of a non-diagonal mass matrix which precludes the use of such schemes for very large scale problems. In [142] an extensive overview of the method is given.

1.9.2 Finite Volumes

The FV method is one of the workhorses of the fluid dynamics community. The basic concept is to treat the variable's average values instead of the variables themselves. These average values are updated due to fluxes through the surfaces separating two cells. The use of numerical fluxes allows for better control of the method's behavior for shock-waves or other strong discontinuities in the solutions. Additionally, the method's accuracy is often related to the choice of numerical flux used for the computation more than other computational aspects and a whole family of such fluxes has been developed in the recent years. They are based upon the integral form of the differential equation rather than the differential form (also known as weak form) used by DG methods. However fluxes are solved in the same way for both methods. In fact, for the $\mathcal{O}1$ case, a DG scheme is identical to an FV one. The method has already been used for seismic wave propagation for the low-order [51] and high-order [56, 57] cases. In this last publication a thorough comparison FV/DG is provided. A good source of additional information is [90].

1.9.3 Triangular Spectral Elements

Following the success of hexahedra-based SEM, a new Triangular Spectral Element Method (TSEM) [96, 111] has been recently developed and applied to the

seismic wave propagation problem. TSEM shares many of the nicest properties
of SEM, including the highly accurate nodal integration and spectral resolution of
the variables. These nodes are known as Fekete points, and the interpolating basis
associated is different from the Dubiner basis employed for DG methods. As with
SEM, continuity is required at all integration nodes. Furthermore, the location of
the Fekete integration points at the triangular elements' boundaries coincide with
the Gauss-Lobatto-Legendre points of SEM, thus potentially allowing for hybrid
SEM/TSEM schemes. However the basis functions used do not provide a diago-
nal mass matrix, thus increasing strongly the computational demands which now
involve a non-trivial matrix inversion. A three-dimensional version has not been
developed to date, but the basis and node positions to tetrahedral elements have
been already studied.

1.10   Concluding Remarks

Through the present Chapter the main aspects of the ADER-DG method have
been shown. The method has been developed by M. Käser and M. Dumbser [55,
75] and is well suited to compute very accurate synthetic seismograms for highly
complex and heterogeneous media. However, in its original form, the method
covers the purely elastic and isotropic regime. It is the aim of this thesis to show
that the ADER-DG method can be adapted to the viscoelastic, anisotropic and
poroelastic cases, as well as combinations of those. Through the next Chapters
these different rheologies will be explored in detail. In particular, the schemes
developed will keep the most advantageous properties of the original ADER-DG
schemes: the high-order integration in space and time and the use of tetrahedral
unstructured meshes.

Chapter 2

Viscoelasticity in ADER-DG Schemes

In this Chapter an overview of viscoelastic mechanics for wave propagation is given as well as the details on its accurate implementation in the ADER-DG schemes. First we present an overview on the attenuation of seismic waves and the viscoelastic modeling. Then will be introduced the system of the three-dimensional anelastic wave equations in velocity-stress formulation including attenuation due to viscoelasticity. The resulting DG method is briefly explained in the following Section together with the ADER time integration approach. We will also show a discussion on the improvement of the approximation of a frequency-independent Q-law when increasing the number n of relaxation mechanisms of the Generalized Maxwell Body. Furthermore, we analyse the additional CPU time requirements for different orders of accuracy of the ADER-DG schemes. Finally, in the last Section we present a comparison of ADER-DG results with those of a Discrete Wavenumber solution and discuss the method's accuracy. The main contents of this Chapter have been published in M. Käser, M. Dumbser, J. de la Puente and H. Igel [76].

2.1 General Overview

A successful model for realistic attenuation of seismic waves is the approximation of the material as a viscoelastic medium. Viscoelastic materials differ from elastic ones in three basic aspects: they produce energy losses, the response to excitation is not instantaneous and the stress state at a given time is a function of the strain state at all preceding times. This behavior can be mathematically described by allowing the wave velocities to be complex quantities. In the Earth, viscoelastic effects are observed at all scales. A particular case is the Earth's internal friction, i.e. the measure of attenuation, is nearly constant over a wide seismic frequency range. This is due to the composition of the Earth's polycrystalline material con-

sisting of different minerals. The superposition of these microscopic physical attenuation (relaxation) processes leads to a flat attenuation band [92, 107].

The stress-strain relation for a linear isotropic viscoelastic medium is given by the so-called Boltzmann principle (causality principle), that states that the stress at a given time t depends on the entire strain history until time t, which mathematically is represented by a time convolution of a relaxation function and the strain rate as shown e.g. by Moczo *et al.* [101]. As the integration of this stress-strain relation in the time domain is intractable in a numerical computation, Day & Minster [47] transformed the stress-strain relation in the time domain into a differential form using a Padé approximation. They obtained n differential equations for n additional *internal variables*, which replace the convolution integral. These equations have to be solved in addition to the elastic wave equations. Furthermore, the sum of the internal variables multiplied with anelastic coefficients leads to additional viscoelastic terms for the elastic stresses. This way storage requirements and computing times were significantly increased.

Emmerich & Korn [63] improved this approach by considering the rheology of a *Generalized Maxwell Body* and showed that their method is superior in accuracy and computational efficiency. They chose the relaxation frequencies logarithmically equidistant in the frequency band of interest and used a least-square method to fit arbitrary quality factor laws.

Independently, a different approach [28, 30] assumed a *Generalized Zener Body* and introduced additional first-order differential equations for *memory variables*. After these revolutionary publications authors incorporating realistic viscoelastic attenuation in time domain methods used the concepts of the Generalized Maxwell or Generalized Zener Body. A recent work by Moczo & Kristek [99] reviewed both models and showed that both approaches are equivalent.

After Emmerich [62] applied the viscoelastic models for the P-SV case, Moczo *et al.* [98] presented a hybrid two-step method for simulating P-SV seismic motion in inhomogeneous viscoelastic structures with free surface topography combining discrete-wavenumber (DW) [18], finite element (FE), e.g. [94] and finite-difference (FD) methods, e.g. [97]. At first coarse spatial sampling of the anelastic functions was introduced [45, 46]. In later work [86] the basic theoretical and algorithmic aspects of a memory-efficient implementation of realistic attenuation was addressed based on a viscoelastic material with material discontinuities mainly for the staggered-grid finite difference approach.

In the present Chapter the ADER-DG method is extended to the viscoelastic case using the Generalized Maxwell Body rheology type. Details on how to obtain almost frequency-independent attenuation will be given, as well as ways to reduce the computational costs caused by the increased number of unknowns and equations to be solved.

2.2 Attenuation of Seismic Waves

It is a broadly observed phenomenon that seismic waves loose energy as they travel through the Earth. This loss corresponds mainly to the fact that the waves propagate through materials which are not perfectly elastic. As waves are cyclic phenomena, a rough number can be used as a quantifier of how *anelastic* a material is by accounting the amplitude losses per cycle [1]. For the case of plane periodic waves one can define the quality factor $\mathcal{Q}$ as

$$\frac{1}{\mathcal{Q}} = -\frac{1}{\pi}\frac{\Delta A}{A} \, , \tag{2.1}$$

where A is the original wave's amplitude and ΔA the amount by which the amplitude of the wave increases per cycle. Given the minus sign in (2.1), a positive $\mathcal{Q}$ value leads actually to a decrease in the amplitudes. From the above equation one can find that the anelastic wave, if propagating in the $x-$direction with velocity c, will decrease its amplitude with time as

$$A(x) = A_0 \exp\left(\frac{-\omega x}{2c\mathcal{Q}}\right) \, . \tag{2.2}$$

On the other hand, observations show that the attenuation is a phenomenon which is roughly independent of frequency. One can now explore how a plane wave behaves under the assumptions just shown. Let's assume the propagation of a delta signal such as

$$p(x,t) = A \cdot \delta\left(t - x/c\right) \, , \tag{2.3}$$

with velocity c in the positive $x-$direction. This pulse in the frequency domain has the shape

$$P(x,\omega) = A \cdot \exp\left(i\omega x/c\right) \, . \tag{2.4}$$

Let's now assume the pulse travels through an anelastic medium such that the amplitude decays as in (2.2). The anelastic pulse can now be expressed again in time domain by using the inverse Fourier transform so that

$$p(x,t) = \frac{1}{2\pi}\int_{-\infty}^{\infty} A_0 \cdot \exp\left(\frac{-\omega x}{2c\mathcal{Q}}\right)\exp\left[i\omega\left(x/c - t\right)\right] d\omega \, . \tag{2.5}$$

The result of this integration is

$$p(x,t) = \frac{1}{\pi}\left[\frac{\frac{x}{2cQ}}{\left(\frac{x}{2c\mathcal{Q}}\right)^2 + \left(\frac{x}{c} - t\right)^2}\right] \, . \tag{2.6}$$
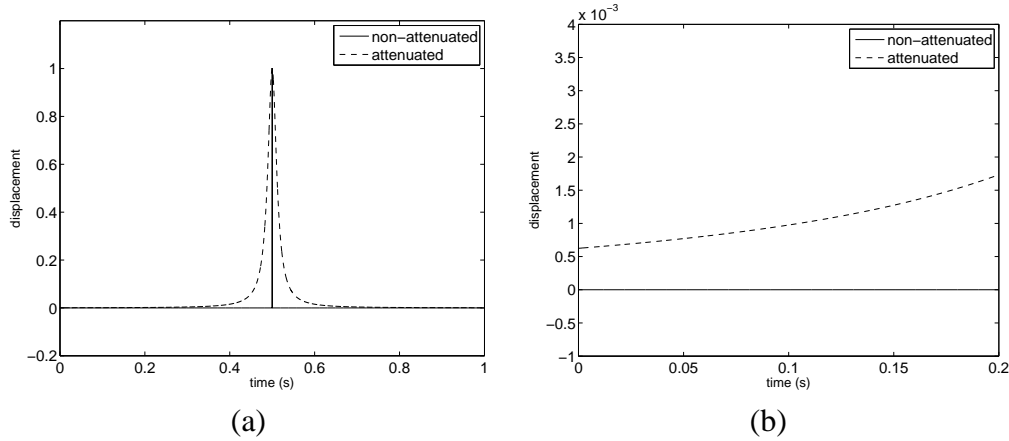
Figure 2.1: (a) Comparison of non-attenuated and attenuated pulses observed at $x = 1$ for $c = 2$ and $\mathcal{Q} = 20$ (amplitudes normalized). (b) Zoom of the early instants of the previous plot, where a non-zero signal even at $t = 0s$ is observed.

An example of such a pulse as (2.6) can be obtained by setting $c = 2$ and $x = 1$, thus obtaining the pulse observed in Figure 2.1 which, among other things, violates the causality principle as it produces a non-zero signal even for $t \leq = 0s$. As this is clearly unphysical, and one wishes $\mathcal{Q}$ to be frequency independent to agree with observations, a certain *velocity dispersion* must be allowed, meaning that $c = c(\omega)$. As seen in Chapter 1, the value of c depends exclusively on the Lamé parameters of the material and, more generally, on the expression of Hooke's Law.

2.3   Viscoelastic Rheological Models

Hooke's law for elastic materials can be expressed as the stress-strain relation

$$\vec{\sigma}_i = M_{ij}\vec{\varepsilon}_j \,, \tag{2.7}$$

being the stresses expressed in array form $\vec{\sigma} = (\sigma_{xx}, \sigma_{yy}, \sigma_{zz}, \sigma_{xy}, \sigma_{yz}, \sigma_{xz})^T$ and the strains $\vec{\varepsilon} = (\varepsilon_{xx}, \varepsilon_{yy}, \varepsilon_{zz}, \varepsilon_{xy}, \varepsilon_{yz}, \varepsilon_{xz})^T$. The tensor M is solely dependent on the material properties. If those, additionally, depend on the frequency, the constitutive relation in the frequency domain

$$\vec{\sigma}_i(\omega) = M_{ij}(\omega)\vec{\varepsilon}_j(\omega) \,, \tag{2.8}$$

can be expressed back in the time domain, using Fourier's inverse transformation, as a convolutional product

$$\vec{\sigma}_i(t) = M_{ij}(t) * \vec{\varepsilon}_j(t) \,. \tag{2.9}$$

For the specific form of M, there are many viscoelastic models available. Only some of them can completely reproduce results of laboratory experiments consisting of measuring the response to instant stress or strain (known as "relaxation" and "creep" responses). All the viscoelastic mechanical models can be expressed ideally as combinations of fundamental Hooke's (springs) and Stokes (dashpots) mechanical elements, compared to elastic models which are only defined by springs. Only the Generalized Maxwell Body rheological type will be investigated in detail in the following, as one of the most successful models for viscoelastic wave propagation problems at present.

2.3.1 Generalized Maxwell Body

The Generalized Maxwell Body (GMB) rheology type is based upon using linear combinations in parallel of so-called Maxwell Bodies, essentially a spring and a dashpot connected in series. These Maxwell Bodies are themselves combined in parallel to a single spring element, as depicted in Figure 2.2(a). This rheological model was proposed in the form presented here by Emmerich and Korn (1987). Then, in the frequency domain, a mechanical system such as the one of Figure 2.2(a) can be substituted by an "equivalent" mechanical element whose modulus M can be found by using the rules for combining mechanical elements. In particular, for a one-dimensional mechanical model composed of n Maxwell Bodies one would have the following expression for a GMB viscoelastic mechanism

$$M(\omega) = M_H + \sum_{\ell=1}^{n} \frac{iM_\ell\omega}{\omega_\ell + i\omega} \,, \tag{2.10}$$

where M_H and M_ℓ are the springs' elastic moduli and $\omega_\ell \equiv M_\ell/\nu_\ell$ being ν_ℓ the viscosities of the dashpots. The reader should notice that the convention of summation for repeated indices will not apply to the ℓ indices in the present work. Sums over ℓ will be always shown explicitly. Now, by finding the value of the modulus $M(\omega)$ for very high-frequencies

$$M_U = \lim_{\omega \to \infty} M(\omega) = M_H + \sum_{\ell=1}^{n} M_\ell \,, \tag{2.11}$$

and using the definition $Y_\ell \equiv M_\ell/M_U$ one can find the final form of the one-dimensional GMB rheology as

$$M(\omega) = M_U \left(1 - \sum_{\ell=1}^{n} \frac{Y_\ell\omega_\ell}{\omega_\ell + i\omega} \right) . \tag{2.12}$$
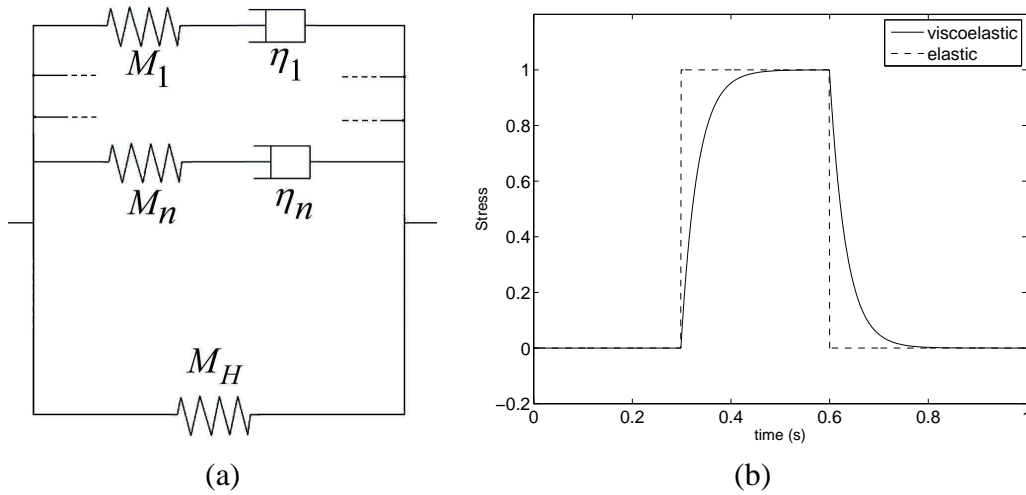
Figure 2.2: (a) Sketch of a Generalized Maxwell Body rheological model. Hooke's elements (springs) are associated with an elastic modulus M while Stokes' elements (dashpots) are associated to a viscous modulus η. (b) Comparison of an elastic and viscoelastic (GMB) responses to the same strain input, a boxcar time function from t=0.3s to t=0.6s.

The GMB model, besides allowing for attenuation of the amplitudes, also fits the non-instantaneous "relaxation" observed in experimental studies with real rocks, thus overcoming the non-causality problems of more primitive models as the ones described in Section 2.2. In Figure 2.2(b) we can observe the response in stresses of a single Maxwell Body to a boxcar time function from $t = 0.3s$ to $t = 0.6s$, which shows the characteristic exponential decay in the relaxation function, with no response happening before the beginning of the actual signal in strain. For this particular case, the full amplitude of the input signal is recovered, as happens for the instantaneous elastic model. The reason for this is that the used boxcar is much wider ($0.3s$ wide) than the characteristic time of the Maxwell mechanism used. We have used in this example a mechanism with $\omega_1 = 30$, meaning that after $t_{0.99} \equiv \log{(0.01)}/(-\omega_1) \approx 0.15s$ a 99% of the maximum amplitude has been recovered. If the boxcar would have been narrower than that value, the full amplitude would not be recovered, thus resulting in an attenuation of the expected elastic response. It can then be seen that the attenuating behavior of GMB models clearly depends on the frequency of the pulses used, unlike classic elastic models which offer instantaneous responses.

2.4 Anelastic Wave Equations

The extension of linear viscoelasticity to three-dimensional problems can be written as

$$\vec{\sigma_i}(\omega) = M_{ij}(\omega)\vec{\varepsilon_j}(\omega) \,, \tag{2.13}$$

where M_{ij} is a matrix including complex, frequency-dependent viscoelastic moduli. The natural moduli for the case of isotropic viscoelasticity are the bulk modulus $\mathcal{K} = \mathcal{K}(\omega)$ and the shear modulus $\mu = \mu(\omega)$. However, given the fact that the moduli are defined as linear functions, one can define new moduli which are linear combinations of the bulk and shear ones without loss of generality. For the isotropic case it can be a good choice to use the two Lamé parameters $\lambda = \lambda(\omega)$ and $\mu = \mu(\omega)$ which fully describe the medium, and are related to the bulk modulus by the expression $\mathcal{K} = \lambda + 2/3\mu$.

Using a GMB viscoelastic model consisting of n Maxwell bodies, the frequency dependent Lamé parameters read

$$\lambda(\omega) = \lambda^U \Big(1 - \sum_{\ell=1}^{n} \frac{Y_\ell^\lambda \omega_\ell}{\omega_\ell + i\omega} \Big) \,, \tag{2.14}$$

$$\mu(\omega) = \mu^U \Big(1 - \sum_{\ell=1}^{n} \frac{Y_\ell^\mu \omega_\ell}{\omega_\ell + i\omega} \Big) \,, \tag{2.15}$$

where $\lambda^U = \lim_{\omega \to \infty} \lambda(\omega)$ and $\mu^U = \lim_{\omega \to \infty} \mu(\omega)$ are the unrelaxed Lamé parameters as used in purely elastic media. The Y_ℓ^λ and Y_ℓ^μ are the anelastic coefficients to be determined and ω_ℓ are the relaxation frequencies of the different mechanisms.

In general, given a viscoelastic modulus, e.g. the shear modulus $\mu(\omega)$, the quality factor $\mathcal{Q}(\omega)$ is defined as (e.g. [63])

$$\mathcal{Q}_\mu(\omega) = \frac{\text{Re}(\mu(\omega))}{\text{Im}(\mu(\omega))} \,. \tag{2.16}$$

Inserting the shear modulus $\mu(\omega)$ from Equation (2.15) into (2.16) leads to

$$\mathcal{Q}_\mu^{-1}(\omega) = \sum_{\ell=1}^{n} \frac{\omega_\ell \omega + \omega_\ell^2 \mathcal{Q}_\mu^{-1}(\omega)}{\omega_\ell^2 + \omega^2} Y_\ell^\mu \,. \tag{2.17}$$

Equation (2.17) can be used to fit any $\mathcal{Q}(\omega)$-law [63, 101]. Observations show, that the quality factor $\mathcal{Q}$ is approximately constant over a large frequency range of interest for most geophysical applications. They propose, that good approximations can be obtained by choosing n relaxation frequencies ω_ℓ, $\ell = 1, ..., n$, that

equidistantly cover the logarithmic frequency range of interest. They suggest to use $2n-1$ known values $\mathcal{Q}(\tilde{\omega}_k)$ at frequencies $\tilde{\omega}_k$, $k = 1, ..., 2n-1$, with $\tilde{\omega}_1 = \omega_1$ and $\tilde{\omega}_{2n-1} = \omega_n$ and solve the overdetermined system in (2.17) for the anelastic coefficients Y_ℓ^μ by the least squares method. A more detailed discussion of the choice of frequency ranges and the corresponding sampling frequencies can be found in [68].

In practice, and corresponding to the seismic P- and S-wave velocities, one has quality factors $\mathcal{Q}_P$ and $\mathcal{Q}_S$ that describe the different degree of attenuation for the different wave types. Relations as (2.17) can be also found for anelastic coefficients Y_ℓ^P and Y_ℓ^S for viscoelastic P- and S-wave propagation and read as

$$\mathcal{Q}_\nu^{-1}(\omega_k) = \sum_{\ell=1}^{n} \frac{\omega_\ell \omega_k + \omega_\ell^2 \mathcal{Q}_\nu^{-1}(\omega_k)}{\omega_\ell^2 + \omega_k^2} Y_\ell^\nu \,, \tag{2.18}$$

with $\nu = P, S$ and $k = 1, ..., 2n - 1$. In the following, however, it is more convenient to express the anelastic coefficients in terms of the Lamé parameters λ and μ, which are obtained by the transformation

$$Y_\ell^\lambda = \left(1 + \frac{2\mu^U}{\lambda^U}\right) Y_\ell^P - \frac{2\mu^U}{\lambda^U} Y_\ell^S \,, \qquad\qquad Y_\ell^\mu = Y_\ell^S \,, \tag{2.19}$$

following directly from Equations (2.14) and (2.15) as the relation of physical parameters, e.g. elastic parameters or velocities, corresponds to the purely elastic case due to the linearity of the expressions in (2.14) and (2.15).

The final step in determining the parameters of $\lambda(\omega)$ and $\mu(\omega)$ is getting knowledge of the values of their corresponding unrelaxed moduli λ^U and μ^U, as expressed in (2.14) and (2.15). To that goal it is common practice to have knowledge of the values of the wave speeds c_P and c_S at a given reference frequency ω_r. Following [101], the phase velocities $c_P(\omega)$ and $c_S(\omega)$ can be obtained from the corresponding moduli using

$$\frac{1}{c_\nu(\omega)} = \mathrm{Re}\left[\left(\frac{M_\nu(\omega)}{\rho}\right)^{-1/2}\right] \qquad \text{with} \quad \nu = P, S \tag{2.20}$$

where $M_\nu(\omega)$ are the viscoelastic moduli, $M_P(\omega) = \lambda(\omega) + 2\mu(\omega)$ for the P waves and $M_S(\omega) = \mu(\omega)$ for the S waves, and $c_P(\omega)$ and $c_S(\omega)$ are the wave velocities for the P- and S-waves respectively. The unrelaxed values of their moduli have then the values [101]

$$M_{U,\nu} = \rho c_\nu^2(\omega_r) \frac{R + \Theta_1}{2R^2} \,, \tag{2.21}$$

(a)

(b)
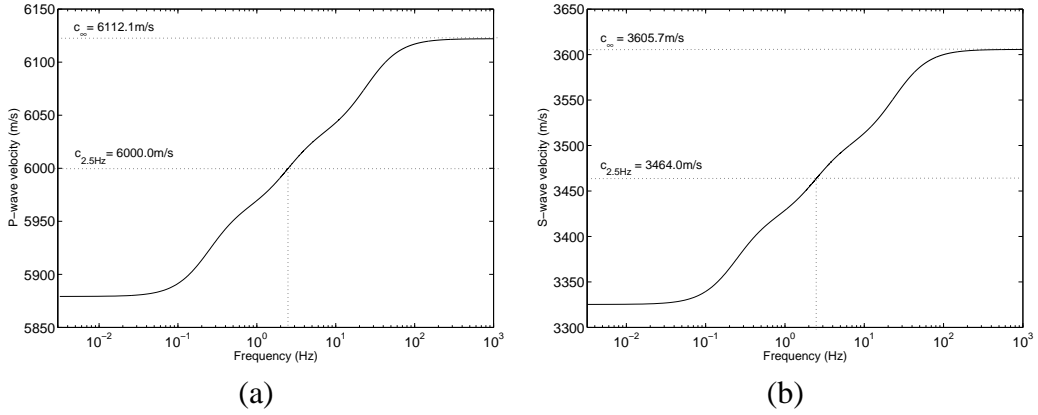
Figure 2.3: Dispersion example of the wave speed for GMB rheologies with 3 mechanisms for the P-wave (a) and the S-wave (b). The unrelaxed velocities, or velocities at infinite frequency, are not the same as the ones at the desired frequency of 2.5Hz.

where

$$R = \left(\Theta_1^2 + \Theta_2^2\right)^{1/2} ,$$

$$\Theta_1 = 1 - \sum_{\ell=1}^{n} Y_\ell^\nu \frac{1}{1 + (\omega_r/\omega_\ell)^2} ,$$

$$\Theta_2 = \sum_{\ell=1}^{n} Y_\ell^\nu \frac{\omega_r/\omega_\ell}{1 + (\omega_r/\omega_\ell)^2} .$$

(2.22)

This way the values of λ^U and μ^U can be determined using (2.21), once the values of Y_ℓ^ν have been obtained from (2.18). In Fig. 2.3 we show an example on how the dispersion curves look like for a case with 3 viscoelastic mechanisms. It can be seen how the unrelaxed moduli are always larger than those at the reference frequency ω_r. This example uses the material properties of the applications shown at the end of the present Chapter.

A set of material-independent anelastic functions introduced by Kristek & Moczo [86] and Moczo & Kristek [99] can be used. They are defined in the form $\vec{\bar{\vartheta}}^\ell = (\bar{\vartheta}_{xx}^\ell, \bar{\vartheta}_{yy}^\ell, \bar{\vartheta}_{zz}^\ell, \bar{\vartheta}_{xy}^\ell, \bar{\vartheta}_{yz}^\ell, \bar{\vartheta}_{xz}^\ell)^T$, and contain the time history of the strain through

$$\bar{\vartheta}_j^\ell(t) = \omega_\ell \int_{-\infty}^{t} \varepsilon_j(\tau) e^{-\omega_\ell(t-\tau)} \, d\tau .$$

(2.23)

Using (2.23) and applying the inverse Fourier transform to the viscoelastic modulus M_{ij}, as presented in detail by Kristek & Moczo [86], the stress-strain relation

(2.13) can be written in the time domain in the form

$$\sigma_{ij} = \lambda \varepsilon_{kk} \delta_{ij} + 2\mu \varepsilon_{ij} - \sum_{\ell=1}^{n} (\lambda Y_\ell^\lambda \bar{\vartheta}_{kk}^\ell \delta_{ij} + 2\mu Y_\ell^\mu \bar{\vartheta}_{ij}^\ell) \,, \qquad (2.24)$$

with $i, j, k \in [x, y, z]$ and where δ_{ij} is the Kronecker Delta and the Einstein summation convention applies. The viscoelastic constitutive relation in (2.24) represents the elastic part minus the anelastic part depending on the anelastic coefficients Y_ℓ^λ and Y_ℓ^μ and the anelastic functions $\bar{\vartheta}_{ij}^\ell$. The remaining problem is the evolution of the anelastic functions $\bar{\vartheta}_{ij}^\ell$ in (2.23) in time. In fact, (2.23) is the solution of the partial differential equation

$$\frac{\partial}{\partial t} \bar{\vartheta}_j^\ell(t) + \omega_\ell \bar{\vartheta}_j^\ell(t) = \omega_\ell \varepsilon_j \,, \qquad (2.25)$$

which completes the linear, hyperbolic system of the anelastic wave equations. However, to express the equation system in the velocity-stress formulation it is convenient to redefine the anelastic functions in the form (see [101])

$$\vartheta_j^\ell = \frac{\partial}{\partial t} \bar{\vartheta}_j^\ell \,. \qquad (2.26)$$

Finally, using the equations of motion, the definition of strain ε_j and Equations (2.24), (2.25) and (2.26) one can formulate the system of the anelastic wave equa-

tions as

$$\frac{\partial}{\partial t}\sigma_{xx} - (\lambda + 2\mu)\frac{\partial}{\partial x}u - \lambda\frac{\partial}{\partial y}v - \lambda\frac{\partial}{\partial z}w = \sum_{\ell=1}^{n} -(\lambda Y_\ell^\lambda + 2\mu Y_\ell^\mu)\vartheta_{xx}^\ell - \lambda Y_\ell^\lambda\vartheta_{yy}^\ell - \lambda Y_\ell^\lambda\vartheta_{zz}^\ell \,,$$

$$\frac{\partial}{\partial t}\sigma_{yy} - \lambda\frac{\partial}{\partial x}u - (\lambda + 2\mu)\frac{\partial}{\partial y}v - \lambda\frac{\partial}{\partial z}w = \sum_{\ell=1}^{n} -\lambda Y_\ell^\lambda\vartheta_{xx}^\ell - (\lambda Y_\ell^\lambda + 2\mu Y_\ell^\mu)\vartheta_{yy}^\ell - \lambda Y_\ell^\lambda\vartheta_{zz}^\ell \,,$$

$$\frac{\partial}{\partial t}\sigma_{zz} - \lambda\frac{\partial}{\partial x}u - \lambda\frac{\partial}{\partial y}v - (\lambda + 2\mu)\frac{\partial}{\partial z}w = \sum_{\ell=1}^{n} -\lambda Y_\ell^\lambda\vartheta_{xx}^\ell - \lambda Y_\ell^\lambda\vartheta_{yy}^\ell - (\lambda Y_\ell^\lambda + 2\mu Y_\ell^\mu)\vartheta_{zz}^\ell \,,$$

$$\frac{\partial}{\partial t}\sigma_{xy} - \mu\Big(\frac{\partial}{\partial x}v + \frac{\partial}{\partial y}u\Big) = \sum_{\ell=1}^{n} -2\mu Y_\ell^\mu\vartheta_{xy}^\ell \,,$$

$$\frac{\partial}{\partial t}\sigma_{yz} - \mu\Big(\frac{\partial}{\partial z}v + \frac{\partial}{\partial y}w\Big) = \sum_{\ell=1}^{n} -2\mu Y_\ell^\mu\vartheta_{yz}^\ell \,,$$

$$\frac{\partial}{\partial t}\sigma_{xz} - \mu\Big(\frac{\partial}{\partial z}u + \frac{\partial}{\partial x}w\Big) = \sum_{\ell=1}^{n} -2\mu Y_\ell^\mu\vartheta_{xz}^\ell \,,$$

$$\rho\frac{\partial}{\partial t}u - \frac{\partial}{\partial x}\sigma_{xx} - \frac{\partial}{\partial y}\sigma_{xy} - \frac{\partial}{\partial z}\sigma_{xz} = 0 \,,$$

$$\rho\frac{\partial}{\partial t}v - \frac{\partial}{\partial x}\sigma_{xy} - \frac{\partial}{\partial y}\sigma_{yy} - \frac{\partial}{\partial z}\sigma_{yz} = 0 \,,$$

$$\rho\frac{\partial}{\partial t}w - \frac{\partial}{\partial x}\sigma_{xz} - \frac{\partial}{\partial y}\sigma_{yz} - \frac{\partial}{\partial z}\sigma_{zz} = 0 \,,$$

$$\frac{\partial}{\partial t}\vartheta_{xx}^1 - \omega_1\frac{\partial}{\partial x}u = -\omega_1\vartheta_{xx}^1 \,,$$

$$\frac{\partial}{\partial t}\vartheta_{yy}^1 - \omega_1\frac{\partial}{\partial y}v = -\omega_1\vartheta_{yy}^1 \,,$$

$$\frac{\partial}{\partial t}\vartheta_{zz}^1 - \omega_1\frac{\partial}{\partial z}w = -\omega_1\vartheta_{zz}^1 \,,$$

$$\frac{\partial}{\partial t}\vartheta_{xy}^1 - \tfrac{1}{2}\omega_1\Big(\frac{\partial}{\partial x}v + \frac{\partial}{\partial y}u\Big) = -\omega_1\vartheta_{xy}^1 \,,$$

$$\frac{\partial}{\partial t}\vartheta_{yz}^1 - \tfrac{1}{2}\omega_1\Big(\frac{\partial}{\partial z}v + \frac{\partial}{\partial y}w\Big) = -\omega_1\vartheta_{yz}^1 \,,$$

$$\frac{\partial}{\partial t}\vartheta_{xz}^1 - \tfrac{1}{2}\omega_1\Big(\frac{\partial}{\partial z}u + \frac{\partial}{\partial x}w\Big) = -\omega_1\vartheta_{xz}^1 \,,$$

$$\vdots \qquad \vdots$$

$$\frac{\partial}{\partial t}\vartheta_{xx}^n - \omega_n\frac{\partial}{\partial x}u = -\omega_n\vartheta_{xx}^n \,,$$

$$\frac{\partial}{\partial t}\vartheta_{yy}^n - \omega_n\frac{\partial}{\partial y}v = -\omega_n\vartheta_{yy}^n \,,$$

$$\frac{\partial}{\partial t}\vartheta_{zz}^n - \omega_n\frac{\partial}{\partial z}w = -\omega_n\vartheta_{zz}^n \,,$$

$$\frac{\partial}{\partial t}\vartheta_{xy}^n - \tfrac{1}{2}\omega_n\Big(\frac{\partial}{\partial x}v + \frac{\partial}{\partial y}u\Big) = -\omega_n\vartheta_{xy}^n \,,$$

$$\frac{\partial}{\partial t}\vartheta_{yz}^n - \tfrac{1}{2}\omega_n\Big(\frac{\partial}{\partial z}v + \frac{\partial}{\partial y}w\Big) = -\omega_n\vartheta_{yz}^n \,,$$

$$\frac{\partial}{\partial t}\vartheta_{xz}^n - \tfrac{1}{2}\omega_n\Big(\frac{\partial}{\partial z}u + \frac{\partial}{\partial x}w\Big) = -\omega_n\vartheta_{xz}^n$$

(2.27)

where n is the number of mechanisms used to approximate a frequency-independent Q-law and ρ is the density. Note, that each mechanism adds 6 further equations, i.e. one for each stress component. Therefore, the system of the purely elastic three-dimensional wave equations consisting of 9 equations increases by $6n$

equations in the anelastic case, when n mechanisms are used. Furthermore, the anelasticity adds reactive source terms on the right hand side of (2.27).

In the following, it will be assumed that the viscoelastic material is described with the same number n of mechanisms throughout the computational domain. Therefore, the notation will be identical as the one used in Chapter 1 treating the purely elastic case.
The above system (2.27) of $n_v = 9 + 6n$ variables and equations can be written in the more compact form

$$\frac{\partial Q_p}{\partial t} + \check{A}_{pq}\frac{\partial Q_q}{\partial x} + \check{B}_{pq}\frac{\partial Q_q}{\partial y} + \check{C}_{pq}\frac{\partial Q_q}{\partial z} = \check{E}_{pq}Q_q. \tag{2.28}$$

Note, that the dimensions of the variable vector Q, the Jacobian matrices $\check{A}$, $\check{B}$, $\check{C}$ and the source matrix $\check{E}$ now depend on the number n of relaxation mechanisms. To keep the notation as simple as possible and without loss of generality, in the following it will be assumed that the order of the variables in (2.28) is such, that $p, q \in [1, ..., 9]$ denote the elastic part and $p, q \in [10, ..., n_v]$, denote the anelastic part of the system as presented in (2.27). As the Jacobian matrices $\check{A}$, $\check{B}$ and $\check{C}$ as well as the source matrix $\check{E}$ are sparse and show some particular symmetry pattern and as their dimensions may become impractical for notation, a block-matrix syntax will be used.
Therefore, the Jacobian matrices are decomposed as follows:

$$\check{A} = \begin{bmatrix} A & 0 \\ A_a & 0 \end{bmatrix}, \qquad \check{B} = \begin{bmatrix} B & 0 \\ B_a & 0 \end{bmatrix}, \qquad \check{C} = \begin{bmatrix} C & 0 \\ C_a & 0 \end{bmatrix}, \tag{2.29}$$

with $\check{A}, \check{B}, \check{C} \in \mathbb{R}^{n_v \times n_v}$ and where $A, B, C \in \mathbb{R}^{9 \times 9}$ are the Jacobians of the purely elastic part as given in [55]. The matrices A_a, B_a, C_a include the anelastic part and exhibit themselves a block structure of the form

$$A_a = \begin{bmatrix} A_1 \\ \vdots \\ A_n \end{bmatrix}, \qquad B_a = \begin{bmatrix} B_1 \\ \vdots \\ B_n \end{bmatrix}, \qquad C_a = \begin{bmatrix} C_1 \\ \vdots \\ C_n \end{bmatrix}, \tag{2.30}$$

with $A_a, B_a, C_a \in \mathbb{R}^{6n \times 9}$ and where each sub-matrix $A_\ell, B_\ell, C_\ell \in \mathbb{R}^{6 \times 9}$, with $\ell = 1, ..., n$, contains the relaxation frequency ω_ℓ of the ℓ-th mechanism in the form

$$A_\ell = \omega_\ell \cdot \begin{pmatrix} 0 & 0 & 0 & 0 & 0 & 0 & -1 & 0 & 0 \\ 0 & 0 & 0 & 0 & 0 & 0 & 0 & 0 & 0 \\ 0 & 0 & 0 & 0 & 0 & 0 & 0 & 0 & 0 \\ 0 & 0 & 0 & 0 & 0 & 0 & 0 & -\frac{1}{2} & 0 \\ 0 & 0 & 0 & 0 & 0 & 0 & 0 & 0 & 0 \\ 0 & 0 & 0 & 0 & 0 & 0 & 0 & 0 & -\frac{1}{2} \end{pmatrix}, \tag{2.31}$$

$$B_\ell = \omega_\ell \cdot \begin{pmatrix} 0 & 0 & 0 & 0 & 0 & 0 & 0 & 0 & 0 \\ 0 & 0 & 0 & 0 & 0 & 0 & 0 & -1 & 0 \\ 0 & 0 & 0 & 0 & 0 & 0 & 0 & 0 & 0 \\ 0 & 0 & 0 & 0 & 0 & 0 & -\frac{1}{2} & 0 & 0 \\ 0 & 0 & 0 & 0 & 0 & 0 & 0 & 0 & -\frac{1}{2} \\ 0 & 0 & 0 & 0 & 0 & 0 & 0 & 0 & 0 \end{pmatrix}, \tag{2.32}$$

$$C_\ell = \omega_\ell \cdot \begin{pmatrix} 0 & 0 & 0 & 0 & 0 & 0 & 0 & 0 & 0 \\ 0 & 0 & 0 & 0 & 0 & 0 & 0 & 0 & 0 \\ 0 & 0 & 0 & 0 & 0 & 0 & 0 & 0 & -1 \\ 0 & 0 & 0 & 0 & 0 & 0 & 0 & 0 & 0 \\ 0 & 0 & 0 & 0 & 0 & 0 & 0 & -\frac{1}{2} & 0 \\ 0 & 0 & 0 & 0 & 0 & 0 & -\frac{1}{2} & 0 & 0 \end{pmatrix}. \tag{2.33}$$

The matrix $\check{E}$ in (2.28) representing a reaction source that couples the anelastic functions to the original elastic system can be decomposed as

$$\check{E} = \begin{bmatrix} 0 & E \\ 0 & E' \end{bmatrix} \in \mathbb{R}^{n_v \times n_v}, \tag{2.34}$$

with E of the block structure

$$E = [E_1, \ldots, E_n] \in \mathbb{R}^{9 \times 6n}, \tag{2.35}$$

where each matrix $E_\ell \in \mathbb{R}^{9 \times 6}$, with $\ell = 1, ..., n$, contains the anelastic coefficients Y_ℓ^λ and Y_ℓ^μ of the ℓ-th mechanism in the form

$$E_\ell = - \begin{pmatrix} PY_\ell^P & \lambda Y_\ell^\lambda & \lambda Y_\ell^\lambda & 0 & 0 & 0 \\ \lambda Y_\ell^\lambda & PY_\ell^P & \lambda Y_\ell^\lambda & 0 & 0 & 0 \\ \lambda Y_\ell^\lambda & \lambda Y_\ell^\lambda & PY_\ell^P & 0 & 0 & 0 \\ 0 & 0 & 0 & 2\mu Y_\ell^\mu & 0 & 0 \\ 0 & 0 & 0 & 0 & 2\mu Y_\ell^\mu & 0 \\ 0 & 0 & 0 & 0 & 0 & 2\mu Y_\ell^\mu \\ 0 & 0 & 0 & 0 & 0 & 0 \\ 0 & 0 & 0 & 0 & 0 & 0 \\ 0 & 0 & 0 & 0 & 0 & 0 \end{pmatrix}. \tag{2.36}$$

where it has been defined $P \equiv \lambda + 2\mu$. The matrix E' in (2.34) is a diagonal matrix and has the structure

$$E' = \begin{bmatrix} E_1' & & 0 \\ & \ddots & \\ 0 & & E_n' \end{bmatrix} \in \mathbb{R}^{6n \times 6n}, \tag{2.37}$$

where each matrix $E_\ell' \in \mathbb{R}^{6 \times 6}$, with $\ell = 1, ..., n$, is itself a diagonal matrix containing only the relaxation frequency ω_ℓ of the ℓ-th mechanism on its diagonal, i.e. $E_\ell' = -\omega_\ell \cdot I$ with $I \in \mathbb{R}^{6 \times 6}$ denoting the identity matrix.

2.5   The Numerical Scheme

Using the expanded Jacobians defined $\check{A}$, $\check{B}$ and $\check{C}$ as well as the source matrix $\check{E}$, the ADER-DG scheme looks identical to the one described in Chapter 1 for the elastic case (1.66), just with the addition of the reaction term. Its full expression has the form

$$\left[\left(\hat{Q}_{pl}^{(m)} \right)^{n+1} - \left(\hat{Q}_{pl}^{(m)} \right)^{n} \right] |J|\, M_{kl} \quad +$$

$$+ \quad \tfrac{1}{2} \sum_{j=1}^{4} \check{T}_{pq}^{j} \left(\check{A}_{qr}^{(m)} + \check{\Theta}_{qr}^{(m)} \right) (\check{T}_{rs}^{j})^{-1} |S_j|\, F_{kl}^{-,j} \cdot I_{slmn}(\Delta t) \left(\hat{Q}_{mn}^{(m)} \right)^{n} +$$

$$+ \quad \tfrac{1}{2} \sum_{j=1}^{4} \check{T}_{pq}^{j} \left(\check{A}_{qr}^{(m)} - \check{\Theta}_{qr}^{(m)} \right) (\check{T}_{rs}^{j})^{-1} |S_j|\, F_{kl}^{+,j,i,h} \cdot I_{slmn}(\Delta t) \left(\hat{Q}_{mn}^{(m_j)} \right)^{n} - \quad (2.38)$$

$$- \quad \check{A}_{pq}^{*} |J|\, K_{kl}^{\xi} \cdot I_{qlmn}(\Delta t) \left(\hat{Q}_{mn}^{(m)} \right)^{n} - \check{B}_{pq}^{*} |J|\, K_{kl}^{\eta} \cdot I_{qlmn}(\Delta t) \left(\hat{Q}_{mn}^{(m)} \right)^{n} -$$

$$- \quad \check{C}_{pq}^{*} |J|\, K_{kl}^{\zeta} \cdot I_{qlmn}(\Delta t) \left(\hat{Q}_{mn}^{(m)} \right)^{n} = |J|\, \check{E}_{pq} \cdot I_{qlmn}(\Delta t) \left(\hat{Q}_{mn}^{(m)} \right)^{n} M_{kl}$$

It can be seen that the total number of unknowns in the viscoelastic case now depends on the number of relaxation mechanisms n and $p, q, r, s = 1, ..., n_v$. As in Chapter 1, M_{kl} is the mass matrix, $F_{kl}^{-,j}$, $F_{kl}^{+,j,i,h}$ are the flux matrices, K_{kl}^{ξ}, K_{kl}^{η} and K_{kl}^{ζ} are the stiffness matrices and $I_{qlmn}(\Delta t)$ is the tensor responsible for the high-order time integration over one time step Δt. $\check{A}_{pq}^{*}$, $\check{B}_{pq}^{*}$ and $\check{C}_{pq}^{*}$ are the Jacobian matrices transformed into the reference tetrahedron $\mathcal{T}_E$. Furthermore, $|J|$ is the determinant of the Jacobian matrix of this transformation, and $|S_j|$ denotes the area of the j-th face of tetrahedron $\mathcal{T}^{(m)}$.

If the viscosity matrix $\check{\Theta}_{qr}$ is associated to the Godunov-type fluxes, then $\left| \check{A}_{qr} \right|$ will have to be redefined in the viscoelastic case.

Similarly to (2.29) it is found that

$$|\check{A}| = \left[\begin{array}{cc} |A| & 0 \\ A^{\|} & 0 \end{array} \right] \in \mathbb{R}^{n_v \times n_v}, \qquad (2.39)$$

where $|A| \in \mathbb{R}^{9 \times 9}$ is identical to the one of the purely elastic part seen in the last Chapter and has the form

$$|A| = \left(\begin{array}{ccccccccc} c_p & 0 & 0 & 0 & 0 & 0 & 0 & 0 & 0 \\ \lambda^U/(c_p \rho) & 0 & 0 & 0 & 0 & 0 & 0 & 0 & 0 \\ \lambda^U/(c_p \rho) & 0 & 0 & 0 & 0 & 0 & 0 & 0 & 0 \\ 0 & 0 & 0 & c_s & 0 & 0 & 0 & 0 & 0 \\ 0 & 0 & 0 & 0 & 0 & 0 & 0 & 0 & 0 \\ 0 & 0 & 0 & 0 & 0 & c_s & 0 & 0 & 0 \\ 0 & 0 & 0 & 0 & 0 & 0 & c_p & 0 & 0 \\ 0 & 0 & 0 & 0 & 0 & 0 & 0 & c_s & 0 \\ 0 & 0 & 0 & 0 & 0 & 0 & 0 & 0 & c_s \end{array} \right), \qquad (2.40)$$

with $c_p = \sqrt{\frac{\lambda^U + 2\mu^U}{\rho}}$ and $c_s = \sqrt{\frac{\mu^U}{\rho}}$ representing the P- and S-wave velocities of the unrelaxed purely elastic material.

The matrix $A^{\parallel}$ includes the anelastic part and exhibits itself a block structure similar to that in (2.30) of the form

$$A^{\parallel} = \begin{bmatrix} A_1^{\parallel} \\ \vdots \\ A_n^{\parallel} \end{bmatrix} \in \mathbb{R}^{6n \times 9}, \tag{2.41}$$

where each sub-matrix $A_\ell^{\parallel} \in \mathbb{R}^{6 \times 9}$, with $\ell = 1, ..., n$, contains the local unrelaxed material parameters and the relaxation frequency ω_ℓ of the ℓ-th relaxation mechanism in the form

$$A_\ell^{\parallel} = \omega_\ell \cdot \begin{pmatrix} 1/(c_p \rho) & 0 & 0 & 0 & 0 & 0 & 0 & 0 & 0 \\ 0 & 0 & 0 & 0 & 0 & 0 & 0 & 0 & 0 \\ 0 & 0 & 0 & 0 & 0 & 0 & 0 & 0 & 0 \\ 0 & 0 & 0 & 1/(2c_s \rho) & 0 & 0 & 0 & 0 & 0 \\ 0 & 0 & 0 & 0 & 0 & 0 & 0 & 0 & 0 \\ 0 & 0 & 0 & 0 & 0 & 1/(2c_s \rho) & 0 & 0 & 0 \end{pmatrix}. \tag{2.42}$$

Similarly, the rotation matrix $\check{T}_{pq}^j$ in (2.38) needs to be enlarged. Skipping the index j for the j-th face of a tetrahedral element, and recalling that the anelastic functions ϑ^ℓ are tensors like the stresses the rotation matrix $\check{T}_{pq}$ for the full anelastic system in (2.38) has the form

$$\check{T} = \begin{bmatrix} T^t & 0 & 0 \\ 0 & T^v & 0 \\ 0 & 0 & T_a \end{bmatrix} \in \mathbb{R}^{n_v \times n_v}, \tag{2.43}$$

where $T^t \in \mathbb{R}^{6 \times 6}$ is the rotation matrix responsible for the stress tensor rotation as in the purely elastic part and is given as

$$T^t = \begin{pmatrix} n_x^2 & s_x^2 & t_x^2 & 2n_x s_x & 2s_x t_x & 2n_x t_x \\ n_y^2 & s_y^2 & t_y^2 & 2n_y s_y & 2s_y t_y & 2n_y t_y \\ n_z^2 & s_z^2 & t_z^2 & 2n_z s_z & 2s_z t_z & 2n_z t_z \\ n_y n_x & s_y s_x & t_y t_x & n_y s_x + n_x s_y & s_y t_x + s_x t_y & n_y t_x + n_x t_y \\ n_z n_y & s_z s_y & t_z t_y & n_z s_y + n_y s_z & s_z t_y + s_y t_z & n_z t_y + n_y t_z \\ n_z n_x & s_z s_x & t_z t_x & n_z s_x + n_x s_z & s_z t_x + s_x t_z & n_z t_x + n_x t_z \end{pmatrix}, \tag{2.44}$$

with the components of the normal vector $\vec{n} = (n_x, n_y, n_z)^T$ and the two tangential vectors $\vec{s} = (s_x, s_y, s_z)^T$ and $\vec{t} = (t_x, t_y, t_z)^T$.

The matrix $T^v \in \mathbb{R}^{3 \times 3}$ is the rotation matrix responsible for the velocity vector rotation as in the purely elastic part and is given as

$$T^v = \begin{pmatrix} n_x & s_x & t_x \\ n_y & s_y & t_y \\ n_z & s_z & t_z \end{pmatrix}. \tag{2.45}$$

The matrix T_a in (2.43) is a block diagonal matrix and has the structure

$$T_a = \begin{bmatrix} T^t & & 0 \\ & \ddots & \\ 0 & & T^t \end{bmatrix} \in \mathbb{R}^{6n \times 6n} , \tag{2.46}$$

where each of the n sub-matrices T^t is the tensor rotation matrix given in (2.44). Using the symmetries of $\check{A}$, $|\check{A}|$ and $\check{T}$ and the particular composition of the source term matrix $\check{E}$ as given in Equations (2.34 - 2.37), one can separate the full system in (2.28) into two parts. The first 9 equations will be called the *elastic part* and the remaining equations 10 to n_v the *anelastic part*. Therefore, the fluxes and volume integrals appearing in the discrete formulation of the Discontinuous Galerkin approach in (2.38) can be computed separately for each part. Furthermore, the computation of the flux and stiffness contributions of the anelastic part can be reduced to 6 instead of $6n$, as for each mechanism the corresponding matrices remain the same. Only the multiplication with the relaxation frequency ω_ℓ depends on the ℓ-th mechanism. However, both parts are still coupled via the Cauchy-Kovalewski procedure of the ADER time integration approach and the source terms $\check{E}$ in (2.28).

In the following Section 2.5.1 we present in detail, how this coupling is accomplished with a new, more efficient time integration approach in order to replace the costly multiplication with the four-dimensional tensor $I_{qlmn}(\Delta t)$ in (2.38).

2.5.1   The ADER Time Discretization

One could use a similar algorithm as presented for the elastic case in Chapter 1 to compute the Cauchy-Kovalewski procedure explicitly using the tensor $I_{plqm}(\Delta t)$, but for huge systems expressed through (2.28) that arise when using a large number of relaxation mechanisms, this approach would be too slow because of the many matrix-matrix multiplications involved. Therefore, in this Section we present a different approach that turns out to be equal to the previous one, however, it is much faster. The unrolled recursive algorithm described in the following becomes especially efficient because the matrices $\check{A}_{pq}$, $\check{B}_{pq}$, $\check{C}_{pq}$ and $\check{E}_{pq}$ are usually very sparse as shown in Section 2.4.

As in Chapter 1, one first writes the governing PDE (2.28) in the reference system as

$$\frac{\partial Q_p}{\partial t} + \check{A}^*_{pq} \frac{\partial Q_q}{\partial \xi} + \check{B}^*_{pq} \frac{\partial Q_q}{\partial \eta} + \check{C}^*_{pq} \frac{\partial Q_q}{\partial \zeta} - \check{E}_{pq} \, Q_q = 0 , \tag{2.47}$$

with

$$\check{A}^*_{pq} = \check{A}_{pq} \frac{\partial \xi}{\partial x} + \check{B}_{pq} \frac{\partial \xi}{\partial y} + \check{C}_{pq} \frac{\partial \xi}{\partial z} ,$$

$$\check{B}^*_{pq} = \check{A}_{pq} \frac{\partial \eta}{\partial x} + \check{B}_{pq} \frac{\partial \eta}{\partial y} + \check{C}_{pq} \frac{\partial \eta}{\partial z} , \tag{2.48}$$

$$\check{C}^*_{pq} = \check{A}_{pq} \frac{\partial \zeta}{\partial x} + \check{B}_{pq} \frac{\partial \zeta}{\partial y} + \check{C}_{pq} \frac{\partial \zeta}{\partial z} .$$

In contrast to the approach in Chapter 1, one now immediately projects the modified governing equation (2.47) onto the DG basis functions and inserts the spatial DG approximation. As a result we obtain

$$
\langle \Phi_k, \Phi_l \rangle \frac{\partial}{\partial t} \hat{Q}_{pl}(t) \quad + \quad \left\langle \Phi_k, \frac{\partial \Phi_l}{\partial \xi} \right\rangle \check{A}^*_{pq} \hat{Q}_{ql}(t) + \left\langle \Phi_k, \frac{\partial \Phi_l}{\partial \eta} \right\rangle \check{B}^*_{pq} \hat{Q}_{ql}(t) +
$$
$$
+ \quad \left\langle \Phi_k, \frac{\partial \Phi_l}{\partial \zeta} \right\rangle \check{C}^*_{pq} \hat{Q}_{ql}(t) - \langle \Phi_k, \Phi_l \rangle \check{E}_{pq} \hat{Q}_{ql}(t) = 0 \,, \tag{2.49}
$$

where $\langle a, b \rangle = \int_{\mathcal{T}_E} a \cdot b \, dV$ denotes the inner product over the reference tetrahedron $\mathcal{T}_E$. Equation (2.49) can be reformulated using the definitions of the mass matrix $M_{kl} = \langle \Phi_k, \Phi_l \rangle$, the stiffness matrices $K^{\xi}_{kl} = \left\langle \frac{\partial \Phi_k}{\partial \xi}, \Phi_l \right\rangle$, $K^{\eta}_{kl} = \left\langle \frac{\partial \Phi_k}{\partial \eta}, \Phi_l \right\rangle$ and $K^{\zeta}_{kl} = \left\langle \frac{\partial \Phi_k}{\partial \zeta}, \Phi_l \right\rangle$, as seen in equations (1.42-1.47), and the Kronecker symbol δ_{nl} as follows:

$$
\frac{\partial}{\partial t} \hat{Q}_{pn}(t) =
$$
$$
= \left(-M^{-1}_{nk} K^{\xi}_{lk} \check{A}^*_{pq} - M^{-1}_{nk} K^{\eta}_{lk} \check{B}^*_{pq} - M^{-1}_{nk} K^{\zeta}_{lk} \check{C}^*_{pq} + \delta_{nl} \check{E}_{pq} \right) \hat{Q}_{ql}(t) \,. \tag{2.50}
$$

Equation (2.50) is a system of ordinary differential equations that governs the time evolution of the degrees of freedom $\hat{Q}_{pn}(t)$ without taking into account effects from the element boundaries. However, it can be used in order to estimate the time evolution during one time step. The m-th time derivative of $\hat{Q}_{pn}(t)$ is then given recursively by

$$
\frac{\partial^m}{\partial t^m} \hat{Q}_{pn}(t) =
$$
$$
= \left(-M^{-1}_{nk} K^{\xi}_{lk} \check{A}^*_{pq} - M^{-1}_{nk} K^{\eta}_{lk} \check{B}^*_{pq} - M^{-1}_{nk} K^{\zeta}_{lk} \check{C}^*_{pq} + \delta_{nl} \check{E}_{pq} \right) \frac{\partial^{m-1}}{\partial t^{m-1}} \hat{Q}_{ql}(t) \,, \tag{2.51}
$$

for all $m \geq 1$. The Taylor series for the degrees of freedom

$$
\hat{Q}_{pn}(t) = \sum_{m=0}^{N} \frac{(t - t^n)^m}{m!} \frac{\partial^m}{\partial t^m} \hat{Q}_{pn}(t^n) \,, \tag{2.52}
$$

can be integrated analytically in time, and with $\Delta t = t^{n+1} - t^n$ the following result is obtained:

$$
\int_{t^n}^{t^{n+1}} \hat{Q}_{pn}(t) dt = \sum_{m=0}^{N} \frac{\Delta t^{m+1}}{(m+1)!} \frac{\partial^m}{\partial t^m} \hat{Q}_{pn}(t^n) := I_{pnql}(\Delta t) \, \hat{Q}_{ql}(t^n) \,. \tag{2.53}
$$

Equation (2.53) together with (2.51) can be seen as a discrete Cauchy-Kovalewski procedure for the system (2.47). Due to the linearity of the governing system, this new approach is equal to the use of the four-dimensional tensor as presented previously in Chapter 1.

Table 2.1: Evolution of the computational effort with respect to the purely elastic case ($n = 0$) with increasing number of mechanisms n for ADER-DG schemes from second- to sixth-order.

n	0	1	2	3	4	5	6	7	8	9	10
$\mathcal{O}2$	1.00	1.39	1.46	1.54	1.65	1.78	1.90	1.99	2.11	2.17	2.31
$\mathcal{O}3$	1.00	1.52	1.67	1.82	1.98	2.13	2.28	2.44	2.61	2.75	2.91
$\mathcal{O}4$	1.00	1.72	1.91	2.05	2.26	2.44	2.65	2.83	3.04	3.21	3.41
$\mathcal{O}5$	1.00	1.84	2.04	2.23	2.45	2.68	2.91	3.08	3.29	3.53	3.73
$\mathcal{O}6$	1.00	1.91	2.13	2.32	2.53	2.78	3.01	3.20	3.43	3.64	3.84

2.6   Quality factor Approximation

It is usual, for practical problems, to aim at modeling a quasi-constant $\mathcal{Q}$ value at the frequency range of interest. However, the GMB mechanisms show a strong dependency with the frequency and one has to tune up the free parameters to obtain the desired $\mathcal{Q}$ approximated value, as shown in detail in (2.18). Using a larger amount of mechanisms improved the fit between the desired and the approximated $\mathcal{Q}$ values, but they also increase dramatically the computational costs. Therefore, it is necessary to perform an analysis of the effect of adding further mechanisms, both in the quality of the fit and in the computational requirements. The additional CPU time requirements when different orders of accuracy of the ADER-DG schemes are used in combination with an increasing number of such mechanisms is further analysed. Fig. 2.4 shows, how a constant $\mathcal{Q}$-law can be fitted by using (a) 2, (b) 3, (c) 5 or (d) 10 relaxation mechanisms on a frequency band of $(0.1, 10)$Hz. It must be pointed out, that following [63] already 3 relaxation mechanisms approximate a constant, frequency-independent $\mathcal{Q}$-law with a maximum deviation of around 5%. Using only 2 relaxation mechanisms seems to be a too rough approximation whereas 5 or more mechanisms already lead to a $\mathcal{Q}$-law approximation which might not even be necessary in most cases. The influence of the number of used relaxation mechanisms on seismograms recorded for an anelastic subsurface model is studied in Section 2.8.

Table 2.1 shows the increasing CPU time, when the number n of mechanisms is increased. The CPU times are normalized with respect to the purely elastic case, where no attenuation is incorporated, i.e. $n = 0$. Recall, that 3 mechanisms, as typically suggested in the literature e.g. by Emmerich & Korn [63] or Moczo *et al.* [98], only increase the computational effort between a factor of 1.46 and 2.32 depending on the order of the used ADER-DG scheme. This efficiency is quite remarkable, in particular, as the anelastic functions, i.e. the anelastic part of (2.28) as described in Section 2.5, are treated with the same (full) order of
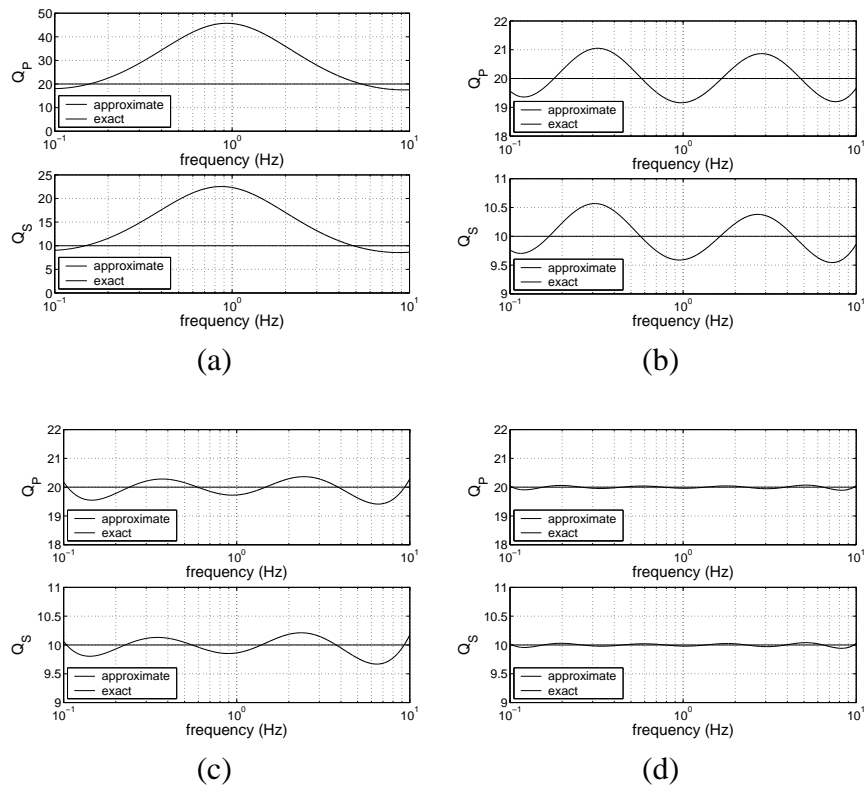
Figure 2.4: Approximation of frequency independent $\mathcal{Q}$-factors using (a) 2, (b) 3, (c) 5 or (d) 10 mechanisms on a frequency band of $(0.1, 10)$Hz.

accuracy. The results of a convergence study in the following Section 2.7 confirm that this way the scheme maintains its high-order approximation properties.

2.7   Convergence Study

In this Section we present the results of a numerical convergence study to confirm the very high accuracy of the proposed ADER-DG method on tetrahedral meshes considering viscoelastic attenuation. Here we show results from second- to seventh-order ADER-DG schemes, which are denoted by ADER-DG $\mathcal{O}2$ to ADER-DG $\mathcal{O}7$, respectively. Furthermore, the proposed ADER-DG schemes automatically obtain the same order for space *and* time.

To determine the convergence orders, the three-dimensional seismic wave equations (2.27) with viscoelastic attenuation are solved in the unit-cube, i.e. in a computational domain $\Omega = [-1, 1] \times [-1, 1] \times [-1, 1] \in \mathbb{R}^3$, as sketched in Fig. 2.5. Periodic boundary conditions are used at the boundaries of Ω. The homogeneous material parameters are set to

$$\lambda = 2, \qquad \mu = 1, \qquad \rho = 1, \qquad Q_P = 20, \qquad Q_S = 10, \qquad (2.54)$$

throughout the computational domain Ω. The $\mathcal{Q}$-factors are assumed to be frequency independent over the frequency band $(0.1, 10)$ Hz. A total of 5 relaxation mechanisms are used, as introduced in Section 2.4, which lead to a satisfying approximation of a constant $\mathcal{Q}$-law as shown in Fig. 2.4(c). These material properties introduce damping and dispersion of the P- and S-waves.

For the convergence test 2 initial conditions are used. One represents a plane P-wave traveling along the space diagonal $\vec{d} = (1, 1, 1)^T$ of the domain Ω and the other represents a plane S-wave traveling in opposite direction as already shown in [55]. The total simulation time T is set to $T = 0.1$s. The CFL number is set in all computations to $C = 0.5$ of the stability limit $\frac{1}{2N+1}$ of Runge-Kutta DG schemes (see (1.67)). For a thorough investigation of the linear stability properties of the ADER-DG schemes based on a *von Neumann* stability analysis see [53].

In the following we explain in detail how the initial condition and the analytic solution for the convergence test problem are found. It is known, e.g. from [107], that the analytic solution to the plane wave problem has the form

$$Q_p(x, y, z, t) = Q_p^0 \cdot e^{i \cdot (\omega t - k_x x - k_y y - k_z z)}, \qquad p = 1, ..., n_v \qquad (2.55)$$

where Q_p^0 is the initial amplitude vector, ω the angular frequency to be determined and

$$\vec{k} = (k_x, k_y, k_z)^T = (\pi, \pi, \pi)^T. \qquad (2.56)$$

is the wave number vector. Equations (2.55) and (2.56) lead to a periodic, plane sinusoidal wave in the unit-cube Ω with the wave front perpendicular to the cube's
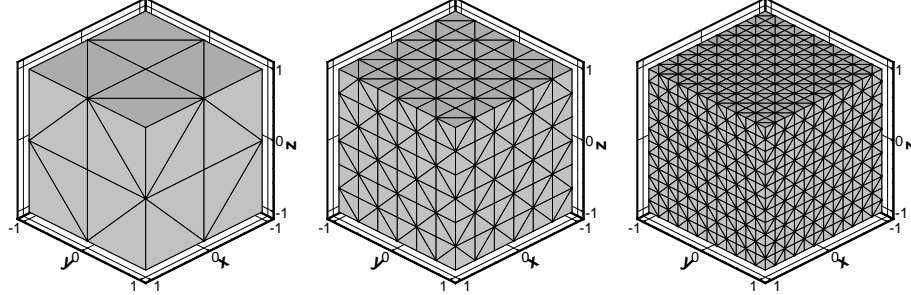
Figure 2.5: Sequence of discretizations of the computational domain Ω via regularly refined tetrahedral meshes, which are used for the numerical convergence analysis.

space diagonal.

In the following we briefly explain how the angular frequencies ω are determined: With the assumption, that (2.55) is the analytic solution of the governing equation (2.28), the first time and space derivatives of (2.55) are calculated analytically and inserted into (2.28). From there, we can derive an eigenproblem of the general form $M\,\vec{v} = \alpha\,\vec{v}$. Here, in particular, we obtain

$$(\check{A}_{pq}k_x + \check{B}_{pq}k_y + \check{C}_{pq}k_z - i \cdot \check{E}_{pq}) \cdot Q_q^0 = \omega \cdot Q_q^0, \qquad p, q = 1, ..., n_v. \quad (2.57)$$

Solving an eigenproblem means finding the p eigenvalues $\alpha^{(j)}$ and eigenvectors $\vec{v}^{(j)}$, $j = 1, ..., p$, of the square matrix $M \in \mathbb{R}^{p \times q}$. In the present case of (2.57), one needs to find the eigenvalues $\omega^{(j)}$ and the matrix R_{pq} of right eigenvectors $\vec{r}_p^{(1)}, ..., \vec{r}_p^{(n_v)} \in \mathbb{R}^{n_v}$, with $p = 1, ..., n_v$.

It is a known fact [133], that the solution of a linear hyperbolic system, as e.g. in (2.28), is given by a linear combination of the right eigenvectors. Therefore, the analytic solution $Q_p(x, y, z, t)$ in (2.55) can be written as $Q_p = \nu_q \cdot R_{pq}$. The coefficients ν_q can be computed via $\nu_q = R_{qp}^{-1}Q_p^0$. Now, the analytic solution $Q_p(x, y, z, t)$ of the convergence test problem can be synthesized in the form

$$Q_p(x, y, z, t) = \sum_{j=1}^{n_v} \nu_j \cdot \vec{r}_p^{(j)}\, e^{i \cdot (\omega^{(j)} \cdot t - k_x x - k_y y - k_z z)} \qquad p = 1, ..., n_v. \quad (2.58)$$

In the special case of the initial condition used here, where one plane P-wave travels along the space diagonal $\vec{d} = (1, 1, 1)^T$ and one plane S-wave travels in the

opposite direction, only two right eigenvectors are needed. The initial condition for the convergence test problem is therefore given by (2.58) using the two right eigenvectors $\vec{r}_p^{(2)}$ and $\vec{r}_p^{(9)}$, i.e. $\nu_2 = \nu_9 = 1$ and zero otherwise.

To determine the convergence orders, the solution of the same convergence test problem is calculated on a sequence of tetrahedral meshes as shown in Fig. 2.5. The mesh sequence is obtained by dividing the computational domain Ω into a number of subcubes, which are then subdivided into five tetrahedrons. It must be remarked, that this subdivision leads to four equal tetrahedrons with 1/6 of the cube's volume and one regular central tetrahedron of 1/3 of the cube's volume. This way, the refinement level is controlled by changing the number of subcubes in each space dimension.

Now, one can arbitrarily pick one of the variables of the vector Q_p of the seismic wave equations (2.28) to numerically determine the convergence order of the used ADER-DG scheme. In Table 2.2 we show the errors for the shear stress component σ_{yz}. The errors of the numerical solution Q_h with respect to the exact solution Q_e obtained from (2.58) is measured in the L^∞-norm and the continuous L^2-norm

$$E_{L^2}^s = \|Q_h - Q_e\|_{L^2(\Omega)} = \left(\int_\Omega |Q_h - Q_e|^2 \, dV \right)^{\frac{1}{2}}, \qquad (2.59)$$

where the integration is approximated by Gaussian integration which is exact for a polynomial degree twice that of the basis functions of the numerical scheme. The L^∞-norm is approximated by the maximum error arising at any of these Gaussian integration points. The convergence orders are then computed through

$$\mathcal{O}_{L^\nu} = \log\left(\frac{E_{L^\nu}^s}{E_{L^\nu}^{s-1}}\right) / \log\left(\frac{h^s}{h^{s-1}}\right), \qquad \text{with} \qquad \nu = 2, \infty \,, \qquad (2.60)$$

where h^s indicates the mesh spacing h of mesh number s in the sequence of meshes.

The first column in Table 2.2 shows the mesh spacing h, represented by the maximum diameter of the circumscribed spheres of the tetrahedrons. The following four columns show the L^∞ and L^2 errors with the corresponding convergence orders $\mathcal{O}_{L^\infty}$ and $\mathcal{O}_{L^2}$ determined by successively refined meshes. Furthermore, the total number N_d of degrees of freedom is presented, which is a measure of required storage space during run-time and is given through the product of the number of total mesh elements and the number N_e of degrees of freedom per element. N_e depends on the order of the scheme, i.e. the degree N of the polynomial basis functions via $N_e(N) = \frac{1}{6}(N+1)(N+2)(N+3)$. In the last two columns is given the number I of iterations and the CPU times in seconds needed to reach the simulation time $T = 0.1$s on one Pentium Xeon 3.6 GHz processor with 4GB of RAM.

Table 2.2: Convergence rates of velocity component v of the ADER-DG $\mathcal{O}2$ up to ADER-DG $\mathcal{O}7$ schemes on tetrahedral meshes with viscoelastic attenuation.

| h	L^∞	$\mathcal{O}_{L^\infty}$	L^2	$\mathcal{O}_{L^2}$	N_d	I	CPU [s]
$1.08 \cdot 10^{-1}$	$5.8094 \cdot 10^{-3}$	—	$4.8622 \cdot 10^{-3}$	—	81920	24	67
$7.21 \cdot 10^{-2}$	$2.5990 \cdot 10^{-3}$	2.0	$2.1265 \cdot 10^{-3}$	2.0	276480	36	341
$5.41 \cdot 10^{-2}$	$1.5287 \cdot 10^{-3}$	1.8	$1.1775 \cdot 10^{-3}$	2.1	655360	46	1043
$4.33 \cdot 10^{-2}$	$9.6624 \cdot 10^{-4}$	2.1	$7.4891 \cdot 10^{-4}$	2.0	1280000	58	2546
$2.16 \cdot 10^{-1}$	$5.1803 \cdot 10^{-3}$	—	$3.2846 \cdot 10^{-3}$	—	25600	20	12
$1.08 \cdot 10^{-1}$	$6.1874 \cdot 10^{-4}$	3.1	$3.4224 \cdot 10^{-4}$	3.3	204800	38	175
$7.21 \cdot 10^{-2}$	$1.6487 \cdot 10^{-4}$	3.3	$1.0294 \cdot 10^{-4}$	3.0	691200	58	857
$5.41 \cdot 10^{-2}$	$7.9007 \cdot 10^{-5}$	2.6	$4.2568 \cdot 10^{-5}$	3.1	1638400	76	2708
$2.16 \cdot 10^{-1}$	$5.4011 \cdot 10^{-4}$	—	$3.2609 \cdot 10^{-4}$	—	51200	28	35
$1.44 \cdot 10^{-1}$	$1.4012 \cdot 10^{-4}$	3.3	$5.7198 \cdot 10^{-5}$	4.3	172800	40	168
$1.08 \cdot 10^{-1}$	$4.3978 \cdot 10^{-5}$	4.0	$1.7152 \cdot 10^{-5}$	4.2	409600	54	504
$7.21 \cdot 10^{-2}$	$9.0642 \cdot 10^{-6}$	3.9	$3.2404 \cdot 10^{-6}$	4.1	1382400	80	2514
$4.33 \cdot 10^{-1}$	$1.8736 \cdot 10^{-3}$	—	$8.2689 \cdot 10^{-4}$	—	11200	18	7
$2.16 \cdot 10^{-1}$	$7.6374 \cdot 10^{-5}$	4.6	$2.2952 \cdot 10^{-5}$	5.2	89600	36	98
$1.44 \cdot 10^{-1}$	$9.2562 \cdot 10^{-6}$	5.2	$2.8210 \cdot 10^{-6}$	5.2	302400	52	482
$1.08 \cdot 10^{-1}$	$2.4829 \cdot 10^{-6}$	4.6	$6.5480 \cdot 10^{-7}$	5.1	716800	70	1483
$8.66 \cdot 10^{-1}$	$2.2965 \cdot 10^{-2}$	—	$5.5321 \cdot 10^{-3}$	—	2240	12	1
$4.33 \cdot 10^{-1}$	$3.4744 \cdot 10^{-4}$	6.0	$9.2044 \cdot 10^{-5}$	5.9	17920	22	17
$2.16 \cdot 10^{-1}$	$6.4859 \cdot 10^{-6}$	5.7	$1.3871 \cdot 10^{-6}$	6.1	143360	42	259
$1.44 \cdot 10^{-1}$	$5.8794 \cdot 10^{-7}$	5.9	$1.1658 \cdot 10^{-7}$	6.1	483840	64	1318
$8.66 \cdot 10^{-1}$	$4.4014 \cdot 10^{-3}$	—	$1.3209 \cdot 10^{-3}$	—	3360	14	3
$4.33 \cdot 10^{-1}$	$4.7643 \cdot 10^{-5}$	6.5	$1.2218 \cdot 10^{-5}$	6.8	26880	26	43
$2.88 \cdot 10^{-1}$	$3.2770 \cdot 10^{-6}$	6.6	$5.8054 \cdot 10^{-7}$	7.5	90720	38	213
$2.16 \cdot 10^{-1}$	$4.4764 \cdot 10^{-7}$	6.9	$7.6709 \cdot 10^{-8}$	7.0	215040	50	673
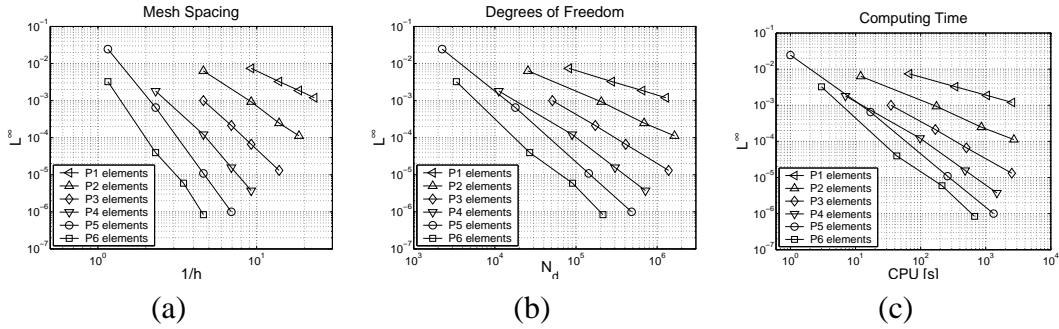
Figure 2.6: Convergence rates of velocity component v of Table 2.2. The symbols P1-P6 stand for the maximum polynomial degree of the basis functions used. The L^∞ error is plotted versus (a) the mesh spacing h, (b) the number of degrees of freedom N_d and (c) the CPU time.

In Fig. 2.6 one can visualize the convergence results of Table 2.2 to demonstrate the dependence of the L^∞ error with respect to (a) mesh width h, (b) number of degrees of freedom N_d and (c) CPU time. With mesh refinement, the higher-order schemes converge faster towards the analytic solution as shown in Fig. 2.6(a). Furthermore, Fig. 2.6(b) illustrates that higher-order schemes reach a desired accuracy requiring a lower number of total degrees of freedom. The total number of degrees of freedom is the product of the number of mesh elements and the degrees of freedom per element. Therefore, obviously the increasing number of degrees of freedom per element is over-compensated by the dramatic decrease of the number of required elements to reach a certain error level. The CPU time comparisons in Fig. 2.6(c) also illustrate that higher accuracy, i.e. smaller errors, are reached in less computational time when using a higher-order ADER-DG scheme. In all three plots of Fig. 2.6 we can clearly see, that for very high accuracy, the higher-order schemes pay off due to their superior convergence properties.

2.8 Application Example

A similar problem setup to that used in Section 1.8 is used to check the performance of the viscoelastic ADER-DG method. This setup was, proposed in the SPICE Code Validation (www.nuquake.eu/SPICECVal) and developed by Peter Moczo, Jean Paul Ampuero, Jozef Kristek, Steven M. Day, Miriam Kristekova, Peter Pazak, Heiner Igel, Renata Tothova, and Martin Galis. The problem itself, named WP1-HSP2a (Wave Propagation, Homogeneous Space, Viscoelastic) aims at assessing dispersion errors and local errors at different distances and propagation directions. The medium is described in Table 1.3, and is strongly attenuative. The seismic source, computational domain and receiver positions are identical to those in problem WP1-HSP1a of Section 1.8. The same mesh could thus be

re-used (see Fig. 1.5). The frequency window expected is from 0.13Hz to 5Hz and the receivers are at a maximum distance of $10,000$m from the source. An ADER-DG $\mathcal{O}6$ scheme was used, meaning that polynomials of 5th degree were used to describe the unknowns, including the anelastic mechanisms. To describe the attenuation, a total of 3 Maxwell Bodies were used to cover a bandwidth of 100Hz, centered at 2.5Hz. The dispersive curves associated to this mechanism for the material parameters of the present problem have already been shown in Figure 2.3. A total of $623,920$ elements were used. The simulation lasted for 51 hours in 128 Intel Itanium2 1.6GHz processors. A local timestepping algorithm is used to save computational time, as is briefly outlined in Section 1.5.4, thus concentrating the computational load in the small tetrahedra of the area of interest. The numerical results are compared to Discrete Wave Number (DWN) solution. The resulting seismograms are shown in Figures 2.7, 2.8 and 2.9 together with the root mean square error (r.m.s) between the ADER-DG numerical solution and the DWN solution. This r.m.s. misfit is computed through

$$E = \sum_{j=1}^{n_t} (s_j - s_j^a)^2 / \sum_{j=1}^{n_t} (s_j^a)^2, \qquad (2.61)$$

where n_t is number of time samples of the seismogram, s_j is the numerical value of the particular seismogram at sample j and s_j^a is the corresponding analytical value. Notice that the numerical results are totally *unfiltered* and *unscaled*. The accuracy is further assessed using the concepts of phase misfit and envelope misfit described in [87]. For the present case, a purely analytical solution is not available and therefore the DWN solution is used as a reference. Despite not being a purely analytical solution, it is often used as a reference because of the accuracy of its results. The ADER-DG method's performance can be seen in Table 2.4. Problems arise at receivers 3, 6, 9 and 12, the farthest receivers which are all equidistant to the source. At such receivers, a spurious pulse appears at around 3.9s in the DWN solution which further pollutes the error estimation in this comparison. The overall maxima of the errors are 2.6% and 1.1% for the envelope and phase misfits respectively, comparable to the results obtained in Section 2.3 for the purely elastic case and having in mind that DWN is also producing uncertainties in the order of those produced by ADER-DG.

2.9 Conclusion

The incorporation of realistic attenuation of seismic waves into the new ADER-Discontinuous Galerkin (ADER-DG) schemes using viscoelastic material has been

Table 2.3: Material parameters for the WP1-HSP2a test case. Note, that attenuation will cause dispersion of the P- and S-waves such that the given wave speeds refer to a reference frequency $f_r = 2.5$Hz.

$c_p(f_r)[m/s]$	$c_s(f_r)[m/s]$	$\rho[kg/m^3]$	Q_p	Q_s
6000	3464	2700	60	30

Table 2.4: Envelope and phase misfits in % for WP-HSP2a against a reference solution.

	x		y		z		$\text{Max}_{(DG)}$	
Rec.	EM	PM	EM	PM	EM	PM	EM	PM
1	1.7	0.2	0.2	0.0	0.2	0.0	1.7	0.2
2	1.3	0.3	0.2	0.0	0.1	0.0	1.3	0.3
3	1.9	0.7	0.1	0.0	0.1	0.0	1.9	0.7
4	1.4	0.2	1.3	0.1	1.0	0.6	1.4	0.6
5	1.1	0.2	1.3	0.2	0.5	0.0	1.3	0.2
6	1.8	0.5	2.6	1.1	1.3	0.8	2.6	1.1
7	1.1	0.2	1.3	0.2	1.2	0.2	1.3	0.2
8	0.8	0.2	0.8	0.2	1.2	0.3	1.2	0.3
9	1.2	0.4	1.2	0.4	1.7	0.6	1.7	0.6
10	1.6	0.2	1.1	0.1	0.5	0.1	1.6	0.2
11	0.8	0.2	1.2	0.3	0.8	0.2	1.2	0.3
12	1.0	0.2	2.0	0.7	1.0	0.4	2.0	0.7

Figure 2.7: Seismograms showing particle velocities for the ADER-DG (solid) and analytical solution (dotted) for receivers 1 to 5. The three columns correspond to the $x-$, $y-$ and $z-$ components. The residuals (dashed) and the r.m.s errors E are shown.

Figure 2.8: Seismograms showing particle velocities for the ADER-DG (solid) and analytical solution (dotted) for receivers 6 to 10. The three columns correspond to the $x-$, $y-$ and $z-$ components. The residuals (dashed) and the r.m.s errors E are shown.
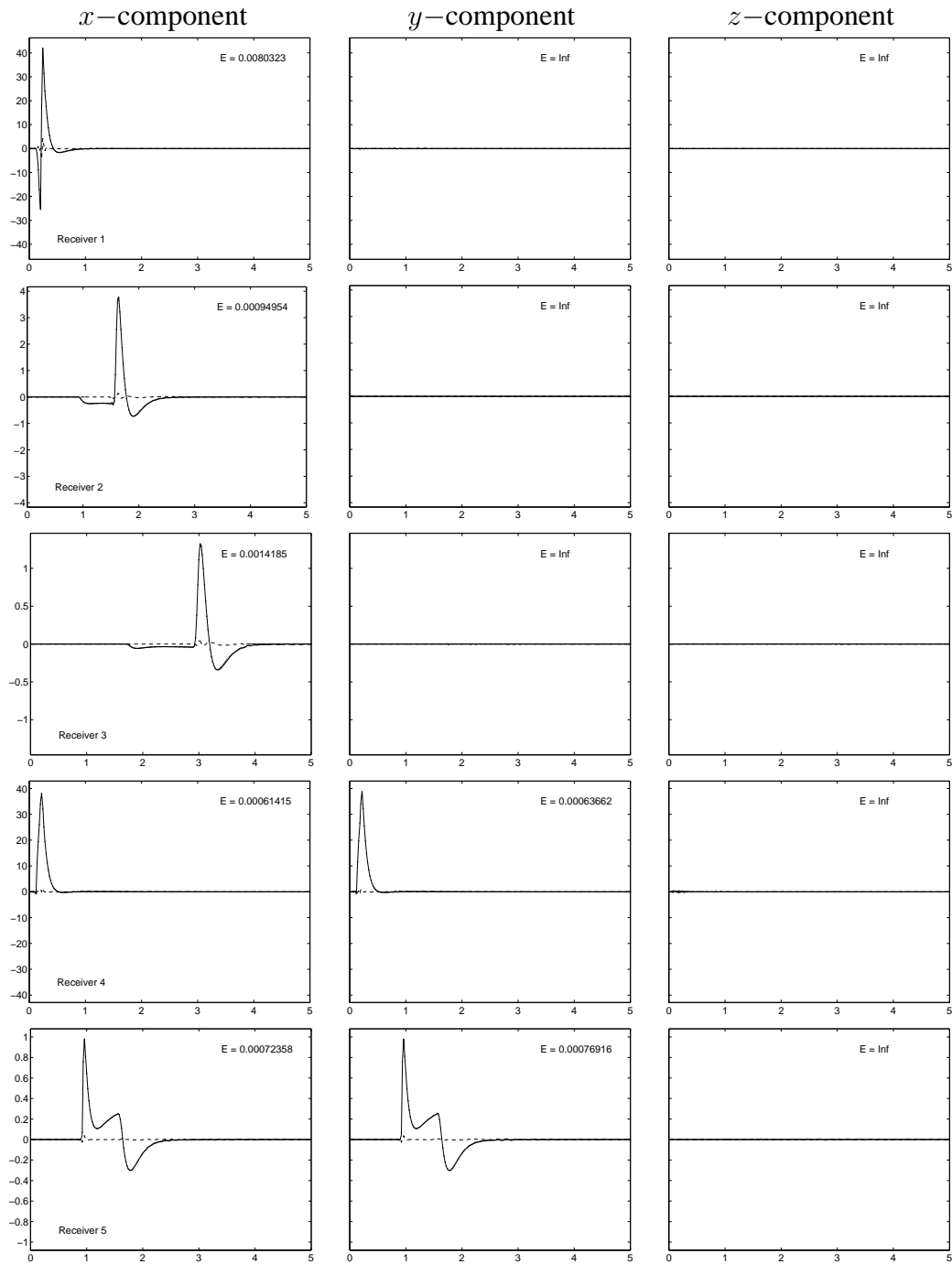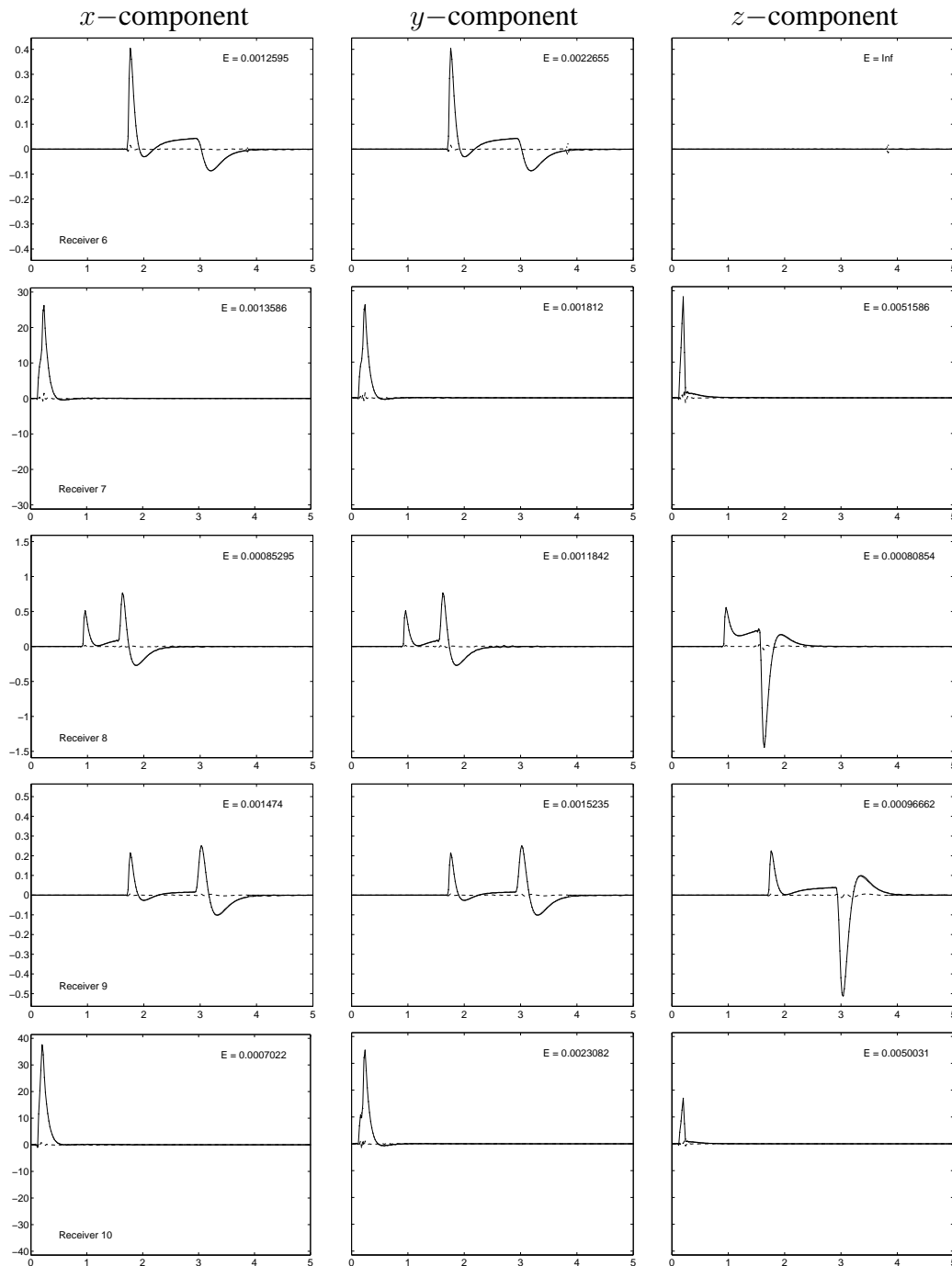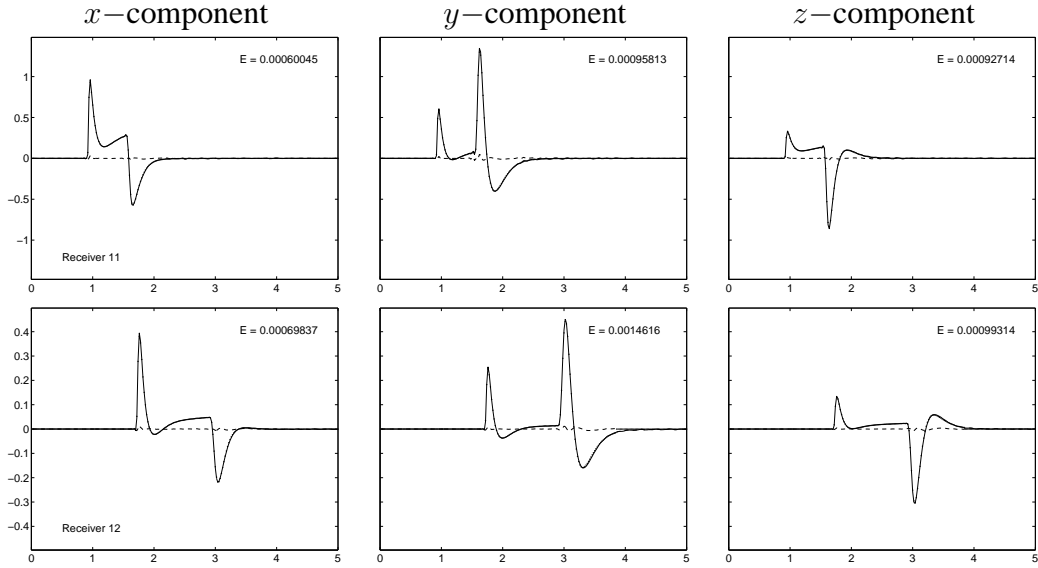
Figure 2.9: Seismograms showing particle velocities for the ADER-DG (solid) and analytical solution (dotted) for receivers 11 to 12. The three columns correspond to the $x-$, $y-$ and $z-$ components. The residuals (dashed) and the r.m.s errors E are shown.

presented. The additional variables, the anelastic functions, can be treated similarly to the elastic ones in the case of viscoelastic material. Therefore, the linear hyperbolic system of the seismic wave equations increases with the number of relaxation mechanisms and includes source terms resulting from the approximating viscoelastic material behaviour by a Generalized Maxwell Body. However, the introduction of a new Cauchy-Kovalewski procedure for the high-order ADER time integration results in a more efficient implementation and therefore does not increase the computation time dramatically when incorporating viscoelastic attenuation. The convergence results demonstrate the high accuracy of the ADER-DG schemes on tetrahedral meshes. In addition, the detailed investigation of the required number of relaxation mechanisms agrees with the suggestions in the literature, which suggests 3 mechanisms as sufficient for the accurate incorporation of realistic attenuation. The solution of a demanding test and the comparison of the obtained results against quasi-analytic solutions clearly shows the remarkable accuracy of the ADER-DG method. Therefore, the proposed method represents a new numerical scheme simulating seismic wave propagation with unprecedented accuracy on unstructured three-dimensional tetrahedral meshes thoroughly including realistic attenuation due to viscoelasticity.

Chapter 3

Anisotropy in ADER-DG Schemes

In this Chapter, the ADER-DG method is extended to model the anisotropic effects on the seismic wavefield. The origins and seismological applications of the anisotropic rheology are introduced in the first part. The modifications of the ADER-DG method to treat anisotropic material are then investigated, with special attention to the coupling of anisotropic and viscoelastic material effects, which often is not mentioned in the literature. Convergence tests will show the high-accuracy properties of the developed scheme and a set of applications will further validate it by direct comparison with analytic solutions and others produced with the Spectral Element Method. The main contents of this Chapter have been published in J. de la Puente, M. Käser, M. Dumbser and H. Igel [50].

3.1 General Overview

The properties of anisotropic materials show different values when measured in different directions. For seismic waves, this means that waves will travel at different velocities for different directions. Furthermore, the polarization of the particle motion is in general not anymore purely parallel or perpendicular to the direction in which the energy propagates. Furthermore, anisotorpy is an ubiquitous phenomenon for seismic waves. For rocks, anisotropy can be either a microscopical anisotropy, due to the crystalline symmetries of the rock's constituents, or macroscopical, being most common the case of finely layered or cracked materials which, macroscopically, behave as homogeneous anisotropic materials. A number of regions in the Earth show clear anisotropic properties. Some examples of such regions are the basaltic ocean bottom and the D" layer.

In the past, many approaches describing anisotropic wave propagation have been developed. Early attempts aimed at the simplification of anisotropic effects for some weakly anisotropic media [124, 130]. Analytical and quasi-analytical solutions of simplified cases exist and ray theory can handle the problem to some extent [35]. However, when heterogeneous materials and complex geometrical

structures are involved only three-dimensional full wave-form simulations are able to address the problem. The most widely used method, the Finite Difference (FD) method, has successfully been extended from isotropic [93, 136, 137] to anisotropic problems using staggered [73, 104] or rotated staggered grids [117]. However, both approaches are forced to interpolate stress and strain off-diagonal values as they are not defined in the same grid points. Pseudospectral (PS) methods [34, 65, 72, 129] have been extended to handle anisotropic material [31, 71, 128]. More recently, the Spectral Element Method (SEM) has considerably gained in popularity due to its accuracy and efficiency on deformable hexahedral elements [82, 85]. The method has been further developed for problems with anisotropic material [80, 108] and successfully been applied to the case of global seismic wave propagation [81]. Recent attempts to incorporate anisotropy on fully unstructured grids [66] represent an alternative approach.

In the present Chapter we present an extension of the ADER-DG scheme to anisotropic material. Special attention will be given to developing an exact flux of the Godunov-type and the coupling of anisotropy and viscoelastic attenuation. The resulting scheme keeps the high-order properties of the original ADER-DG scheme and is able to model the most general triclinic anisotropic case on completely unstructured tetrahedral meshes.

3.2   Elastic Anisotropy

The most general, linear and elastic stress-strain relation can be expressed as a tensorial constitutive law (Hooke's Law), see e.g. [107], of the form

$$\sigma_{ij} = c_{ijkl}\varepsilon_{kl}\,, \tag{3.1}$$

The entries of the fourth-order elasticity tensor c_{ijkl} can be reduced to a maximum of 21 independent real coefficients in the most general case due to symmetry considerations. Using matrix notation, the stresses σ_{ij} and strains ε_{kl} are defined as the arrays $\vec{\sigma} = (\sigma_{xx}, \sigma_{yy}, \sigma_{zz}, \sigma_{yz}, \sigma_{xz}, \sigma_{xy})^T$ and $\vec{\varepsilon} = (\varepsilon_{xx}, \varepsilon_{yy}, \varepsilon_{zz}, \varepsilon_{yz}, \varepsilon_{xz}, \varepsilon_{xy})^T$, so that one can rewrite (3.1) using an anisotropic elastic matrix M_{ij} as

$$\vec{\sigma_i} = M_{ij}\vec{\varepsilon_j}\,, \tag{3.2}$$

which extended in more detail reads as

$$
\begin{pmatrix} \sigma_{xx} \\ \sigma_{yy} \\ \sigma_{zz} \\ \sigma_{yz} \\ \sigma_{xz} \\ \sigma_{xy} \end{pmatrix} =
\begin{pmatrix}
c_{11} & c_{12} & c_{13} & 2c_{14} & 2c_{15} & 2c_{16} \\
c_{12} & c_{22} & c_{23} & 2c_{24} & 2c_{25} & 2c_{26} \\
c_{13} & c_{23} & c_{33} & 2c_{34} & 2c_{35} & 2c_{36} \\
c_{14} & c_{24} & c_{34} & 2c_{44} & 2c_{45} & 2c_{46} \\
c_{15} & c_{25} & c_{35} & 2c_{45} & 2c_{55} & 2c_{56} \\
c_{16} & c_{26} & c_{36} & 2c_{46} & 2c_{56} & 2c_{66}
\end{pmatrix}
\begin{pmatrix} \varepsilon_{xx} \\ \varepsilon_{yy} \\ \varepsilon_{zz} \\ \varepsilon_{yz} \\ \varepsilon_{xz} \\ \varepsilon_{xy} \end{pmatrix}\,. \tag{3.3}
$$

Whenever a material possesses more than 2 independent parameters defining the entries of M_{ij}, the material's properties depend on the direction and the material is said to be *anisotropic*. Considering all 21 independent coefficients in M_{ij} a triclinic material can be modelled, which is the most general case of anisotropy and includes as special cases all other crystalline symmetry classes, i.e. monoclinic, trigonal, tetragonal, orthorhombic, hexagonal, cubic and isotropic, see [106, 109]. The most important for seismic purposes are the following. For monoclinic materials, considering a symmetry plane (x, z), one has

$$
M_{\text{monoclinic}} = \begin{pmatrix}
c_{11} & c_{12} & c_{13} & 0 & 2c_{15} & 0 \\
c_{12} & c_{22} & c_{23} & 0 & 2c_{25} & 0 \\
c_{13} & c_{23} & c_{33} & 0 & 2c_{35} & 0 \\
0 & 0 & 0 & 2c_{44} & 0 & 2c_{46} \\
c_{15} & c_{25} & c_{35} & 0 & 2c_{55} & 0 \\
0 & 0 & 0 & 2c_{46} & 0 & 2c_{66}
\end{pmatrix}, \tag{3.4}
$$

for an orthorhombic material is obtained

$$
M_{\text{orthorhombic}} = \begin{pmatrix}
c_{11} & c_{12} & c_{13} & 0 & 0 & 0 \\
c_{12} & c_{22} & c_{23} & 0 & 0 & 0 \\
c_{13} & c_{23} & c_{33} & 0 & 0 & 0 \\
0 & 0 & 0 & 2c_{44} & 0 & 0 \\
0 & 0 & 0 & 0 & 2c_{55} & 0 \\
0 & 0 & 0 & 0 & 0 & 2c_{66}
\end{pmatrix}, \tag{3.5}
$$

and, finally, for a transversely isotropic material holds

$$
M_{\text{trans. iso.}} = \begin{pmatrix}
c_{11} & c_{12} & c_{13} & 0 & 0 & 0 \\
c_{12} & c_{11} & c_{13} & 0 & 0 & 0 \\
c_{13} & c_{13} & c_{33} & 0 & 0 & 0 \\
0 & 0 & 0 & 2c_{44} & 0 & 0 \\
0 & 0 & 0 & 0 & 2c_{55} & 0 \\
0 & 0 & 0 & 0 & 0 & c_{11} - c_{12}
\end{pmatrix}, \tag{3.6}
$$

Therefore, isotropy can be understood as the particular case, in which $c_{11} = c_{22} = c_{33} = \lambda + 2\mu$, $c_{12} = c_{13} = c_{23} = \lambda$, $c_{44} = c_{55} = c_{66} = \mu$ and all other coefficients are equal to zero. In addition, the entries of the matrices M_{ij} just shown will change depending on the Cartesian reference system used to describe them, with the notable exception of the isotropic case, which is totally invariant under reference system rotation, hence its name. To visualize anisotropic behavior for wave propagation, in Figure 3.1 one can see examples of the four most important symmetry classes for anisotropic materials. The figures show velocities for the compressional waves, using as example materials mesaverde clay (transversely isotropic, values taken from [130]), olivine (orthorhombic, values
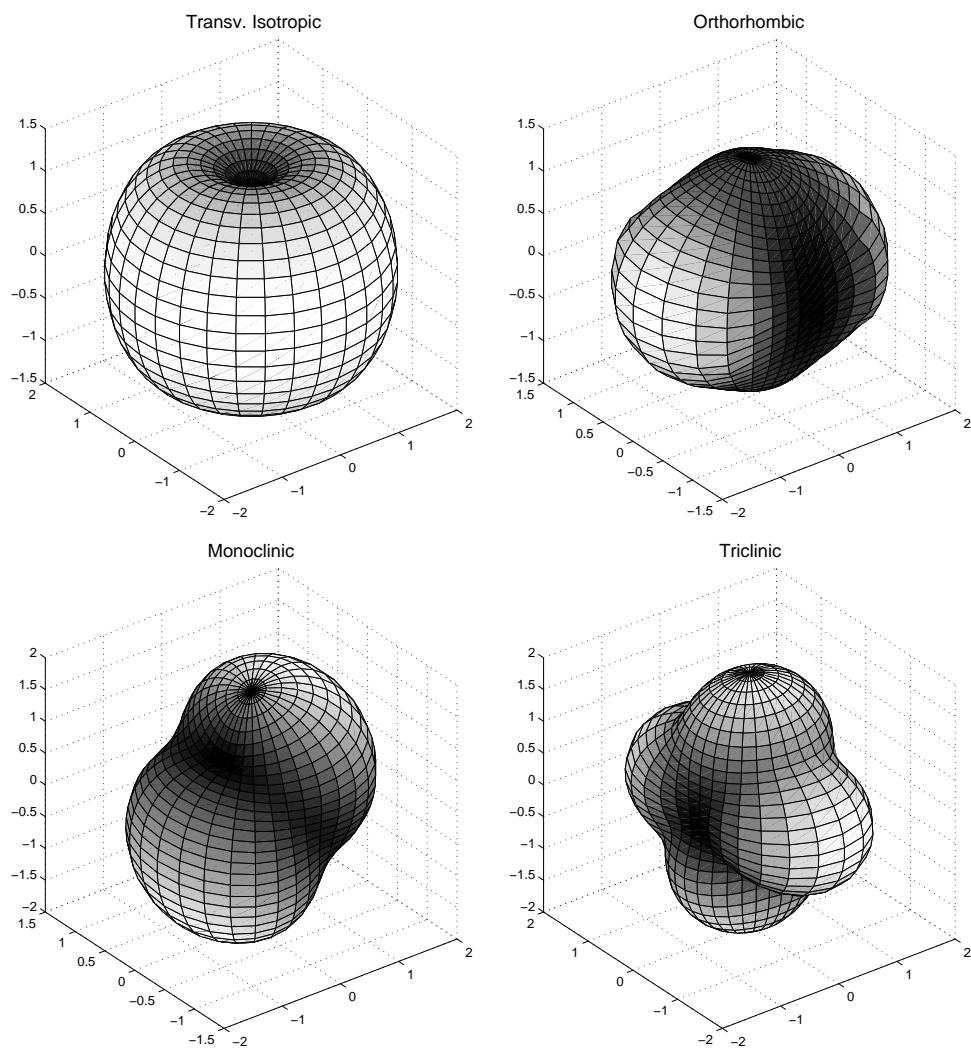
Figure 3.1: Examples of velocity surfaces for materials of the 4 most frequent anisotropic symmetry classes in seismology. All figures depict the highest wave velocities at each propagation direction. The figures have been renormalized to show velocity 1 at the slowest directions and 2 at the fastest directions, to enhance the anisotropic structure.

from [64]), diopside (monoclinic, values from [2]) and low albite (triclinic, values from [20]).

Seismic waves traveling through anisotropic material will propagate at different velocities depending on their propagation direction and the polarization of the particle motion associated. Thus a commonly observed phenomenon in the Earth's interior is that of an S-wave propagating through an anisotropic material being split into two waves orthogonally polarized and traveling at different speed [67].

The anisotropic properties of a material are very dependent on the scale considered. Minerals often show large anisotropic properties, due to their molecular structure. However, their disposition in the Earth is random to some extent, thus being the anisotropic properties smeared macroscopically. A usual example is that of olivine. P-waves travelling through the mineral can have propagation velocities up to 28% different depending on the direction [5]. However, being a major constituent of the mantle, no such large anisotropy is observed in that region. On the other hand, some anisotropy in the upper mantle seems to be related to an alignment of olivine crystals with the mantle flow, and could then be an indicator of the mantle flow direction [139].

The effect of large stresses in the rocks can also cause it to create large cracked regions, where the cracks follow similar orientations. Those cracks, often fluid-filled, are also macroscopically treated as anisotropic material, even though the mineral constituent of the bedrock might be isotropic. For the case of a set of cracks all with the same alignment, transversely isotropic symmetry is expected, although for more complex cases others might apply [138].

The oceanic lithosphere is also a largely anisotropic area where olivine crystals tend to orient themselves in the direction of spreading from the mid-ocean ridge [105]. Other major source of anisotropy is the fine horizontal layering characteristic of sedimentary basins which behaves as a transversely isotropic material with the symmetry axis oriented vertically [113].

The inner core also shows signs of anisotropy, being the travel time of PKIKP waves about $3s$ faster along the Earth's rotation axis than along the equatorial plane [126]. Finally an exotic case is that of the very fine layer at the core-mantle boundary, known as D", whose strong and varying anisotropic structure is currently a major study topic in seismology [79].

3.3 Anisotropic Seismic Wave Equations

In the following, the elastic properties of anisotropic media will be considered with respect to the global reference coordinate system that also defines the orientation of stresses and strains. In a similar way to Chapter 1 for the isotropic case, Hooke's law (3.3) can be combined with Newton's dynamic equations to obtain a set of 9 equations and unknowns. Those build up the stress-velocity formula-

tion of three-dimensional anisotropic wave propagation. The partial differential equation system has the same form as the one described in Chapter 1

$$\frac{\partial Q_p}{\partial t} + A_{pq}\frac{\partial Q_q}{\partial x} + B_{pq}\frac{\partial Q_q}{\partial y} + C_{pq}\frac{\partial Q_q}{\partial z} = 0, \tag{3.7}$$

where Q is the vector

$$Q = \left(\sigma_{xx}, \sigma_{yy}, \sigma_{zz}, \sigma_{xy}, \sigma_{yz}, \sigma_{xz}, u, v, w\right)^T, \tag{3.8}$$

of the unknown stresses and velocities. Note, that here the ordering of stresses in the vector Q is different from the one used for the stress-strain relation in Equation (3.3). This ordering is chosen in order to be consistent with the formulation of the ADER-DG scheme used through the present thesis. The matrices $A_{pq} = A_{pq}(\vec{x})$, $B_{pq} = B_{pq}(\vec{x})$, and $C_{pq} = C_{pq}(\vec{x})$, where $\vec{x} = (x, y, z)$ and $p, q = 1, ..., 9$, are the space dependent Jacobian matrices for the general anisotropic case and are given through

$$A_{pq} = \begin{pmatrix} 0 & 0 & 0 & 0 & 0 & 0 & -c_{11} & -c_{16} & -c_{15} \\ 0 & 0 & 0 & 0 & 0 & 0 & -c_{12} & -c_{26} & -c_{25} \\ 0 & 0 & 0 & 0 & 0 & 0 & -c_{13} & -c_{36} & -c_{35} \\ 0 & 0 & 0 & 0 & 0 & 0 & -c_{16} & -c_{66} & -c_{56} \\ 0 & 0 & 0 & 0 & 0 & 0 & -c_{14} & -c_{46} & -c_{45} \\ 0 & 0 & 0 & 0 & 0 & 0 & -c_{15} & -c_{56} & -c_{55} \\ -\frac{1}{\rho} & 0 & 0 & 0 & 0 & 0 & 0 & 0 & 0 \\ 0 & 0 & 0 & -\frac{1}{\rho} & 0 & 0 & 0 & 0 & 0 \\ 0 & 0 & 0 & 0 & 0 & -\frac{1}{\rho} & 0 & 0 & 0 \end{pmatrix}, \tag{3.9}$$

$$B_{pq} = \begin{pmatrix} 0 & 0 & 0 & 0 & 0 & 0 & -c_{16} & -c_{12} & -c_{14} \\ 0 & 0 & 0 & 0 & 0 & 0 & -c_{26} & -c_{22} & -c_{24} \\ 0 & 0 & 0 & 0 & 0 & 0 & -c_{36} & -c_{23} & -c_{34} \\ 0 & 0 & 0 & 0 & 0 & 0 & -c_{66} & -c_{26} & -c_{46} \\ 0 & 0 & 0 & 0 & 0 & 0 & -c_{46} & -c_{24} & -c_{44} \\ 0 & 0 & 0 & 0 & 0 & 0 & -c_{56} & -c_{25} & -c_{45} \\ 0 & 0 & 0 & -\frac{1}{\rho} & 0 & 0 & 0 & 0 & 0 \\ 0 & -\frac{1}{\rho} & 0 & 0 & 0 & 0 & 0 & 0 & 0 \\ 0 & 0 & 0 & 0 & -\frac{1}{\rho} & 0 & 0 & 0 & 0 \end{pmatrix}, \tag{3.10}$$

$$C_{pq} = \begin{pmatrix} 0 & 0 & 0 & 0 & 0 & 0 & -c_{15} & -c_{14} & -c_{13} \\ 0 & 0 & 0 & 0 & 0 & 0 & -c_{25} & -c_{24} & -c_{23} \\ 0 & 0 & 0 & 0 & 0 & 0 & -c_{35} & -c_{34} & -c_{33} \\ 0 & 0 & 0 & 0 & 0 & 0 & -c_{56} & -c_{46} & -c_{36} \\ 0 & 0 & 0 & 0 & 0 & 0 & -c_{45} & -c_{44} & -c_{34} \\ 0 & 0 & 0 & 0 & 0 & 0 & -c_{55} & -c_{45} & -c_{35} \\ 0 & 0 & 0 & 0 & 0 & -\frac{1}{\rho} & 0 & 0 & 0 \\ 0 & 0 & 0 & 0 & -\frac{1}{\rho} & 0 & 0 & 0 & 0 \\ 0 & 0 & -\frac{1}{\rho} & 0 & 0 & 0 & 0 & 0 & 0 \end{pmatrix}, \qquad (3.11)$$

with the coefficients c_{ij} as given in matrix M_{ij} of (3.2) and (3.3) and ρ as the mass density.

The Jacobians (3.9)- (3.11) have entries c_{ij} which are defined in a global reference system. However, one has often to make computations in other reference systems. Therefore it is crucial to change the c_{ij} values under such rotations. For the particular case of the ADER-DG schemes, fluxes are computed in the local coordinate system aligned with *each element's face*. This local coordinate system, as previously shown in Chapter 1, is defined by the normal vector $\vec{n} = (n_x, n_y, n_z)^T$ and the two tangential vectors $\vec{s} = (s_x, s_y, s_z)^T$ and $\vec{t} = (t_x, t_y, t_z)^T$, which lie in the plane determined by the face of the tetrahedron and are orthogonal to each other and to the normal vector $\vec{n}$. The rotation into this local coordinate system is done by applying the so-called Bond's matrix $\mathcal{N}$ [17, 109]

$$\mathcal{N} = \begin{pmatrix} n_x^2 & n_y^2 & n_z^2 & 2n_z n_y & 2n_z n_x & 2n_y n_x \\ s_x^2 & s_y^2 & s_z^2 & 2s_z s_y & 2s_z s_x & 2s_y s_x \\ t_x^2 & t_y^2 & t_z^2 & 2t_z t_y & 2t_z t_x & 2t_y t_x \\ s_x t_x & s_y t_y & s_z t_z & s_y t_z + s_z t_y & s_x t_z + s_z t_x & s_y t_x + s_x t_y \\ t_x n_x & t_y n_y & t_z n_z & n_y t_z + n_z t_y & n_x t_z + n_z t_x & n_y t_x + n_x t_y \\ n_x s_x & n_y s_y & n_z s_z & n_y s_z + s_z n_y & n_x s_z + n_z s_x & n_y s_x + n_x s_y \end{pmatrix} (3.12)$$

to the Hooke's matrix $\mathcal{C}$ of the global reference system

$$\mathcal{C} = \begin{pmatrix} c_{11} & c_{12} & c_{13} & c_{14} & c_{15} & c_{16} \\ c_{12} & c_{22} & c_{23} & c_{24} & c_{25} & c_{26} \\ c_{13} & c_{23} & c_{33} & c_{34} & c_{35} & c_{36} \\ c_{14} & c_{24} & c_{34} & c_{44} & c_{45} & c_{46} \\ c_{15} & c_{25} & c_{35} & c_{45} & c_{55} & c_{56} \\ c_{16} & c_{26} & c_{36} & c_{46} & c_{56} & c_{66} \end{pmatrix}, \qquad (3.13)$$

leading to the rotated Hooke's matrix $\widetilde{\mathcal{C}}$ in the local reference system of the tetrahedron's boundary face

$$\widetilde{\mathcal{C}} = \mathcal{N} \cdot \mathcal{C} \cdot \mathcal{N}^T. \qquad (3.14)$$

Note, that in the isotropic case the matrix $\mathcal{C}$ is invariant under coordinate transformation due to the distribution of the non-zero coefficients c_{ij}, i.e. $\widetilde{\mathcal{C}}_{iso} = \mathcal{C}_{iso}$, and

therefore this rotation can be skipped for the isotropic case.

Another necessary element of ADER-DG schemes is the knowledge of the eigen-structure of the Jacobian matrices. For the anisotropic case, the non-zero eigenvalues α_i with $i = 1, \cdots, 6$ are the roots of the polynomial

$$XYZ - Xc_{56}^2 - Yc_{15}^2 - Zc_{16}^2 + 2c_{15}c_{16}c_{56} = 0 \,, \tag{3.15}$$

where the coefficients c_{ij} are the entries of the rotated Hooke's matrix $\widetilde{\mathcal{C}}$ of (3.14). Using the substitutions $X = c_{11} - \alpha^2\rho$, $Y = c_{66} - \alpha^2\rho$ and $Z = c_{55} - \alpha^2\rho$ it can be seen that the roots of a polynomial of degree 6 in α have to be found. However, the substitutions of X, Y and Z tell us that there are only three different values to search for, as (3.15) represents a cubic polynomial of α^2. Note, that the possibility of having complex eigenvalues, i.e. $\alpha^2 < 0$, can be excluded as this would imply the loss of hyperbolicity of the PDE system in (3.7). The eigenvalues can be interpreted as the speed at which the different wave types are propagating in normal direction through the element interface. This is a known result for the anisotropic phase wave speeds [43] and appears here naturally from the eigendecomposition of the Jacobians of the scheme (3.9). In general the resulting waves are called *quasi*-waves qP, qS_1 and qS_2; ordered in decreasing magnitude of their velocities [43]. For the isotropic case one would get the positive and negative P-wave velocities and two positive and negative S-wave velocities of the same absolute value from this analysis.
The fluxes, for the Rusanov-type case, can be then determined by making use of the largest of the α_i eigenvalues from (3.15) as has been explained in Section 1.4.2. However the Godunov-type fluxes can only be built if also the eigenvectors are known. As this is a much more difficult computation than for the purely isotropic case, the Godunov flux computation will be treated in the following Section 3.3.1.

3.3.1   Elastic Anisotropic Godunov Flux

The Godunov flux has been thoroughly described in the first Chapter of this thesis and represents an exact flux type for hyperbolic systems, a flux that ensures the theoretical minimum viscosity, and therefore the highest resolution, using the matrix $|A|$ as the stabilizing term. The matrix $|A|$ decomposes the characteristic waves at an interface between two elements into outgoing and incoming waves and is given through

$$|A| = R\,|\Lambda|\,R^{-1} \,, \tag{3.16}$$

where the matrix $|\Lambda|$ is a diagonal matrix containing the absolute values of the eigenvalues of the Jacobian matrix A, which has to be oriented in the interface's normal direction. The columns of matrix R in equation (3.16) contain the right eigenvectors of A. Note, that both matrices, R and Λ, have to have the same ordering, i.e. the first eigenvector in the first column of R has to correspond to the

first eigenvalue of A appearing in the diagonal of Λ. It should be remarked, that the non-zero eigenvalues of A in the elastic and viscoelastic cases can be found by solving the cubic equation (3.15). In the following, a strictly descending order of the eigenvalues in Λ will be assumed.

Consider the 9 right eigenvectors $\vec{R}_i = (r_i^1, r_i^2, r_i^3, r_i^4, r_i^5, r_i^6, r_i^7, r_i^8, r_i^9)^T$, with $i = 1, ..., 9$, and the corresponding eigenvalues α_i, that form the eigenproblem $A\vec{R}_i = \alpha_i \vec{R}_i$. The eigendecomposition is then obtained by explicitly solving the 9 equations

$$
\begin{aligned}
c_{11}r_i^7 + c_{16}r_i^8 + c_{15}r_i^9 &= \alpha_i r_i^1 , \\
c_{12}r_i^7 + c_{26}r_i^8 + c_{25}r_i^9 &= \alpha_i r_i^2 , \\
c_{13}r_i^7 + c_{36}r_i^8 + c_{35}r_i^9 &= \alpha_i r_i^3 , \\
c_{16}r_i^7 + c_{66}r_i^8 + c_{56}r_i^9 &= \alpha_i r_i^4 , \\
c_{14}r_i^7 + c_{46}r_i^8 + c_{45}r_i^9 &= \alpha_i r_i^5 , \\
c_{15}r_i^7 + c_{56}r_i^8 + c_{55}r_i^9 &= \alpha_i r_i^6 , \\
\frac{r_i^1}{\rho} &= \alpha_i r_i^7 , \\
\frac{r_i^4}{\rho} &= \alpha_i r_i^8 , \\
\frac{r_i^6}{\rho} &= \alpha_i r_i^9 .
\end{aligned}
\tag{3.17}
$$

Due to the dependency of some equations, the solution of the equations in (3.17) can be obtained by solving the more compact homogeneous linear system

$$
\begin{pmatrix} X & c_{16} & c_{15} \\ c_{16} & Y & c_{56} \\ c_{15} & c_{56} & Z \end{pmatrix} \begin{pmatrix} r_i^7 \\ r_i^8 \\ r_i^9 \end{pmatrix} = \begin{pmatrix} 0 \\ 0 \\ 0 \end{pmatrix} ,
\tag{3.18}
$$

with $X = c_{11} - \alpha_i^2 \rho$, $Y = c_{66} - \alpha_i^2 \rho$ and $Z = c_{55} - \alpha_i^2 \rho$. Note that this represents the Kelvin-Christoffel equation for anisotropic media, which is also obtained from plane-wave analysis by Carcione [27]. However, this equation arises naturally through the eigendecomposition of the Jacobian A in the hyperbolic system (3.7). In addition, the solution of the linear system (3.17) for the values r_i^j, $i, j = 1, \ldots, 9$, completely defines the 9 right eigenvectors $\vec{R}_i$. The fact that the determinant of the matrix of the system in (3.18) is always zero is ensured by equation (3.15). Therefore, there will always be a non-trivial solution of (3.18). Having determined the values of r_i^7, r_i^8 and r_i^9 in (3.18), one can use equations (3.17) to obtain all other elements of the eigenvector $\vec{R}_i$. Finally, the explicit form of the

matrix of right eigenvectors is given as

$$
R = \begin{pmatrix}
r_1^1 & r_2^1 & r_3^1 & 0 & 0 & 0 & -r_3^1 & -r_2^1 & -r_1^1 \\
r_1^2 & r_2^2 & r_3^2 & 1 & 0 & 0 & -r_3^2 & -r_2^2 & -r_1^2 \\
r_1^3 & r_2^3 & r_3^3 & 0 & 1 & 0 & -r_3^3 & -r_2^3 & -r_1^3 \\
r_1^4 & r_2^4 & r_3^4 & 0 & 0 & 0 & -r_3^4 & -r_2^4 & -r_1^4 \\
r_1^5 & r_2^5 & r_3^5 & 0 & 0 & 1 & -r_3^5 & -r_2^5 & -r_1^5 \\
r_1^6 & r_2^6 & r_3^6 & 0 & 0 & 0 & -r_3^6 & -r_2^6 & -r_1^6 \\
r_1^7 & r_2^7 & r_3^7 & 0 & 0 & 0 & r_3^7 & r_2^7 & r_1^7 \\
r_1^8 & r_2^8 & r_3^8 & 0 & 0 & 0 & r_3^8 & r_2^8 & r_1^8 \\
r_1^9 & r_2^9 & r_3^9 & 0 & 0 & 0 & r_3^9 & r_2^9 & r_1^9
\end{pmatrix} . \tag{3.19}
$$

For the left eigenvectors $\vec{L}_i = (l_i^1, l_i^2, l_i^3, l_i^4, l_i^5, l_i^6, l_i^7, l_i^8, l_i^9)$, the eigenproblem reads as $\vec{L}_i A = \alpha_i \vec{L}_i$ and the eigendecomposition leads to the 9 equations

$$
\begin{aligned}
c_{11}l_i^1 + c_{16}l_i^4 + c_{15}l_i^6 &= \alpha_i l_i^7 , \\
c_{16}l_i^1 + c_{66}l_i^4 + c_{56}l_i^6 &= \alpha_i l_i^8 , \\
c_{15}l_i^1 + c_{56}l_i^4 + c_{55}l_i^6 &= \alpha_i l_i^9 , \\
l_i^2 &= 0 , \\
l_i^3 &= 0 , \\
l_i^5 &= 0 , \\
\frac{l_i^7}{\rho} &= \alpha_i l_i^1 , \\
\frac{l_i^8}{\rho} &= \alpha_i l_i^4 , \\
\frac{l_i^9}{\rho} &= \alpha_i l_i^6 ,
\end{aligned} \tag{3.20}
$$

which similarly to the case of the right eigenvectors lead to the more compact homogeneous system

$$
\begin{pmatrix}
X & c_{16} & c_{15} \\
c_{16} & Y & c_{56} \\
c_{15} & c_{56} & Z
\end{pmatrix}
\begin{pmatrix}
l_i^1 \\
l_i^4 \\
l_i^6
\end{pmatrix}
=
\begin{pmatrix}
0 \\
0 \\
0
\end{pmatrix} . \tag{3.21}
$$

A symmetry between the left and right eigenvectors can be observed, namely $r_i^1 = l_i^7$, $r_i^4 = l_i^8$, $r_i^6 = l_i^9$, $r_i^7 = l_i^1$, $r_i^8 = l_i^4$ and $r_i^9 = l_i^6$. This allows us to find the left eigenvectors of A. Furthermore, to avoid scaling problems, it is convenient that the left eigenvectors fulfil the condition $L = R^{-1}$, which is obtained by using the normalization

$$
\left(\frac{\vec{L}_i}{2\alpha_i S_i} \right) \vec{R}_i = 1 . \tag{3.22}
$$

From equation (3.22) one can conclude, that $S_i = \rho \left[(r_i^7)^2 + (r_i^8)^2 + (r_i^9)^2 \right]$. Then the matrix $L = R^{-1}$ of left eigenvectors can be finally written down, which

depends exclusively on the components of the right eigenvectors, in the form

$$
L = \begin{pmatrix}
\frac{r_1^7}{2\alpha_1 S_1} & 0 & 0 & \frac{r_1^8}{2\alpha_1 S_1} & 0 & \frac{r_1^9}{2\alpha_1 S_1} & \frac{r_1^1}{2\alpha_1 S_1} & \frac{r_1^4}{2\alpha_1 S_1} & \frac{r_1^6}{2\alpha_1 S_1} \\
\frac{r_2^7}{2\alpha_2 S_2} & 0 & 0 & \frac{r_2^8}{2\alpha_2 S_2} & 0 & \frac{r_2^9}{2\alpha_2 S_2} & \frac{r_2^1}{2\alpha_2 S_2} & \frac{r_2^4}{2\alpha_2 S_2} & \frac{r_2^6}{2\alpha_2 S_2} \\
\frac{r_3^7}{2\alpha_3 S_3} & 0 & 0 & \frac{r_3^8}{2\alpha_3 S_3} & 0 & \frac{r_3^9}{2\alpha_3 S_3} & \frac{r_3^1}{2\alpha_3 S_3} & \frac{r_3^4}{2\alpha_3 S_3} & \frac{r_3^6}{2\alpha_3 S_3} \\
0 & 1 & 0 & 0 & 0 & 0 & 0 & 0 & 0 \\
0 & 0 & 1 & 0 & 0 & 0 & 0 & 0 & 0 \\
0 & 0 & 0 & 0 & 1 & 0 & 0 & 0 & 0 \\
-\frac{r_3^7}{2\alpha_3 S_3} & 0 & 0 & -\frac{r_3^8}{2\alpha_3 S_3} & 0 & -\frac{r_3^9}{2\alpha_3 S_3} & \frac{r_3^1}{2\alpha_3 S_3} & \frac{r_3^4}{2\alpha_3 S_3} & \frac{r_3^6}{2\alpha_3 S_3} \\
-\frac{r_2^7}{2\alpha_2 S_2} & 0 & 0 & -\frac{r_2^8}{2\alpha_2 S_2} & 0 & -\frac{r_2^9}{2\alpha_2 S_2} & \frac{r_2^1}{2\alpha_2 S_2} & \frac{r_2^4}{2\alpha_2 S_2} & \frac{r_2^6}{2\alpha_2 S_2} \\
-\frac{r_1^7}{2\alpha_1 S_1} & 0 & 0 & -\frac{r_1^8}{2\alpha_1 S_1} & 0 & -\frac{r_1^9}{2\alpha_1 S_1} & \frac{r_1^1}{2\alpha_1 S_1} & \frac{r_1^4}{2\alpha_1 S_1} & \frac{r_1^6}{2\alpha_1 S_1}
\end{pmatrix} . \tag{3.23}
$$

Using equation (3.16) and substituting $\bar{r}_j^i = \frac{r_j^i}{\sqrt{S_i}}$ one gets the final expression of $|A|$ as

$$
|A| = \sum_{i=1}^{3} \begin{pmatrix}
\bar{r}_i^1 \bar{r}_i^7 & 0 & 0 & \bar{r}_i^1 \bar{r}_i^8 & 0 & \bar{r}_i^1 \bar{r}_i^9 & 0 & 0 & 0 \\
\bar{r}_i^2 \bar{r}_i^7 & 0 & 0 & \bar{r}_i^2 \bar{r}_i^8 & 0 & \bar{r}_i^2 \bar{r}_i^9 & 0 & 0 & 0 \\
\bar{r}_i^3 \bar{r}_i^7 & 0 & 0 & \bar{r}_i^3 \bar{r}_i^8 & 0 & \bar{r}_i^3 \bar{r}_i^9 & 0 & 0 & 0 \\
\bar{r}_i^4 \bar{r}_i^7 & 0 & 0 & \bar{r}_i^4 \bar{r}_i^8 & 0 & \bar{r}_i^4 \bar{r}_i^9 & 0 & 0 & 0 \\
\bar{r}_i^5 \bar{r}_i^7 & 0 & 0 & \bar{r}_i^5 \bar{r}_i^8 & 0 & \bar{r}_i^5 \bar{r}_i^9 & 0 & 0 & 0 \\
\bar{r}_i^6 \bar{r}_i^7 & 0 & 0 & \bar{r}_i^6 \bar{r}_i^8 & 0 & \bar{r}_i^6 \bar{r}_i^9 & 0 & 0 & 0 \\
0 & 0 & 0 & 0 & 0 & 0 & \bar{r}_i^1 \bar{r}_i^7 & \bar{r}_i^1 \bar{r}_i^8 & \bar{r}_i^1 \bar{r}_i^9 \\
0 & 0 & 0 & 0 & 0 & 0 & \bar{r}_i^4 \bar{r}_i^7 & \bar{r}_i^4 \bar{r}_i^8 & \bar{r}_i^4 \bar{r}_i^9 \\
0 & 0 & 0 & 0 & 0 & 0 & \bar{r}_i^6 \bar{r}_i^7 & \bar{r}_i^6 \bar{r}_i^8 & \bar{r}_i^6 \bar{r}_i^9
\end{pmatrix} . \tag{3.24}
$$

Note, that only the 3 positive eigenvalues of the Jacobian matrix A need to be known in order to compute all entries of the matrix in (3.24) by solving (3.18) and using (3.17) and (3.22). Furthermore, note that the computation of $|A|$ only depends on the material properties and therefore has to be computed only once for each tetrahedral element as long as the material does not change with time.
Note that the isotropic case can be recovered by setting $(r_1^7, r_1^8, r_1^9) = (1, 0, 0)$, $(r_2^7, r_2^8, r_2^9) = (0, 1, 0)$ and $(r_3^7, r_3^8, r_3^9) = (0, 0, 1)$.

3.4 The Numerical Scheme

The numerical scheme produced by (3.7) is very similar to the elastic ADER-DG scheme (1.66). Just the final form of the fully discrete ADER-DG scheme will be reformulated, which after transformation into the canonical reference element $\mathcal{T}_E$

and time integration over one time step Δt from time level n to $n + 1$ reads as

$$
\left[\left(\hat{Q}_{pl}^{(m)} \right)^{n+1} - \left(\hat{Q}_{pl}^{(m)} \right)^{n} \right] |J|\, M_{kl} \quad +
$$

$$
+ \quad \frac{1}{2} \sum_{j=1}^{4} \left(T_{pq}^{j} \widetilde{A}_{qr}^{(m)} (T_{rs}^{j})^{-1} + \Theta_{ps}^{j,(m)} \right) |S_j|\, F_{kl}^{-,j} \cdot I_{qlmn}(\Delta t) \left(\hat{Q}_{mn}^{(m)} \right)^{n} +
$$

$$
+ \quad \frac{1}{2} \sum_{j=1}^{4} \left(T_{pq}^{j} \widetilde{A}_{qr}^{(m)} (T_{rs}^{j})^{-1} - \Theta_{ps}^{j,(m)} \right) |S_j|\, F_{kl}^{+,j,i,h} \cdot I_{qlmn}(\Delta t) \left(\hat{Q}_{mn}^{(m_j)} \right)^{n} - \quad {}^{(3.25)}
$$

$$
- \quad A_{pq}^{*} |J|\, K_{kl}^{\xi} \cdot I_{qlmn}(\Delta t) \left(\hat{Q}_{mn}^{(m)} \right)^{n} - B_{pq}^{*} |J|\, K_{kl}^{\eta} \cdot I_{qlmn}(\Delta t) \left(\hat{Q}_{mn}^{(m)} \right)^{n} -
$$

$$
- \quad C_{pq}^{*} |J|\, K_{kl}^{\zeta} \cdot I_{qlmn}(\Delta t) \left(\hat{Q}_{mn}^{(m)} \right)^{n} = 0 \,.
$$

Here the matrix $\widetilde{A}^{(m)}$ has the same structure as the matrix A in (3.9), but with the entries c_{ij} rotated from the global reference coordinate system to the local coordinate system of the j-th face of tetrahedron (m) using (3.14). The tensor $I_{plqm}(\Delta t)$ represents the high-order ADER time integration operator that is applied to the degrees of freedom $\left(\hat{Q}_{mn}^{(m)} \right)^{n}$ at time level n. The matrices M_{kl}, F_{kl} and K_{kl} are the mass, flux and stiffness matrices, respectively, and include space integrations of the basis functions that can be computed beforehand as shown in detail Chapter 1. A_{pq}^{*}, B_{pq}^{*} and C_{pq}^{*} are the Jacobian matrices transformed into the reference tetrahedron $\mathcal{T}_E$. Notice, that $\Theta_{ps}^{j,(m)}$ now includes a j dependence as the wave velocities will vary depending on the propagation direction for anisotropic media. Furthermore, $|J|$ is the determinant of the Jacobian matrix of this transformation, and $|S_j|$ denotes the area of the j-th face of tetrahedron $\mathcal{T}^{(m)}$. The symbol $|S_j|$ refers to the surface of the tetrahedrons face j and should not be confused with the normalization coefficient S_i introduced in last Chapter.

The resulting ADER-DG scheme keeps the high-order approximation in space and time for anisotropic material using the proposed numerical fluxes and allows us to update the values of the unknown variables from a time level n to $n + 1$. Here, we will treat the fully triclinic symmetry because, even if the modelled materials could exhibit some symmetries, the element interfaces are in general arbitrarily oriented within an unstructured tetrahedral mesh. It is also worth mentioning that treating anisotropy with the ADER-DG scheme doesn't pose a significant increase in terms of computational costs, even while treating the triclinic case, with respect to the isotropic case.

3.5   Viscoelastic Anisotropy

Anisotropy plays an important role as secondary effect in seismic wave propagation modeling. However, in realistic applications viscoelastic attenuation ad-

ditionally affects the wave forms, which makes the incorporation of both effects inevitable. In order to accurately couple both effects within the ADER-DG framework, the concepts of mean and deviatoric stresses [23] are used and combined with the rheological model of the Generalized Maxwell Body, see [63], as shown in Section 2.3.1.

Introducing viscoelasticity in seismic wave propagation problems leads to a substitution of Hooke's tensor by a new tensor, whose entries are frequency-dependent as was shown in (2.13). In the time domain the constitutive relation (3.2) then includes the matrix M_{ij} depending on time resulting in convolution products. The time dependence of M_{ij} can be expressed by a linear combination of viscoelastic mechanisms, representing combinations of fictitious springs and dashpots that reproduce the physical behaviour of a viscoelastic material in a selected frequency range. The problem of computing the expensive convolution products can be avoided by defining a set of anelastic variables [101].

The mean stress $\overline{\sigma}$ and mean strain $\overline{\varepsilon}$, as well as the deviatoric stress $\vec{\sigma}^D$ and deviatoric strain $\vec{\varepsilon}^D$ are defined as

$$\overline{\sigma} \equiv \frac{1}{3}\left(\sigma_{xx} + \sigma_{yy} + \sigma_{zz}\right), \tag{3.26}$$

$$\overline{\varepsilon} \equiv \frac{1}{3}\left(\varepsilon_{xx} + \varepsilon_{yy} + \varepsilon_{zz}\right), \tag{3.27}$$

$$\vec{\sigma}^D \equiv \vec{\sigma} - \overline{\sigma}, \tag{3.28}$$

$$\vec{\varepsilon}^D \equiv \vec{\varepsilon} - \overline{\varepsilon}, \tag{3.29}$$

where it should be remarked that the mean stress and strain are both invariant under coordinate transformation. As shown by Carcione [27] one needs a total of four attenuation moduli to model viscoelastic attenuation in an anisotropic medium: one purely dilatational modulus and three shear moduli. Those are associated to the four possible viscoelastic modes allowed in anisotropic media, which will be referred to as modes $k = 1$ (dilatational) and $k = 2, 3, 4$ (shear). It can be shown that the mean stress $\overline{\sigma}$ depends only on the dilatational modulus while the deviatoric stress $\vec{\sigma}^D$ only depends on the shear moduli. The stress-strain relation can either be expressed in the frequency or in the time domain [101] for the isotropic case, which in the anisotropic case [23] read as

$$\vec{\sigma}_i(\omega) = M_{ij}(\omega)\vec{\varepsilon}_j(\omega), \tag{3.30}$$

$$\vec{\sigma}_i(t) = \frac{\partial}{\partial t}\left(\mathbf{\Psi}_{ij}(t)\right) * \vec{\varepsilon}_j(t) = M_{ij}(t) * \vec{\varepsilon}_j(t), \tag{3.31}$$

where $*$ denotes the convolution operator and the *relaxation matrix* $\mathbf{\Psi}_{ij}(t)$ is given by

$$
\mathbf{\Psi}_{ij}(t) = \begin{pmatrix}
\Psi_{11} & \Psi_{12} & \Psi_{13} & 2c_{14} & 2c_{15} & 2c_{16} \\
\Psi_{12} & \Psi_{22} & \Psi_{23} & 2c_{24} & 2c_{25} & 2c_{26} \\
\Psi_{13} & \Psi_{23} & \Psi_{33} & 2c_{34} & 2c_{35} & 2c_{36} \\
c_{14} & c_{24} & c_{34} & 2\Psi_{44} & 2c_{45} & 2c_{46} \\
c_{15} & c_{25} & c_{35} & 2c_{45} & 2\Psi_{55} & 2c_{56} \\
c_{16} & c_{26} & c_{36} & 2c_{46} & 2c_{56} & 2\Psi_{66}
\end{pmatrix} \cdot H(t) .
\tag{3.32}
$$

Here, $H(t)$ is the Heaviside step function and the components $\Psi_{ij}(t)$ can be expressed as

$$
\Psi_{ij}(t) = \sum_{k=0}^{4} g_{ij}^{(k)} \chi^{(k)}(t) \qquad \text{with} \qquad g_{ij}^{(k)} \in \mathbb{R} .
\tag{3.33}
$$

The real numbers $g_{ij}^{(k)}$ are combinations of the entries c_{ij} of the elastic Hooke's tensor and the *relaxation functions* $\chi^{(k)}$ contain the time functionality of the relaxation matrix's entries. These are normalized such that $\chi^{(k)} = 1$ for $t = 0$ and by imposing that the mode's complex modulus, defined as $M^{(k)}(t) = d(\chi^{(k)}(t)H(t))/dt$, behaves in the frequency domain as $M^{(k)}(\omega) \to 1$ for $\omega \to \infty$. A formulation of the normalized Generalized Maxwell Body relaxation mechanisms [101] can be used to express the $\chi^{(k)}(t)$ as

$$
\begin{aligned}
\chi^{(k)}(t) &= 1 - \sum_{\ell=1}^{n} Y_{\ell}^{(k)} \left(1 - e^{-\omega_\ell t}\right), & \text{for} \quad k &= 1, 2, 3, 4 \\
\chi^{(k)}(t) &= 1, & \text{for} \quad k &= 0
\end{aligned}
\tag{3.34}
$$

where n is the number of attenuating mechanisms used. The $Y_{\ell}^{(k)}$ are the anelastic coefficients of each mechanism for the mode k which are related to the strength of the attenuation. A general theory on viscoelasticity for anisotropic media leads to the possibility of having anisotropy in the attenuating parameters themselves [27]. This means having different attenuation values for different propagation directions. However, the knowledge of the quality factors $\mathcal{Q}$ inside the Earth is often poor and rarely would allow us to consider any dependence of the $\mathcal{Q}$-factors on direction. Therefore, in the following the attenuation will be considered as an isotropic effect, even if the medium is elastically anisotropic. As a consequence only one single $\mathcal{Q}^P$ and $\mathcal{Q}^S$ value are allowed. Thus, one can use only a bulk and a shear attenuating modes by defining

$$
\begin{aligned}
\chi^{(\mathcal{K})} &= \chi^{(1)}, \\
\chi^{(\mu)} &= \chi^{(2)} = \chi^{(3)} = \chi^{(4)}
\end{aligned}
\tag{3.35}
$$

Finally the ω_ℓ are the relaxation frequencies of each mechanism, which in the following will be assumed to be the same for all the viscoelastic modes.

The coefficients $g_{ij}^{(k)}$ in (3.33) that ensure the separation of the dilatational and shear modes of the attenuation [27] are

$$
\begin{aligned}
\Psi_{ii}(t) &= c_{ii} - \left(\overline{\lambda} + 2\overline{\mu}\right) + \left(\overline{\lambda} + \tfrac{4}{3}\overline{\mu}\right)\chi^{(\mathcal{K})}(t) + \left(\tfrac{2}{3}\overline{\mu}\right)\chi^{(\mu)}(t)\,, \\
\Psi_{ij}(t) &= c_{ij} - \overline{\lambda} + \left(\overline{\lambda} + \tfrac{2}{3}\overline{\mu}\right)\chi^{(\mathcal{K})}(t) - \tfrac{2}{3}\overline{\mu}\chi^{(\mu)}(t)\,, \\
\Psi_{44}(t) &= c_{44}\chi^{(\mu)}(t)\,, \\
\Psi_{55}(t) &= c_{55}\chi^{(\mu)}(t)\,, \\
\Psi_{66}(t) &= c_{66}\chi^{(\mu)}(t)\,,
\end{aligned}
\tag{3.36}
$$

where $i, j \leq 3$ and $i \neq j$. In addition, the following definitions of the average Lamé constants have been used

$$
\overline{\mu} \equiv \frac{1}{3}\left(c_{44} + c_{55} + c_{66}\right)\,,
\tag{3.37}
$$

$$
\overline{\lambda} \equiv \frac{1}{3}\left(c_{11} + c_{22} + c_{33}\right) - 2\overline{\mu}\,.
\tag{3.38}
$$

Now one can use the anelastic coefficients Y_ℓ^λ computed from

$$
Y_\ell^\lambda = \frac{\overline{\lambda} + 2/3\overline{\mu}}{\overline{\lambda}}Y_\ell^{\mathcal{K}} - \frac{2/3\overline{\mu}}{\overline{\lambda}}Y_\ell^\mu\,,
\tag{3.39}
$$

to obtain the viscoelastic stress-strain relation of the form

$$
\begin{pmatrix} \sigma_{xx} \\ \sigma_{yy} \\ \sigma_{zz} \\ \sigma_{yz} \\ \sigma_{xz} \\ \sigma_{xy} \end{pmatrix} =
\begin{pmatrix}
c_{11} & c_{12} & c_{13} & 2c_{14} & 2c_{15} & 2c_{16} \\
c_{12} & c_{22} & c_{23} & 2c_{24} & 2c_{25} & 2c_{26} \\
c_{13} & c_{23} & c_{33} & 2c_{34} & 2c_{35} & 2c_{36} \\
c_{14} & c_{24} & c_{34} & 2c_{44} & 2c_{45} & 2c_{46} \\
c_{15} & c_{25} & c_{35} & 2c_{45} & 2c_{55} & 2c_{56} \\
c_{16} & c_{26} & c_{36} & 2c_{46} & 2c_{56} & 2c_{66}
\end{pmatrix}
\begin{pmatrix} \varepsilon_{xx} \\ \varepsilon_{yy} \\ \varepsilon_{zz} \\ \varepsilon_{yz} \\ \varepsilon_{xz} \\ \varepsilon_{xy} \end{pmatrix} -
$$

$$
- \sum_{\ell=1}^{n}
\begin{pmatrix}
\overline{P}Y_\ell^P & \overline{\lambda}Y_\ell^\lambda & \overline{\lambda}Y_\ell^\lambda & 0 & 0 & 0 \\
\overline{\lambda}Y_\ell^\lambda & \overline{P}Y_\ell^P & \overline{\lambda}Y_\ell^\lambda & 0 & 0 & 0 \\
\overline{\lambda}Y_\ell^\lambda & \overline{\lambda}Y_\ell^\lambda & \overline{P}Y_\ell^P & 0 & 0 & 0 \\
0 & 0 & 0 & 2c_{44}Y_\ell^\mu & 0 & 0 \\
0 & 0 & 0 & 0 & 2c_{55}Y_\ell^\mu & 0 \\
0 & 0 & 0 & 0 & 0 & 2c_{66}Y_\ell^\mu
\end{pmatrix}
\begin{pmatrix} \vartheta_{xx}^\ell \\ \vartheta_{yy}^\ell \\ \vartheta_{zz}^\ell \\ \vartheta_{yz}^\ell \\ \vartheta_{xz}^\ell \\ \vartheta_{xy}^\ell \end{pmatrix}
\tag{3.40}
$$

where $\overline{P}Y_\ell^P \equiv \overline{\lambda}Y_\ell^\lambda + 2\overline{\mu}$ and n is the total number of attenuation mechanisms. The anelastic functions $\vec{\vartheta^\ell} = (\vartheta_{xx}^\ell, \vartheta_{yy}^\ell, \vartheta_{zz}^\ell, \vartheta_{yz}^\ell, \vartheta_{xz}^\ell, \vartheta_{xy}^\ell)^T$ are defined by

$$
\vartheta_j^\ell(t) = \omega_\ell \frac{\partial}{\partial t}\left(\int_{-\infty}^{t} \varepsilon_j(\tau)e^{-\omega_\ell(t-\tau)}\,d\tau\right),
\tag{3.41}
$$

if using the rheological model of the Generalized Maxwell Body [63, 101]. The anelastic coefficients $Y_\ell^{(k)}$ relate to the strength of the attenuation and have to be fitted to the desired $\mathcal{Q}$-law over a certain frequency range. Therefore, a number of relaxation frequencies ω_ℓ is used as already described in more detail in the previous Chapter.

Note, that the anisotropic elastic case can be inferred from the stress-strain relation (3.40) by setting $Y_\ell^\lambda = 0$ and $Y_\ell^\mu = 0$, thus recovering (3.3). The viscoelastic isotropic case is obtained by setting $c_{11} = c_{22} = c_{33} = \lambda + 2\mu$, $c_{12} = c_{13} = c_{23} = \lambda$ and $c_{44} = c_{55} = c_{66} = \mu$ with all other coefficients c_{ij} equal to zero. This way, is also obtained $\overline{\lambda} = \lambda$ and $\overline{\mu} = \mu$ from (3.37) and (3.38) as a consequence.

In three space dimensions the use of the anelastic functions ϑ_j^ℓ requires the storage of 6 new variables per attenuation mechanism, one for each stress component as shown in (3.40), that have to be updated at every time step. This is accomplished by solving an additional set of $6n$ linear partial differential equations given by

$$\frac{\partial}{\partial t}\vartheta_j^\ell(t) + \omega_\ell \vartheta_j^\ell(t) = \omega_\ell \frac{\partial}{\partial t}\varepsilon_j(t)\,, \tag{3.42}$$

where $j = 1,...,6$. It is worth noticing that the usage of GMB mechanisms in the form shown in [86] for the viscoelastic anisotropy creates a set of anelastic variables which are independent of the local material properties. Therefore, those anelastic variables are also independent of the attenuating modes, bulk and shear, unlike the analogous result obtained in [27] with a GZB rheology type. A brief description of the resulting coupled linear system of equations is given in the following Section 3.5.2.

3.5.1   Viscoelastic Anisotropic Godunov Flux

The anelastic part of $|A|$ can be found by a similar procedure as described in Section 3.3.1. Let's consider the more general case of viscoelastic material, in which n attenuating mechanisms are used to describe the viscoelastic properties of a material. For each attenuating mechanism 6 new eigenvectors and eigenvalues are introduced, as shown in Chapter 2. However, these new eigenvalues have value zero. Following the convention of decreasing ordering, the eigenvalues are now given through $\alpha_1 = -\alpha_{9+6n}$, $\alpha_2 = -\alpha_{8+6n}$, $\alpha_3 = -\alpha_{7+6n}$ and $\alpha_i = 0$ for $i = 4,\ldots,6+6n$. The right and left eigenvectors now have the shape

$$
\begin{aligned}
\vec{R}_i &= \left(\vec{R}_i^{\text{el}}, \frac{\omega_1 \bar{r}_i^7}{\alpha_i}, 0, 0, \frac{\omega_1 \bar{r}_i^8}{2\alpha_i}, 0, \frac{\omega_1 \bar{r}_i^9}{2\alpha_i}, \ldots, \frac{\omega_n \bar{r}_i^7}{\alpha_i}, 0, 0, \frac{\omega_n \bar{r}_i^8}{2\alpha_i}, 0, \frac{\omega_n \bar{r}_i^9}{2\alpha_i}\right)^T, \\
\vec{L}_i &= \left(\vec{L}_i^{\text{el}}, 0, 0, 0, 0, 0, 0, \ldots, 0, 0, 0, 0, 0, 0\right),
\end{aligned}
\tag{3.43}
$$

with $\vec{R}_i^{\mathrm{el}} = (\bar{r}_i^1, \bar{r}_i^2, \bar{r}_i^3, \bar{r}_i^4, \bar{r}_i^5, \bar{r}_i^6, \bar{r}_i^7, \bar{r}_i^8, \bar{r}_i^9)$ and $\vec{L}_i^{\mathrm{el}} = (\bar{r}_i^7, 0, 0, \bar{r}_i^8, 0, \bar{r}_i^9, \bar{r}_i^1, \bar{r}_i^4, \bar{r}_i^6)$ being the elastic right and left eigenvectors. The expression (3.43) gives us the possibility of constructing the blocks of the matrix $|A|$ for the anelastic case. The block structure is equivalent to the one given in Chapter 2, and is given as

$$|\check{A}| = \begin{bmatrix} |A| & 0 \\ A^{\|} & 0 \end{bmatrix} \in \mathbb{R}^{n_v \times n_v}, \qquad A^{\|} = \begin{bmatrix} A_1^{\|} \\ \vdots \\ A_n^{\|} \end{bmatrix} \in \mathbb{R}^{6n \times 9}, \qquad (3.44)$$

where $|A| \in \mathbb{R}^{9 \times 9}$ is the matrix of the purely anisotropic elastic part as given in (3.24) and the matrix $|A_a|$ includes the block structured anelastic part where each sub-matrix $A_\ell^{\|} \in \mathbb{R}^{6 \times 9}$, with $\ell = 1, ..., n$, contains the relaxation frequency ω_ℓ of the ℓ-th attenuation mechanism in the form

$$A_\ell^{\|} = \omega_\ell \sum_{i=1}^{3} \begin{pmatrix} \frac{\bar{r}_i^7 \bar{r}_i^7}{\alpha_i} & 0 & 0 & \frac{\bar{r}_i^7 \bar{r}_i^8}{\alpha_i} & 0 & \frac{\bar{r}_i^7 \bar{r}_i^9}{\alpha_i} & 0 & 0 & 0 \\ 0 & 0 & 0 & 0 & 0 & 0 & 0 & 0 & 0 \\ 0 & 0 & 0 & 0 & 0 & 0 & 0 & 0 & 0 \\ \frac{\bar{r}_i^7 \bar{r}_i^8}{2\alpha_i} & 0 & 0 & \frac{\bar{r}_i^8 \bar{r}_i^8}{2\alpha_i} & 0 & \frac{\bar{r}_i^8 \bar{r}_i^9}{2\alpha_i} & 0 & 0 & 0 \\ 0 & 0 & 0 & 0 & 0 & 0 & 0 & 0 & 0 \\ \frac{\bar{r}_i^7 \bar{r}_i^9}{2\alpha_i} & 0 & 0 & \frac{\bar{r}_i^8 \bar{r}_i^9}{2\alpha_i} & 0 & \frac{\bar{r}_i^9 \bar{r}_i^9}{2\alpha_i} & 0 & 0 & 0 \end{pmatrix}, \qquad (3.45)$$

Note that, again, the isotropic case can be recovered by setting $(r_1^7, r_1^8, r_1^9) = (1, 0, 0)$, $(r_2^7, r_2^8, r_2^9) = (0, 1, 0)$ and $(r_3^7, r_3^8, r_3^9) = (0, 0, 1)$.

3.5.2 The Coupled Equation System

The new enlarged system of $n_v = 9 + 6n$ partial differential equations including 9 elastic and $6n$ anelastic variables can be written in the compact form

$$\frac{\partial Q_p}{\partial t} + \check{A}_{pq} \frac{\partial Q_q}{\partial x} + \check{B}_{pq} \frac{\partial Q_q}{\partial y} + \check{C}_{pq} \frac{\partial Q_q}{\partial z} = \check{E}_{pq} Q_q \,, \qquad (3.46)$$

where E denotes the so-called *reaction term* and takes into account the energy losses introduced by the viscoelastic medium. Note that the dimensions of the variable vector Q, the Jacobian matrices $\check{A}$, $\check{B}$, $\check{C}$ and the source matrix $\check{E}$ now depend on the number n of attenuation mechanisms. The Jacobians have exactly the same shape and block-matrix structure as shown in Chapter 2 with the exception that the upper leftmost 9x9 blocks are now the corresponding anisotropic Jacobians defined in (3.9 - 3.11). The matrix $\check{E}$ in (3.46) representing the reactive source term that couples the anelastic functions to the original elastic system can be decomposed as

$$\check{E} = \begin{bmatrix} 0 & E \\ 0 & E' \end{bmatrix} \in \mathbb{R}^{n_v \times n_v}, \qquad (3.47)$$

with E exhibiting the block-matrix structure

$$E = [E_1, \ldots, E_n] \in \mathbb{R}^{9 \times 6n}. \tag{3.48}$$

Here, each matrix $E_\ell \in \mathbb{R}^{9 \times 6}$, with $\ell = 1, ..., n$, contains the anelastic coefficients Y_ℓ^λ and Y_ℓ^μ of the ℓ-th mechanism in the form:

$$E_\ell = \begin{pmatrix} \overline{P}Y_\ell^P & \overline{\lambda}Y_\ell^\lambda & \overline{\lambda}Y_\ell^\lambda & 0 & 0 & 0 \\ \overline{\lambda}Y_\ell^\lambda & \overline{P}Y_\ell^P & \lambda Y_\ell^\lambda & 0 & 0 & 0 \\ \overline{\lambda}Y_\ell^\lambda & \overline{\lambda}Y_\ell^\lambda & \overline{P}Y_\ell^P & 0 & 0 & 0 \\ 0 & 0 & 0 & 2c_{66}Y_\ell^\mu & 0 & 0 \\ 0 & 0 & 0 & 0 & 2c_{44}Y_\ell^\mu & 0 \\ 0 & 0 & 0 & 0 & 0 & 2c_{55}Y_\ell^\mu \\ 0 & 0 & 0 & 0 & 0 & 0 \\ 0 & 0 & 0 & 0 & 0 & 0 \\ 0 & 0 & 0 & 0 & 0 & 0 \end{pmatrix}. \tag{3.49}$$

Note, that the different ordering of the entries with respect to (3.40) is a consequence of the different order of the anelastic variables inside the variable vector Q. The matrix E' in (3.47) is again identical to that defined in Chapter 2.

The discrete formulation of the ADER-DG scheme for anisotropic elastic media as given in (3.25) is now written as

$$\left[\left(\hat{Q}_{pl}^{(m)} \right)^{n+1} - \left(\hat{Q}_{pl}^{(m)} \right)^n \right] |J| \, M_{kl} \quad +$$

$$+ \quad \frac{1}{2} \sum_{j=1}^{4} \left(\check{T}_{pr}^j \widetilde{\check{A}}_{rs}^{(m)} (\check{T}_{sq}^j)^{-1} + \Theta_{pq}^{j,(m)} \right) |S_j| \, F_{kl}^{-,j} \cdot I_{qlmn}(\Delta t) \left(\hat{Q}_{mn}^{(m)} \right)^n +$$

$$+ \quad \frac{1}{2} \sum_{j=1}^{4} \left(\check{T}_{pr}^j \widetilde{\check{A}}_{rs}^{(m)} (\check{T}_{sq}^j)^{-1} - \Theta_{pq}^{j,(m)} \right) |S_j| \, F_{kl}^{+,j,i,h} \cdot I_{qlmn}(\Delta t) \left(\hat{Q}_{mn}^{(m_j)} \right)^n \quad (3.50)$$

$$- \quad \check{A}_{pq}^* |J| \, K_{kl}^\xi \cdot I_{qlmn}(\Delta t) \left(\hat{Q}_{mn}^{(m)} \right)^n - \check{B}_{pq}^* |J| \, K_{kl}^\eta \cdot I_{qlmn}(\Delta t) \left(\hat{Q}_{mn}^{(m)} \right)^n -$$

$$- \quad \check{C}_{pq}^* |J| \, K_{kl}^\zeta \cdot I_{qlmn}(\Delta t) \left(\hat{Q}_{mn}^{(m)} \right)^n = |J| \, \check{E}_{pq} \cdot I_{qlmn}(\Delta t) \left(\hat{Q}_{mn}^{(m)} \right)^n M_{kl},$$

where Θ_{ps} is specified by the particular numerical flux in (1.21) or (1.22). The matrix $\widetilde{\check{A}}_{rs}^{(m)}$ now represents the enlarged matrix given in (3.46) with the entries of (3.9) rotated through the Bond's transformation (3.14) as discussed in Section 3.4. Furthermore, the reactive source term E_{pq} appears on the right hand side introduced by the viscoelastic medium. Additionally, the α_i non-zero eigenvalues of the enlarged Jacobian matrices remain the same in the viscoelastic case, as the enlargement of these matrices introduces only new eigenvalues equal to zero. All other matrices in the scheme (3.50) are identical to those described previously in Chapter 2.

Table 3.1: Coefficients for the anisotropic, orthorhombic material given in $[N \cdot m^{-2}]$ as used in the convergence study. All other coefficients are zero. The material density ρ is given in $kg \cdot m^{-3}$.

ρ	c_{11}	c_{12}	c_{13}	c_{22}	c_{23}	c_{33}	c_{44}	c_{55}	c_{66}
1	192	66	60	160	56	272	60	62	49

3.6 Convergence Study

In this section we present a numerical convergence study of the proposed ADER-DG approach on tetrahedral meshes, in order to demonstrate its arbitrarily high-order of convergence in the presence of anisotropic material. The procedure is very similar to that used previously in Section 2.7. Here we show results from second- to seventh-order ADER-DG schemes denoted by ADER-DG $\mathcal{O}2$ to ADER-DG $\mathcal{O}7$, respectively. It will be shown that the same order for space and time accuracy is obtained automatically.

Similar to Section 2.7, the convergence orders can be determined by solving the three-dimensional, anisotropic, seismic wave equations on the unit-cube, i.e. on a computational domain $\Omega = [-1, 1] \times [-1, 1] \times [-1, 1] \in \mathbb{R}^3$ with periodic boundary conditions.

The homogeneous anisotropic material parameters are given in Table 3.1 and represent an anisotropic (orthorhombic) material, similar in its anisotropic properties to olivine as given in [38]. To confirm that anisotropy is treated correctly, three plane waves $Q_p^{(l)}$, $l = 1, ..., 3$ are superimposed. Those have the form given in (2.55) traveling perpendicular to each other along the coordinate axes, i.e. the three wave number vectors are

$$\vec{k}^{(1)} = (k_x^{(1)}, k_y^{(1)}, k_z^{(1)})^T = (\pi, 0, 0)^T, \tag{3.51}$$

$$\vec{k}^{(2)} = (k_x^{(2)}, k_y^{(2)}, k_z^{(2)})^T = (0, \pi, 0)^T, \tag{3.52}$$

$$\vec{k}^{(3)} = (k_x^{(3)}, k_y^{(3)}, k_z^{(3)})^T = (0, 0, \pi)^T. \tag{3.53}$$

leading to periodic, sinusoidal waves in the unit-cube.

In the convergence test, three superimposed plane qP-waves traveling perpendicular to each other are used. However, the symmetry axes of the anisotropic, orthorhombic material is tilted with respect to the coordinate system, i.e. the symmetry axes point into the directions $(1, 1, 1)$,$(-1, 1, 0)$ and $(-1, -1, 2)$, respectively. The initial condition at $t = 0$ is given by (2.58) using the combination of three right eigenvectors $R_{p1}^{(1)}$, $R_{p1}^{(2)}$ and $R_{p1}^{(3)}$ with the coefficients $\nu_1^{(1)} = \nu_1^{(2)} = \nu_1^{(3)} = 100$ and zero otherwise.

The total simulation time T is set to $T = 0.02s$. The CFL number is set in all computations to $C = 0.5$ of the stability limit $\frac{1}{2N+1}$ of Runge-Kutta DG schemes

(see (1.67)).

As in Section 2.7, the numerical analysis to determine the convergence orders is performed on a sequence of tetrahedral meshes.

One of the variables of the system of the seismic wave equations (3.7) can be arbitrarily picked to numerically determine the convergence order of the used ADER-DG schemes. In Tables 3.2 and 3.3 are shown the errors for the vertical velocity component w obtained by two different flux formulations. The errors and orders of convergence are computed using (2.59) and (2.60).

The first column in both Tables 3.2 and 3.3 shows the mesh spacing h, represented by the maximum diameter of the circumscribed spheres of the tetrahedra. The following four columns show the L^∞ and L^2 errors with the corresponding convergence orders $\mathcal{O}_{L^\infty}$ and $\mathcal{O}_{L^2}$ determined by successively refined meshes. Additionally, we present the total number N_d of degrees of freedom, which is a measure of required storage space during run-time and is given through the product of the number of total mesh elements and the number N_e of degrees of freedom per element. N_e depends on the order of the scheme, i.e. the degree N of the polynomial basis functions via $N_e(N) = \frac{1}{6}(N + 1)(N + 2)(N + 3)$. In the last two columns we give the number I of iterations and the CPU times in seconds needed to reach the simulation time $T = 0.02$s on a Pentium Xeon 3.6 GHz processor with 4GB of RAM.

In the convergence study two different numerical fluxes are compared: the Rusanov flux [90] as given in Section 1.4.2 and a Godunov flux as has been constructed in Sections 3.3.1 and 3.5.1. Fig. 3.2 visualizes the convergence results of Tables 3.2 and 3.3 to demonstrate the dependence of the L^∞ error with respect to (a) mesh width h, (b) number of degrees of freedom N_d and (c) CPU time. With mesh refinement, for both choices of the numerical flux the higher-order schemes converge faster as shown in Fig. 3.2(a). Furthermore, Fig. 3.2(b) demonstrates that higher-order schemes reach a desired accuracy requiring a lower number of total degrees of freedom. The total number of degrees of freedom is the product of the number of mesh elements and the degrees of freedom per element. Therefore, obviously the increasing number of degrees of freedom of higher-order schemes is over-compensated by the dramatic decrease of the number of required mesh elements to reach a certain error level. Also the CPU time comparisons in Fig. 3.2(c) show that the higher-order methods reach a desired error level in less computational time. It should be remarked that in all three plots of Fig. 3.2 is clearly shown, that for very high accuracy, the higher-order schemes with both, the Rusanov or Godunov fluxes, pay off due to their superior convergence properties.

Furthermore, it can be seen in all plots that the Godunov flux is slightly more accurate than the Rusanov flux, which is due to the dissipative property of the Rusanov flux. Additionally, notice, that with increasing order of the scheme the choice of the numerical flux seems to become less important. However, the Godunov flux always provides slightly more accurate results at the same CPU time as illustrated in Fig. 3.2. This result, shown here for the case of anisotropic seis-
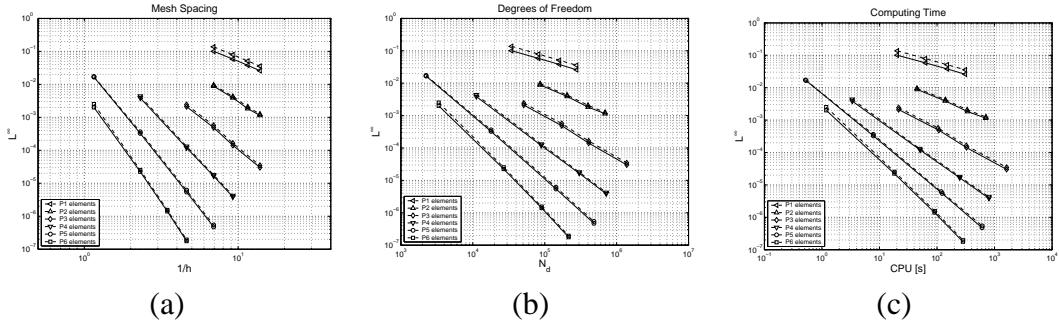
Figure 3.2: Visualization of the convergence results of the vertical velocity component w for the Rusanov flux (dashed) of Table 3.2 and the Godunov flux (solid) of Table 3.3. The symbols P1-P6 stand for the maximum polynomial degree of the basis functions used. The L^∞ error is plotted versus (a) the mesh spacing h, (b) the number of degrees of freedom N_d and (c) the CPU time.

mic wave propagation, can be extended to the other rheology types with similar results.

3.7 Application Examples

In this Section two applications are presented to verify the proper implementation of anisotropy in the Discontinuous Galerkin framework. First, the correct behaviour of anisotropic heterogeneities is verified by comparing ADER-DG results to those obtained with the SEM method. Second, a full 3D example shows the capability of the code to handle arbitrary anisotropy as well as viscoelastic-anisotropic effects.

3.7.1 Heterogeneous Anisotropic Material

To validate the proposed ADER-DG scheme for anisotropic material in two space dimensions results of a heterogeneous anisotropic test case proposed by Carcione [31] and Komatitsch *et al.* [80] are shown. The computational domain $\Omega = [-32.5; 32.5]cm \times [-32.5; 32.5]cm$ is discretized by 37944 triangles with an average edge length of $0.5cm$, equal to the edge length of the square shaped elements used by Komatitsch *et al.* [80]. Along the boundary of Ω absorbing boundary conditions are used. The domain Ω contains two materials separated by a straight line at $x = 0$. On one side ($x < 0$) there is an anisotropic (transversely isotropic) zinc crystal with the symmetry axis in y-direction, whereas on the other side ($x > 0$) there is an isotropic material. The corresponding material properties are given in Table 3.4. The source represents a point force at location $s = (-2, 0)cm$, i.e. $2cm$ from the material interface inside the anisotropic ma-

Table 3.2: Convergence rates of the vertical velocity component w of the ADER-DG $\mathcal{O}2$ up to ADER-DG $\mathcal{O}7$ schemes on tetrahedral meshes with anisotropic material and Rusanov flux.

h	L^∞	$\mathcal{O}_{L^\infty}$	L^2	$\mathcal{O}_{L^2}$	N_d	I	CPU [s]
$1.44 \cdot 10^{-1}$	$1.3726 \cdot 10^{-1}$	—	$7.1719 \cdot 10^{-2}$	—	34560	28	20.4
$1.08 \cdot 10^{-1}$	$7.9448 \cdot 10^{-2}$	1.9	$4.0897 \cdot 10^{-2}$	2.0	81920	37	62.7
$8.66 \cdot 10^{-2}$	$5.1013 \cdot 10^{-2}$	2.0	$2.6304 \cdot 10^{-2}$	2.0	160000	46	150.4
$7.21 \cdot 10^{-2}$	$3.5739 \cdot 10^{-2}$	2.0	$1.8280 \cdot 10^{-2}$	2.0	276480	55	309.9
$1.44 \cdot 10^{-1}$	$9.6109 \cdot 10^{-3}$	—	$3.0957 \cdot 10^{-3}$	—	86400	46	44.8
$1.08 \cdot 10^{-1}$	$4.2996 \cdot 10^{-3}$	2.8	$1.3268 \cdot 10^{-3}$	2.9	204800	61	140.0
$8.66 \cdot 10^{-2}$	$2.0774 \cdot 10^{-3}$	3.3	$6.8331 \cdot 10^{-4}$	3.0	400000	76	334.7
$7.21 \cdot 10^{-2}$	$1.2533 \cdot 10^{-3}$	2.8	$3.7909 \cdot 10^{-4}$	3.2	691200	92	709.4
$2.16 \cdot 10^{-1}$	$2.4197 \cdot 10^{-3}$	—	$6.0996 \cdot 10^{-4}$	—	51200	43	21.5
$1.44 \cdot 10^{-1}$	$5.6764 \cdot 10^{-4}$	3.6	$1.1436 \cdot 10^{-4}$	4.1	172800	64	104.5
$1.08 \cdot 10^{-1}$	$1.6407 \cdot 10^{-4}$	4.3	$3.8141 \cdot 10^{-5}$	3.8	409600	85	322.6
$7.21 \cdot 10^{-2}$	$3.4818 \cdot 10^{-5}$	3.8	$7.4515 \cdot 10^{-6}$	4.0	1382400	128	1623.5
$4.33 \cdot 10^{-1}$	$4.3718 \cdot 10^{-3}$	—	$8.3266 \cdot 10^{-4}$	—	11200	28	3.4
$2.16 \cdot 10^{-1}$	$1.3161 \cdot 10^{-4}$	5.0	$2.2487 \cdot 10^{-5}$	5.2	89600	55	50.0
$1.44 \cdot 10^{-1}$	$1.7960 \cdot 10^{-5}$	4.9	$2.9100 \cdot 10^{-6}$	5.0	302400	82	248.7
$1.08 \cdot 10^{-1}$	$4.2391 \cdot 10^{-6}$	5.0	$7.1098 \cdot 10^{-7}$	4.9	716800	110	801.3
$8.66 \cdot 10^{-1}$	$1.7247 \cdot 10^{-2}$	—	$3.0907 \cdot 10^{-3}$	—	2240	17	0.5
$4.33 \cdot 10^{-1}$	$3.6214 \cdot 10^{-4}$	5.6	$5.2490 \cdot 10^{-5}$	5.9	17920	34	7.8
$2.16 \cdot 10^{-1}$	$6.1905 \cdot 10^{-6}$	5.9	$7.8147 \cdot 10^{-7}$	6.0	143360	67	118.8
$1.44 \cdot 10^{-1}$	$5.4051 \cdot 10^{-7}$	6.0	$6.5986 \cdot 10^{-8}$	6.1	483840	101	611.0
$8.66 \cdot 10^{-1}$	$2.5263 \cdot 10^{-3}$	—	$4.0569 \cdot 10^{-4}$	—	3360	20	1.2
$4.33 \cdot 10^{-1}$	$2.5296 \cdot 10^{-5}$	6.6	$2.8757 \cdot 10^{-6}$	7.1	26880	40	18.3
$2.88 \cdot 10^{-1}$	$1.5502 \cdot 10^{-6}$	6.9	$1.6396 \cdot 10^{-7}$	7.0	90720	60	91.8
$2.16 \cdot 10^{-1}$	$1.9551 \cdot 10^{-7}$	7.2	$2.1993 \cdot 10^{-8}$	7.0	215040	79	285.1

Table 3.3: Convergence rates of the vertical velocity component w of the ADER-DG $\mathcal{O}2$ up to ADER-DG $\mathcal{O}7$ schemes on tetrahedral meshes with anisotropic material and Godunov flux.

h	L^∞	$\mathcal{O}_{L^\infty}$	L^2	$\mathcal{O}_{L^2}$	N_d	I	CPU [s]
$1.44 \cdot 10^{-1}$	$1.0041 \cdot 10^{-1}$	—	$5.4423 \cdot 10^{-2}$	—	34560	28	20.3
$1.08 \cdot 10^{-1}$	$5.8267 \cdot 10^{-2}$	1.9	$3.0369 \cdot 10^{-2}$	2.0	81920	37	63.3
$8.66 \cdot 10^{-2}$	$3.7871 \cdot 10^{-2}$	1.9	$1.9512 \cdot 10^{-2}$	2.0	160000	46	151.0
$7.21 \cdot 10^{-2}$	$2.5901 \cdot 10^{-2}$	2.1	$1.3477 \cdot 10^{-2}$	2.0	276480	55	310.2
$1.44 \cdot 10^{-1}$	$8.8110 \cdot 10^{-3}$	—	$2.7851 \cdot 10^{-3}$	—	86400	46	45.2
$1.08 \cdot 10^{-1}$	$3.9071 \cdot 10^{-3}$	2.8	$1.1894 \cdot 10^{-3}$	3.0	204800	61	138.6
$8.66 \cdot 10^{-2}$	$1.8371 \cdot 10^{-3}$	3.4	$6.1510 \cdot 10^{-4}$	3.0	400000	76	341.2
$7.21 \cdot 10^{-2}$	$1.1421 \cdot 10^{-3}$	2.6	$3.3983 \cdot 10^{-4}$	3.3	691200	92	703.3
$2.16 \cdot 10^{-1}$	$2.1082 \cdot 10^{-3}$	—	$5.3961 \cdot 10^{-4}$	—	51200	43	21.5
$1.44 \cdot 10^{-1}$	$4.8616 \cdot 10^{-4}$	3.6	$9.8006 \cdot 10^{-5}$	4.2	172800	64	107.7
$1.08 \cdot 10^{-1}$	$1.4123 \cdot 10^{-4}$	4.3	$3.3024 \cdot 10^{-5}$	3.8	409600	85	326.0
$7.21 \cdot 10^{-2}$	$3.0079 \cdot 10^{-5}$	3.8	$6.3742 \cdot 10^{-6}$	4.1	1382400	128	1620.8
$4.33 \cdot 10^{-1}$	$3.8588 \cdot 10^{-3}$	—	$7.3824 \cdot 10^{-4}$	—	11200	28	3.4
$2.16 \cdot 10^{-1}$	$1.1900 \cdot 10^{-4}$	5.0	$2.0750 \cdot 10^{-5}$	5.2	89600	55	51.0
$1.44 \cdot 10^{-1}$	$1.6555 \cdot 10^{-5}$	4.9	$2.6735 \cdot 10^{-6}$	5.0	302400	82	248.1
$1.08 \cdot 10^{-1}$	$3.8443 \cdot 10^{-6}$	5.1	$6.5261 \cdot 10^{-7}$	4.9	716800	110	799.5
$8.66 \cdot 10^{-1}$	$1.6633 \cdot 10^{-2}$	—	$2.9909 \cdot 10^{-3}$	—	2240	17	0.5
$4.33 \cdot 10^{-1}$	$3.2571 \cdot 10^{-4}$	5.7	$4.7736 \cdot 10^{-5}$	6.0	17920	34	7.8
$2.16 \cdot 10^{-1}$	$5.4583 \cdot 10^{-6}$	5.9	$7.0059 \cdot 10^{-7}$	6.1	143360	67	123.0
$1.44 \cdot 10^{-1}$	$4.7499 \cdot 10^{-7}$	6.0	$5.8732 \cdot 10^{-8}$	6.1	483840	101	606.7
$8.66 \cdot 10^{-1}$	$2.0000 \cdot 10^{-3}$	—	$3.4171 \cdot 10^{-4}$	—	3360	20	1.2
$4.33 \cdot 10^{-1}$	$2.2341 \cdot 10^{-5}$	6.5	$2.6403 \cdot 10^{-6}$	7.0	26880	40	18.1
$2.88 \cdot 10^{-1}$	$1.4003 \cdot 10^{-6}$	6.8	$1.5055 \cdot 10^{-7}$	7.1	90720	60	90.2
$2.16 \cdot 10^{-1}$	$1.7634 \cdot 10^{-7}$	7.2	$2.0326 \cdot 10^{-8}$	7.0	215040	79	281.4

Table 3.4: Coefficients for the heterogeneous anisotropic model given in $[10^{10}N \cdot m^{-2}]$ for the anisotropic and isotropic materials. All other coefficients are zero. The material density ρ is given in $[kg \cdot m^{-3}]$.

	ρ	c_{11}	c_{12}	c_{22}	c_{66}
isotropic	7100	16.5	8.58	16.5	3.96
anisotropic	7100	16.5	5.00	6.2	3.96

terial and is acting in y-direction. The source time function is given by a Ricker wavelet with dominant frequency $f_0 = 170kHz$ and delay $t_0 = 6\mu s$ which acts on the vertical velocity component v with a maximum amplitude of $1 \cdot 10^{13} m \cdot s^{-1}$. Seismograms are calculated at four different locations $r_i = (x_i, y_i)$, $i = 1, ..., 4$, with $x_1 = -10.5cm$, $x_2 = -3.5cm$, $x_3 = -1.0cm$, $x_4 = 10.5cm$ and $y_i = -8cm$ for all $i = 1, ..., 4$ in order to compare the results of the ADER-DG method with those of Komatitsch *et al.* [80]. The simulation is carried out using an ADER-DG $\mathcal{O}6$ scheme, i.e. with polynomial basis functions of degree $N = 5$, and the Rusanov flux presented in Section 3.6. The time step size was $20.58ns$ such that the final simulation time $T = 100\mu s$ was reached after 4860 iterations.

Two snapshots illustrate the evolving wavefield for a qualitative comparison. In Fig. 3.3(a) we show the vertical velocity component v after $30\mu s$ in a zoomed region together with the simulation mesh. Note, that the triangular elements are aligned with the material interface at $x = 0$. The locations of the source and the four receivers are also indicated by a full and empty circles, respectively. Fig. 3.3(b) illustrates the wavefield of the velocity v after $60\mu s$ in the entire computational domain Ω together with the source and receiver locations. This result can be visually compared to the Figure 4 shown in Komatitsch *et al.* [80]. One can then observe that the ADER-DG $\mathcal{O}6$ scheme resolves the same wave phases. The typical cuspidal triangular wave structures and the refracted waves at the interface are clearly visible.

The seismograms calculated with the ADER-DG $\mathcal{O}6$ scheme at the four receiver locations r_i, $i = 1, ..., 4$, are plotted in Fig. 3.4 (solid line). The results obtained by Komatitsch *et al.* [80] with the SEM of spatial order 6 (spectral degree 5) were recomputed with the $SEM2DPACK$ software and are superimposed (dashed line). The agreement is excellent for all phases. The residuals between both computations have been plotted (dotted line), amplified by a factor of 10, to show to which extent both results produce equivalent results. However it should be remarked, that for the ADER-DG computation a completely irregular triangular grid is used.

3.7.2 Transversely Isotropic Material with Tilted Symmetry Axis

A computation of the test case proposed in [80] for a 3D transversely isotropic medium with a tilted symmetry axis is performed to verify the accuracy of the proposed scheme for a fully three-dimensional problem. Here, the tilt angle of $30°$ with respect to the Cartesian coordinate axis creates additional complexity, as the rotation introduces a major number of non-zero entries in the Hooke's tensor. Note, that in the present case numerical fluxes are computed with respect to a
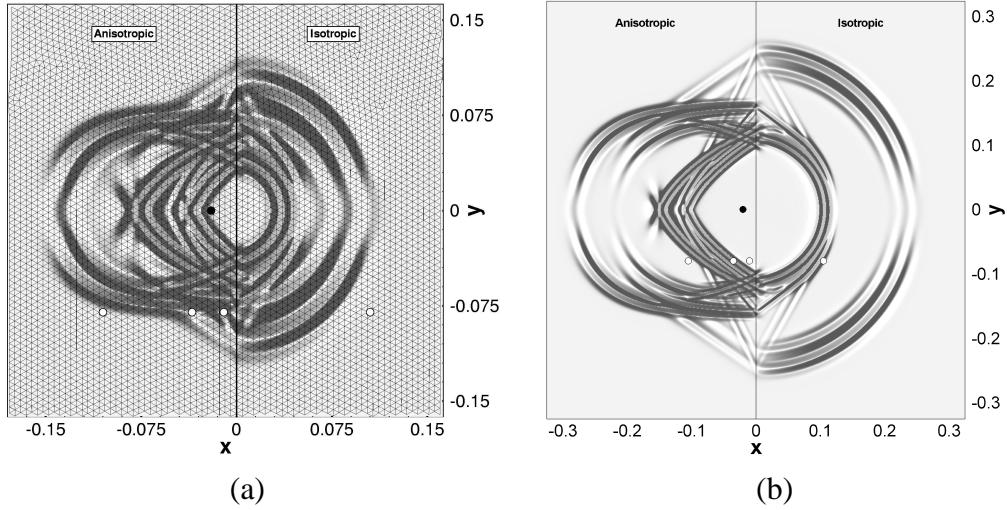
Figure 3.3: (a) Vertical velocity v and computational mesh in the zoomed region $[-0.18; 0.1625] \times [-0.1625; 0.1625]$ at $30 \mu s$. The source location is indicated by a full (black) circle, the four receiver locations are indicated by empty (white) circles. (b) Vertical velocity v at $60 \mu s$ with the whole computational domain. A variety of different phases can be identified. The source location is indicated by a full (black) circle, the four receiver locations are indicated by empty (white) circles.

local coordinate system each aligned with a face of a tetrahedron as shown in Section 3.4 and therefore tilted material properties do not add additional complexity. The computational domain $\Omega = [0; 2500]m \times [0; 2500]m \times [0; 2500]m$ is discretized with $48 \times 48 \times 48$ cubes, each subdivided in 5 tetrahedral elements, leading to a total of 552960 elements. The source is a point force placed at $(x, y, z) = (1250, 1562.5, 937.5)\, m$ and acting in the direction of the material's symmetry axis. The source time function is a Ricker wavelet with dominant frequency $f_0 = 16 Hz$ and delay $t_0 = 0.07s$. A receiver is located at $(x, y, z) = (1250, 1198.05, 1568.75)\, m$ to register the propagating waves. The material is homogeneous and the material parameters given in the coordinate system aligned with the anisotropic symmetry axis can be found in Table 3.5. Notice, that for a transversely isotropic material $c_{22} = c_{11}$, $c_{23} = c_{13}$ and $c_{55} = c_{44}$.

An ADER-DG $\mathcal{O}7$ scheme is used, meaning that the variables are resolved with polynomials of degree $N = 6$ in space and time inside each element. Godunov fluxes, as described in 3.3.1, have been used for enhanced accuracy. The time step size was $166.91 \mu s$ such that the final simulation time $T = 0.7s$ was reached after 4194 iterations.

In Fig. 3.5(a) we can visualized the wavefield of the normal stress σ_{xx} at $t = 0.25s$ in the yz-plane at $x = 1250m$. A visual comparison with the result of Komatitsch *et al.* [80] shows the characteristic wave pattern for the case of a tilted anisotropic material. A vector plot illustrating the total particle velocity
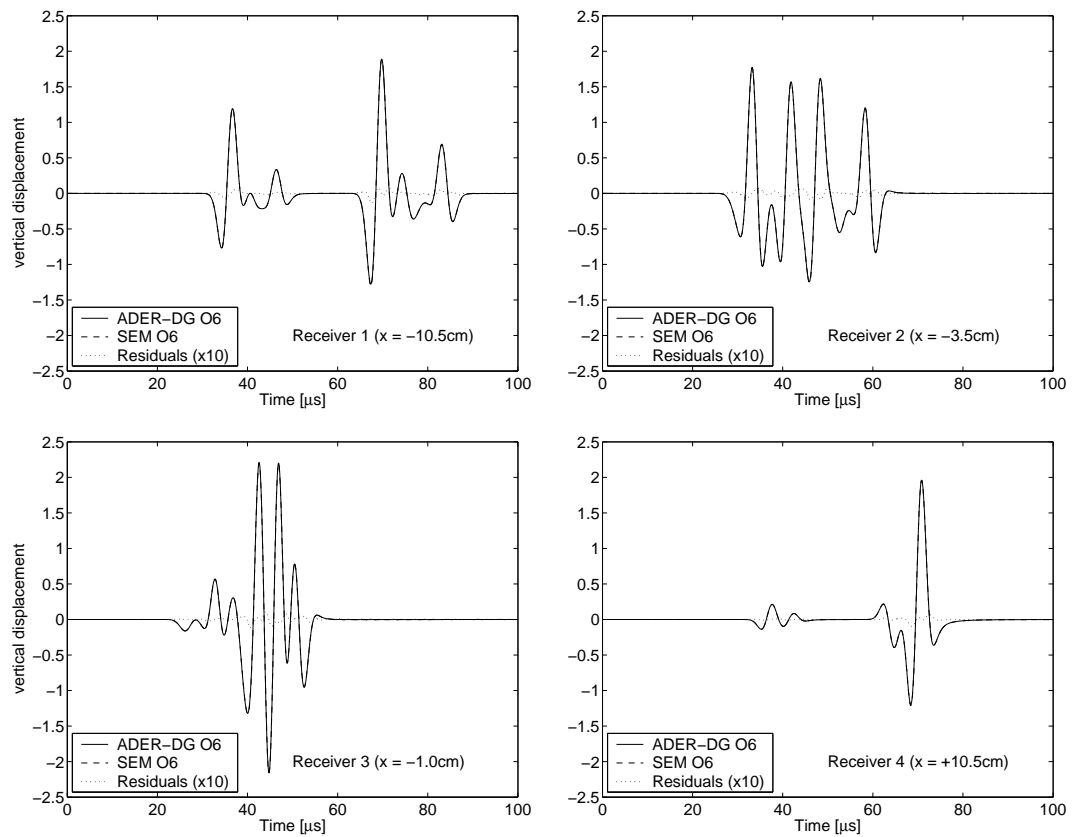
Figure 3.4: Seismograms showing vertical displacements for the ADER-DG (solid) and SEM (dashed) computations. The good agreement of both solutions is shown by the amplified residuals (dotted).

Table 3.5: Coefficients for the transversely isotropic material (Mesaverde clay shale) given in $[10^9 N \cdot m^{-2}]$. All other coefficients are zero. The material density ρ is given in $[kg \cdot m^{-3}]$.

ρ	c_{11}	c_{12}	c_{13}	c_{22}	c_{23}	c_{33}	c_{44}	c_{55}	c_{66}
2590	66.6	19.7	39.4	66.6	39.4	39.9	10.9	10.9	23.45

at $t = 0.25s$ in a zoomed region of one of the cuspidal triangles is shown in Fig. 3.5(b) to visualize the complexity of the seismic wavefield in more detail. The corresponding seismogram calculated at the receiver is plotted in Fig. 3.6 and compared with the analytical solution [29]. We can see the excellent agreement between analytical and numerical solutions, where the early qP wave followed by the stronger qSV wave can be observed. The root mean square error E between the analytical and the numerical solutions is given. Absorbing boundaries for the domain Ω are used to avoid spurious reflected waves.

Additionally, Fig. 3.6 shows the seismogram calculated for the same anisotropic test case but coupled with viscoelastic attenuation as introduced in Section 3.5. The quality factors $\mathcal{Q}^P = 80$ and $\mathcal{Q}^S = 40$ have been used to see a strong effect due to anelasticity. Attenuation is implemented with 3 relaxation mechanisms as described in detail in [76]. The frequency bandwidth of $100Hz$ is centered at the dominant frequency $16Hz$ of the source. With respect to the purely elastic case the damping and dispersion caused by the viscoelastic material is clearly visible. However, an analytical solution for the coupled case was not found and, therefore, it can only be shown a qualitative change of the seismogram. For the computation of the numerical solution of the anisotropic-elastic case the CPU time was 14 hours on 128 Intel Xeon EM64T 64-bit 3.2-GHz processors. For the anisotropic-viscoelastic case approximately 34 hours were needed on the same computer. However, note that no special code optimization that e.g. exploits the sparsity of the Jacobian matrices was used. Furthermore, the code is kept very flexible to handle all types of currently treatable problems and therefore does not provide the computational efficiency as a possible pure production code for massive applications could achieve.

3.8 Conclusion

A new high-order scheme for solving problems of anisotropic seismic wave propagation on unstructured tetrahedral meshes has been presented. The proposed ADER-DG method has proved to be suited to achieve highly accurate results for anisotropic heterogeneous media. A thorough convergence study confirms the high-order accuracy of the scheme regardless of the choice of the suggested nu-
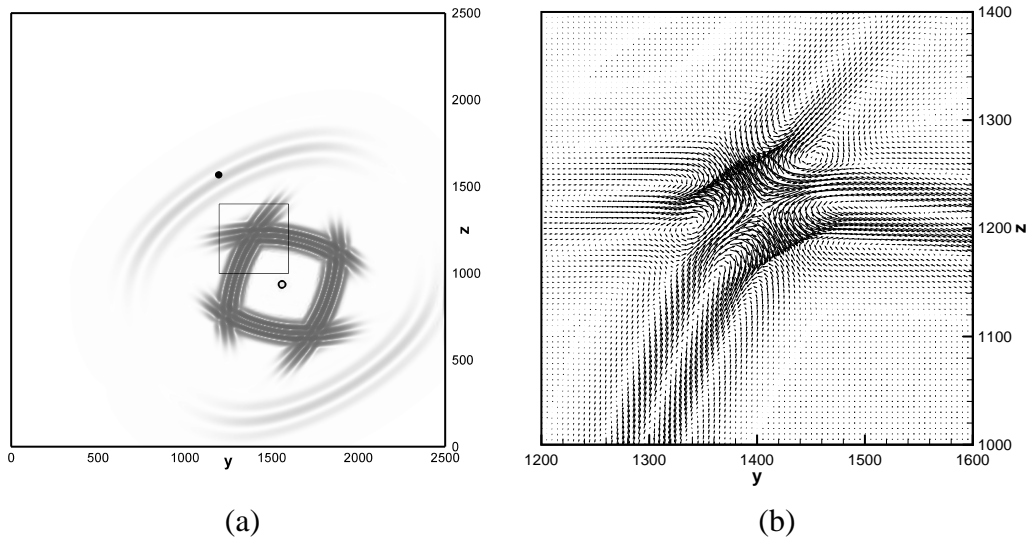
(a)   (b)

Figure 3.5: (a) Snapshot of the normal stress σ_{xx} at $t = 0.25s$ in the yz-plane at $x = 1250m$ (top). The source and receiver positions are indicated by the empty and full circles, respectively. The zoom region for Fig. 3.5(b) is indicated by the box. (b) Vector field of the particle velocity at $t = 0.25s$ in the zoom region.

(a)   (b)
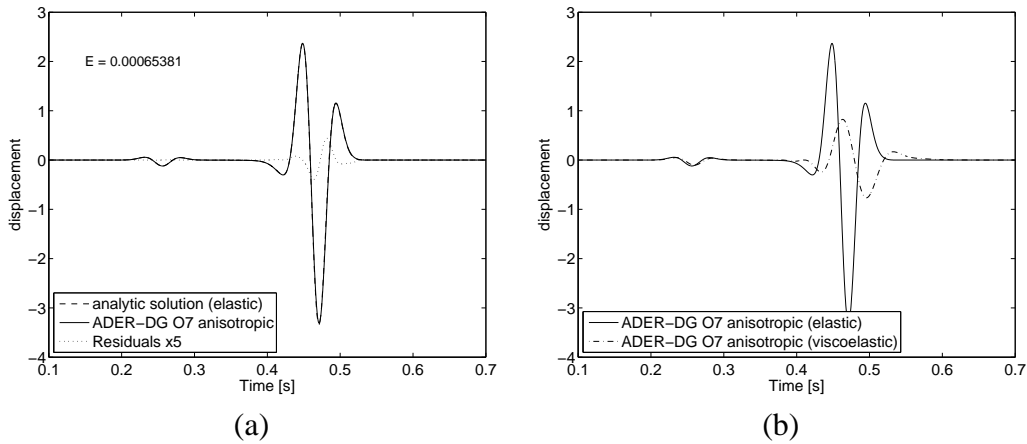
Figure 3.6: (a) Numerical (solid) and analytical (dashed) displacements along the symmetry axis recorded at 728.9m from the source. The r.m.s. error is also displayed. The numerical solution is computed with an ADER-DG $\mathcal{O}7$ scheme and shows excellent agreement with the analytical solution. (b) Numerical elastic (solid) and viscoelastic (dashed) seismogram shows the effects of viscoelasticity for the same receiver and computational order than in (a), with clear physical dissipation and attenuation effects.

merical fluxes. However, the proposed Godunov type flux turns out to be the better choice. Additionally, a formulation to couple anisotropic and viscoelastic effects for seismic wave propagation has been developed, presenting the necessary changes in the explicit expression of the numerical scheme. Results of different application examples in 2D and 3D involving qP, qS_1 and qS_2 wave propagation in both homogeneous and heterogeneous media are in very good agreement with analytical solutions or results obtained by the Spectral Element Method. It can be concluded, that the ADER-DG method represents a new numerical approach to solve seismic wave propagation problems, where geometrical flexibility and numerical accuracy are fundamental. Therefore, the new approach combines the advantages of automatic unstructured mesh generation for complex geometries, which might be difficult to treat with hexahedral meshes, with the advantage of high space and time accuracy. In particular, the ADER-DG scheme provides important advantages for future applications of realistic wave propagation scenarios, where heterogeneous material properties like anisotropy and viscoelasticity play an important role.

Chapter 4

Poroelasticity in ADER-DG Schemes

In this Chapter the ADER-DG schemes are used to model poroelastic wave propagation. First an overview of Biot's theory and its mathematical expression are given, as well as an introduction to the nomenclature. Afterwards the theory is extended to the anisotropic poroelastic material and the main ingredients to incorporate poroelasticity into the DG framework are presented. In the following we outline how to build the new numerical scheme for the poroelastic case, based on the original explicit ADER-DG approach for tetrahedral meshes. Then a new time integration schemes is presented, which is able to overcome the stability issue that arises due to the stiff source term in the viscous low-frequency case, based on the new local space-time DG approach. The convergence behavior of the proposed schemes is further tested to confirm the high-order accuracy of the new approach. Additionally, a series of application examples for both, high- and low-frequency cases, are presented to further validate the scheme by comparing its results to analytical solutions and reference solutions obtained by other numerical methods. The main contents of this Chapter have been submitted in J. de la Puente, M. Dumbser, M. Käser and H. Igel [49].

4.1   Introduction

Wave propagation through fluid-saturated porous rock is a topic of increasing interest in many fields of geosciences. The information carried by a seismic wavefield includes much more than just the geometry of the geological structure. Amplitudes and wave forms provide also information about the material properties in the subsurface and can be used in exploration geophysics, earthquake engineering, soil mechanics and hydrology. The study of wave propagation in porous media has improved the understanding of elastic properties of rock, its deformation characteristics, the dynamic response of structures and foundations and its interaction with pore-fluids. In particular, with respect to enhanced oil recovery techniques the exploration industry faces the challenging task of extracting valuable information about the porosity, permeability and fluid-saturation from seis-

mic waves. Permeability, in particular, is related to the preferential directions of fluid flow. As a consequence, the bedding of sedimentary layers or the alignment of microcracks and fractures plays an important role on the poroelastic properties, which often will present a strong anisotropy. Oil reservoir monitoring today is often based on time-lapse seismics where seismic measurements are repeated from time to time to investigate the temporal variations of the rock and fluid properties during production. The change of the structural and petrophysical parameters of the reservoir is included in the seismic signature. Therefore, a profound understanding of the characteristics of the seismic wavefield has to be developed as the key issue is the relation between the variations in the amplitudes and wave forms and the change of the subsurface properties.

A first study of the effects of mixed solid and fluid phases on elastic deformation was formally carried out by Biot in the early 40s, leading to the constitutive equations for anisotropic porous media in the fundamental publication of his theory of fluid-saturated porous solids and mechanics of deformation in porous media in the following decade [11, 12, 13, 14]. Biot's theory applies continuum mechanics to media composed of a solid rock matrix fully saturated with a fluid. The theory assumes that the size of the pores is much smaller than the wavelengths investigated. In this framework the pores are supposed to be all connected meaning that the liquid of the pores is a continuum. Any disconnected pores are part of the solid matrix. In order to derive the corresponding wave equations, the rheology of the porous media is combined with Darcy's Laws which describe the dynamics of the liquid system. Biot's theory has been extensively validated [9, 112] and is now widely accepted in the field of poroelastic wave propagation.

The main difference between the wavefields in a poroelastic material and those in an elastic one is the existence of a wave *of the second kind*, in addition to the standard compressional and shear waves. This wave, also called *slow* P-wave, is of compressional type but propagates at a very slow speed through the medium. As a further effect, the amplitudes of the wavefield are attenuated due to energy losses in the presence of a viscous fluid. Finally, in the low-frequency range, the *slow* P-wave becomes a diffusive mode that propagates at a time scale completely different from that of the other waves in the medium. As a consequence, this wave is significant only very close to the source or near material heterogeneities.

Analytical solutions for wave propagation problems in poroelastic media exist [19, 21, 78], but are usually limited to very simple model problems. Therefore, many studies consider the numerical solution of Biot's equations. The Finite-Difference method has been one of the early methods applied for this purpose in two dimensions [44, 88, 140, 141] and three dimensions [127]. Pseudo-Spectral methods have been successfully implemented [24, 110], as well as the reflectivity method [120, 125]. A different approach is followed, e.g. by [117, 118], where the micro-scale is fully taken into account by individually discretizing the pore content and the solid matrix. The use of numerical simulations has played an important role in the understanding of the effects of poroelastic material properties

on the seismic wave forms and frequency spectra (e.g. [16]).

4.2 Biot's Theory

The mechanical properties of a porous solid material filled with a fluid have been developed in many theoretical frameworks (e.g. [48]). However, M.A. Biot was the first to introduce a full theory from fundamental principles, based upon the material properties of the solid rock constituent (solid, denoted by the subindex "S" in the following), the frame including the pore structure (matrix, "M") and the fluid constituent ("F"). Although later extended to more complicated setups [10, 119], the fundamentals of the theory are based upon the following assumptions:

- linear continuum mechanics can be applied.

- the wavelength is significantly larger than largest dimension of the pores.

- the pores are all interconnected (unconnected pores are considered part of the solid matrix).

- thermoelastic and chemical effects don't apply.

- the fluid fills completely the pores.

- the rock constituent is isotropic, although the pore structure might be not.

A first analysis can be done assuming the pores to be totally isotropic. We will use in the following the upper indices m and f to refer to variables of the solid matrix and of the fluid, respectively. To describe the mechanics of the poroelastic material chosen, in addition to the solid matrix stresses σ_{ij}^m and strains ε_{ij}^m, two fluid equivalents as are the fluid's pressure p and the fluid strains ε_{ij}^f, which don't support shear deformation, i.e. $\varepsilon_{ij}^f = 0$ for $i \neq j$. The quantity ϕ, called porosity, can be defined

$$\phi \equiv \frac{V_P}{V_T},$$
(4.1)

where V_P is the volume that takes the pore space and V_T is the total volume of the material.

A poroelastic material, in Biot's theory, can be described using measurable quantities from the solid, matrix and fluid, which are summarized together with their corresponding units as follows:

- **SOLID**

    K_S : Bulk modulus [Pa]

ρ_S : Density [Kg/m^3]

- **MATRIX**

    λ_M : Lamé parameter [Pa]

    μ_M : Shear modulus [Pa]

    ϕ : Porosity

    κ : Permeability [m^2]

    T : Tortuosity

- **FLUID**

    K_F : Bulk modulus [Pa]

    ρ_F : Density [Kg/m^3]

    ν : Viscosity [Pa s]

Most of these quantities are well-known from fundamental physics and elastic mechanics, except for the permeability and tortuosity. Those two parameters are related to the properties of fluid flow through conduits. The tortuosity T can be interpreted as a ratio between the diffusivity of a fluid in the open space and in a particular porous material. This quantity is related to the ratio between the minimum (straight) and actual distance between two points of the pore space, due to the "tortuous" path of the pore connection. The permeability κ is a measure of the ability of a porous material to transmit fluids.

4.2.1 Constitutive Equations

The most general form of the constitutive equation for a fluid-filled porous material, from energetic considerations [27], is given as

$$
\begin{aligned}
\sigma_{ij}^m &= 2G\left(\varepsilon_{ij}^m - \tfrac{1}{3}\varepsilon_{kk}^m\delta_{ij}\right) + K\varepsilon_{kk}^m\delta_{ij} + Q\varepsilon_{kk}^f\delta_{ij}\,, \\
\sigma^f &= Q\varepsilon_{kk}^m + R\varepsilon_{kk}^f\,,
\end{aligned}
\tag{4.2}
$$

where $\sigma^f = -\phi p$. The parameters G, K, Q and R are unknown, although they can be assessed by using a series of ideal experiments, as proposed originally by Biot and Willis [15]. First of all one can subject the material described in (4.2) to a pure shear deformation, so that $\varepsilon_{ij}^m = \varepsilon_{ij}^f = 0$ for $i = j$. It can then be seen that $\sigma_{ij}^m = 2G\varepsilon_{ij}^m$, so that the parameter G can be identified with the matrix's shear modulus: $G = \mu_M$. The two further experiments, which involve no shear but only compression, are described in the following.

The second experiment is the so-called jacketed compressibility test. It consists of taking a sample of fluid-filled poroelastic material and closing it in an impermeable, flexible jacket. The jacket is then compressed with an external pressure p^{ext} while the pressure of the fluid is kept at zero by using a tube that connects it to the atmosphere. In this case, all the external pressure is transmitted to the frame, and therefore one can define the bulk modulus of the matrix as $K_M = -p^{\text{ext}}/\varepsilon_{kk}^m$. Using (4.2) under the conditions just described one obtains

$$
\begin{aligned}
-p^{\text{ext}} &= K\varepsilon_{kk}^m\delta_{ij} + Q\varepsilon_{kk}^f\delta_{ij}\,, \\
0 &= Q\varepsilon_{kk}^m + R\varepsilon_{kk}^f\,,
\end{aligned}
\tag{4.3}
$$

so that one can obtain a relation between K_M and the still unknown poroelastic parameters K, Q and R

$$
K_M = K - \frac{Q^2}{R}\,.
\tag{4.4}
$$

The last experiment is the unjacketed compressibility test. The whole poroelastic sample is now immersed in a fluid so that a pressure p is applied. This pressure will distribute itself among the $1 - \phi$ part of the frame and the ϕ fluid part of the surface of the material. In this case (4.2) becomes

$$
\begin{aligned}
-(1-\phi)p &= K\varepsilon_{kk}^m\delta_{ij} + Q\varepsilon_{kk}^f\delta_{ij}\,, \\
-\phi p &= Q\varepsilon_{kk}^m + R\varepsilon_{kk}^f\,.
\end{aligned}
\tag{4.5}
$$

Now it can be seen that the pressure is acting from the inside of the porous rock, and therefore the compressional properties deduced from this experiment are those of the rock or solid instead of those of the matrix. One can use $K_S = -p/\varepsilon_{kk}^m$ and $K_F = -p/\varepsilon_{kk}^f$ for this particular experiment to obtain a further set of constraints on the unknown parameters K, Q and R as follows

$$
\begin{aligned}
1 - \phi &= \frac{K}{K_S} + \frac{Q}{K_F}\,, \\
\phi &= \frac{R}{K_F} + \frac{Q}{K_S}\,,
\end{aligned}
\tag{4.6}
$$

which, combined with (4.4), builds up a system of three equations and unknowns which can be solved as follows

$$
\begin{aligned}
K &= \frac{(1-\phi)(1-\phi-K_M/K_S)K_S+\phi K_S K_M/K_F}{1-\phi-K_M/K_S+\phi K_S/K_F}\,, \\
Q &= \frac{(1-\phi-K_M/K_S)\phi K_S}{1-\phi-K_M/K_S+\phi K_S/K_F}\,, \\
R &= \frac{\phi^2 K_S}{1-\phi-K_M/K_S+\phi K_S/K_F}\,.
\end{aligned}
\tag{4.7}
$$

Now, (4.2) can be expressed by using only the material properties of the solid, matrix and fluid through (4.7). However it is convenient to define some new parameters. In particular, the following relations can be found

$$
\begin{aligned}
K &= K_M + M(\alpha - \phi)^2\,, \\
Q &= \phi M(\alpha - \phi)\,, \\
R &= M\phi^2\,,
\end{aligned}
\tag{4.8}
$$

where the fluid-solid coupling modulus M is

$$
M = \frac{K_S}{1 - \phi - K_M/K_S + \phi K_S/K_F}\,,
\tag{4.9}
$$

and the effective stress component α is

$$
\alpha = 1 - \frac{K_M}{K_S}\,.
\tag{4.10}
$$

With this one can express the constitutive relation (4.2) as

$$
\begin{aligned}
\sigma_{ij}^m &= 2\mu_M\left(\varepsilon_{ij}^m - \tfrac{1}{3}\varepsilon_{kk}^m\delta_{ij}\right) + K_M\varepsilon_{kk}^m\delta_{ij} + \\
&\quad + \left[M(\alpha-\phi)^2\varepsilon_{kk}^m + \phi M(\alpha-\phi)\varepsilon_{kk}^f\right]\delta_{ij}\,, \\
\sigma^f &= \phi M(\alpha-\phi)\varepsilon_{kk}^m + M\phi^2\varepsilon_{kk}^f\,,
\end{aligned}
\tag{4.11}
$$

whose first expression can be further simplified by adapting Hooke's law for the solid matrix with the definition

$$
c_{ijkl}^m = \left(K_M - \frac{2}{3}\mu_M\right)\delta_{ij}\delta_{kl} + \mu_M\left(\delta_{ik}\delta_{jl} + \delta_{il}\delta_{jk}\right)\,,
\tag{4.12}
$$

so that (4.11) becomes

$$
\begin{aligned}
\sigma_{ij}^m &= c_{ijkl}^m\varepsilon_{kl}^m + \left[M(\alpha-\phi)^2\varepsilon_{kk}^m + \phi M(\alpha-\phi)\varepsilon_{kk}^f\right]\delta_{ij}\,, \\
\sigma^f &= \phi M(\alpha-\phi)\varepsilon_{kk}^m + M\phi^2\varepsilon_{kk}^f\,.
\end{aligned}
\tag{4.13}
$$

The very last transformation required to reach a useful constitutive relation for wave propagation problems is to express (4.13) in terms of the total stress $\sigma_{ij} = \sigma_{ij}^m + \sigma^f\delta_{ij}$ and the variation of fluid content $\varsigma \equiv -\phi(\varepsilon_{kk}^f - \varepsilon_{kk}^m)$, thus obtaining

$$
\begin{aligned}
\sigma_{ij}^m &= c_{ijkl}^m\varepsilon_{kl}^m - \alpha p\delta_{ij}\,, \\
p &= M(\varsigma - \alpha\varepsilon_{kk}^m)\,,
\end{aligned}
\tag{4.14}
$$

which is the final form of the poroelastic constitutive laws for the isotropic case.

4.2.2 Equations of Motion

The dynamics of the solid and the fluid need to be explored to build up a full set of wave equations for the poroelastic case. For solids this is always Newton's laws, while for confined fluids one uses Darcy's laws. Biot extended both equations to the poroelastic case in order to describe particle motion for the solid and fluid constituents. It will be convenient to define the velocity vectors $\vec{v} = (u, v, w)$ of the solid particle velocities and $\vec{v_f} = (u_f, v_f, w_f)$ of the fluid particle velocities. These last are defined $\vec{\nabla} \cdot \vec{v_f} \equiv -\varsigma$ while the first follow from the standard elastic definitions using the matrix strains $\bar{\varepsilon}^m$. We will use the average density of the poroelastic material which can be computed from $\rho \equiv (1 - \phi)\, \rho_s + \phi \rho_f$. Further, the index i will be used to refer to the three cartesian directions $i = x, y, z$ and the notation $\partial/\partial x_i$ for the corresponding space derivatives. For a Poiseuille-type fluid, without turbulence, one can set a combination of Biot's dynamic equations and Darcy's law to obtain the expressions

$$
\begin{aligned}
\frac{\partial \sigma_{ij}}{\partial x_i} &= \rho \frac{\partial v_i}{\partial t} + \rho_F \frac{\partial v_i^f}{\partial t}\,, \\
-\frac{\partial p}{\partial x_i} &= \rho_F \frac{\partial v_i}{\partial t} + m \frac{\partial v_i^f}{\partial t} + \frac{\nu}{\kappa} v_i^f\,,
\end{aligned}
\tag{4.15}
$$

where the parameter $m = \rho_f T/\phi$ has been introduced. The second expression of (4.15) shows that the viscosity ν is causing energy dissipation in the system. The expression (4.15) is not anymore valid when the fluid gets away from a Poiseuille-type behavior and for that case we get

$$
\begin{aligned}
\frac{\partial \sigma_{ij}}{\partial x_i} &= \rho \frac{\partial v_i}{\partial t} + \rho_F \frac{\partial v_i^f}{\partial t}\,, \\
-\frac{\partial p}{\partial x_i} &= \rho_F \frac{\partial v_i}{\partial t} + \Psi * \frac{\partial v_i^f}{\partial t}\,,
\end{aligned}
\tag{4.16}
$$

where $*$ denotes a convolutional product in time. Note that (4.15) is just a particular case of (4.16) with $\Psi(t) = m\delta(t) + (\nu H(t)/\kappa)$, where $\delta(t)$ is the Dirac delta function, $H(t)$ the Heaviside function. The consequences of this different behavior in the propagation of waves through poroelastic media will be further studied in the following Sections.

At this moment, a full wave equation system for poroelastic material can be built from expressions (4.14) and (4.16).

4.3 Poroelastic Wave Equations

A velocity-stress formulation of the poroelastic wave equations includes the unknowns σ_{ij} (total stress) and $\vec{v}$ (matrix particle velocity) as well as the pore pressure p and the relative fluid velocities $\vec{v}_f = (u_f, v_f, w_f)$, as defined in Sections

4.2.1 and 4.2.2. Following Biot's studies [11, 12, 13] and the matrix notation of Carcione [26] the tensorial constitutive equation (4.14) extended to general anisotropic poroelastic media can be written in matrix-vector form as

$$\vec{\sigma}_i = M_{ij}\vec{\varepsilon}_j\,, \tag{4.17}$$

where

$$
\begin{aligned}
\vec{\sigma}_i &= \left(\sigma_{xx}, \sigma_{yy}, \sigma_{zz}, \sigma_{yz}, \sigma_{xz}, \sigma_{xy}, -p\right)\,, &(4.18)\\
\vec{\varepsilon}_j &= \left(\varepsilon_{xx}, \varepsilon_{yy}, \varepsilon_{zz}, \varepsilon_{yz}, \varepsilon_{xz}, \varepsilon_{xy}, -\varsigma\right)\,, &(4.19)
\end{aligned}
$$

and

$$
M_{ij} = \begin{pmatrix}
c^u_{11} & c^u_{12} & c^u_{13} & c^u_{14} & c^u_{15} & c^u_{16} & M\alpha_1 \\
c^u_{12} & c^u_{22} & c^u_{23} & c^u_{24} & c^u_{25} & c^u_{26} & M\alpha_2 \\
c^u_{13} & c^u_{23} & c^u_{33} & c^u_{34} & c^u_{35} & c^u_{36} & M\alpha_3 \\
c^u_{14} & c^u_{24} & c^u_{34} & c^u_{44} & c^u_{45} & c^u_{46} & M\alpha_4 \\
c^u_{15} & c^u_{25} & c^u_{35} & c^u_{45} & c^u_{55} & c^u_{56} & M\alpha_5 \\
c^u_{16} & c^u_{26} & c^u_{36} & c^u_{46} & c^u_{56} & c^u_{66} & M\alpha_6 \\
M\alpha_1 & M\alpha_2 & M\alpha_3 & M\alpha_4 & M\alpha_5 & M\alpha_6 & M
\end{pmatrix}\,. \tag{4.20}
$$

As entries of the matrix (4.20) appear $c^u_{ij} \equiv c^m_{ij} + M\alpha_i\alpha_j$, which are called the components of the undrained stiffness tensor, c^m_{ij} the components of the elastic Hooke's tensor of the solid matrix, α_i the generalized effective stress components and M, the fluid-solid coupling modulus, which are generalized for the anisotropic case as

$$
\begin{aligned}
\alpha_1 &= 1 - \left(c_{11} + c_{12} + c_{13}\right)/\left(3K_s\right)\,, &(4.21)\\
\alpha_2 &= 1 - \left(c_{12} + c_{22} + c_{23}\right)/\left(3K_s\right)\,, &(4.22)\\
\alpha_3 &= 1 - \left(c_{13} + c_{23} + c_{33}\right)/\left(3K_s\right)\,, &(4.23)\\
\alpha_4 &= -\left(c_{14} + c_{24} + c_{34}\right)/\left(3K_s\right)\,, &(4.24)\\
\alpha_5 &= -\left(c_{15} + c_{25} + c_{35}\right)/\left(3K_s\right)\,, &(4.25)\\
\alpha_6 &= -\left(c_{16} + c_{26} + c_{36}\right)/\left(3K_s\right)\,, &(4.26)\\
M &= \frac{K_s}{\left(1 - \bar{K}/K_s\right) - \phi\left(1 - K_s/K_f\right)} \quad \text{with} &(4.27)\\
\bar{K} &= \frac{1}{9}\left[c_{11} + c_{22} + c_{33} + 2\left(c_{12} + c_{13} + c_{23}\right)\right]\,. &(4.28)
\end{aligned}
$$

In order to obtain the wave equations, the dynamics of the fluid for the poroelastic case are expressed by Biot's dynamic equations and Darcy's law (4.16), which

can be written explicitly in the form

$$
\begin{aligned}
\frac{\partial \sigma_{xx}}{\partial x} + \frac{\partial \sigma_{xy}}{\partial y} + \frac{\partial \sigma_{xz}}{\partial z} &= \rho \frac{\partial u}{\partial t} + \rho_f \frac{\partial u_f}{\partial t}, \\
\frac{\partial \sigma_{xy}}{\partial x} + \frac{\partial \sigma_{yy}}{\partial y} + \frac{\partial \sigma_{yz}}{\partial z} &= \rho \frac{\partial v}{\partial t} + \rho_f \frac{\partial v_f}{\partial t}, \\
\frac{\partial \sigma_{xz}}{\partial x} + \frac{\partial \sigma_{yz}}{\partial y} + \frac{\partial \sigma_{zz}}{\partial z} &= \rho \frac{\partial w}{\partial t} + \rho_f \frac{\partial w_f}{\partial t}, \\
-\frac{\partial\, p}{\partial x} &= \rho_f \frac{\partial u}{\partial t} + \Psi_x * \frac{\partial u_f}{\partial t}, \\
-\frac{\partial\, p}{\partial y} &= \rho_f \frac{\partial v}{\partial t} + \Psi_y * \frac{\partial v_f}{\partial t}, \\
-\frac{\partial\, p}{\partial z} &= \rho_f \frac{\partial w}{\partial t} + \Psi_z * \frac{\partial w_f}{\partial t},
\end{aligned}
\tag{4.29}
$$

The Poiseuille-type viscodynamic operator in the anisotropic case is

$$
\Psi_i(t) = m_i \delta(t) + (\nu/\kappa_i) H(t), \tag{4.30}
$$

where we use the anisotropic permeability κ_i in the principal directions $i = x, y, z$. Furthermore, the substitution $m_i = \rho_f T_i / \phi$ is applied, which includes the anisotropic tortuosity T_i of the solid matrix in the principal directions.

It should be remarked, that the time-dependent functions Ψ_i behave very differently depending on the frequency range of the propagating waves. Consequently, Biot's equations (4.29) are frequency dependent and Biot's characteristic frequency

$$
f_c = \min_i \left(\frac{\nu \phi}{T_i \kappa_i \rho_f} \right) \qquad i = x, y, z \tag{4.31}
$$

defines the limit between the high- and low-frequency ranges. In the present thesis, "high" and "low" frequencies will be referred to exclusively in terms of being above or below Biot's frequency (4.31).

The discussed expression for the Ψ functions (4.30) is valid for the low-frequency range. For high frequencies it is required to introduce different viscodynamic effects [13], which will be further discussed in Section 4.3.1. For the moment, only the low-frequency case will be treated.

Inserting the definition of Ψ into equations (4.29) and combining them with the constitutive equation (4.17) provides the governing equations for wave propagation in porous media as an inhomogeneous linear hyperbolic system of 13 first-order partial differential equations that can be expressed in the matrix-vector form

$$
\frac{\partial Q_p}{\partial t} + A_{pq} \frac{\partial Q_q}{\partial x} + B_{pq} \frac{\partial Q_q}{\partial y} + C_{pq} \frac{\partial Q_q}{\partial z} = E_{pq} Q_q. \tag{4.32}
$$

Note, that classical tensor notation is used in equation (4.32), which implies summation over each index that appears twice. The vector

$$
\vec{Q} = (\sigma_{xx}, \sigma_{yy}, \sigma_{zz}, \sigma_{xy}, \sigma_{yz}, \sigma_{xz}, u, v, w, p, u_f, v_f, w_f)^T \tag{4.33}
$$

contains the 13 unknown variables and A_{pq}, B_{pq}, and C_{pq} are the space-dependent Jacobian matrices of dimension 13×13 and are explicitly given through

$$
A_{pq} = - \begin{pmatrix}
0 & 0 & 0 & 0 & 0 & 0 & c_{11}^u & c_{16}^u & c_{15}^u & 0 & M\alpha_1 & 0 & 0 \\
0 & 0 & 0 & 0 & 0 & 0 & c_{12}^u & c_{26}^u & c_{25}^u & 0 & M\alpha_2 & 0 & 0 \\
0 & 0 & 0 & 0 & 0 & 0 & c_{13}^u & c_{36}^u & c_{35}^u & 0 & M\alpha_3 & 0 & 0 \\
0 & 0 & 0 & 0 & 0 & 0 & c_{16}^u & c_{66}^u & c_{56}^u & 0 & M\alpha_6 & 0 & 0 \\
0 & 0 & 0 & 0 & 0 & 0 & c_{14}^u & c_{46}^u & c_{45}^u & 0 & M\alpha_4 & 0 & 0 \\
0 & 0 & 0 & 0 & 0 & 0 & c_{15}^u & c_{56}^u & c_{55}^u & 0 & M\alpha_5 & 0 & 0 \\
\frac{1}{\rho_x^{(1)}} & 0 & 0 & 0 & 0 & 0 & 0 & 0 & 0 & \frac{\beta_x^{(1)}}{\rho_x^{(1)}} & 0 & 0 & 0 \\
0 & 0 & 0 & \frac{1}{\rho_y^{(1)}} & 0 & 0 & 0 & 0 & 0 & 0 & 0 & 0 & 0 \\
0 & 0 & 0 & 0 & 0 & \frac{1}{\rho_z^{(1)}} & 0 & 0 & 0 & 0 & 0 & 0 & 0 \\
0 & 0 & 0 & 0 & 0 & 0 & -M\alpha_1 & -M\alpha_6 & -M\alpha_5 & 0 & -M & 0 & 0 \\
\frac{1}{\rho_x^{(2)}} & 0 & 0 & 0 & 0 & 0 & 0 & 0 & 0 & \frac{\beta^{(2)}}{\rho_x^{(2)}} & 0 & 0 & 0 \\
0 & 0 & 0 & \frac{1}{\rho_y^{(2)}} & 0 & 0 & 0 & 0 & 0 & 0 & 0 & 0 & 0 \\
0 & 0 & 0 & 0 & 0 & \frac{1}{\rho_z^{(2)}} & 0 & 0 & 0 & 0 & 0 & 0 & 0
\end{pmatrix},
\tag{4.34}
$$

$$
B_{pq} = - \begin{pmatrix}
0 & 0 & 0 & 0 & 0 & 0 & c_{16}^u & c_{12}^u & c_{14}^u & 0 & 0 & M\alpha_1 & 0 \\
0 & 0 & 0 & 0 & 0 & 0 & c_{26}^u & c_{22}^u & c_{24}^u & 0 & 0 & M\alpha_2 & 0 \\
0 & 0 & 0 & 0 & 0 & 0 & c_{36}^u & c_{23}^u & c_{34}^u & 0 & 0 & M\alpha_3 & 0 \\
0 & 0 & 0 & 0 & 0 & 0 & c_{66}^u & c_{26}^u & c_{46}^u & 0 & 0 & M\alpha_6 & 0 \\
0 & 0 & 0 & 0 & 0 & 0 & c_{46}^u & c_{24}^u & c_{44}^u & 0 & 0 & M\alpha_4 & 0 \\
0 & 0 & 0 & 0 & 0 & 0 & c_{56}^u & c_{25}^u & c_{45}^u & 0 & 0 & M\alpha_5 & 0 \\
0 & 0 & 0 & \frac{1}{\rho_x^{(1)}} & 0 & 0 & 0 & 0 & 0 & 0 & 0 & 0 & 0 \\
0 & \frac{1}{\rho_y^{(1)}} & 0 & 0 & 0 & 0 & 0 & 0 & 0 & \frac{\beta_y^{(1)}}{\rho_y^{(1)}} & 0 & 0 & 0 \\
0 & 0 & 0 & 0 & \frac{1}{\rho_z^{(1)}} & 0 & 0 & 0 & 0 & 0 & 0 & 0 & 0 \\
0 & 0 & 0 & 0 & 0 & 0 & -M\alpha_6 & -M\alpha_2 & -M\alpha_4 & 0 & 0 & -M & 0 \\
0 & 0 & 0 & \frac{1}{\rho_x^{(2)}} & 0 & 0 & 0 & 0 & 0 & 0 & 0 & 0 & 0 \\
0 & \frac{1}{\rho_y^{(2)}} & 0 & 0 & 0 & 0 & 0 & 0 & 0 & \frac{\beta_y^{(2)}}{\rho_y^{(2)}} & 0 & 0 & 0 \\
0 & 0 & 0 & 0 & \frac{1}{\rho_z^{(2)}} & 0 & 0 & 0 & 0 & 0 & 0 & 0 & 0
\end{pmatrix},
\tag{4.35}
$$

$$
C_{pq}=-\begin{pmatrix}
0 & 0 & 0 & 0 & 0 & 0 & c_{15}^u & c_{14}^u & c_{13}^u & 0 & 0 & 0 & M\alpha_1 \\
0 & 0 & 0 & 0 & 0 & 0 & c_{25}^u & c_{24}^u & c_{23}^u & 0 & 0 & 0 & M\alpha_2 \\
0 & 0 & 0 & 0 & 0 & 0 & c_{35}^u & c_{34}^u & c_{33}^u & 0 & 0 & 0 & M\alpha_3 \\
0 & 0 & 0 & 0 & 0 & 0 & c_{56}^u & c_{46}^u & c_{36}^u & 0 & 0 & 0 & M\alpha_6 \\
0 & 0 & 0 & 0 & 0 & 0 & c_{45}^u & c_{44}^u & c_{34}^u & 0 & 0 & 0 & M\alpha_4 \\
0 & 0 & 0 & 0 & 0 & 0 & c_{55}^u & c_{45}^u & c_{35}^u & 0 & 0 & 0 & M\alpha_5 \\
0 & 0 & 0 & 0 & 0 & \frac{1}{\rho_x^{(1)}} & 0 & 0 & 0 & 0 & 0 & 0 & 0 \\
0 & 0 & 0 & 0 & 0 & \frac{1}{\rho_y^{(1)}} & 0 & 0 & 0 & 0 & 0 & 0 & 0 \\
0 & 0 & \frac{1}{\rho_z^{(1)}} & 0 & 0 & 0 & 0 & 0 & 0 & \frac{\beta_z^{(1)}}{\rho_z^{(1)}} & 0 & 0 & 0 \\
0 & 0 & 0 & 0 & 0 & 0 & -M\alpha_5 & -M\alpha_4 & -M\alpha_3 & 0 & 0 & 0 & -M \\
0 & 0 & 0 & 0 & 0 & \frac{1}{\rho_x^{(2)}} & 0 & 0 & 0 & 0 & 0 & 0 & 0 \\
0 & 0 & 0 & 0 & \frac{1}{\rho_y^{(2)}} & 0 & 0 & 0 & 0 & 0 & 0 & 0 & 0 \\
0 & 0 & \frac{1}{\rho_z^{(2)}} & 0 & 0 & 0 & 0 & 0 & 0 & \frac{\beta_z^{(2)}}{\rho_z^{(2)}} & 0 & 0 & 0
\end{pmatrix}. \tag{4.36}
$$

The reaction term on the right hand side of equation (4.32) is given by

$$
E_{pq}=\begin{pmatrix}
0 & 0 & 0 & 0 & 0 & 0 & 0 & 0 & 0 & 0 & 0 & 0 & 0 \\
0 & 0 & 0 & 0 & 0 & 0 & 0 & 0 & 0 & 0 & 0 & 0 & 0 \\
0 & 0 & 0 & 0 & 0 & 0 & 0 & 0 & 0 & 0 & 0 & 0 & 0 \\
0 & 0 & 0 & 0 & 0 & 0 & 0 & 0 & 0 & 0 & 0 & 0 & 0 \\
0 & 0 & 0 & 0 & 0 & 0 & 0 & 0 & 0 & 0 & 0 & 0 & 0 \\
0 & 0 & 0 & 0 & 0 & 0 & 0 & 0 & 0 & 0 & 0 & 0 & 0 \\
0 & 0 & 0 & 0 & 0 & 0 & 0 & 0 & 0 & 0 & \frac{\beta_x^{(1)}\nu}{\rho_x^{(1)}\kappa_x} & 0 & 0 \\
0 & 0 & 0 & 0 & 0 & 0 & 0 & 0 & 0 & 0 & 0 & \frac{\beta_y^{(1)}\nu}{\rho_y^{(1)}\kappa_y} & 0 \\
0 & 0 & 0 & 0 & 0 & 0 & 0 & 0 & 0 & 0 & 0 & 0 & \frac{\beta_z^{(1)}\nu}{\rho_z^{(1)}\kappa_z} \\
0 & 0 & 0 & 0 & 0 & 0 & 0 & 0 & 0 & 0 & 0 & 0 & 0 \\
0 & 0 & 0 & 0 & 0 & 0 & 0 & 0 & 0 & 0 & \frac{\beta_x^{(2)}\nu}{\rho_x^{(2)}\kappa_x} & 0 & 0 \\
0 & 0 & 0 & 0 & 0 & 0 & 0 & 0 & 0 & 0 & 0 & \frac{\beta_y^{(2)}\nu}{\rho_y^{(2)}\kappa_y} & 0 \\
0 & 0 & 0 & 0 & 0 & 0 & 0 & 0 & 0 & 0 & 0 & 0 & \frac{\beta_z^{(2)}\nu}{\rho_z^{(2)}\kappa_z}
\end{pmatrix}. \tag{4.37}
$$

Note, that for the matrix entries of A_{pq}, B_{pq},C_{pq} and E_{pq} we introduce the substitutions

$$
\begin{aligned}
\rho_i^{(1)} &= \rho - \rho_f^2/m_i\,, & \beta_i^{(1)} &= \rho_f/m_i\,, \\
\rho_i^{(2)} &= \rho_f - m_i\rho/\rho_f\,, & \beta^{(2)} &= \rho/\rho_f & \text{with} \qquad i = x, y, z.
\end{aligned} \tag{4.38}
$$

The equation system in (4.32) describes the phenomena of anisotropic poroelastic wave propagation in the framework of Biot's theory for the low-frequency case. Concerning the eigenstructure of this system, we observe that the Jacobians in (4.34) - (4.36) have 8 different non-zero eigenvalues, of which 4 have the same

value than the other four but with opposite sign. These values are the 4 phase velocities related to the 4 different modes propagating in an inviscid poroelastic medium. In general, there are one *fast* P-wave, two S-waves and one *slow* P-wave. The first three are analogous to those existing in elastic materials, whereas the fourth is a compressional wave which propagates at a speed which is generally even lower than the S-wave speed. The *slow* P-wave is physically associated to out-of-phase liquid and solid compressional particle motions. In the anisotropic case these 4 waves become *quasi*-waves, namely qP_1, qS_1, qS_2 and qP_2, respectively. In this case, the particle motions are generally not anymore purely aligned or perpendicular to the wave propagation directions.

Physically, at low frequencies $f < f_c$, Biot's theory predicts that the *slow* P-wave becomes extremely dissipative, behaving as a diffusion-type wave. This wave does not propagate over long distances, thus being only significant very close to the source or to material interfaces. For homogeneous media the wave types propagating in a poroelastic material at low-frequencies are almost indistinguishable from those in a single-phase medium properly attenuated [25]. However, using Biot's theory to model poroelastic wave propagation in the low-frequency range poses the problem of solving a hyperbolic equation system with stiff source terms [70]. The diffusive behavior induced by the existence of a large reactive source term produces wave effects at a very different time scale than the wave propagation phenomenon. As a consequence traditional explicit time integration schemes encounter problems of numerical stability. Some recent work has avoided this by deactivating the viscous boundary layers in the pores from Biot's theory [95]. In Section 4.4, the DG scheme will be constructed we will discuss two ways of overcoming the numerical stability problem using full Biot's theory, either by splitting the equation system (4.32) into a stiff and a non-stiff part or by using a new space-time Discontinuous Galerkin scheme. Before that, a way to introduce realistic high-frequency poroelastic wave propagation will be shown in the following Section.

4.3.1   High-Frequency Viscodynamic Operator

The Poiseuille flow assumption leading to (4.30) breaks down at a certain frequency [13] if using a study of the flow through a closed channel with oscillatory pressure pulses. Thus a different, more general, viscodynamic operator has to be introduced. Unfortunately for this case the operator's actual expression is very sensitive to the pore structure and thus for each material the frequency dependence might have to be analyzed separately [4]. A way around this problem is using a similar analysis as in Section 2.3 for the viscoelastic problem, thus substituting the convolutional products by a Generalized Maxwell Body. Thus, a phenomenological attenuating law can be used fitted to the experimentally observed wave dispersion for a given material in the high frequency range. The main difference with respect to Section 2.3 is that one has now to face a dynamical mechanism (af-

fecting a vector quantity: velocities) instead of a stiffness mechanism (affecting a tensor quantity: strains). Through the present Section the notation $i = x, y, z$ and $u_{f,x} = u_f$, $u_{f,y} = v_f$ and $u_{f,z} = w_f$ will be used for simplicity. A general high-frequency viscodynamic operator seen in Section 4.2.2 can be defined in the anisotropic case as

$$\Psi_i(t) = m_i \delta(t) + b_i(t), \tag{4.39}$$

where $b_i(t)$ will be a dissipation operator. This can be expressed as a GMB of n dissipating mechanisms, similar to (3.34), in the following manner

$$b_i(t) = \frac{\nu}{\kappa_i} \chi^{(i)}(t) H(t) = \frac{\nu}{\kappa_i} \left[1 - \sum_{\ell=1}^{n} Y_\ell^{(i)} \left(1 - e^{-\omega_\ell t} \right) \right] H(t). \tag{4.40}$$

A series of properties of the Dirac's delta and Heaviside functions will be recalled in the following:

$$
\begin{array}{llrcl}
\text{Property 1:} & & f(t) * \delta(t) & = & f(t) \\[2mm]
\text{Property 2:} & & \frac{\partial H(t)}{\partial t} & = & \delta(t) \\[2mm]
\text{Property 3:} & & f(t)\delta(t) & = & f(0)\delta(t) \\[2mm]
\text{Property 4:} & & \int_{-\infty}^{\infty} f(a) H(t-a) da & = & \int_{-\infty}^{t} f(a) da\,.
\end{array}
$$

Using Property 1 and the identity $f(t) * (\partial g(t)/\partial t) = (\partial f(t)/\partial t) * g(t)$ one may write

$$-\frac{\partial p}{\partial x} = \rho_f \frac{\partial u}{\partial t} + m_i \frac{\partial u_{f,i}}{\partial t} + \frac{\nu}{\kappa_i} \frac{\partial \left(\chi^{(i)}(t) H(t) \right)}{\partial t} * u_{f,i}\,. \tag{4.41}$$

At this point the last term of (4.41) has to be examined more carefully. First, one can apply the chain rule and Properties 2 and 3 to obtain

$$\frac{\partial \left(\chi^{(i)}(t) H(t) \right)}{\partial t} = \frac{\partial \left(\chi^{(i)}(t) \right)}{\partial t} H(t) + \chi^{(i)}(0)\delta(t). \tag{4.42}$$

The equation (4.41) can be further developed and, using $\chi^{(i)}(0) = 1$ from (4.40) and Property 1, we obtain

$$
\begin{aligned}
-\frac{\partial p}{\partial x} = {} & \rho_f \frac{\partial u}{\partial t} + m_i \frac{\partial u_{f,i}}{\partial t} + \frac{\nu}{\kappa_i} u_{f,i} - \\[2mm]
& -\frac{\nu}{\kappa_i} \sum_{\ell=1}^{n} Y_\ell^{(i)} \omega_\ell \int_{-\infty}^{\infty} u_{f,i}(\tau) e^{-\omega_\ell(t-\tau)} H(t-\tau) d\tau\,.
\end{aligned}
\tag{4.43}
$$

Finally one can use Property 4 to obtain

$$
\begin{aligned}
-\frac{\partial\, p}{\partial x} \;=\;\; & \rho_f \frac{\partial u}{\partial t} + m_i \frac{\partial u_{f,i}}{\partial t} + \frac{\nu}{\kappa_i} u_{f,i} - \\
& -\frac{\nu}{\kappa_i} \sum_{\ell=1}^{n} Y_\ell^{(i)} \omega_\ell \int_{-\infty}^{t} u_{f,i}(\tau) e^{-\omega_\ell(t-\tau)} d\tau\,.
\end{aligned}
\tag{4.44}
$$

It is now possible to introduce a set of anelastic-dynamic variables $\vec{\vartheta}^\ell = (\vartheta_x^\ell, \vartheta_y^\ell, \vartheta_z^\ell)^T$, similar to those in (2.23), as

$$
\vartheta_i^\ell(t) = \omega_\ell \int_{-\infty}^{t} u_{f,i}(\tau) e^{-\omega_\ell(t-\tau)}\, d\tau\,.
\tag{4.45}
$$

This leaves the dynamic equations as

$$
\begin{aligned}
-\frac{\partial\, p}{\partial x} \;=\;\; & \rho_f \frac{\partial u}{\partial t} + m_i \frac{\partial u_{f,i}}{\partial t} + \frac{\nu}{\kappa_i} u_{f,i} - \\
& -\frac{\nu}{\kappa_i} \sum_{\ell=1}^{n} Y_\ell^{(i)} \vartheta_i^\ell\,,
\end{aligned}
\tag{4.46}
$$

and the anelastic-dynamic variables evolve as (2.25), thus adding the following linear ordinary differential equations to the PDE system

$$
\frac{\partial}{\partial t}\vartheta_i^\ell(t) + \omega_\ell \vartheta_i^\ell(t) = \omega_\ell u_{f,i}(t)\,.
\tag{4.47}
$$

Note, that the Fourier transform of (4.39) collapses into (4.30) for $\omega \to 0$, thus being both operators consistent in the low-frequency case. In addition, for any frequency, (4.30) and (4.39) are identical in the inviscid case ($\nu = 0$). Various $\mathcal{Q}$-laws can be used to describe phenomenologically the observed frequency-dependent dissipation of a given poroelastic material, using expressions analogous to (2.18). In practice it often suffices to use a single mechanism ($n = 1$) and try to model a very narrow frequency band around a known $\mathcal{Q}$ value.

By introducing (4.46) and (4.47), we now obtain $n_v = 13 + 3n$ new variables and equations. Thus one can substitute (4.32) with the following

$$
\frac{\partial Q_p}{\partial t} + \check{A}_{pq}\frac{\partial Q_q}{\partial x} + \check{B}_{pq}\frac{\partial Q_q}{\partial y} + \check{C}_{pq}\frac{\partial Q_q}{\partial z} = \check{E}_{pq}Q_q.
\tag{4.48}
$$

where $p, q = 1, \cdots, n_v$. It will be assumed that $\vec{Q}$ contains the poroelastic 13 variables first, and the anelastic-viscodynamic variables (4.45) ordered in increasing mechanism number. The $\check{A}$, $\check{B}$, $\check{C}$ and $\check{E}$ are enlarged matrices which contain (4.34), (4.35), (4.36) and (4.37), as seen in Chapter 2. The Jacobians $\check{A}$, $\check{B}$, $\check{C}$ will only get new zero entries, while the $\check{E}$ matrix will change as follows, using the block structure

$$\check{E} = \begin{bmatrix} E^{LF} & E' \\ E'' & E''' \end{bmatrix} \in \mathbb{R}^{n_v \times n_v}, \tag{4.49}$$

where E^{LF} is exactly the low-frequency reaction matrix (4.37) and E' has the block structure

$$E' = [E'_1, \dots, E'_n] \in \mathbb{R}^{13 \times 3n}, \tag{4.50}$$

where each matrix $E'_\ell \in \mathbb{R}^{13 \times 3}$, with $\ell = 1, ..., n$, contains the anelastic-dynamic coefficients $Y_\ell^{(i)}$ of the ℓ-th mechanism in the form

$$E'_\ell = \begin{pmatrix} 0 & 0 & 0 \\ 0 & 0 & 0 \\ 0 & 0 & 0 \\ 0 & 0 & 0 \\ 0 & 0 & 0 \\ 0 & 0 & 0 \\ -\frac{\beta_x^{(1)}\nu}{\rho_x^{(1)}\kappa_x}Y_\ell^{(x)} & 0 & 0 \\ 0 & -\frac{\beta_y^{(1)}\nu}{\rho_y^{(1)}\kappa_y}Y_\ell^{(y)} & 0 \\ 0 & 0 & -\frac{\beta_z^{(1)}\nu}{\rho_z^{(1)}\kappa_z}Y_\ell^{(z)} \\ 0 & 0 & 0 \\ -\frac{\beta^{(2)}\nu}{\rho_x^{(2)}\kappa_x}Y_\ell^{(x)} & 0 & 0 \\ 0 & -\frac{\beta^{(2)}\nu}{\rho_y^{(2)}\kappa_y}Y_\ell^{(y)} & 0 \\ 0 & 0 & -\frac{\beta^{(2)}\nu}{\rho_z^{(2)}\kappa_z}Y_\ell^{(z)} \end{pmatrix}. \tag{4.51}$$

The matrix E''' in (4.49) is a diagonal matrix and has the structure

$$E''' = \begin{bmatrix} E'''_1 & & 0 \\ & \ddots & \\ 0 & & E'''_n \end{bmatrix} \in \mathbb{R}^{3n \times 3n}, \tag{4.52}$$

where each matrix $E'''_\ell \in \mathbb{R}^{3 \times 3}$, with $\ell = 1, ..., n$, is itself a diagonal matrix containing only the relaxation frequency ω_ℓ of the ℓ-th mechanism on its diagonal, i.e. $E'''_\ell = -\omega_\ell \cdot I$ with $I \in \mathbb{R}^{3 \times 3}$ denoting the identity matrix.

Finally the E'' block in (4.49) has the structure

$$E'' = \begin{bmatrix} E_1'' \\ \vdots \\ E_n'' \end{bmatrix} \in \mathbb{R}^{3n \times 13}, \tag{4.53}$$

where each sub-matrix $E_\ell'' \in \mathbb{R}^{3 \times 13}$, with $\ell = 1, ..., n$, contains the relaxation frequency ω_ℓ of the ℓ-th mechanism in the form

$$E_\ell'' = \omega_\ell \cdot \begin{pmatrix} 0 & 0 & 0 & 0 & 0 & 0 & 0 & 0 & 0 & 0 & 1 & 0 & 0 \\ 0 & 0 & 0 & 0 & 0 & 0 & 0 & 0 & 0 & 0 & 0 & 1 & 0 \\ 0 & 0 & 0 & 0 & 0 & 0 & 0 & 0 & 0 & 0 & 0 & 0 & 1 \end{pmatrix}. \tag{4.54}$$

It will later be seen that the incorporation of the high-frequency operator, as it doesn't affect the entries of the Jacobian matrices, can be ignored in the computation of the flux and stiffnesses. Only the ADER time integration procedure will have to now incorporate the new enlarged $\check{E}$ matrix, and the reaction term of the scheme will incorporate the additional operations involving the enlarged $\check{E}Q$ products. In the rest of the present thesis, the high-frequency cases studied will be the inviscid ones, for which we showed that the low-frequency formulation can be used. Therefore only the low-frequency equations will be developed in detail in the following.

4.4   The Numerical Scheme

The numerical scheme produced by (4.32) is very similar to the viscoelastic scheme (2.38). Let's reformulate the final form of the fully discrete ADER-DG scheme. In this case we will refer to the reference tetrahedron as $\mathcal{T}_E^S$ where the S is to explicitly state that this is a reference element only in space and not in time. The need to use such notation will become clear in Section 4.4.2. The discrete ADER-DG, after transformation into the canonical reference element $\mathcal{T}_E^S$ and time integration over one time step Δt from time level n to the following time level $n+1$ reads

$$\left[\left(\hat{Q}_{pl}^{(m)} \right)^{n+1} - \left(\hat{Q}_{pl}^{(m)} \right)^n \right] |J| \, M_{kl} \quad +$$

$$+ \quad \frac{1}{2} \sum_{j=1}^4 T_{pq}^j \left(\widetilde{A}_{qr}^{(m)} + \Theta_{ps}^{j,(m)} \right) (T_{rs}^j)^{-1} |S_j| \, F_{kl}^{-,j} \cdot I_{qlmn}(\Delta t) \left(\hat{Q}_{mn}^{(m)} \right)^n +$$

$$+ \quad \frac{1}{2} \sum_{j=1}^4 T_{pq}^j \left(\widetilde{A}_{qr}^{(m)} - \Theta_{ps}^{j,(m)} \right) (T_{rs}^j)^{-1} |S_j| \, F_{kl}^{+,j,i,h} \cdot I_{qlmn}(\Delta t) \left(\hat{Q}_{mn}^{(m_j)} \right)^n \tag{4.55}$$

$$- \quad A_{pq}^* |J| \, K_{kl}^\xi \cdot I_{qlmn}(\Delta t) \left(\hat{Q}_{mn}^{(m)} \right)^n - B_{pq}^* |J| \, K_{kl}^\eta \cdot I_{qlmn}(\Delta t) \left(\hat{Q}_{mn}^{(m)} \right)^n -$$

$$- \quad C_{pq}^* |J| \, K_{kl}^\zeta \cdot I_{qlmn}(\Delta t) \left(\hat{Q}_{mn}^{(m)} \right)^n = E_{pq} |J| \, M_{kl} \cdot I_{qlmn}(\Delta t) \left(\hat{Q}_{mn}^{(m)} \right)^n,$$

where $I_{plqm}(\Delta t)$ represents the high-order ADER time integration operator that is applied to the degrees of freedom $\left(\hat{Q}_{mn}^{(m)}\right)^n$ at time level n. The matrices M_{kl}, $F_{kl}^{\pm,j}$ and K_{kl} are the mass matrix, flux and stiffness matrices, respectively, and include space integrations of the basis functions that can be computed before-hand as shown in more detail in [55]. A_{pq}^*, B_{pq}^* and C_{pq}^* are the Jacobian matrices transformed into the reference tetrahedron $\mathcal{T}_E^S$. The matrix $\widetilde{A}_{qr}^{(m)}$ is similar to the matrix A_{qr} in (4.34), however, with the entries c_{ij}^u rotated from the global coordinate system to a local coordinate system of a tetrahedron's face. The rotation to this local coordinate system is done by applying the so-called Bond's matrix (3.12), see [36]. Furthermore, $|J|$ is the determinant of the Jacobian matrix of this transformation, see the Appendix in [55], and $|S_j|$ denotes the area of the j-th face of tetrahedron $\mathcal{T}^{(m)}$.

In the poroelastic case, new variables are introduced and thus the rotation matrix T_{pq} that transforms all variables of Q_p from the governing equation (4.32) into the reference system associated to the tetrahedron's j-th face reads differently. Its expression, in block-matrix form, is

$$T = \begin{bmatrix} T^t & 0 & 0 & 0 \\ 0 & T^v & 0 & 0 \\ 0 & 0 & T^p & 0 \\ 0 & 0 & 0 & T^v \end{bmatrix} \in \mathbb{R}^{13 \times 13}, \tag{4.56}$$

where $T^t \in \mathbb{R}^{6 \times 6}$ is the rotation matrix responsible for the stress tensor rotation as in the purely elastic part and is given as

$$T^t = \begin{pmatrix} n_x^2 & s_x^2 & t_x^2 & 2n_x s_x & 2s_x t_x & 2n_x t_x \\ n_y^2 & s_y^2 & t_y^2 & 2n_y s_y & 2s_y t_y & 2n_y t_y \\ n_z^2 & s_z^2 & t_z^2 & 2n_z s_z & 2s_z t_z & 2n_z t_z \\ n_y n_x & s_y s_x & t_y t_x & n_y s_x + n_x s_y & s_y t_x + s_x t_y & n_y t_x + n_x t_y \\ n_z n_y & s_z s_y & t_z t_y & n_z s_y + n_y s_z & s_z t_y + s_y t_z & n_z t_y + n_y t_z \\ n_z n_x & s_z s_x & t_z t_x & n_z s_x + n_x s_z & s_z t_x + s_x t_z & n_z t_x + n_x t_z \end{pmatrix}, \tag{4.57}$$

with the components of the normal vector $\vec{n} = (n_x, n_y, n_z)^T$ and the two tangential vectors $\vec{s} = (s_x, s_y, s_z)^T$ and $\vec{t} = (t_x, t_y, t_z)^T$, which lie in the plane determined by the boundary face of the tetrahedron and are orthogonal to each other and the normal vector $\vec{n}$ as shown in [55].

The matrix $T^v \in \mathbb{R}^{3 \times 3}$ is the rotation matrix responsible for the velocity vector rotation and is given as

$$T^v = \begin{pmatrix} n_x & s_x & t_x \\ n_y & s_y & t_y \\ n_z & s_z & t_z \end{pmatrix}. \tag{4.58}$$

The matrix T^p in equation (4.56) is responsible for the rotation of the p variable, and therefore has the simple expression $T^p = 1$.

The resulting ADER-DG scheme (4.55) provides automatically a high-order approximation in space and time and allows us to update the values of the unknown variables from a time step t^n to a following t^{n+1} without storing any intermediate values. The scheme (4.55) using ADER time integration provides accurate results for the high-frequency inviscid case, as will be shown by convergence tests further in this paper. However for the low-frequency case, as most explicit time-domain schemes, it becomes unstable. In the following Sections 4.4.1 and 4.4.2 two ways of avoiding these instabilities will be shown.

4.4.1   Fractional-Step Method

As discussed in previous Sections, the solution of Biot's equations for the low-frequency range poses a problem of instability due to the solution of a problem which includes two largely different timescales. In mathematical terms this is understood as a "stiff" problem. In order to solve it with an explicit time-integration scheme one could strongly reduce the time step in order to capture the diffusive effects, according to the stability limit of parabolic equations, but this would dramatically reduce the performance of the solver. The use of a partition method was suggested in [24, 32], which is formally equivalent to the solution introduced in the present Section.

The underlying concept of this fractional-step (FS) method (see [90] for a detailed description), also known as Godunov-splitting, is the separation of a PDE system into two separate ones, one stiff and the other non-stiff. Then both systems are solved in an alternating manner, introducing the solution of one of them as the initial condition for the other in a sequential way. The big advantage of the FS method is that it allows us to use different solvers for each of the parts and thus optimize the time step required by both methods. Furthermore, it is very easy to implement in existing explicit solvers. In the present case the equation system (4.32) would be split in the two following ones

$$
\begin{aligned}
\frac{\partial Q_p}{\partial t} + A_{pq}\frac{\partial Q_q}{\partial x} + B_{pq}\frac{\partial Q_q}{\partial y} + C_{pq}\frac{\partial Q_q}{\partial z} &= 0, \\
\frac{\partial Q_p}{\partial t} &= E_{pq}Q_q.
\end{aligned}
\tag{4.59}
$$

The first equation of (4.59) is non-stiff, as there is no reaction term, and can thus be solved using explicit time-integration schemes. The second, on the contrary, is stiff when the entries of E are large. First of all, we solve the second equation system for a Δt as large as the solver used for the first equation allows. This can be done analytically as it is a set of linear ordinary differential equations. The

solution to this system has non-zero components

$$
\begin{aligned}
u^*(\Delta t) &= \tfrac{\beta_x^{(1)}\rho_x^{(2)}}{\beta^{(2)}\rho_x^{(1)}} \left[\exp\left(\tfrac{\beta^{(1)}\nu}{\rho_x^{(1)}\kappa_x}\Delta t\right) - 1\right] u_f(0) + u(0)\,, \\[4pt]
v^*(\Delta t) &= \tfrac{\beta_y^{(1)}\rho_y^{(2)}}{\beta^{(2)}\rho_y^{(1)}} \left[\exp\left(\tfrac{\beta^{(1)}\nu}{\rho_y^{(1)}\kappa_y}\Delta t\right) - 1\right] v_f(0) + v(0)\,, \\[4pt]
w^*(\Delta t) &= \tfrac{\beta_z^{(1)}\rho_z^{(2)}}{\beta^{(2)}\rho_z^{(1)}} \left[\exp\left(\tfrac{\beta^{(1)}\nu}{\rho_z^{(1)}\kappa_z}\Delta t\right) - 1\right] w_f(0) + w(0)\,, \\[4pt]
u_f^*(\Delta t) &= \exp\left(\tfrac{\beta_x^{(2)}\nu}{\rho_x^{(2)}\kappa_x}\Delta t\right) u_f(0)\,, \\[4pt]
v_f^*(\Delta t) &= \exp\left(\tfrac{\beta_y^{(2)}\nu}{\rho_y^{(2)}\kappa_y}\Delta t\right) v_f(0)\,, \\[4pt]
w_f^*(\Delta t) &= \exp\left(\tfrac{\beta_z^{(2)}\nu}{\rho_z^{(2)}\kappa_z}\Delta t\right) w_f(0)\,.
\end{aligned}
\tag{4.60}
$$

The second step is then to solve the first equation in (4.59) for the same Δt but, as requested by the FS theory, using the Q_p^* variables instead. Here, the vector Q_p^* includes the standard entries of Q_p except that the variables u, v, w, u_f, v_f and w_f are substituted by their *star* counterparts obtained in (4.60). To solve this second step one can use the ADER-DG scheme (4.55) but now without the reaction matrix E. The solution of this last part will be then the solution of the full equation system (4.32) for a single time step advancement of size Δt. The maximum size of this time step is limited to the maximum Δt allowed by the standard ADER-DG scheme for the non-stiff case. In the following, the combined FS method and the ADER-DG method described in this Section will be referred to as ADER-DG(FS).

Note, that the splitting of the system using FS schemes leads to a solution which is formally first-order accurate [90], although second-order accuracy is reached often in practice. Higher-order convergence is not possible, even by using highly accurate time-integration for both fractional-steps, unless the operators associated to the non-stiff and stiff terms commute. In the present case it should hold from equations in (4.59) that $(A\partial_x + B\partial_y + C\partial_z)\cdot E = E\cdot(A\partial_x + B\partial_y + C\partial_z)$, which is not true in the poroelastic case. In fact, when the solutions are not smooth, it is not even clear if a FS method converges at all to the exact solution, as the resulting wave speeds are often wrong [91]. Its usage can give qualitatively good solutions for wave propagation models under certain conditions but is far away from producing quantitatively reliable results, as will be further shown with convergence tests.

4.4.2 Space-Time DG Method

The local Space-Time Discontinuous Galerkin method was first introduced in [54] for non-linear one-dimensional stiff problems. The main idea is to avoid the Taylor expansion in time, commonly used for the ADER time discretization, and to

use a fully discontinuous scheme in time as well as in space. Discontinuities are handled by using numerical fluxes, resulting in a scheme of arbitrary high order. Furthermore, and unlike FS-based methods, it is asymptotically consistent as will be shown numerically in a chapter of its own. Additionally, it is a robust enough method to work on space-time grids as coarse as the non-stiff equation system would allow. In the following the scheme described in [54] is extended to three-dimensional DG schemes and we give a brief outline on how to use it together with the algorithm (4.55) to develop a local space-time ADER-DG method, referred to as ADER-DG(ST) in the following.

First of all one can assume, instead of the usual DG assumption in expression (1.23), that the variables are represented in a space-time basis as

$$\left(Q_h^{(m)} \right)_p (\xi, \eta, \zeta, \tau) = \hat{Q}_{pln}^{(m)} \chi_n(\tau) \Phi_l(\xi, \eta, \zeta) , \qquad (4.61)$$

so that now the degrees of freedom are *time-independent*. The time basis functions $\chi_n(\tau)$ are chosen to be Legendre polynomials. Notice, that now the total amount of degrees of freedom is $N + 1$ times that of a standard ADER-DG scheme. Let's write down the governing equation (4.32) in the reference element as

$$\frac{\partial Q_o}{\partial t} + A_{oq}^* \frac{\partial Q_q}{\partial x} + B_{oq}^* \frac{\partial Q_q}{\partial y} + C_{oq}^* \frac{\partial Q_q}{\partial z} = E_{oq}^* Q_q, \qquad (4.62)$$

being A^*, B^*, C^* and E^* the Jacobian and reaction matrices transformed into the space-time reference tetrahedron $\mathcal{T}_E^{ST} = \mathcal{T}_E^S \times \mathcal{T}_E^T$, where $\mathcal{T}_E^S$ is the space reference element, or reference tetrahedron, $\mathcal{T}_E^T$ the one dimensional time reference element and $\times$ denotes a tensorial product. As the time reference element is defined for $\tau = [0, 1]$, for a time increment Δt the star matrices appearing in the local governing equation (4.62) are the ones for the time continuous ADER-DG (see [55]), multiplied by Δt. The following notation for the space-time and the purely space inner products can be used:

$$[f, g] = \int_{\mathcal{T}_E^{ST}} f(\xi, \eta, \zeta, \tau) \cdot g(\xi, \eta, \zeta, \tau) \, d\xi d\eta d\zeta d\tau;$$

$$\langle f, g \rangle = \int_{\mathcal{T}_E^S} f(\xi, \eta, \zeta, \tau) \cdot g(\xi, \eta, \zeta, \tau) \, d\xi d\eta d\zeta . \qquad (4.63)$$

Then one can multiply equation (4.62) by a space-time test function and integrate over $\mathcal{T}_E^{ST}$. Instead of integrating the second term by parts as in expression (1.29) one can integrate by parts the first term. This way, unlike in [135], the approach

is kept local, thus resulting in the system

$$
\begin{aligned}
\delta_{oq} \left\langle \chi_s(1)\Phi_r, \chi_k(1)\Phi_l \right\rangle \left(\hat{Q}_{qlk}^{(m)} \right)^{(n)} \quad &- \quad \delta_{om} \left\langle \chi_s(0)\Phi_r, \Phi_n \right\rangle \left(\hat{Q}_{mn}^{(m)} \right)^{(\tau=0)} - \\
&- \quad \delta_{oq} \left[\tfrac{\partial}{\partial \tau}\chi_s\Phi_r, \chi_k\Phi_l \right] \left(\hat{Q}_{qlk}^{(m)} \right)^{(n)} + \\
&+ \quad A_{oq}^* \left[\chi_s\Phi_r, \chi_k\tfrac{\partial}{\partial \xi}\Phi_l \right] \left(\hat{Q}_{qlk}^{(m)} \right)^{(n)} + \\
&+ \quad B_{oq}^* \left[\chi_s\Phi_r, \chi_k\tfrac{\partial}{\partial \eta}\Phi_l \right] \left(\hat{Q}_{qlk}^{(m)} \right)^{(n)} + \\
&+ \quad C_{oq}^* \left[\chi_s\Phi_r, \chi_k\tfrac{\partial}{\partial \zeta}\Phi_l \right] \left(\hat{Q}_{qlk}^{(m)} \right)^{(n)} = \\
&= \quad E_{oq}^* \left[\chi_s\Phi_r, \chi_k\Phi_l \right] \left(\hat{Q}_{qlk}^{(m)} \right)^{(n)} .
\end{aligned}
\tag{4.64}
$$

The notation $\left(\hat{Q}^{(m)} \right)^{(n)}$ has been employed to denote the degrees of freedom inside the spatial element (m) and time element (n), and $\left(\hat{Q}^{(m)} \right)^{(\tau=0)}$ the *space only* degrees of freedom evaluated at the boundary between time elements $(n-1)$ and (n). The integration by parts allows us to use the theory of numerical fluxes, not in the spatial dimension as in any DG method, but in the time dimension. Due to causality, the time fluxes at both ends of the time interval $[0,1]$ are exclusively dependent on the previous values of the variables and never on the posterior ones. It can be seen that all the integrals in expression (4.64) are performed in the reference elements $\mathcal{T}_E^S$ and $\mathcal{T}_E^{ST}$ and can therefore be pre-computed and stored. Now the matrices applied to $\left(\hat{Q}^{(m)} \right)^{(n)}$ can be grouped as the tensor Y_{oqsrlk} and the matrices applied to $\left(\hat{Q}^{(m)} \right)^{(\tau=0)}$ as $\delta_{om}F_{srn}^0$, thus obtaining

$$
Y_{oqsrlk} \left(\hat{Q}_{qlk}^{(m)} \right)^{(n)} = \delta_{om}F_{srn}^0 \left(\hat{Q}_{mn}^{(m)} \right)^{(\tau=0)}
\tag{4.65}
$$

and by isolating the space-time degrees of freedom of the $(m) \times (n)$ element we obtain

$$
\left(\hat{Q}_{qlk}^{(m)} \right)^{(n)} = \left(Y_{oqsrlk} \right)^{-1} \cdot \delta_{om}F_{srn}^0 \left(\hat{Q}_{mn}^{(m)} \right)^{(\tau=0)} .
\tag{4.66}
$$

Notice, that if one aims at knowing the time integral of the degrees of freedom over the interval $t = [t, t + \Delta t]$, they can be obtained by just taking $k = 1$ in the expression (4.66) and multiplying by the size of the time element Δt. One can thus define

$$
I_{qlmn}^{ST} \equiv \Delta t \left(Y_{oqsrl1} \right)^{-1} \cdot \delta_{om}F_{srn}^0
\tag{4.67}
$$

and substitute I_{qlmn}^{ST} for the standard I_{qlmn} in the scheme (4.55) to obtain the desired fully discrete local ADER-DG(ST) scheme. Notice that, although the time-integration is locally implicit, the global scheme remains an explicit time-domain method. This is the main difference to previous formulations of space-time Discontinuous Galerkin methods [135]. In addition, the time degrees of freedom are

exclusively internal to the I_{qlmn}^{ST} calculation. This means that these degrees of freedom are not stored and the running algorithm has exactly the same number of degrees of freedom as the standard ADER-DG scheme. The tensor Y is different for each element (m) and therefore its inversion has to be performed once per each element. As its value is constant in time it can be precomputed and stored before the actual time marching of the scheme. This is of great advantage compared to globally implicit schemes where a linear system has to be inverted, whose size is proportional to the total number of elements in the computational mesh. It should also be noticed that the additional degrees of freedom used in the derivation of expression (4.65) are internal to the computation Y_{oqsrl1} so that they are neither stored or evolved in time during run time. General properties of the local space-time discontinuous method applied to high-order finite volume schemes can be found in [54].

4.5   Convergence Study

In this Section a numerical convergence study of the proposed ADER-DG approaches on tetrahedral meshes is presented, in order to demonstrate its arbitrarily high order of convergence in the presence of poroelastic material. Results from second- to sixth-order DG schemes are shown, denoted by $\mathcal{O}2$ to $\mathcal{O}6$, respectively. The schemes compared are ADER-DG, ADER-DG(FS) and ADER-DG(ST), as shown in the three last Sections.

Similar to previous Section 2.7, the convergence orders are determined by solving the three-dimensional, poroelastic wave equations on a computational domain $\Omega = [-1,1] \times [-1,1] \times [-1,1] \in \mathbb{R}^3$ with periodic boundary conditions.

Two major cases are studied: inviscid and viscous fluid content. The first case has high-frequency properties, while the second lies in the low-frequency range. The homogeneous poroelastic material is a brine-saturated sandstone, similar to that described in [32] for the poroacoustic case, and its parameters are given in Table 4.1.

To confirm that poroelasticity is treated correctly, let's superimpose three plane waves $Q_p^{(l)}$, $l = 1, ..., 3$, (a *fast* P-, an S- and a *slow*-P wave) of the form given in expression (2.55) traveling along the diagonal of the cube, that is the $(1, 1, 1)$ direction, i.e. one has the three wave number vectors

$$\vec{k}^{(1)} = (k_x^{(1)}, k_y^{(1)}, k_z^{(1)})^T = (\pi, \pi, \pi)^T \,, \tag{4.68}$$

$$\vec{k}^{(2)} = (k_x^{(2)}, k_y^{(2)}, k_z^{(2)})^T = (\pi, \pi, \pi)^T \,, \tag{4.69}$$

$$\vec{k}^{(3)} = (k_x^{(3)}, k_y^{(3)}, k_z^{(3)})^T = (\pi, \pi, \pi)^T \,. \tag{4.70}$$

leading to periodic, sinusoidal waves in the unit-cube. A strictly descending order of the 13 eigenvalues of the matrices (4.34)-(4.36) is chosen, so that the eigenvalue corresponding to the P-wave is the first, the one for the S-wave is the second

Table 4.1: Coefficients for the isotropic poroelastic material given in $S.I.$ units as used in the convergence tests. The inviscid case is identical but with $\nu = 0$

ρ_s	ρ_f	λ^{matrix}	μ^{matrix}	K_s	K_f	ν	ϕ	κ	T
2500	1040	$12.0e9$	$10.0e9$	$40.0e9$	$2.5e9$	0.001	0.2	$600.0 \cdot 10^{-15}$	3

and the one for the *slow* P-wave is the fourth. Note, that the chosen poroelastic material possesses a Biot frequency for the viscous case of $f_c^{VIS} = 1.068 \cdot 10^5 Hz$ and $f_c^{INV} = 0 Hz$ for the inviscid case. The maximum frequencies of the present problem are $f^{VIS} = 3459.6 Hz$ and $f^{INV} = 3482.4 Hz$ for the viscous and inviscid cases respectively, thus being both of them clear examples of low- and high-frequency poroelastic wave propagation. Notice that, for the low-frequency case, the *slow*-P wave becomes a quasi-static diffusive wave, as predicted by Biot. The total simulation time T is set to $T = 5.0 \cdot 10^{-5}$s. The CFL number is set in all computations to $C = 0.5$ of the stability limit $\frac{1}{2N+1}$ of Runge-Kutta DG schemes (see (1.67)). Notice that the time step used for each mesh and order is the same for all three methods.

The numerical analysis to determine the convergence orders is performed on a sequence of tetrahedral meshes. The mesh sequence is obtained by dividing the computational domain Ω into a number of sub cubes, which are then subdivided into five tetrahedra.

A total of 3 series of simulations, namely convergence tests, were performed:

- Inviscid high frequency with ADER-DG,

- Viscous low frequency with ADER-DG(ST),

- Viscous low frequency with ADER-DG(FS).

For all the convergence tests we picked the variable of the solid velocity component u of the system of equations (4.32) to numerically determine the convergence order of the used DG schemes. The errors and convergence orders are computed the same way as in Section 2.7. The results of the convergence tests are shown in Tables 4.2 and 4.3 and plotted in Figs. 4.1 and 4.2, demonstrating the dependence of the L^∞ error with respect to (a) mesh width h, (b) number of degrees of freedom per variable N_d and (c) CPU time. The simulations were performed on a Pentium IV 2.8 GHz processor with 2GB of RAM. With mesh refinement the higher-order schemes, in the present case the standard ADER-DG and ADER-DG(ST), converge faster as shown in Figs. 4.1(a) and 4.2(a) than lower-order schemes as ADER-DG(FS). Furthermore, Figs. 4.1(b) and 4.2(b) demonstrate that higher-order schemes reach a desired accuracy requiring a lower number of total degrees of freedom. The total number of degrees of freedom is the product of the
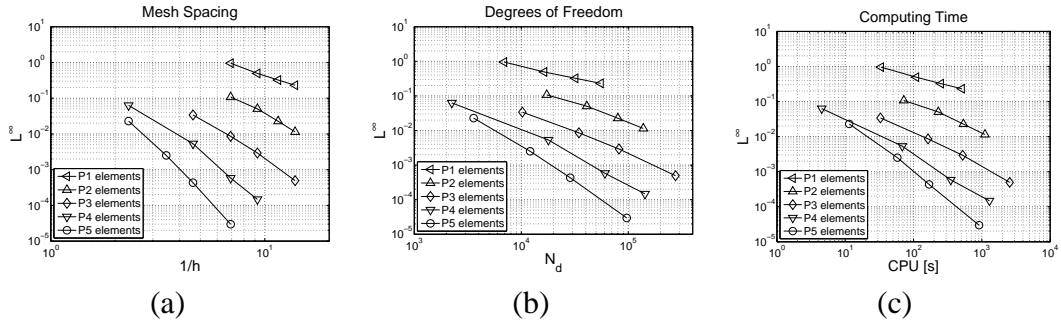
Figure 4.1: Visualization of the convergence results for the ADER-DG scheme in the inviscid high-frequency case. The symbols P1-P6 stand for the maximum polynomial degree of the basis functions used. Notice that the slope of the lines is proportional to the computed convergence order. The L^∞ error of variable u is plotted versus (a) the mesh spacing h, (b) the number of degrees of freedom N_d and (c) the CPU time.

number of mesh elements and the degrees of freedom per element. Therefore, obviously the increasing number of degrees of freedom of higher-order schemes is over-compensated by the dramatic decrease of the number of required mesh elements to reach a certain error level. Also the CPU time comparisons in Figs. 4.1(c) and 4.2(c) show that the higher-order methods reach a desired error level in less computational time.

It is clear from Fig. 4.2 and Tables 4.2 and 4.3 that the fractional-step method as is ADER-DG(FS) is not well suited for the accurate simulation of low-frequency range poroelastic waves. Although in some cases it can reach second order, its convergence properties do not improve when high-order polynomials are used to represent the variables. Particularly, in Table 4.3 it can be seen that the method cannot converge beyond some certain error value. In particular, Fig. 4.2(a) shows that computationally it is much more efficient to use the ADER-DG(ST) method because a desired accuracy can be reached using coarser computational cells and therefore less elements. This has an effect on the computational time as can be seen in Fig. 4.2(c).

The computational time required by all three methods is comparable, the high-frequency case being slightly faster in all cases. For the low-frequency it can be observed that the ADER-DG(FS) methods require less computational time, mainly due to the fact that they don't include the reaction term E into the time-integration procedure. However the accuracy is consistently better for the ADER-DG(ST) for all setups with the only exception of the very low-order case $P1$. At higher orders the increase in accuracy is more evident, the errors being orders of magnitude smaller than those obtained with the ADER-DG(FS) method.

Table 4.2: Convergence rates of the velocity component u of the ADER-DG $\mathcal{O}2$ up to ADER-DG $\mathcal{O}6$ schemes on tetrahedral meshes for the inviscid high-frequency case.

			ADER-DG		
h	N_d	I	L^∞	$\mathcal{O}_{L\infty}$	$CPU[s]$
$1.44 \cdot 10^{-1}$	6912	68	$3.8885 \cdot 10^{-1}$	–	79.7
$1.08 \cdot 10^{-1}$	16384	91	$2.0983 \cdot 10^{-1}$	2.1	251.7
$8.66 \cdot 10^{-2}$	32000	113	$1.3071 \cdot 10^{-1}$	2.1	610.5
$7.21 \cdot 10^{-2}$	55296	136	$9.0967 \cdot 10^{-2}$	2.0	1268.3
$1.44 \cdot 10^{-1}$	17280	113	$2.5256 \cdot 10^{-2}$	–	173.9
$1.08 \cdot 10^{-1}$	40960	151	$1.0518 \cdot 10^{-2}$	3.0	550.0
$8.66 \cdot 10^{-2}$	80000	189	$5.5229 \cdot 10^{-3}$	2.9	1340.3
$7.21 \cdot 10^{-2}$	138240	226	$3.3461 \cdot 10^{-3}$	2.7	2767.1
$2.16 \cdot 10^{-1}$	10240	106	$7.9373 \cdot 10^{-3}$	–	82.1
$1.44 \cdot 10^{-1}$	34560	158	$2.0592 \cdot 10^{-3}$	3.3	411.3
$1.08 \cdot 10^{-1}$	81920	211	$6.8809 \cdot 10^{-4}$	3.8	1300.8
$7.21 \cdot 10^{-2}$	276480	316	$1.5594 \cdot 10^{-4}$	3.7	6571.8
$4.33 \cdot 10^{-1}$	2240	68	$1.1778 \cdot 10^{-2}$	–	12.1
$2.16 \cdot 10^{-1}$	17920	136	$5.0270 \cdot 10^{-4}$	4.6	192.1
$1.44 \cdot 10^{-1}$	60480	204	$8.1186 \cdot 10^{-5}$	4.5	971.2
$1.08 \cdot 10^{-1}$	143360	271	$2.0913 \cdot 10^{-5}$	4.7	3062.9
$4.33 \cdot 10^{-1}$	3584	83	$1.0803 \cdot 10^{-3}$	–	29.3
$2.88 \cdot 10^{-1}$	12096	125	$1.2239 \cdot 10^{-4}$	5.4	147.7
$2.16 \cdot 10^{-1}$	28672	166	$2.3855 \cdot 10^{-5}$	5.7	464.7
$1.44 \cdot 10^{-1}$	96768	249	$2.6912 \cdot 10^{-6}$	5.4	2349.5

Table 4.3: Convergence rates of the velocity component u of the ADER-DG $\mathcal{O}2$ up to ADER-DG $\mathcal{O}6$ schemes on tetrahedral meshes for the viscous low-frequency case. Values of the number of degrees of freedom N_d and of the iterations I are identical to those in Table 4.2.

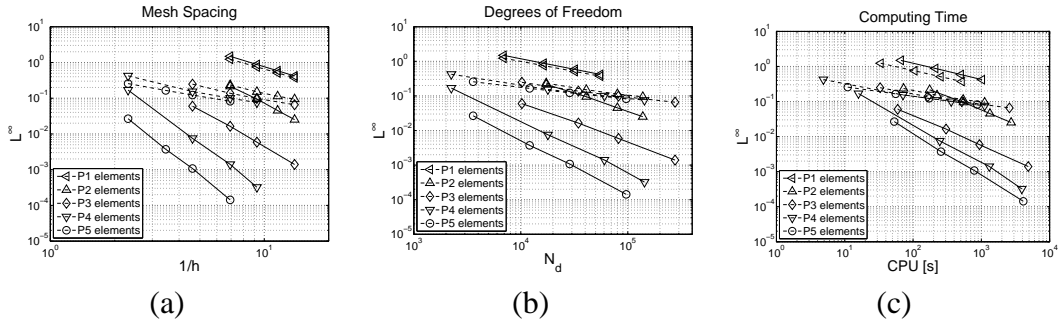|	ADER-DG(ST)			ADER-DG(FS)		
h	L^∞	$\mathcal{O}_{L^\infty}$	$CPU[s]$	L^∞	$\mathcal{O}_{L^\infty}$	$CPU[s]$
$1.44 \cdot 10^{-1}$	$2.7850 \cdot 10^{-1}$	—	81.0	$2.8139 \cdot 10^{-1}$	—	91.5
$1.08 \cdot 10^{-1}$	$1.5006 \cdot 10^{-1}$	2.1	256.0	$1.5252 \cdot 10^{-1}$	2.1	299.7
$8.66 \cdot 10^{-2}$	$9.3845 \cdot 10^{-2}$	2.1	619.7	$9.6237 \cdot 10^{-2}$	2.1	702.2
$7.21 \cdot 10^{-2}$	$6.4034 \cdot 10^{-2}$	2.1	1289.4	$6.6379 \cdot 10^{-2}$	2.0	1458.4
$1.44 \cdot 10^{-1}$	$2.1170 \cdot 10^{-2}$	—	203.9	$2.2990 \cdot 10^{-2}$	—	197.6
$1.08 \cdot 10^{-1}$	$7.3896 \cdot 10^{-2}$	3.7	647.8	$9.4670 \cdot 10^{-3}$	3.1	640.5
$8.66 \cdot 10^{-2}$	$4.1012 \cdot 10^{-3}$	2.6	1577.4	$6.1988 \cdot 10^{-3}$	1.9	1525.3
$7.21 \cdot 10^{-2}$	$2.4781 \cdot 10^{-3}$	2.8	3259.7	$4.5885 \cdot 10^{-3}$	1.6	3161.1
$2.16 \cdot 10^{-1}$	$6.8010 \cdot 10^{-3}$	—	138.1	$8.8264 \cdot 10^{-3}$	—	90.7
$1.44 \cdot 10^{-1}$	$1.6704 \cdot 10^{-3}$	3.5	692.3	$3.7300 \cdot 10^{-3}$	2.1	454.7
$1.08 \cdot 10^{-1}$	$5.6757 \cdot 10^{-4}$	3.8	2190.8	$2.6524 \cdot 10^{-3}$	1.2	1461.1
$7.21 \cdot 10^{-2}$	$1.3162 \cdot 10^{-4}$	3.6	11114.1	$2.2356 \cdot 10^{-3}$	0.4	7207.7
$4.33 \cdot 10^{-1}$	$8.8939 \cdot 10^{-3}$	—	32.0	$1.0877 \cdot 10^{-2}$	—	13.0
$2.16 \cdot 10^{-1}$	$4.3880 \cdot 10^{-4}$	4.3	510.7	$2.4746 \cdot 10^{-3}$	2.1	201.2
$1.44 \cdot 10^{-1}$	$6.5967 \cdot 10^{-5}$	4.7	2587.5	$2.1599 \cdot 10^{-3}$	0.3	1018.6
$1.08 \cdot 10^{-1}$	$1.8116 \cdot 10^{-5}$	4.5	8122.6	$2.1241 \cdot 10^{-3}$	0.1	3215.5
$4.33 \cdot 10^{-1}$	$8.6298 \cdot 10^{-4}$	—	116.6	$2.8564 \cdot 10^{-3}$	—	30.6
$2.88 \cdot 10^{-1}$	$9.5154 \cdot 10^{-5}$	5.4	592.1	$2.2066 \cdot 10^{-3}$	0.6	153.5
$2.16 \cdot 10^{-1}$	$2.0776 \cdot 10^{-5}$	5.3	1860.0	$2.1271 \cdot 10^{-3}$	0.1	482.2
$1.44 \cdot 10^{-1}$	$2.2545 \cdot 10^{-6}$	5.5	9412.7	$2.1184 \cdot 10^{-3}$	0.0	2441.9

Figure 4.2: Visualization of the convergence results for the ADER-DG(ST) (solid) and ADER-DG(FS) (dashed) schemes in the viscous low-frequency case. The symbols P1-P6 stand for the maximum polynomial degree of the basis functions used. Notice that the slope of the lines is proportional to the computed convergence order. The L^∞ error of variable u is plotted versus (a) the mesh spacing h, (b) the number of degrees of freedom N_d and (c) the CPU time.

4.6 Asymptotic Consistency

As a main result of the numerical convergence studies in the previous section, it has already been found that the fractional-step (FS) method is not able to achieve the desired order of accuracy in space and time, albeit a very high-order spatial discretization was chosen and although even a high-order accurate time discretization was used in each of the FS sub-steps. However, the combination of the individual sub-steps of the FS scheme resulting from the splitting of the governing equations is formally only first-order accurate for stiff systems. This is a severe limitation of this very simple approach to stiff partial differential equations. The lack of formal order of accuracy of the FS method will also be seen in this Section, where the stiff asymptotic limit behavior of the governing equations will be discussed.

It is well known that hyperbolic systems with stiff source terms usually tend to some reduced asymptotic PDE systems that may also change their type, see [37]. The original hyperbolic system may for example become hyperbolic-parabolic or even entirely parabolic. Hence, in the asymptotic limit the hyperbolic system of the governing equations may tend towards a convection-diffusion or purely diffusive system. For this reason, one calls the stiff asymptotic limit also the diffusion limit of the hyperbolic governing equations.

4.6.1 Asymptotic limit equations

In this section we study the asymptotic limit behavior of the equations of poroelasticity in one space dimension in the low-frequency range in connection with the corresponding behavior of the numerical methods presented above. For notational simplicity, the one-dimensional system of poroelasticity can be derived

from (4.32)-(4.37) and is written with the definitions $\sigma = \sigma_{xx}$, $v = u^f$, $\frac{1}{\epsilon_1} = \frac{\beta_x^{(1)}\nu}{\rho_x^{(1)}\kappa_x}$ and $\frac{1}{\epsilon_2} = \frac{\beta^{(2)}\nu}{\rho_x^{(2)}\kappa_x}$ as follows:

$$
\begin{aligned}
\frac{\partial}{\partial t}\sigma - c\frac{\partial}{\partial x}u - \alpha M\frac{\partial}{\partial x}v &= 0, \\
\frac{\partial}{\partial t}u - \frac{1}{\rho_1}\frac{\partial}{\partial x}\sigma - \frac{\beta_1}{\rho_1}\frac{\partial}{\partial x}p &= \frac{1}{\epsilon_1}v, \\
\frac{\partial}{\partial t}p + \alpha M\frac{\partial}{\partial x}u + M\frac{\partial}{\partial x}v &= 0, \\
\frac{\partial}{\partial t}v - \frac{1}{\rho_2}\frac{\partial}{\partial x}\sigma - \frac{\beta_2}{\rho_2}\frac{\partial}{\partial x}p &= \frac{1}{\epsilon_2}v.
\end{aligned}
\tag{4.71}
$$

In order to obtain the reduced asymptotic limit system of (4.71) for the case $\epsilon_2 \to 0$, standard asymptotic series expansion techniques are used, which expand variable v appearing in the stiff source in a power series in terms of the small parameter ϵ_2 as

$$
v = v_0 + \epsilon_2^1 v_1 + \mathcal{O}(\epsilon_2^2).
\tag{4.72}
$$

For the present purposes it is sufficient to consider in the following only terms up to first order in ϵ_2, i.e. terms of $\mathcal{O}(\epsilon_2^1)$. Inserting (4.72) into the last equation of the system (4.71) one gets

$$
\frac{\partial}{\partial t}v_0 + \epsilon_2\frac{\partial}{\partial t}v_1 - \frac{1}{\rho_2}\frac{\partial}{\partial x}\sigma - \frac{\beta_2}{\rho_2}\frac{\partial}{\partial x}p = \epsilon_2^{-1}v_0 + v_1.
\tag{4.73}
$$

Since equation (4.73) must hold for *any* value of ϵ_2, one can collect terms of equal powers in ϵ_2 and set each individual coefficient of the resulting expansion in ϵ_2 to zero. The leading order term ϵ_2^{-1} immediately yields

$$
v_0 = 0.
\tag{4.74}
$$

Inserting this result into (4.73) and considering the terms of the following order ϵ_2^0 one can deduce

$$
v_1 = -\frac{1}{\rho_2}\frac{\partial}{\partial x}\sigma - \frac{\beta_2}{\rho_2}\frac{\partial}{\partial x}p.
\tag{4.75}
$$

Inserting the asymptotic expansion (4.72) together with the results (4.74) and (4.75) into the set of equations (4.71), the following reduced asymptotic system is obtained in the stiff limit $\epsilon_2 \to 0$:

$$
\begin{aligned}
\frac{\partial}{\partial t}\sigma - c\frac{\partial}{\partial x}u + \epsilon_2\alpha M\left(\frac{1}{\rho_2}\frac{\partial^2}{\partial x^2}\sigma + \frac{\beta_2}{\rho_2}\frac{\partial^2}{\partial x^2}p\right) &= 0, \\
\frac{\partial}{\partial t}u\left(\frac{\epsilon_2}{\epsilon_1}\frac{1}{\rho_2} - \frac{1}{\rho_1}\right)\frac{\partial}{\partial x}\sigma + \left(\frac{\epsilon_2}{\epsilon_1}\frac{\beta_2}{\rho_2} - \frac{\beta_1}{\rho_1}\right)\frac{\partial}{\partial x}p &= 0, \\
\frac{\partial}{\partial t}p + \alpha M\frac{\partial}{\partial x}u + \epsilon_2 M\left(\frac{1}{\rho_2}\frac{\partial^2}{\partial x^2}\sigma + \frac{\beta_2}{\rho_2}\frac{\partial^2}{\partial x^2}p\right) &= 0.
\end{aligned}
\tag{4.76}
$$

The reduced asymptotic limit system (4.76) is a mixed hyperbolic-parabolic system of three convection-diffusion equations without source terms, instead of the original four hyperbolic equations with stiff source terms (4.71).

In the following Sections we perform a comparative study of the accuracy of the proposed ADER-DG(ST) with the ADER-DG(FS) schemes. It has been shown by LeVeque and Yee [91] that a classical FS method for hyperbolic systems with stiff source terms is not asymptotically consistent with the stiff limit of the governing equations. More precisely, this means that the numerical solution of a scheme which is using standard fractional-stepping applied to the set of equations (4.71) will not converge to the correct asymptotic limit system (4.76). Despite this important finding by LeVeque and Yee in 1990, fractional-step methods still enjoy high popularity in engineering sciences.

4.6.2 Numerical Test Case in One Space Dimension

In this Section we propose the following test case for the validation of numerical methods that are applied to poroelastic wave propagation in the viscous low frequency range. For this test problem it is of great importance that the numerical scheme is asymptotically consistent with the diffusion limit (4.76) of the original hyperbolic system (4.71). The computational domain is chosen to be $\Omega = [-0.5; 0.5]$ with Dirichlet boundary conditions consistent with the initial condition

$$(\sigma, u, p, v)(x, 0) = \begin{cases} (10, 0, 99, 0) & \text{if } x \leq 0, \\ (1, 0, 9.9, 0) & \text{if } x > 0. \end{cases} \tag{4.77}$$

The parameters for this test case are chosen in a dimensionless setting as $c = 0.5$, $\alpha = 0.25$, $\rho_1 = 1$, $\rho_2 = -10$, $M = 2$, $\beta_1 = 0.1$, $\beta_2 = 20$, $\epsilon_1 = 10^4$ and $\epsilon_2 = -10^5$. The eigenvalues of the original inhomogeneous hyperbolic system with four equations (4.71) are ± 2.0074 and ± 0.6086, corresponding to the *fast* P-waves and the *slow* P-waves. The eigenvalues of the hyperbolic part of the reduced asymptotic system of three convection-diffusion equations (4.76) are ± 0.7382 and 0. One immediately notes that the presence of the stiff source terms in (4.71) is reducing the speed of the *fast* P-waves and is melting the two *slow* P-waves to one single diffusion wave with zero propagation speed. All the following computations are performed on the *original* hyperbolic system (4.71) with stiff source terms on a mesh with 100 elements using ADER-DG(FS) and ADER-DG(ST) schemes of second and fourth order of accuracy in space and time.

The first computation is done up to the final time $t = 0.5$. The numerical solutions obtained with $\mathcal{O}2$ and $\mathcal{O}4$ schemes are presented in Fig. 4.3. The reference solution has been computed solving directly the asymptotic limit equations (4.76) on a very fine mesh of 10000 elements using a standard second-order accurate finite volume scheme. The fourth variable of the reference solution (v) is obtained from the other variables using the asymptotic ansatz (4.72) together with relations (4.74) and (4.75). Looking at the structure of the reference solution one can
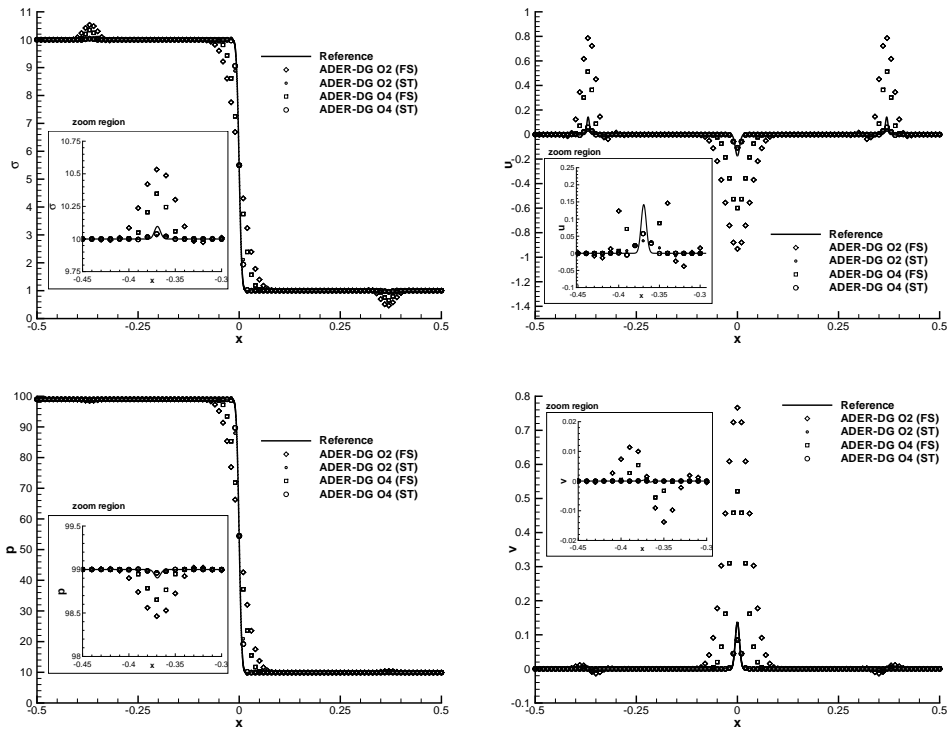
Figure 4.3: Numerical solutions for the stiff one-dimensional test case at $t = 0.5$ obtained with ADER-DG(FS) and ADER-DG(ST) $\mathcal{O}2$ and $\mathcal{O}4$ schemes.
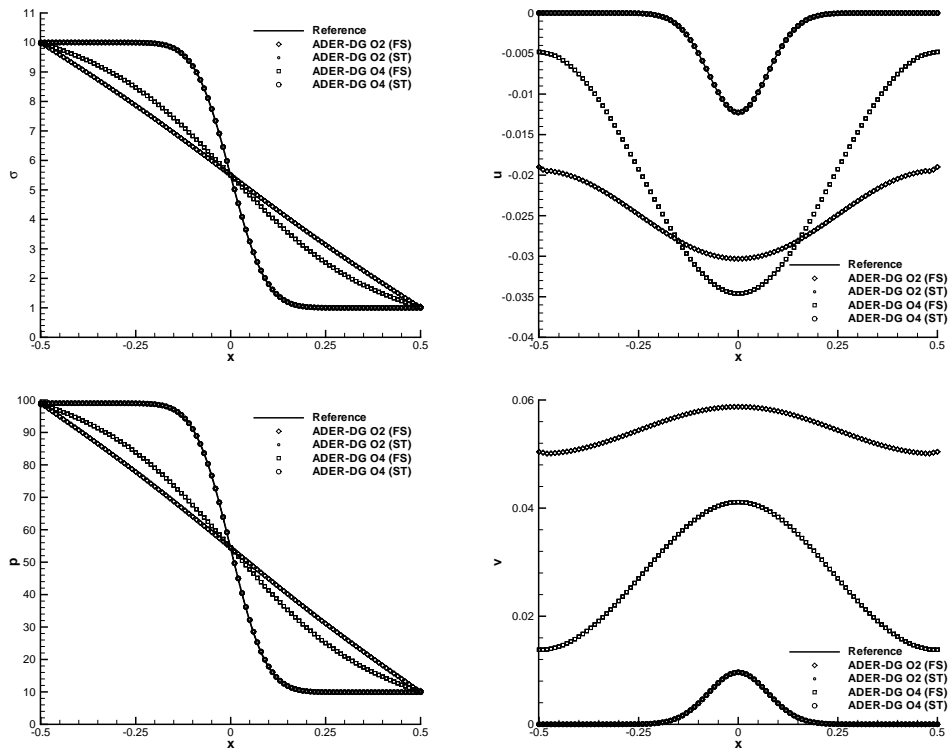
Figure 4.4: Numerical solutions for the stiff one-dimensional test case at $t = 100$ obtained with ADER-DG(FS) and ADER-DG(ST) $\mathcal{O}2$ and $\mathcal{O}4$ schemes.

clearly observe that only three waves are present: the two *fast* P-waves as well as the stationary diffusion wave at the origin instead of the two *slow* P-waves of the original governing equations (4.71). For all four variables, a very good agreement with the reference solution has been obtained using the proposed ADER-DG(ST) $\mathcal{O}2$ and $\mathcal{O}4$.

In contrast, the ADER-DG(FS) scheme produces wrong results, although very high-order accuracy in space and time is used in each of the fractional sub-steps. Especially the fluid and solid velocities, u and v respectively, show extreme overshoots as well as too much diffusion. This simulation shows that the standard FS method is stable, but not asymptotically consistent with the limit equations.

The final simulation time of the same test problem can be increased to $t = 100$ in order to study the behavior of the proposed numerical methods at large time scales. The ADER-DG(FS) and ADER-DG(ST) $\mathcal{O}2$ and $\mathcal{O}4$ schemes are used again on the same mesh. The obtained numerical results are depicted in Fig. 4.4, together with the reference solution, computed by solving again directly the asymptotic limit equations (4.76) on a mesh of 10000 elements with a second-order accurate finite volume scheme. A remarkable disagreement can be observed in FS-based solutions. First of all, an excessive amount of numerical diffusion is visible for the normal stress σ and the fluid pressure p. Second, the numerical solution of the velocity components u and v obtained via the ADER-DG(FS) approach are completely wrong. The results obtained for this test case at large output times reveal once again very clearly that a classical fractional time stepping scheme, although very popular, is not asymptotically consistent with the stiff limit of the governing equations. In contrast, the numerical solutions obtained with the ADER-DG(ST) scheme are in perfect agreement with the reference solution for all variables.

Table 4.4: Coefficients for the material given in $S.I.$ units as used for the 3D explosion example in Section 4.7.1.

ρ_s	ρ_f	λ^{matrix}	μ^{matrix}	K_s	K_f	ν	ϕ	κ	T
2500	1040	19.6e9	26.1e9	80.0e9	2.5e9	0.0	0.5	$300.0 \cdot 10^{-15}$	2

4.7 Application Examples

In this Section we present a series of applications to verify the proper implementation of Biot's equations in the Discontinuous Galerkin framework. Examples both in the low- and in the high-frequency ranges are discussed, using the ADER-DG and ADER-DG(ST) schemes introduced in this work. Results are compared to analytical or numerical reference solutions obtained from other schemes.

4.7.1 High-Frequency 3D Explosion

In this application we assess the accuracy of the proposed scheme against an analytical solution proposed by [44]. The problem setup is that of a homogeneous poroelastic material where a point explosion is applied to both the solid frame and the inviscid fluid. The parameter values of the material are given in Table 4.4. The domain is a cube $\Omega = [-450; 450] \, \text{m} \times [-450; 450] \, \text{m} \times [-450; 450] \, \text{m}$. It is discretized with 455625 regular tetrahedra, each with a side length of 20m. The source is situated at the point $x_s = (-50, 0, 0)$m and has a Ricker time signal of peak frequency 30Hz and time delay 0.04s. The receiver is situated at $x_r = (50, 0, 0)$m. An ADER-DG $\mathcal{O}6$ scheme is chosen for solving the problem, meaning that polynomials of fifth order in space and time are used. The final simulation time is 0.25s, with a time step of $\Delta t = 5.56 \cdot 10^{-5}$s and a total number of 4500 iterations. The computation was performed in 256 Intel Itanium2 1.6GHz processors and lasted for a total of approximately 7 hours. The results are shown in Figure 4.5(a), together with the root-mean-square (r.m.s.) error. Both P-waves, *fast* and *slow*, appear in this case as the viscosity ν is set to zero.

4.7.2 Low-Frequency 3D Explosion

The result of the proposed scheme is compared with an analytical solution for the case of a point explosion in the low-frequency range. The setup is similar to the poroacoustic problem proposed in [33] but applied to a poroelastic material whose properties are described Table 4.1, i.e. the same material as in the convergence tests is used in the present application. The domain is a cube $\Omega = [-5000; 5000] \, \text{m} \times [-5000; 5000] \, \text{m} \times [-5000; 5000]$m. It is discretized with 625000 regular tetrahedra, with a side length of 200m each. The point source only
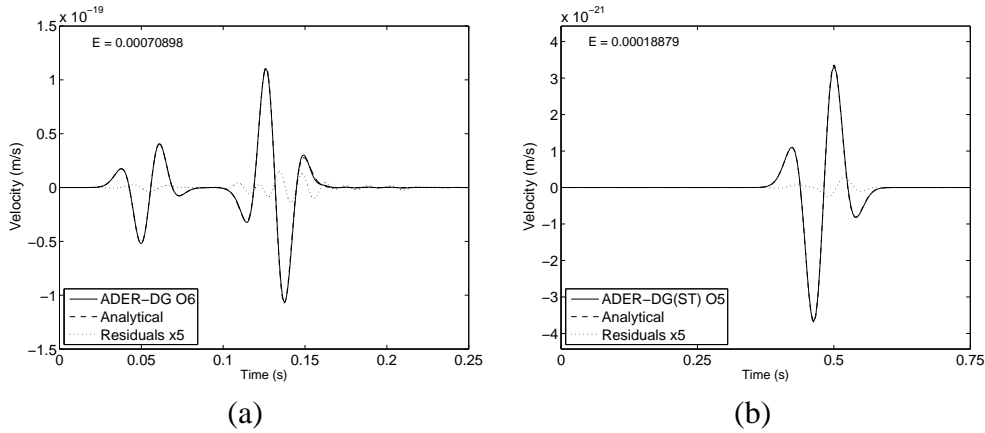
Figure 4.5: Comparison between the analytical (dashed) and numerical (solid) solutions of the solid particle velocity component u in a homogeneous medium with explosive sources for (a) the high-frequency inviscid case and (b) the low-frequency case. The residuals (dotted) are enlarged by a factor 5 for easier visualization. Also the r.m.s. errors (E) are included.

affects the solid matrix and is situated at the coordinate origin $x_s = (0,0,0)$m. The receiver is placed at $x_r = (1000,0,0)$m. The source is a Ricker pulse with peak frequency at 4.5Hz and with a time delay of $7 \cdot 10^{-4}$s. The simulated seismograms cover a total time of 1.5s. The simulation is carried out with an ADER-DG(ST) $\mathcal{O}5$ scheme and the final result is reached after 1573 iterations using time steps of $9.54 \cdot 10^{-4}$s. The run time of the simulation was 4.7 hours in 128 Intel Itanium2 1.6GHz cores. The result is shown in Figure 4.5(b), together with the r.m.s. error. One can observe that only one P phase is observed as the slow wave has become a diffusive mode, that does not appear in the seismogram.

4.7.3   Anisotropic Poroelasticity

In order to assess qualitatively the capability of the method to include anisotropic material, the results shown in [24] for brine-saturated epoxy-glass and sandstone are reproduced here with the ADER-DG scheme. The actual material values used are shown in Table 4.5. It can be seen that both materials present anisotropy of the transversely isotropic class in the matrix values as well as anisotropic permeability and tortuosity. The two-dimensional domain is a square $\Omega = [-9.35; 9.35]$ m $\times$ $[-9.35; 9.35]$ m discretized in a total of 78654 triangular elements with an average side length of 0.1m. The source is situated at $x_s = (0,0)$m and acts on the σ_{yy} and on the fluid pressure p simultaneously. Its source time function is given by a Ricker wavelet with frequencies 3135Hz and 3730Hz for the epoxy-glass and the sandstone respectively, with time delays of $t_0 = 4 \cdot 10^{-4}$s. In both cases this frequency lies well below the materials' minimum Biot's frequency. The

simulations were carried out with an ADER-DG(ST) $\mathcal{O}4$ scheme and performed in a 2GB Pentium IV 2.8GHz computer. The run-time was of approximately 9 hours, reaching a maximum time of $1.8 \cdot 10^{-3}$s for the epoxy-glass and $1.56 \cdot 10^{-3}$s for the sandstone. The time steps used are 0.294μs and 0.255μs respectively thus leading to a total of 6123 and 6118 iterations respectively to complete the simulation. The resulting snapshots of the solid particle velocities u and v are shown in Figures 4.6 and 4.7, where the inviscid results for the same setup have been added to point out the differences between the high-frequency and the low-frequency regimes. The *slow* wave at low-frequencies becomes a diffusive mode centered at the source location which, due to its very small magnitude, cannot be observed in the solid particle velocity snapshots. The snapshots of Figs. 4.6 and 4.7 can be directly compared to those presented in [24] obtained with a pseudo-spectral simulation using an FS-equivalent splitting technique. The same phases are observed with both methods. Notice however that in the aforementioned publication the time function has a different expression, although with the same peak frequency. We can observe that, for the inviscid high-frequency case, a clear slow qP-wave is present propagating at a much lower velocity than the rest of the waves. As seen in the Table 4.5, the solid matrix of the sandstone is less anisotropic than that of the epoxy-glass. However, they both share identical anisotropy of the permeability and the tortuosity, which are responsible for the anisotropic flow of fluid through the pores. Comparing Figures 4.6 and 4.7 we can observe that the slow qP-wave is actually showing the same ellipticity for both materials, and is therefore more sensitive to the anisotropy of the tortuosity and the permeability than to the solid matrices'. Another interesting fact is that, for both materials, the wave forms for the viscous and inviscid cases are almost identical for the qS- and fast qP-waves. Additionally, the typical cuspidal triangles appearing in anisotropic elastic case in the directions of the symmetry axes of the material, are now also visible for the slow qP-wave (see Fig. 4.6). In Fig. 4.8 we show the results of the same simulation in the sandstone but now focusing on the differences between the solid particle velocity v and the fluid particle velocity v_f in the viscous case. It can be seen how for the low-frequencies a diffusion peak appears at the source location, only visible for our plotting scales in the fluid particle velocity.

4.7.4 Heterogeneous Poroelastic Material

Finally we show an example to confirm that the ADER-DG method correctly treats material heterogeneities. In the present case we use a domain composed of two different poroelastic materials, a shale and a sandstone, both filled with inviscid brine, as described in Table 4.6. The two-dimensional domain is a rectangle $\Omega = [0; 1500]$ m $\times [0; 1400]$ m with an interface at the $y = 700$m axis. The source

Table 4.5: Coefficients for the anisotropic, poroelastic materials given in $S.I.$ units as used for the 2D anisotropic example. Both are of the transversely isotropic symmetry class.

MATERIAL	ρ_s	ρ_f	c_{11}	c_{12}	c_{22}	c_{66}	K_s
Epoxy	1815	1040	39.4e9	5.8e9	13.1e9	3.0e9	40.0e9
Sandstone	2500	1040	71.8e9	1.2e9	53.4e9	26.1e9	80.0e9

MATERIAL	K_f	ν	ϕ	κ_x	κ_y	T_x	T_y
Epoxy	2.5e9	$1.0e-3$	0.2	$600.0e-15$	$100.0e-15$	2	3.6
Sandstone	2.5e9	$1.0e-3$	0.2	$600.0e-15$	$100.0e-15$	2	3.6
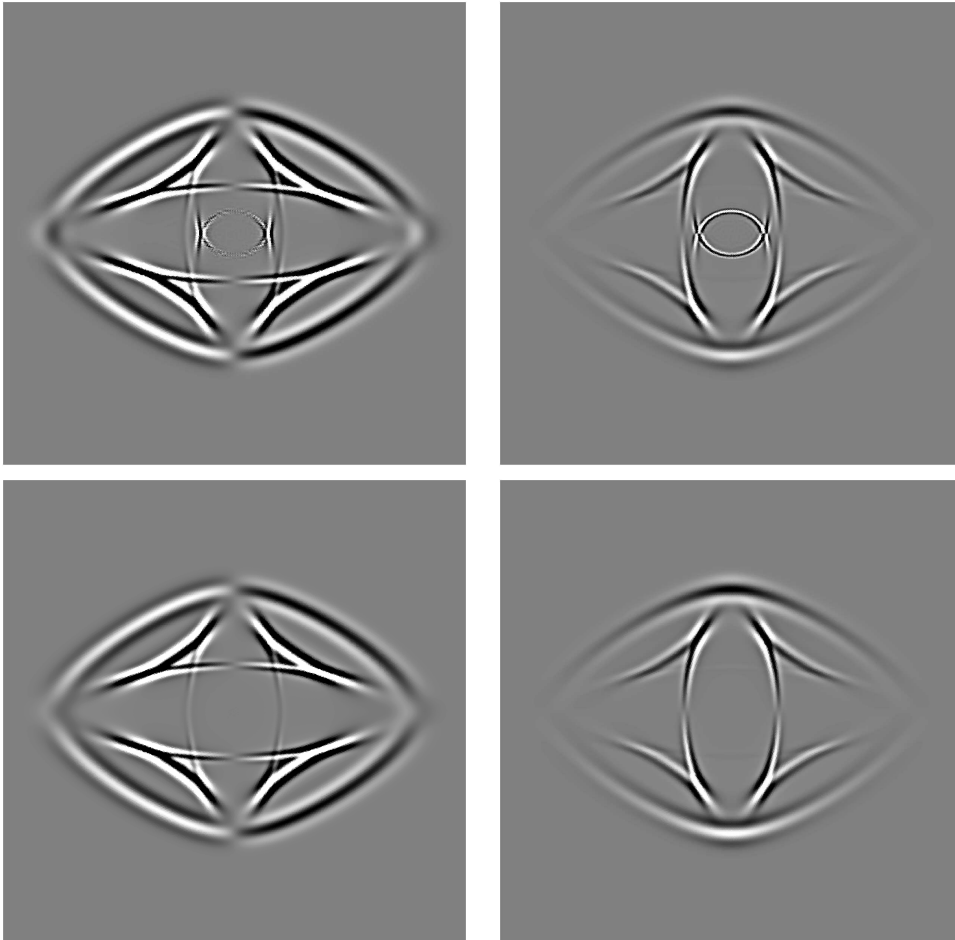
Figure 4.6: Snapshots showing velocity fields in an epoxy-glass material. Upper figures show the inviscid case ($\nu = 0$) and lower figures the viscous case. On the left hand side is the solid particle velocity u in the $x-$direction and in the right hand side the velocity v in the $y-$direction. These snapshots can be directly compared to those in [24].
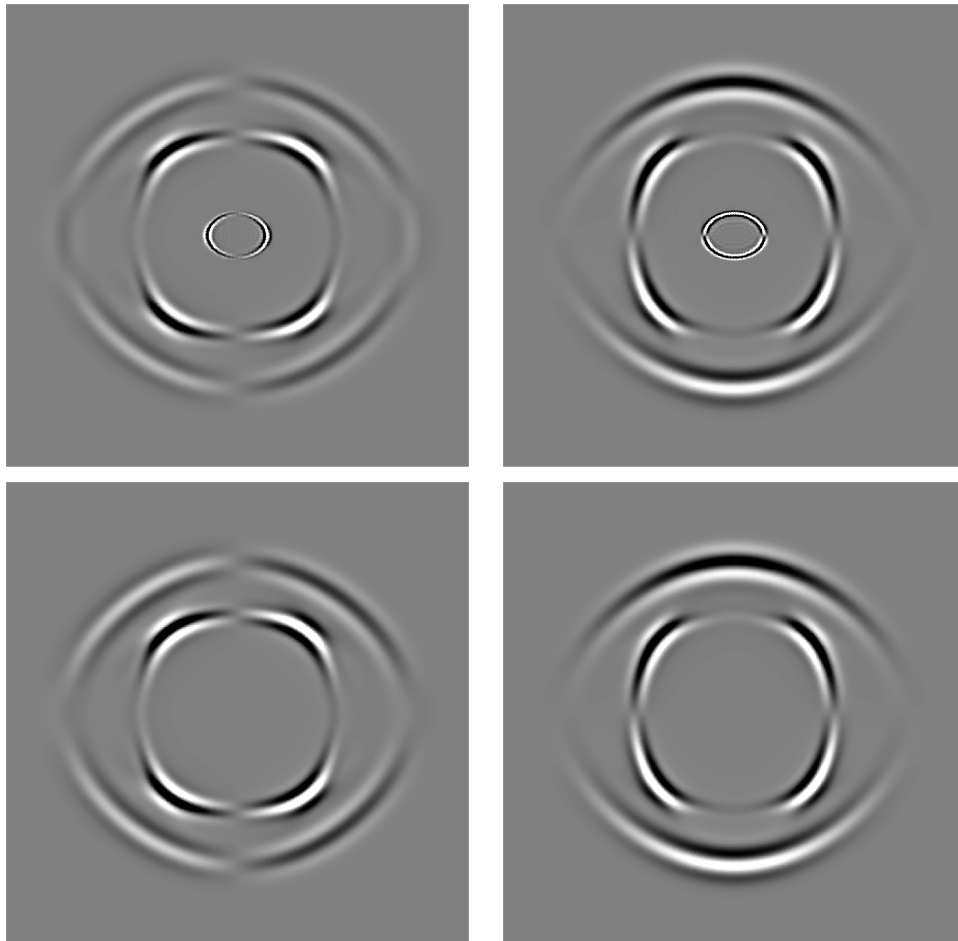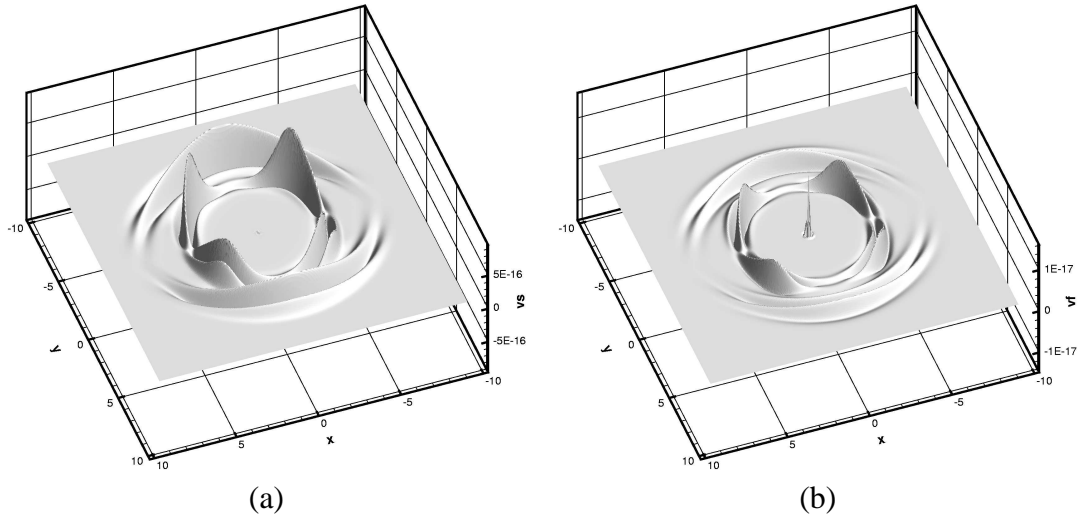
Figure 4.7: Snapshots showing velocity fields in a sandstone material. Upper figures show the inviscid case ($\nu = 0$) and lower figures the viscous case. On the left hand side is the solid particle velocity u in the $x-$direction and in the right hand side the velocity v in the $y-$direction. These snapshots can be directly compared to those in [24].

Figure 4.8: Comparison of solid (a) and fluid (b) particle velocities in $y-$direction in a sandstone material for the viscous low-frequency case.

is a point source situated at $x_s = (750, 900)$m acting on the σ_{yy} and the p components with equal magnitude but opposite signs. Its time content is a Ricker wavelet of 50Hz peak frequency and time delay $t_0 = 4 \cdot 10^{-2}$s. The domain is meshed with an irregular triangular mesh of 132014 elements, of 6m average side and the simulation time is set to 0.5s. The time step of the computation is approximately $\Delta t = 2.34 \cdot 10^{-5}$s, thus leading to a total of 21390 iterations. The computation was performed using an ADER-DG $\mathcal{O}5$ scheme and lasted for approximately 3 hours on 64 Intel Itanium2 1.6GHz cores. Three receivers are placed at points $x_{r1} = (950, 750)$m, $x_{r2} = (950, 650)$m and $x_{r3} = (950, 500)$m respectively. In Figure 4.9 the waveforms of the solid particle velocity v generated by such a setup as well as the computational mesh used can be observed. The source described above produces all 3 wave types allowed in poroelastic isotropic materials, two compressional and one shear wave. Those waves can be transmitted, reflected and refracted at the material discontinuity, thus creating a much more complex wavefield than those at elastic interfaces. In Figure 4.10 we compare the resulting seismograms to those generated with a rotated staggered-grid finite-difference scheme [88] using 1m regular grid spacing, meaning approximately 6 points per minimum wavelength. One can observe a very satisfactory fit of all direct, reflected and refracted phases. However there is a slight phase difference in the *slow* P-wave.

4.8   Conclusion

A new numerical method to simulate wave propagation in poroelastic material has been introduced. The proposed method can achieve arbitrarily high approxima-

Table 4.6: Coefficients for the isotropic poroelastic materials given in $S.I.$ units as used in heterogeneous material test.

MATERIAL	ρ_s	ρ_f	λ^{matrix}	μ^{matrix}	K_s
Shale	2210	1040	$3.96e9$	$3.96e9$	$7.6e9$
Sandstone	2500	1040	$12.0e9$	$12.0e9$	$40.0e9$

MATERIAL	K_f	ν	ϕ	κ	T
Shale	$2.5e9$	0.0	0.16	$1.0 \cdot 10^{-13}$	2
Sandstone	$2.5e9$	0.0	0.2	$600.0 \cdot 10^{-15}$	2
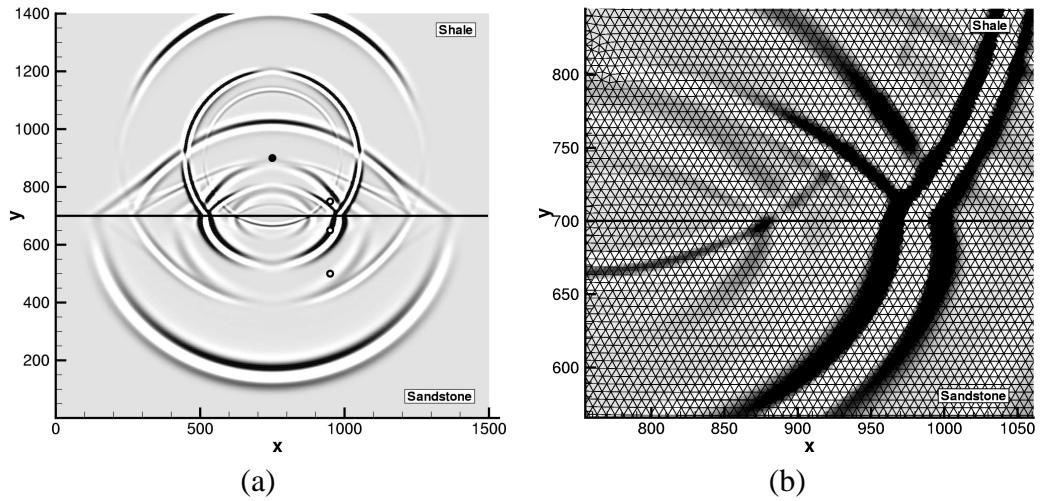
Figure 4.9: (a) Snapshot of the solid particle velocity v in the $y-$direction at $t = 0.25$s. The source location is indicated by a full circle and the receivers by empty circles. (b) Zoomed region showing the mesh required to resolve the slow compressional wave.
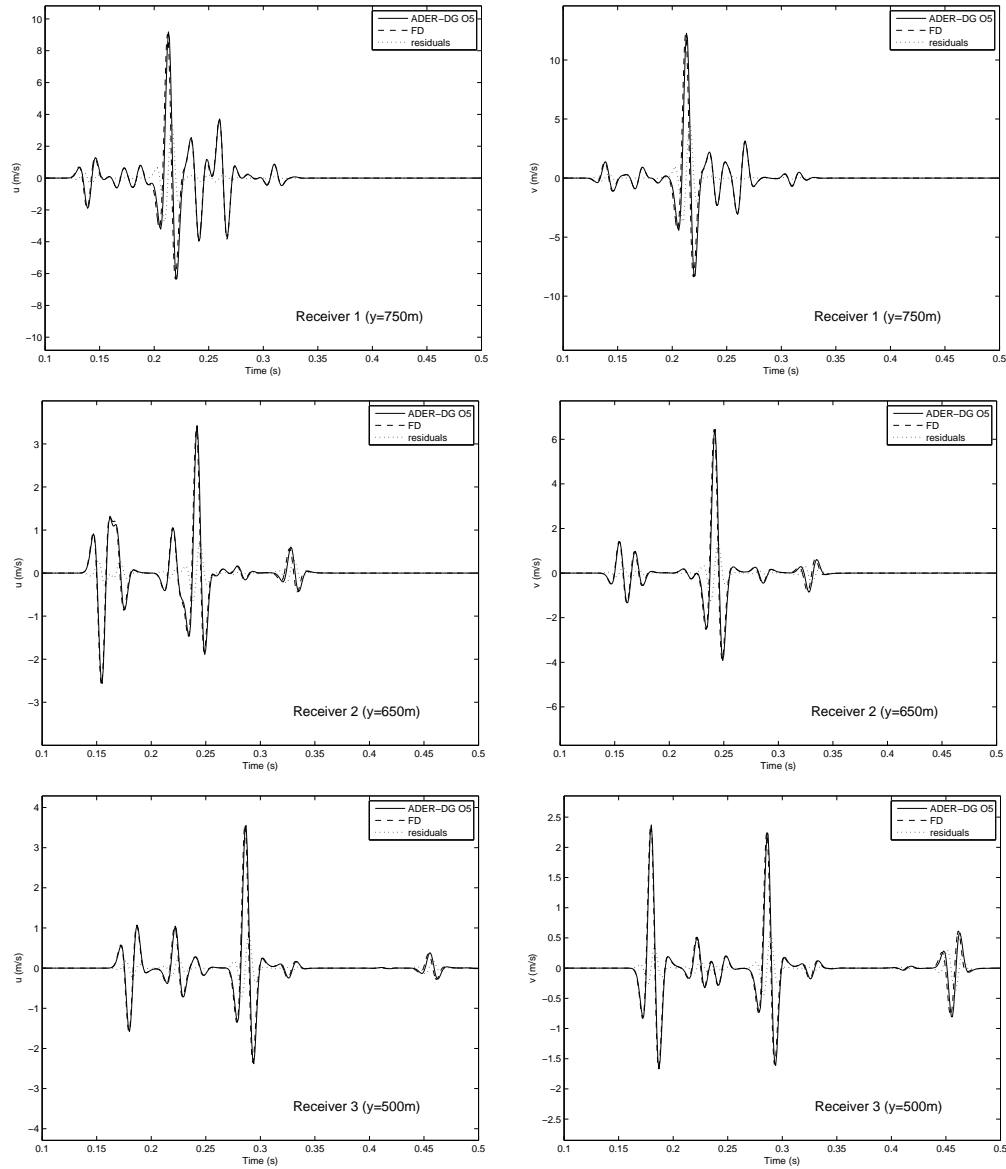
Figure 4.10: Seismograms recorded at the three receivers with the ADER-DG method (solid) and compared to the results with an FD code (dashed). The seismograms on the left hand side correspond to the u solid particle velocity component while on the right hand side is plotted the v solid particle velocity component. The residuals between ADER-DG and FD are also included (dotted).

tion order in space and time on unstructured tetrahedral meshes as confirmed by numerical convergence analysis. It is the first numerical scheme that conserves the high-order approximation properties for all frequency ranges for poroelastic material. In particular, the wave equations in the case of a viscous pore fluid change their character in the low-frequency range from hyperbolic to parabolic and become diffusion-dominated due to a stiff source term as predicted by Biot's theory. Therefore, the stability condition for classical explicit time stepping schemes is very restrictive and the time step length has to be chosen too small to perform realistic computations of practical applications. In the proposed approach, this problem is overcome by introducing a local space-time Discontinuous Galerkin method termed ADER-DG(ST), where the usual Cauchy-Kovalewski procedure inside each element has been replaced by the space-time DG framework. This achieves the same coupling of time and space discretization as ADER-DG based on the time Taylor expansion, but is able to deal with stiff source terms. The important fact is, that the new time discretization scheme assures computational robustness for usual hyperbolic equation systems, and shows asymptotic consistency in the stiff limit. It should be remarked, that classical splitting schemes, like the typically used fractional-step method for such problems, do not have this property and therefore do not achieve high-order convergence or do not even converge to the correct solution. Additionally, the most general case of anisotropy due to the pore structure has been included. the performance of the proposed method is confirmed by validating the results against either known analytical solutions or reference solutions obtained by well-established numerical schemes.

Outlook

This work has shown that a precise representation of the physics involved in wave propagation is not compromised by the use of tetrahedral unstructured meshes when using the novel ADER-DG method. Such tetrahedral meshes are recommendable for two main reasons: they allow an optimization of the stability limits posed by explicit time integration schemes by relating the element sizes to the maximum velocity of wave propagation and they can be used to further refine the resolution of interesting areas or capture more complicated geometries.

In Chapter 1 the fundamental principles of the method have been introduced as well as the features that make it an exceptional technique, as it is the mixture of spectral resolution with numerical fluxes and the usage of highly accurate time integration schemes.

Chapter 2 has centered the attention to the problem of reproducing the attenuating and dispersive effects of viscoelastic rheologies. A choice has been made in favor of the Generalized Maxwell Body description for its compromise between accuracy and costs for time-domain calculations. Although expensive in terms of memory and computational time required, the results show very good agreement with reference solutions. Ways to optimize the time-integration and flux computations taking advantage of the sparsity of the systems are further shown, which help making the method competitive.

In Chapter 3 the problem of wave propagation through anisotropic material has been explored. Although the mapping of anisotropy in the Earth's interior is a difficult task, models are available describing zones with a marked anisotropic behavior. While using an unstructured mesh in the modeling of anisotropic wave propagation, the problem of having elements not aligned to the material's principal axes leads to the need to solve the most general anisotropic case for each element, as their orientation is arbitrary. This drawback doesn't affect the efficiency of the scheme, which is comparable to that for the isotropic case. It has further been shown that the simultaneous modeling of anisotropy and viscoelasticity requires a careful description of the physics involved. The principles governing this coupling and their effect in the equation systems to be solved are shown in detail, implemented in the method and tested qualitatively.

Finally, Chapter 4 shows that the ADER-DG method is well suited to solve the poroelastic case, where both propagatory and diffusive phenomena coexist when the filling fluid is viscous. The space-time-discontinuous version of the method

has the unique robustness properties, which make it able to solve the coupled problem with high-order accuracy, a so far unsolved problem.

The method, however, is not free of drawbacks. The price to be payed by the increased accuracy and the meshing flexibility is a higher computational cost. Additionally, the algorithms become rather complex and cumbersome to tackle without a strong effort by the reader, thus being it difficult for potential users to implement their own codes based upon an ADER-DG method. Last but not least, the efficient usage of the method is strongly dependent on the quality of the meshes used. At the present moment, unfortunately, most good meshing software is commercial and requires some training to use it properly.

Still, the ADER-DG method poses a unified scheme to solve linear seismic wave propagation on media of very demanding geometrical and physical complexity. It has been proved that, for this technique, accuracy is not compromised with flexibility. Other novel ideas associated with the method, as the local-timestepping, have shown that even stability criteria, a burden for large scale simulations, can be downplayed and their effect severely reduced.

Future development of the method will aim at extending the computational domains to hybrid hexahedral/tetrahedral meshes. Although tetrahedra do a better job meshing complex structures, they are much less efficient than hexahedra for a given volume of space and accuracy. As a consequence, combining tetrahedral meshes there where the geometry is demanding with hexahedra in simpler zones would optimize the accuracy/efficiency ratio for large simulations. Another interesting future application will be that of extending the ADER-DG method to the problem of dynamic rupture, where the physics of the contact surfaces at a fault are dynamically linked to those of the rock surrounding it. For this problem, the accuracy and flexibility of the ADER-DG method could be crucial in accurately describing the processes involved in the seismic fault slip for non-planar and heterogeneous fault systems. Other developments will necessarily aim at optimizing computational issues as are efficient memory access and load balance between multiple processors involved in parallel computations. With the constant upgrade on computers' performance, larger and more complex problems can be solved. Although often the focus of researchers has lead into the usage of such increased computational power for solving the same problems up to higher frequencies, the ADER-DG method opens the doors to an increase in the ambitions in terms of the detail of description and sophistication of the problems that can be solved in seismology. The present work shows a numerical methodology ready to be used in the future to simulate earthquake scenarios including strong topographies and sedimentary layers showing both low-velocity and high dissipative properties. Other problems that can be explored in forthcoming research are those related to coastal subduction zones, which are complex multi-component setups where solid, fluid and partly molten phases coexist in a well constrained geometrical environment. Various solid-fluid interaction phenomena in porous and unconsolidated materials can be further studied, as for example soil liquefaction or reservoir signature

characterization. Also wave propagation through man-made structures such as buildings can be at hand in the upcoming years. Such structures are very demanding in terms of geometry as they include pillars or thin walls and are attached to soft sediments. With the capabilities of the method shown in this thesis, such problems will be handled in full three-dimensional setups, with the additional advantage of minimizing the errors introduced by the numerical approach chosen as a solver. The combination of modern algorithms and computational resources is pushing computational seismology towards overcoming its classical limitations and the ADER-DG method is just an example.

Appendix A

Orthogonal Basis Functions

The ADER-DG method, as implemented in this thesis, uses orthogonal hierarchical basis functions as given in [39]. The basis functions are given in terms of the Jacobi polynomials $P_n^{\alpha,\beta}(x)$, which are solutions of the Jacobi differential equation:

$$\left(1 - x^2\right) y'' + [\beta - \alpha - (\alpha + \beta + 2) x] y' + n (n + \alpha + \beta + 1) y = 0. \quad \text{(A.1)}$$

They are given on the interval $[-1; 1]$ by

$$P_n^{\alpha,\beta}(x) = \frac{(-1)^n}{2^n n!} (1 - x)^{-\alpha} (1 + x)^{-\beta} \frac{d^n}{dx^n} \left[(1 - x)^{\alpha+n} (1 + x)^{\beta+n} \right]. \quad \text{(A.2)}$$

For $\alpha = \beta = 0$ the Jacobi polynomials $P_n^{0,0}(x)$ reduce to the Legendre polynomials. The Discontinuous Galerkin basis functions are then constructed using products of up to three primal functions, given by

$$\Theta_i^a(x) = P_i^{0,0}(x), \quad \text{(A.3)}$$

$$\Theta_{ij}^b(x) = \left(\frac{1-x}{2}\right)^i P_j^{2i+1,0}(x), \quad \text{(A.4)}$$

$$\Theta_{ijk}^c(x) = \left(\frac{1-x}{2}\right)^{i+j} P_k^{2i+2j+2,0}(x). \quad \text{(A.5)}$$

The sets of basis functions Φ_k will then constitute an orthogonal basis systems with respect to the inner product on the respective reference elements $\mathcal{T}_E$.

A.1   Triangular Elements

For triangles the reference element $\mathcal{T}_E$ is defined as

$$\mathcal{T}_E = \left\{ (\xi, \eta) \in \mathbb{R}^2 \mid 0 \leq \xi \leq 1 \;\wedge\; 0 \leq \eta \leq 1 - \xi \right\}.$$

The basis functions $\Phi_k (\xi, \eta)$ are defined on this reference element as the following product of the primal functions:

$$\Phi_{k(p,q)} (\xi, \eta) = \Theta_p^a (r) \cdot \Theta_{pq}^b (s). \tag{A.6}$$

with

$$r = \frac{2\,\xi}{1 - \eta} - 1, \quad s = 2\,\eta - 1. \tag{A.7}$$

The mono-index $k = k(p, q)$ is again a function of the index couple (p, q).

The two-dimensional basis functions up to degree three for a fourth order scheme are:

$$
\begin{aligned}
\Phi_0 &= 1, \\
\Phi_1 &= -1 + 2\,\xi + \eta, \\
\Phi_2 &= -1 + 3\,\eta, \\
\Phi_3 &= 1 - 6\,\xi + 6\,\xi^2 - 2\,\eta + 6\,\xi\eta + \eta^2, \\
\Phi_4 &= 1 - 2\,\xi - 6\,\eta + 10\,\xi\eta + 5\,\eta^2, \\
\Phi_5 &= 1 - 8\,\eta + 10\,\eta^2, \\
\Phi_6 &= -1 + 12\,\xi - 30\,\xi^2 + 20\,\xi^3 + 3\,\eta - 24\,\xi\eta + 30\,\xi^2\eta - 3\,\eta^2 + 12\,\xi\eta^2, \\
\Phi_7 &= -1 + 6\,\xi - 6\,\xi^2 + 9\,\eta - 48\,\xi\eta + 42\,\xi^2\eta - 15\,\eta^2 + 42\,\xi * \eta^2 + 7\,\eta^3, \\
\Phi_8 &= -1 + 2\,\xi + 13\,\eta - 24\,\xi\eta - 33\,\eta^2 + 42\,\xi\eta^2 + 21\eta^3, \\
\Phi_9 &= -1 + 15\,\eta - 45\,\eta^2 + 35\,\eta^3,
\end{aligned}
\tag{A.8}
$$

A.2   Tetrahedral Elements

For tetrahedrons the reference element $\mathcal{T}_E$ is defined as

$$\mathcal{T}_E = \left\{ (\xi, \eta, \zeta) \in \mathbb{R}^3 \mid 0 \leq \xi \leq 1 \;\wedge\; 0 \leq \eta \leq 1 - \xi \;\wedge\; 0 \leq \zeta \leq 1 - \xi - \eta \right\}.$$

The basis functions $\Phi_k (\xi, \eta, \zeta)$ are defined on this reference element as the following product of the primal functions:

$$\Phi_{k(p,q,r)} (\xi, \eta, \zeta) = \Theta_p^a (r) \cdot \Theta_{pq}^b (s) \cdot \Theta_{pqr}^c (t). \tag{A.9}$$

with

$$r = \frac{\eta - 1 + \zeta + 2\xi}{1 - \eta - \zeta}, \quad s = \frac{2\eta - 1 + \zeta}{1 - \zeta}, \quad t = 2\zeta - 1. \quad \text{(A.10)}$$

The mono-index $k = k(p, q, r)$ is again a function of the index triple (p, q, r).

The three-dimensional basis functions up to degree two for a third order scheme are:

$$
\begin{aligned}
\Phi_0 &= 1, \\
\Phi_1 &= -1 + 2\xi + \eta + \zeta, \\
\Phi_2 &= -1 + 3\eta + \zeta, \\
\Phi_3 &= -1 + 4\zeta, \\
\Phi_4 &= 1 - 6\xi + 6\xi^2 - 2\eta + 6\xi\eta + \eta^2 - 2\zeta + 6\xi\zeta + 2\eta\zeta + \zeta^2, \\
\Phi_5 &= 1 - 2\xi - 6\eta + 10\xi\eta + 5\eta^2 - 2\zeta + 2\xi\zeta + 6\eta\zeta + \zeta^2, \\
\Phi_6 &= 1 - 8\eta + 10\eta^2 - 2\zeta + 8\eta\zeta + \zeta^2, \\
\Phi_7 &= 1 - 2\xi - \eta - 7\zeta + 12\xi\zeta + 6\eta\zeta + 6\zeta^2, \\
\Phi_8 &= 1 - 3\eta - 7\zeta + 18\eta\zeta + 6\zeta^2, \\
\Phi_9 &= 1 - 10\zeta + 15\zeta^2,
\end{aligned}
\quad \text{(A.11)}
$$

Appendix B

Coordinate Transformation

The coordinate transformation of a tetrahedron in the global, Cartesian xyz-coordinate system into the $\xi\eta\zeta$-reference system as shown in Figure 1.1 is defined by

$$
\begin{aligned}
\xi \;=\; & \tfrac{1}{|J|}\Big[x_1(y_4z_3 - y_3z_4) + x_3(y_1z_4 - y_4z_1) + x_4(y_3z_1 - y_1z_3) + \\
& \Big(y_1(z_3 - z_4) + y_3(z_4 - z_1) + y_4(z_1 - z_3)\Big)x + \\
& \Big(x_1(z_4 - z_3) + x_3(z_1 - z_4) + x_4(z_3 - z_1)\Big)y + \\
& \Big(x_1(y_3 - y_4) + x_3(y_4 - y_1) + x_4(y_1 - y_3)\Big)z\Big] \\[4pt]
\eta \;=\; & \tfrac{1}{|J|}\Big[y_1(x_4z_2 - x_2z_4) + y_2(x_1z_4 - x_4z_1) + y_4(x_2z_1 - x_1z_2) + \\
& \Big(y_1(z_4 - z_2) + y_2(z_1 - z_4) + y_4(z_2 - z_1)\Big)x + \\
& \Big(x_1(z_2 - z_4) + x_2(z_4 - z_1) + x_4(z_1 - z_2)\Big)y + \\
& \Big(x_1(y_4 - y_2) + x_2(y_1 - y_4) + x_4(y_2 - y_1)\Big)z\Big] \\[4pt]
\zeta \;=\; & \tfrac{1}{|J|}\Big[z_1(x_3y_2 - x_2y_3) + z_2(x_1y_3 - x_3y_1) + z_3(x_2y_1 - x_1y_2) + \\
& \Big(y_1(z_2 - z_3) + y_2(z_3 - z_1) + y_3(z_1 - z_2)\Big)x + \\
& \Big(x_1(z_3 - z_2) + x_2(z_1 - z_3) + x_3(z_2 - z_1)\Big)y + \\
& \Big(x_1(y_2 - y_3) + x_2(y_3 - y_1) + x_3(y_1 - y_2)\Big)z\Big]
\end{aligned}
\tag{B.1}
$$

where

$$
\begin{aligned}
|J| \;=\; & x_1\Big(y_2(z_4 - z_3) + y_3(z_2 - z_4) + y_4(z_3 - z_2)\Big) + \\
& x_2\Big(y_1(z_3 - z_4) + y_3(z_4 - z_1) + y_4(z_1 - z_3)\Big) + \\
& x_3\Big(y_1(z_4 - z_2) + y_2(z_1 - z_4) + y_4(z_2 - z_1)\Big) + \\
& x_4\Big(y_1(z_2 - z_3) + y_2(z_3 - z_1) + y_3(z_1 - z_2)\Big),
\end{aligned}
\tag{B.2}
$$

155

is the determinant of the Jacobian matrix J of the transformation being equal to 6 times the volume of the tetrahedron.

The back-transformation is given through

$$
\begin{aligned}
x &= x_1 + (x_2 - x_1)\,\xi + (x_3 - x_1)\,\eta + (x_4 - x_1)\,\zeta, \\
y &= y_1 + (y_2 - y_1)\,\xi + (y_3 - y_1)\,\eta + (y_4 - y_1)\,\zeta, \\
z &= z_1 + (z_2 - z_1)\,\xi + (z_3 - z_1)\,\eta + (z_4 - z_1)\,\zeta.
\end{aligned}
\tag{B.3}
$$

In equations (B.1), (B.2) and (B.3) the x_i, y_i and z_i denote the physical vertex coordinates of the tetrahedron.

Bibliography

[1] K. Aki and P. G. Richards. *Quantitative Seismology*. University Science Books, Sausalito, California, 2002.

[2] D. Anderson. *Theory the Earth*. Blackwell Scientific Publications, 1989.

[3] H. Atkins and C. W. Shu. Quadrature-free implementation of the discontinuous Galerkin method for hyperbolic equations. *AIAA Journal*, 36:775–782, 1998.

[4] J. Auriault, L. Borne, and R. Chambon. Dynamics of porous saturated media, checking of the generalized law of Darcy. *J. Acoust. Soc. Am.*, 77:1641–1650, 1985.

[5] V. Babuska and M. Cara. *Seismic anisotropy in the Earth*. Kluwer Academic Publishers, 1991.

[6] C. Bassin, G. Laske, and G. Masters. The current limits of resolution for surface wave tomography in North America. *EOS*, 81:F897, 2004.

[7] A. Bedford and D. S. Drumheller. *Elastic Wave Propagation*. Wiley, 1994.

[8] J.-P. Berenger. A Perfectly Matched Layer for the absorption of electromagnetic waves. *J. Comput. Phys.*, 114:185–200, 1994.

[9] J. Berryman. Confirmation of Biot's theory. *Appl. Phys. Lett.*, 37:382–384, 1980.

[10] J. Berryman and H. Wang. Elastic wave propagation and attenuation in a double-porosity dual-permeability medium. *Internat. J. Rock. Mech. Min. Sci.*, 37:1385–1391, 2000.

[11] M. Biot. Theory of deformation of a porous viscoelastic anisotropic solid. *J. Appl. Phys.*, 27:459–467, 1956.

[12] M. Biot. Theory of propagation of elastic waves in a fluid-saturated porous solid. I. low frequency range. *J. Acoust. Soc. Am.*, 28:168–178, 1956.

[13] M. Biot. Theory of propagation of elastic waves in a fluid-saturated porous solid. II. higher-frequency range. *J. Acoust. Soc. Am.*, 28:179–191, 1956.

[14] M. Biot. Mechanics of deformation and acoustic propagation in porous media. *J. App. Phys.*, 33:1482–1498, 1962.

[15] M. Biot and D. Willis. The elastic coefficients of the theory of consolidation. *J. Appl. Mech.*, 24:594–601, 1957.

[16] F. Boadu. Wave propagation in fluid-saturated media: waveform and spectral analysis. *Geophys. J. Int.*, 141:227–240, 2000.

[17] W. Bond. *Crystal Technology*. Wiley, New York, 1976.

[18] M. Bouchon. A simple method to calculate Green's functions for elastic layered media. *Bull. Seism. Soc. Am.*, 71:959–971, 1981.

[19] C. Boutin, G. Bonnet, and P. Bard. Green functions and associated source in infinite and stratified poroelastic media. *Geophys. J. Roy. Astr. Soc.*, 90:521–550, 1987.

[20] J. Brown, E. Abramson, and R. Angel. Triclinic elastic constants for low albite. *Phys. Chem. Minerals*, 33:256–265, 2006.

[21] R. Burridge and C. Vargas. The fundamental solution in dynamic poroelasticity. *Geophys. J. Roy. Astr. Soc.*, 58:61–90, 1979.

[22] M. Cara. *Seismic Anisotropy, in International Handbook of Earthquake and Engineering Seismology, Part A*. Academic Press, London, 2002.

[23] J. Carcione. Constitutive model and wave equations for linear, viscoelastic, anisotropic media. *Geophysics*, 60:537–548, 1995.

[24] J. Carcione. Wave propagation in anisotropic, saturated porous media: Plane-wave theory and numerical simulation. *J. Acous. Soc. Am.*, 99:2655–2666, 1996.

[25] J. Carcione. Viscoelastic effective rheologies for modelling wave propagation in porous media. *Geophys. Pros.*, 46:249–270, 1998.

[26] J. Carcione. Energy balance and fundamental relations in dynamic anisotropic poro-viscoealsticity. *Proc. R. Soc. Lond. A.*, 457:331–348, 2001.

[27] J. Carcione. *Wave Fields in Real Media: Wave Propagation in Anisotropic, Anelastic and Porous Media: Handbook of Geophysical Exploration, Seismic Exploration*. Pergamon Press, 2002.

[28] J. Carcione and F. Cavallini. A rheological model for anelastic anisotropic media with applications to seismic wave propagation. *Geophys. J. Int.*, 119:338–348, 1994.

[29] J. Carcione, D. Kosloff, A. Behle, and G. Seriani. A spectral scheme for wave propagation simulation in 3-D elastic anisotropic media. *Geophysics*, 57:1593–1607, 1992.

[30] J. Carcione, D. Kosloff, and R. Kosloff. Wave propagation simulation in a linear viscoelastic medium. *Geophys. J.*, 95:597–611, 1988.

[31] J. Carcione, D. Kosloff, and R. Kosloff. Wave propagation simulation in an elastic anisotropic (transversely isotropic) solid. *Q. J. Mech. Appl. Math.*, 41:319–345, 1988.

[32] J. Carcione and G. Quiroga-Goode. Some aspects of the physics and numerical modelling of Biot compressional waves. *Jou. Comp. Acou.*, 3:261–280, 1995.

[33] J. Carcione and G. Quiroga-Goode. Full frequency-range transient solution for compressional waves in a fluid-saturated viscoacoustic porous medium. *Geophys. Pros.*, 44:99–129, 1996.

[34] J. M. Carcione. The wave equation in generalised coordinates. *Geophysics*, 59:1911–1919, 1994.

[35] V. Cervený. *Seismic Ray Theory*. Cambridge University Press, Cambridge, 2001.

[36] C. Chapman. *Fundamentals of Seismic Wave Propagation*. Cambridge University Press, 2004.

[37] G. Chen, C. Levermore, and T. Liu. Hyperbolic conservation laws with stiff relaxation terms and entropy. *Comm. Pure Appl. Math.*, 47(6):787–830, 1994.

[38] J. B. S. Chevrot. Decomposition of the elastic tensor and geophysical applications. *Geophys. J. Int.*, 159:667–678, 2004.

[39] B. Cockburn, G. E. Karniadakis, and C. W. Shu. *Discontinuous Galerkin Methods*. Lecture Notes in Computational Science and Engineering. Springer, 2000.

[40] B. Cockburn and C. W. Shu. The runge-kutta local projection p1-discontinuous Galerkin finite element method for scalar conservation laws. *Mathematical Modelling and Numerical Analysis*, 25:337–361, 1991.

[41] F. Collino and C. Tsogka. Application of the PML absorbing layer model to the linear elastodynamic problem in anisotropic heterogeneous media. *Geophysics*, 66:294–307, 2001.

[42] R. Courant, K. Friedrichs, and H. Lewy. Über die partiellen Differenzialgleichungen der mathematischen Physik. *Mathematische Annalen*, 100:32–74, 1928.

[43] S. Crampin. A review of wave motion in anisotropic and cracked elastic media. *Wave Motion*, 3:343–391, 1981.

[44] N. Dai, A. Vafidis, and E. Kanasewich. Wave propagation in heterogeneous, porous media: A velocity-stress, finite-difference method. *Geophysics*, 60:327–340, 1995.

[45] S. Day. Efficient simulation of constant Q using coarse-grained memory variables. *Bull. Seism. Soc. Am.*, 88:1051–1062, 1998.

[46] S. Day and C. Bradley. Memory-efficient simulation of anelastic wave propagation. *Bull. Seism. Soc. Am.*, 91:520–531, 2001.

[47] S. Day and J. Minster. Numerical simulation of wave-fields using a Padé approximant method. *Geophys. J. Roy. Astr. Soc.*, 78:105–118, 1984.

[48] V. de la Cruz and T. Spanos. Seismic wave propagation in a porous medium. *Geophysics*, 50:15561565, 1985.

[49] J. de la Puente, M. Dumbser, M. Käser, and H. Igel. Discontinuous Galerkin methods for wave propagation in poroelastic media. *submitted to Geophysics*, 2007.

[50] J. de la Puente, M. Käser, M. Dumbser, and H. Igel. An arbitrary high order discontinuous Galerkin method for elastic waves on unstructured meshes IV: Anisotropy. *Geophys. J. Int.*, 169(3):1210–1228, 2007.

[51] E. Dormy and A. Tarantola. Numerical simulation of elastic wave propagation using a finite volume method. *J. Geophys. Res.*, 100:2123–2133, 1995.

[52] M. Dumbser. On the improvement of efficiency and storage requirements of the discontinuous Galerkin method for aeroacoustics. *PAMM*, 3:426–427, 2003.

[53] M. Dumbser. *Arbitrary High Order Schemes for the Solution of Hyperbolic Conservation Laws in Complex Domains*. PhD thesis, Universität Stuttgart, Institut für Aerodynamik und Gasdynamik, 2005.

[54] M. Dumbser, C. Enaux, and E. Toro. Explicit finite volume schemes of arbitrary high order of accuracy for hyperbolic systems with stiff source terms. *submitted*, 2007.

[55] M. Dumbser and M. Käser. An arbitrary high order discontinuous Galerkin method for elastic waves on unstructured meshes II: The three-dimensional case. *Geophys. J. Int.*, 167(1):319–336, 2006.

[56] M. Dumbser and M. Käser. Arbitrary high order non-oscillatory finite volume schemes on unstructured meshes for linear hyperbolic systems. *J. Comput. Phys.*, 221:693–723, 2007.

[57] M. Dumbser, M. Käser, and J. de la Puente. Arbitrary high order finite volume schemes for seismic wave propagation on unstructured meshes in 2D and 3D. *to appear in Geophys. J. Int.*, 2007.

[58] M. Dumbser, M. Käser, and E. Toro. An arbitrary high order discontinuous Galerkin method for elastic waves on unstructured meshes V: Local time stepping and p-adaptivity. *to appear in Geophys. J. Int.*, 2007.

[59] M. Dumbser and C. Munz. Building blocks for arbitrary high order discontinuous Galerkin schemes. *J. Sci. Comput.*, 27:215–230, 2006.

[60] M. Dumbser and C. D. Munz. ADER discontinuous Galerkin schemes for aeroacoustics. *Comptes Rendus Mécanique*, 333:683–687, 2005.

[61] M. Dumbser and C. D. Munz. Arbitrary high order discontinuous Galerkin schemes. In S. Cordier, T. Goudon, M. Gutnic, and E. Sonnendrucker, editors, *Numerical Methods for Hyperbolic and Kinetic Problems*, IRMA series in mathematics and theoretical physics, pages 295–333. EMS Publishing House, 2005.

[62] H. Emmerich. PSV-wave propagation in a medium with local heterogeneities: a hybrid formulation and its application. *Geophys. J. Int.*, 109:54–64, 1992.

[63] H. Emmerich and M. Korn. Incorporation of attenuation into time-domain computations of seismic wave fields. *Geophysics*, 52:1252–1264, 1987.

[64] A. Every and A. McCardy. *Numerical Data and Fundamental Relationships in Science and Technology, 29a.* Springer Berlin, 1992.

[65] B. Fornberg. *A Practical Guide to Pseudospectral Methods.* Cambridge University Press, 1996.

[66] H. Gao and J. Zhang. Parallel 3-D simulation of seismic wave propagation in heterogeneous anisotropic media: a grid method approach. *Geophys. J. Int.*, 165:875–888, 2006.

[67] K. Gledhill and D. Gubbins. SKS splitting and the seismic anisotropy of the mantle beneath the Hikurangi subduction zone. *Phys. Earth Planet. Inter.*, 95:227–236, 1996.

[68] R. Graves and S. Day. Stability and accuracy analysis of coarse-grain viscoelastic simulations. *Bull. Seism. Soc. Am.*, 93:283–300, 2003.

[69] Y. Gung and B. Romanowicz. Q tomography of the upper mantle using three component long-period waveforms. *Geophys. J. Int.*, 157:813–830, 2004.

[70] E. Hairer and G. Wanner. *Solving Ordinary Differential Equations II: Stiff and Differential-Algebraic Problems*. Springer Verlag, 1991.

[71] S. Hung and D. Forsyth. Modeling anisotropic wave propagation in oceanic inhomogeneous structures using the parallel multidomain pseudo-spectral method. *Geophys. J. Int.*, 133:726–740, 1998.

[72] H. Igel. Wave propagation in three-dimensional spherical sections by the Chebyshev spectral method. *Geophys. J. Int.*, 136:559–566, 1999.

[73] H. Igel, P. Mora, and B. Riollet. Anisotropic wave propagation through finite-difference grids. *Geophysics*, 60:1203–1216, 1995.

[74] G. Karypis and V. Kumar. Multilevel k-way partitioning scheme for irregular graphs. *J. Parallel Distrib. Comput.*, 48:96–129, 1998.

[75] M. Käser and M. Dumbser. An arbitrary high order discontinuous Galerkin method for elastic waves on unstructured meshes I: The two-dimensional isotropic case with external source terms. *Geophys. J. Int.*, 166(2):855–877, 2006.

[76] M. Käser, M. Dumbser, J. de la Puente, and H. Igel. An arbitrary high order discontinuous Galerkin method for elastic waves on unstructured meshes III: Viscoelastic attenuation. *Geophys. J. Int.*, 168(1):224–242, 2007.

[77] M. Käser, P. Mai, and M. Dumbser. On the accurate treatment of finite source rupture models using ADER-DG on tetrahedral meshes. *Bull. Seism. Soc. Am.*, 2006. in press.

[78] M. Kazi-Aoual, G. Bonnet, and P. Jouanna. Green's functions in an infinite transversely isotropic saturated poroelastc medium. *J. Acoust. Soc. Am.*, 84:1883–1889, 1988.

[79] J. Kendall and P. Silver. Constraints from seismic anisotropy on the nature of the lowermost mantle. *Nature*, 381:409–412, 1996.

[80] D. Komatitsch, C. Barnes, and J. Tromp. Simulation of anisotropic wave propagation based upon a spectral element method. *Geophysics*, 65:1251–1260, 2000.

[81] D. Komatitsch, C. Barnes, and J. Tromp. Spectral-element simulations of global seismic wave propagation - I. validation. *Geophys. J. Int.*, 149:390–412, 2002.

[82] D. Komatitsch and J. Tromp. Introduction to the spectral-element method for 3-D seismic wave propagation. *Geophys. J. Int.*, 139:806–822, 1999.

[83] D. Komatitsch and J. Tromp. Spectral-element simulations of global seismic wave propagation - i. validation. *Geophys. J. Int.*, 149:390–412, 2002.

[84] D. Komatitsch and J. Tromp. A perfectly matched layer absorbing boundary condition for the second-order seismic wave equation. *Geophys. J. Int.*, 154:146–153, 2003.

[85] D. Komatitsch and J. P. Vilotte. The spectral-element method: an efficient tool to simulate the seismic response of 2D and 3D geological structures. *Bull. Seism. Soc. Am.*, 88:368–392, 1998.

[86] J. Kristek and P. Moczo. Seismic-wave propagation in viscoelastic media with material discontinuities: A 3D fourth-order staggered-grid finite-difference modeling. *Bull. Seism. Soc. Am.*, 93:2273–2280, 2003.

[87] M. Kristeková, J. Kristek, P. Moczo, and S. Day. Misfit criteria for quantitative comparison of seismograms. *Bull. Seism. Soc. Am.*, 96(5):1836–1850, 2006.

[88] F. Krzikalla and T. Müller. Simulation of wave propagation in poroelastic structures using a modified finite-difference scheme. *69th Ann. Mtg., European Association of Geoscientists and Engineers, Extended abstracts*, page 327, 2007.

[89] A. R. Levander. Fourth-order finite difference P-SV seismograms. *Geophysics*, 53:1425–1436, 1988.

[90] R. LeVeque. *Finite Volume Methods for Hyperbolic Problems*. Cambridge University Press, Cambridge, 2002.

[91] R. LeVeque and H. Lee. A study of numerical methods for hyperbolic conservation laws with stiff source terms. *J. Comput. Phys.*, 86:187–210, 1990.

[92] H. Liu, D. Anderson, and H. Kanamori. Velocity dispersion due to anelasticity; implications for seismology and mantle composition. *Geophys. J. Roy. Astr. Soc.*, 47:41–58, 1976.

[93] R. Madariaga. Dynamics of an expanding circular fault. *Bull. Seism. Soc. Am.*, 65:163–182, 1976.

[94] K. Marfurt. Accuracy of finite-difference and finite-element modeling of the scalar and elastic wave equations. *Geophysics*, 49:533–549, 1984.

[95] Y. J. Masson, S. R. Pride, and K. T. Nihei. Finite difference modeling of Biot's poroelastic equations at seismic frequencies. *J. Geophys. Res.*, 111:B10305, doi:10.1029/2006JB004366, 2006.

[96] E. Mercerat, J.-P. Vilotte, and F. Sánchez-Sesma. Triangular spectral element simulation of two-dimensional elastic wave propagation using unstructured triangular grids. *Geophys. J. Int.*, 166:679–698, 2006.

[97] P. Moczo and P. Bard. Wave diffraction, amplification and differential motion near strong lateral discontinuities. *Bull. Seism. Soc. Am.*, 83:85–106, 1993.

[98] P. Moczo, E. Bystricky, J. Kristek, J. Carcione, and M. Bouchon. Hybrid modeling of P-SV seismic motion at inhomogeneous viscoelastic topographic structures. *Bull. Seism. Soc. Am.*, 87:1305–1323, 1997.

[99] P. Moczo and J. Kristek. On the rheological models used for time-domain methods of seismic wave propagation. *Geophys. Res. Lett.*, 32:L01306, 2005.

[100] P. Moczo, J. Kristek, M. Galis, P. Pazak, and M. Balazovjech. The finite-difference and finite-element modeling of seismic wave propagation and earthquake motion. *Acta physica slovaca*, 57(2):177–406, 2007.

[101] P. Moczo, J. Kristek, and L. Halada. *The Finite Difference Method for Seismologists. An Introduction.* Comenius University, Bratislava, 2004.

[102] P. Moczo, J. Kristek, V. Vavrycuk, R. J. Archuleta, and L. Halada. 3D heterogeneous staggered-grid finite-difference modeling of seismic motion with volume harmonic and arithmetic averaging of elastic moduli and densities. *Bull. Seism. Soc. Am.*, 92:3042–3066, 2002.

[103] R. Montelli, G. Nolet, F. Dahlen, G. Masters, E. Engdahl, and S. Hung. Finite-frequency tomography reveals a variety of mantle plumes. *Science*, 303:338–343, 2004.

[104] P. Mora. Modeling anisotropic seismic waves in 3-D. *59th Ann. Int. Mtg Exploration Geophysicists, expanded abstracts*, pages 1039–1043, 1989.

[105] G. Morris, R. Raitt, and G. Shor jr. Velocity anisotropy and delay-time maps of the mantle near Hawaii. *J Geophys. Res.*, 74:4300–4316, 1969.

[106] J. Nye. *Physical Properties of Crystals*. Oxford University Press, London, 1985.

[107] J. Nye. *An Introduction to Seismology, Earthquakes, and Earth Structure*. Blackwell Publishing, 2003.

[108] D. Okaya and T. McEvilly. Modeling waves in anisotropic media by a spectral element method. *Third international conference on mathematical and numerical aspects of wave propagation*, pages 289–298, 1995.

[109] D. Okaya and T. McEvilly. Elastic wave propagation in anisotropic crustal material possessing arbitrary internal tilt. *Geophys. J. Int.*, 153:344–358, 2003.

[110] T. Özdenvar and G. McMechan. Algorithms for staggered-grid computations for poroelastic, elastic, acoustic and scalar wave equations. *Geophys. Prospect.*, 45:403–420, 1997.

[111] R. Pasquetti and F. Rapetti. Spectral element methods on unstructured meshes: Comparisons and recent advances. *J. Sci. Comput.*, 27:377–387, 2006.

[112] T. Plona. Observation of a second bulk compressional wave in a porous medium at ultrasonic frequencies. *Appl. Phys. Lett.*, 36:259–261, 1980.

[113] G. Postma. Wave propagation in a stratified medium. *Geophysics*, 20:780–806, 1955.

[114] E. Priolo, J. M. Carcione, and G. Seriani. Numerical simulation of interface waves by high-order spectral modeling techniques. *J. acoust. Soc. Am.*, 95:681–693, 1994.

[115] W. H. Reed and T. R. Hill. Triangular mesh methods for the neutron transport equation. Technical Report LA-UR-73-479, Los Alamos Scientic Laboratory, 1973.

[116] J. Ritsema, H. van Heijst, and J. Woodhouse. Complex shear velocity structure imaged beneath Africa and Iceland. *Science*, 286:1925–1928, 1999.

[117] E. H. Saenger and T. Bohlen. Finite-difference modeling of viscoelastic and anisotropic wave propagation using the rotated staggered grid. *Geophysics*, 69:583–591, 2004.

[118] E. H. Saenger, S. A. Shapiro, and Y. Keehm. Seismic effects of viscous Biot-coupling, finite difference simulations on micro-scale. *Geophys. Res. Lett.*, 32:L14310, 2005.

[119] J. Santos, J. Douglas jr., and J. Corberó. Static and dynamic behaviour of a porous solid saturated by a two-phase fluid. *J. Acoust. Soc. Am.*, 87:1428–1438, 1990.

[120] H. Schmidt and G. Tango. Efficient global matrix approach to the computation of synthetic seismograms. *Geophys. J. Roy. Astr. Soc.*, 84:331–359, 1986.

[121] T. Schwartzkopff, M. Dumbser, and C. D. Munz. Fast high order ADER schemes for linear hyperbolic equations. *Journal of Computational Physics*, 197:532–539, 2004.

[122] T. Schwartzkopff, C. D. Munz, and E. F. Toro. ADER: A high-order approach for linear hyperbolic systems in 2D. *J. Sci. Comput.*, 17:231–240, 2002.

[123] G. Seriani. 3-D large-scale wave propagation modeling by a spectral-element method on a Cray T3E multiprocessor. *Comput. Methods Appl. Mech. Eng.*, 164:235–247, 1998.

[124] L. Song, A. Every, and C. Wright. Linearized approximations for phase velocities of elastic waves in weakly anisotropic media. *J. Phys. D: Appl. Phys.*, 34:2052–2062, 2001.

[125] M. Stern, A. Bedford, and H. Millwater. Wave reflection from a sediment layer with depth-dependent properties. *J. Acoust. Soc. Am.*, 77:1781–1788, 1985.

[126] L. Stixrude and R. Cohen. High-pressure elasticity of iron and anisotropy of Earth's inner core. *Science*, 267:1972–1975, 1995.

[127] W. Sun and H. Yang. Elastic wavefield calculation for heterogeneous anistropic porous media using the 3-D irregular-grid finite-difference. *A. Mech. Sol. Sin.*, 16:283–299, 2003.

[128] E. Tessmer. 3-D seismic modelling of general material anisotropy in the presence of the free surface by a Chebyshev spectral method. *Geophys. J. Int.*, 121:557–575, 1995.

[129] E. Tessmer and D. Kosloff. 3-D elastic modelling with surface topography by a Chebyshev spectral method. *Geophysics*, 59:464–473, 1994.

[130] L. Thomsen. Weak elastic anisotropy. *Geophysics*, 51:1954–1966, 1986.

[131] V. A. Titarev and E. F. Toro. ADER: Arbitrary high order Godunov approach. *J. Sci. Comput.*, 17:609–618, 2002.

[132] E. Toro and V. Titarev. Solution of the generalized Riemann problem for advection-reaction equations. *Proc. Roy. Soc. London*, pages 271–281, 2002.

[133] E. F. Toro. *Riemann Solvers and Numerical Methods for Fluid Dynamics*. Springer, Berlin, 1999.

[134] E. F. Toro, R. C. Millington, and L. A. M. Nejad. Towards very high order godunov schemes. In E. F. Toro, editor, *Godunov methods; Theory and applications*, pages 907–940, Oxford, 2001. Kluwer Academic Plenum Publishers. International Conference.

[135] J. van der Vegt and H. van der Ven. Space-time discontinuous Galerkin finite-element method with dynamics grid motion for inviscid compressible flows, part I. general formulation. *J. Comput. Phys.*, 182:546–585, 2002.

[136] J. Virieux. SH-wave propagation in heterogeneous media: Velocity-stress finite-difference method. *Geophysics*, 49:1933–1942, 1984.

[137] J. Virieux. P-SV wave propagation in heterogeneous media: Velocity-stress finite-difference method. *Geophysics*, 51:889–901, 1986.

[138] D. Winterstein. Velocity anisotropy: terminology for geophysicists. *Geophysics*, 52:810–814, 1987.

[139] C. Wolfe and S. Solomon. Shear-wave splitting and implications for mantle flow beneath the MELT region of the east Pacific rise. *Science*, 280:1230–1232, 1998.

[140] J. Zhang. Quadrangle-grid velocity-stress finite difference method for poroelastic wave equations. *Geophys. J. Int.*, 139:171–182, 1999.

[141] X. Zhu and G. McMechan. Finite-difference modelling of the seismic response of fluid-saturated, porous, elastic media using Biot theory. *Geophysics*, 56:328–339, 1991.

[142] O. C. Zienkiewicz and R. L. Taylor. *The Finite Element Method*, volume 1. McGraw Hill, New York, 1989.

Curriculum Vitae

Name: Josep de la Puente Álvarez

Geburtsdatum: 26. September 1979

Geburtsort: Barcelona, Spanien

Familienstand: Ledig

Staatsangehörigkeit: Spanisch

Schulbildung

1984-1994: Grundschule "CEIP Príncep de Viana" in Barcelona

1994-1999: Gymnasium "IES Príncep de Viana" in Barcelona

1999: C.O.U. "IES Príncep de Viana" in Barcelona (Abitur)

Ausbildung

1999-2004: Studium der Physik an der Universitat de Barcelona (Diplom)

März-Juli 2004: Wissenschaftliche Mitarbeiter an der Universitat de Barcelona

2004-2007: Doktorarbeit zum Thema "Seismic Wave Simulation for Complex Rheologies on Unstructured Meshes" im Geophysik an der Ludwig-Maximilians-Universität

Publikationen

De la Puente, J., M. Dumbser, M. Käser and H. Igel (2007), "Discontinuous Galerkin Methods for Wave Propagation in Poroelastic Media", submitted to *Geophysics*.

De la Puente, J., M. Käser, M. Dumbser, and H. Igel (2007), "An Arbitrary High Order Discontinuous Galerkin Method for Elastic Waves on Unstructured Meshes IV: Anisotropy", *Geophysical Journal International*, 169 (3), 1210-1228.

Dumbser, M., M. Käser, and J. de la Puente (2007), "Arbitrary High Order Finite Volume Schemes for Seismic Wave Propagation on Unstructured Meshes in 2D and 3D", *Geophysical Journal International*, in press.

Käser, M., M. Dumbser, J. de la Puente and H. Igel (2006): "An Arbitrary High Order Discontinuous Galerkin Method for Elastic Waves on Unstructured Meshes III: Viscoelastic Attenuation", *Geophysical Journal International*, 168, 224-242.

Käser, M., H. Igel, J. de la Puente, B. Schuberth and H.P. Bunge (2006): "Erdbebenforschung durch Höchstleistungsrechnen Moderne Supercomputer ermöglichen die Simulationen realistischer Erdbeben-Szenarien unter Berücksichtigung komplizierter, geophysikalischer Erdmodelle", Technical Report 02/2006 in *Akademie Aktuell* of the BAYERISCHE AKADEMIE DER WISSENSCHAFTEN.

Käser, M., M. Dumbser and J. de la Puente (2006): "An Efficient ADER-DG Method for 3-Dimensional Seismic Wave Propagation in Media with Complex Geometry", 3rd International Symposium on *THE EFFECTS OF SURFACE GEOLOGY ON SEISMIC MOTION*, ESG 2006 Grenoble, vol. 1, pp. 455-464, Laboratoire Central des Ponts et Chausses.